Development of a characterization technique, the Time-of-Flight electron Beam Induced Current, and design of diamond detectors for the identification of short range particles.

Alexandre Portier

To cite this version:

Alexandre Portier. Development of a characterization technique, the Time-of-Flight electron Beam Induced Current, and design of diamond detectors for the identification of short range particles.. Physics [physics]. Université Grenoble Alpes [2020-..], 2023. English. NNT : 2023GRALY026 . tel-04166868

HAL Id: tel-04166868
https://theses.hal.science/tel-04166868v1

Submitted on 20 Jul 2023

THÈSE

Pour obtenir le grade de

DOCTEUR DE L'UNIVERSITÉ GRENOBLE ALPES

École doctorale : PHYS - Physique
Spécialité : Physique Subatomique et Astroparticules
Unité de recherche : Laboratoire de Physique Subatomique et Cosmologie

Développement d'une technique de caractérisation, le courant induit par faisceau d'électrons à temps de vol, et conception de détecteurs en diamant pour l'identification des particules à faible parcours

Development of a characterization technique, the Time-of-Flight electron Beam Induced Current, and design of diamond detectors for the identification of short range particles.

Présentée par :

Alexandre PORTIER

Direction de thèse :

Marie-Laure GALLIN-MARTEL Directeur de recherche, CNRS Délégation Alpes	Directrice de thèse
Julien PERNOT Professeur des Universités, Université Grenoble Alpes	Co-directeur de thèse

Rapporteurs :

JOCELYN ACHARD
Professeur des Universités, UNIVERSITE SORBONNE PARIS NORD
PHILIPPE BERGONZO
Docteur en sciences HDR, Cornes Technologies Ltd

Thèse soutenue publiquement le **27 mars 2023**, devant le jury composé de :

JOCELYN ACHARD Professeur des Universités, UNIVERSITE SORBONNE PARIS NORD	Rapporteur
DANIEL ARAUJO Professeur, Universidad de Cádiz	Examinateur
PHILIPPE BERGONZO Docteur en sciences HDR, Cornes Technologies Ltd	Rapporteur
ANA LACOSTE Professeure des Universités, UNIVERSITE GRENOBLE ALPES	Présidente
HEINZ PERNEGGER Docteur en sciences, CERN	Examinateur
HITOSHI UMEZAWA Docteur en sciences, National Institute of Adv. Ind. Sc. Tech	Examinateur

Invités :

SATOSHI KOIZUMI
Docteur en sciences, National Institute for Materials Science (NIMS)

Résumé

Les travaux menés au cours de cette thèse portent sur la mise en œuvre et le développement d'outils de caractérisation de dispositifs instrumentaux (télescope, jonction *pn*), en technologie diamant destinés à la détection de particules à faible parcours dans la matière (particules alpha, fragments de fission, ...) pour des applications au domaine de la physique nucléaire et de la radioprotection. Dans un premier temps, des substrats en diamant synthétique ont été caractérisés à température ambiante. Leurs excellentes propriétés de transport (mobilités et vitesses de saturation élevées) et de collecte de charges (100 % d'efficacité de collection de charge) ont été mis en évidence. En parallèle, un banc de tests permettant d'induire un courant dans un échantillon diamant à l'aide d'un faisceau d'électrons pulsé (eBIC pour electron Beam Induce Current) a été mis au point. L'objectif était de reproduire un dépôt d'énergie similaire à celui de particules faiblement pénétrantes et d'étudier les processus de collection de charge dans les détecteurs en diamant. Cette technique de ToF – eBIC (ToF pour Time of Flight) a ainsi permis de caractériser les propriétés de transport de charges du diamant sur une large gamme de températures (de 13 à 300 K) et d'étayer l'état de l'art grâce à une mesure de la mobilité à faible champs des trous de $(1.03 \pm 0.04) \times 10^6\,\mathrm{cm^2/(V{\cdot}s)}$ à 13 K, ouvrant ainsi la voie à de futures applications liées notamment au transport d'informations quantiques. Par ailleurs, un télescope ΔE-E innovant en technologie diamant a été conçu et fabriqué. Ce type de détecteur, permettant l'identification de particules incidentes, joue un rôle crucial en physique nucléaire alliant compacité, bonne résistance aux radiations et efficacité de détection. Une particule incidente, à faible parcours, va traverser l'étage ΔE et être stoppée dans l'étage E. Son identification s'effectuera par comparaison des deux dépôts d'énergie. Le défi de cet aspect du projet a résidé en la conception d'une électrode en diamant fortement dopée en bore, qui surmonte l'étage E, suivie par une reprise d'épitaxie et la croissance d'une couche diamant avec un dopage résiduel pour former l'étage ΔE. Les performances du détecteur ΔE-E, évaluées en laboratoire, avec une source alpha, ont pu être comparées avec celles d'une jonction *pn* en diamant, fabriquée au Japon, et ce dans le cadre d'une collaboration internationale dans laquelle le projet s'est inscrit.

Abstract

The work carried out during this thesis concerns the implementation and the development of characterization tools for instrumental devices (telescope, *pn* junction), in diamond technology intended for the detection of particles with a short range in matter (alpha particles, fission fragments, ...) for applications in the field of nuclear physics and radioprotection. In a first step, synthetic diamond substrates were characterized at room temperature. Their excellent transport properties (high mobilities and saturation velocity) and charge collection properties (100 % charge collection efficiency) were demonstrated. In parallel, a test bench allowing to induce a current in a diamond sample using a pulsed electron beam (eBIC for electron Beam Induce Current) was developed. The objective was to reproduce an energy deposition similar to weakly penetrating particles and to study the charge collection processes in diamond detectors. This ToF - eBIC (ToF for Time of Flight) technique allowed to characterize the charge transport properties of diamond over a wide temperature range (from 13 to 300 K) and to support the state of the art with a hole low field mobility measurement of $(1.03 \pm 0.04) \times 10^6\,\mathrm{cm^2/(V{\cdot}s)}$ at

13 K, thus opening the way to future applications related to quantum information transport. In addition, an innovative ΔE-E telescope in diamond technology was designed and built. This type of detector, allowing the identification of incident particles, has a crucial role in nuclear physics combining compactness, good resistance to radiation and detection efficiency. An incident particle, with a short path, will pass through the ΔE stage and be stopped in the E stage. Its identification will be done by comparing the two energy deposits. The challenge in this aspect of the project was the design of a heavily boron-doped diamond electrode overlying the E-stage, followed by epitaxial rework and growth of a diamond layer with residual doping to form the ΔE stage. The performance of the ΔE-E detector, evaluated in the laboratory, with an alpha source, could be compared with that of a diamond *pn* junction, fabricated in Japan, as part of an international collaboration in which the project was involved.

Acknowledgement

A PhD is an adventure that I would recommend to anyone who is curious about science. But I need to warn the newcomers: it's not a piece of cake, there are hard times ahead, and as in any epic story, you need great fellow adventurers to deal with these difficulties. At the end of my journey, there are many different people I would like to sincerely thank.

First of all, I would like to thank Dr. Arnaud Lucotte and Pr. Laurent Derome, the directors of LPSC, for welcoming me as a PhD student.

Then, I would like to sincerely thank the people who agreed to be part of my PhD jury and evaluate this work. Thank you very much to Pr. Ana Lacoste for agreeing to chair my PhD jury. Many thanks to Pr. Daniel Araujo, Dr. Heiz Pernegger and Dr. Hitoshi Umezawa for examining this work. I would also like to extend my warmest thanks to Pr. Jocelyn Achard and Dr. Philippe Bergonzo for their careful review of my thesis manuscript, and for their helpful corrections and suggestions. In particular, thank you very much to Dr. Philippe Bergonzo for our fruitful conversations. Finally, I would like to thank Dr. Satoshi Koizumi for attending my defense from Japan as a guest member.

I would also like to sincerely thanks the members of the collaboration PRC CNRS and JSPS & TYL IN2P3, and in particular Dr. Satoshi Koizumi and Dr. Takehiro Shimaoka for letting me conduct experiments on their device. It was a pleasure to be able to collaborate with you.

Je souhaite maintenant remercier mes directeurs de thèse Marie-Laure Gallin-Martel et Julien Pernot qui m'ont permis d'accomplir ce travail et qui ont toujours été à mon écoute. Marie-Laure, merci d'avoir été là au quotidien dans les moments heureux et ceux plus compliqués. Julien, merci pour avoir été là quand j'avais besoin de toi, tes idées ambitieuses et tes conseils avisés. Vous êtes pour moi les parents spirituels de ce travail de thèse.

Je desire à présent remercier Fabrice Donatini sans qui ce travail n'aurait pas été possible. Tu as été la clé de voute de cette thèse. Je suis ravi d'avoir pu maniper à tes côtés. Avec toi, toutes les expériences semblaient plus faciles.

Je voudrais aussi remercier chaleureusement Denis Dauverne pour ses avis éclairés et sa rigueur. Merci pour ton investissement dans ce projet et pour tout ce que tu as apporté.

Je souhaite aussi remercier Juliette Letellier pour avoir participé activement à ce projet et pour m'avoir formé sur les différentes techniques de gravure. Merci de ta patience et de ta bonne humeur.

Je souhaite bien évidemment remercier tout les équiques physique nucléaire et applications médicales et semi-conducteur à grand gap. Un grand merci à Ludovic, Rachel, Sara, Yannik, Olivier et Gabriella pour m'avoir accueilli au sein l'équipe. Un grand merci à tous les doctorants de l'équipe, Sebby, Nico, Maxou, Pierre, Robin, Victor, Adélie et Claire. Faire une thèse avec des gens que l'on aime est un vrai plaisir. C'est grâce à vous que j'en garde un si bon souvenir. Je souhaite remercier particulièrement Maxou pour avoir été le collègue de bureau rêvé et Pierre pour n'avoir jamais refusé de m'héberger alors qu'il avait toutes les raisons de le faire. Je souhaite dire merci à David, Etienne, Etienne, Gwénolé et Philippe et aux doctorants de l'équipe SC2G : Jesus, Rémy, Sylvain, Béa, Martin, Duc-Duy, Hussein, Julien, Coralie et tous ceux que j'oublie. Merci pour tous les bons moments passés ensemble.

Un grand merci à toute l'équipe de DIAMFAB d'avoir été à mon écoute et pour nos échanges fructueux. Je tiens aussi à remercier l'équipe de NANOFAB, en particulier Bruno, pour m'avoir ouvert les portes de la salle blanche et pour m'avoir formé sur les différentes installations.

Finalement je souhaite remercier les services éléctronique et instrumentation du LPSC sans qui nous aurions bien du mal à utiliser nos détecteurs diamants.

Merci aussi aux personnes du LP2i Bordeaux, et en particulier Philippe, Stephanie et Jean, qui nous ont permis de réaliser des expériences sur la plateforme à AIFIRA.

Je souhaite bien évidemment remercier toute ma famille et mes amis qui m'ont accompagné dans cette aventure. Je vous remercie infiniment d'avoir toujours été là pour moi. I would also like to thank my in-laws for welcoming me kindly in their family.

And finally, I would like to thank my wonderful wife Maggie. Maggie, my PhD is also our story: I met you at the beginning of this journey and married you at the end. Thank you for always encouraging me and making me so happy.

Acronyms

- ***CASINO*** *monte CArlo SImulation of electroN trajectory in sOlids*
- ***CBM*** *Conduction Band Minimum*
- ***CCE*** *Charge Collection Efficiency*
- ***CVD*** *Chemical Vapor Deposition*
- ***DOI*** *Diamond On Iridium*
- ***eBIC*** *electron Beam Induced Current*
- ***ESRF*** *European Synchrotron Radiation Facility*
- ***FWHM*** *Full Width at Half Maximum*
- ***GGD*** *General Gaussian Distribution*
- ***GND*** *Ground potential*
- ***HPHT*** *High-Pressure High-Temperature*
- ***HV*** *High Voltage*
- ***IBIC*** *Ion Beam Induced Current*
- ***ILL*** *Institut Laue-Langevin*
- ***LP2i*** *Laboratoire de Physique des Deux Infinis de Bordeaux*
- ***LPSC*** *Laboratoire de Physique Subatomique et de Cosmologie*
- ***MIP*** *Minimum Ionizing Particle*
- ***MPCVD*** *Microwave Plasma Enhanced Chemical Vapor Deposition*
- ***PA*** *Preamplifier*
- ***pCVD*** *polycrystalline CVD*
- ***RMS*** *Root Mean Square*
- ***ROE*** *Read-Out Electronics*
- ***sCVD*** *single-crystal CVD*
- ***SEM*** *Scanning Electron Microscope*
- ***SNR*** *Signal over Noise Ratio*
- ***SRIM*** *Stopping and Ranges of Ions in Matter*

- ***TCT*** *Transient Current Technique*
- ***LET*** *Linear Energy Transfer*
- ***ToF*** *Time-of-Flight*
- ***ToF*** *Time-of-Flight electron Beam Induced Current*
- ***VBM*** *Valence Band Maximum*
- ***XBIC*** *X-ray Beam Induced Current*

Contents

Introduction

Semiconductors have contributed to technological breakthroughs in numerous fields of physics, such as electronic development, light-emitting diode evolution, power generation, ionized particle detection, among others. For detecting ionizing particles, semiconductors provide a compact solution for high-energy resolution and fast measurement. Nowadays, silicon is still mainly used for these applications, but new physics experiments required the development of faster and radiation-hard devices. Ultra-wide band gap semiconductors have the desired characteristics. Among them, diamond could be the most promising. In fact, its impressive properties (high resistivity, large breakdown field, radiation hardness, excellent charge transport properties) make this material well-suited for fast counting of charged particles, for applications in high radiation environments, or for dosimetry with large spatial gradients. Nevertheless, some limitations on diamond's use as a semiconductor have been observed experimentally. In particular, when studying particles stopped in the bulk diamond, a reduction of the collected charge has been reported. This phenomenon, caused by inhomogeneous trapping of the free carriers, is known as polarization effects. It is essential to better understand and limit these polarization effects in order to develop state-of-the-art detectors. At the same time, the properties of diamond, especially at cryogenic temperatures, need to be studied in order to achieve specific developments such as the coherent transport of charge carriers for quantum information applications.

This PhD project, which is part of an IDEX project (DIATEL), has been carried out within the Laboratoire de Physique Subatomique et de Cosmologie (LPSC), Grenoble, and the Institut Néel, Grenoble. It focuses on studying the interaction of low range charged particles with diamond samples to achieve new characterization procedures and innovative detectors. In particular, this project aims to develop a new technique to characterize the diamond sample over a wide range of temperatures and electric fields while limiting polarization effects. This setup can be used to characterize and improve new designs of diamond devices. In this context, two detectors dedicated to the detection of short-range particles will be studied. First, a monolithic diamond telescope ΔE-E composed of two stages: a thin top layer, ΔE, will serve as an energy loss transmission detector, while a thick substrate, E, will serve as a calorimeter for the residual energy of the particles. Then, a *pn* junction, fabricated at NIMS (National Institute for Materials Science) in Tsukuba (Japan), which is a promising alternative for high performance detectors, allowing use with low bias voltage, increased charge carrier collection efficiency, and charge amplification (Schottky).

The present document reports the different developments realized during this PhD work. It is organized as follows:

1. The Chapter 1 presents the characteristics of diamond as a particle detector. In a first time, I will introduce the properties which make diamond so interesting for particle detection. Afterwards, the techniques used to produce synthetic diamond and the dopants incorporated to obtain n-type and p-type devices will be detailed. Then, I will focus on interactions of charged particles in matter and the use of diamond as an ionization chamber. In particular, I will describe the electrical signal induced by such a system. The impact of defects on the induced current and the collected charge will also be highlighted

and methods to limit these effects will be discussed. Finally, I will present a commonly Time-of-Flight technique used method to characterize the charge transport properties.

2. The Chapter 2 describes different methods used to characterize the diamond samples with radioactive sources. After explaining the characteristics of the diamond samples and the readout electronics involved, the encapsulation steps are presented. Then, three characterization methods will be presented. The first one consists in characterizing the leakage current of the samples. The other two are based on a test bench using an alpha source to study the transport and charge collection properties in diamond. The limitations of these methods will be finally discussed.

3. The Chapter 3 presents a new setup: the ToF-eBIC (Time-of-Flight electron Beam Induced Current). It is based on a Scanning Electron Microscope, which used the current induced by the primary electrons to investigate the charge and transport properties of intrinsic diamond. The implemented technique allows a better control on the injection conditions and enables the development of complex bias voltage cycling procedures. Thus the polarization effect can be limited and the transport properties accurately estimated on large electric field ranges. The setup was also used to investigate the properties of diamond at low temperatures. Finally, the mapping of charge collection will be exposed, opening the way to other applications: characterization of defects induced during growth or its exposure to ionizing radiation, optimization of the design of pad and strip detectors, among others.

4. The Chapter 4 describes the conception, fabrication and characterization of the monolithic diamond ΔE-E telescope. After explaining the benefits of such detectors and reporting on existing devices, the requirements of this development will be exposed. Then, the design of the detector meeting the requirements of the project will be reported and the fabrication steps will be detailed. The operation and performances of this detector, as well as those of the Japanese *pn* junction, have been studied under different irradiation sources: eBIC (electron Beam Induced Current), ToF-eBIC, alpha spectroscopy, IBIC (Ion Beam Induced Current). These experiments have highlighted possible improvements for the development of future prototypes.

This study is cross disciplinary between solid state physics and nuclear physics. The objective of this work is twofold: to implement a new method to characterize diamonds over a wide range of temperatures and electric fields and to promote as diamond material for the design of innovative detectors. The ultimate goal is to address current challenges in nuclear physics and electronics in a societal context combining medical applications and environmental issues.

1

Diamond detector

Contents

This chapter deals with the use of diamond as a particle detector. I will discuss of the properties of intrinsic diamond at room temperature, the different growth techniques and doping. Then, after a brief presentation of the interaction of short range particles in matter, I will present the concept of solid-state ionization chamber for diamond detectors. The generated signal and the impact of traps will be emphasized. Finally, I will conclude on the transient current techniques, used to study the transport properties of charge carriers.

1.1 Diamond properties

1.1.1 Crystalline structure

Diamond is a specific arrangement of carbon atoms (Z = 6) which is stable at high pressure. Its exceptional properties are due to its crystallographic structure. As described in the Figure 1.1, the latter is equivalent to two Face-Centred Cubic (FCC) lattices shifted by a vector ($a/4$, $a/4$, $a/4$), with $a = 3.567\,\text{Å}$ the lattice parameter. Due to the carbon low atomic number, the closest carbon atoms covalent bond length is equal to 1.545 Å. The atomic packing factor of the diamond, equal to 0.34, is small compared to other common crystalline structures (HCP: 0.74[1], FCC: 0.74, BCC: 0.68[2]) and its atomic density, equal to 1.77×10^{23} atoms/cm^3, is the highest on Earth. Diamond is also relatively dense (about 3.52 g/cm^3). Diamond is well known for its hardness (10 on the Mohs scale), which can be explained by the high strength of the bound. The latter property explains also the high radiation hardness of diamond and especially its very high displacement energy (43 eV).

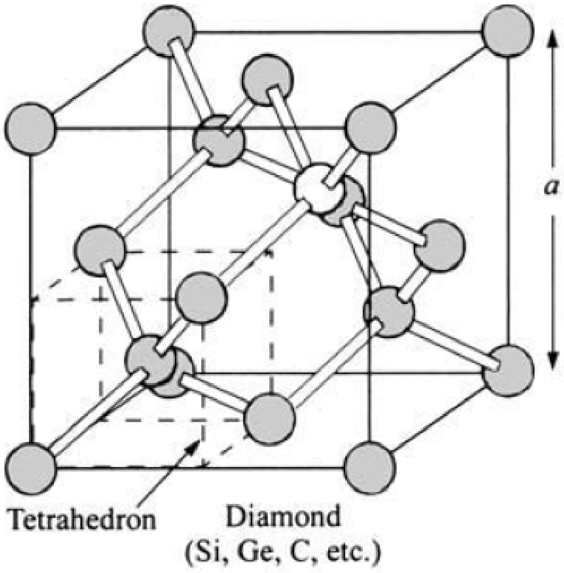

Figure 1.1: The diamond cubic crystal structure from [Sze, 2006].

---

[1] Hexagonal close-packed

[2] Body-centered cubic

1.1.2 Band structure

The diamond has an indirect gap with an energy of $E_g = 5.47\,\mathrm{eV}$. Regarding the relatively high energy of the forbidden band (see Table 1.1), diamond is considered as an ultra-wide bandgap semiconductor.

In a semiconductor, the electrons and the holes can only occupied specific energy levels in the k—-space (wave vector space). In particular, there are specific energy levels which cannot be occupied by the charge carriers (forbidden band). This relation between the energy and the wave vector k is described by the band structure of the semiconductor.

The diamond band structure is represented in Figure 1.2 (a). The Valence Band Maximum (VBM) is obtained at the point Γ. On the contrary, the Conduction Band Minimum (CBM) is between the points Γ and X of the Brillouin zone (indirect gap). As mentioned in [Pomorski, 2008], *"Due to the crystal symmetry, the CB*[1] *of diamond contains six equivalent minima (valleys) located along the <100> crystallographic directions"* (see Figure 1.2 (b)). Due to the ellipsoidal shape of the valleys, the longitudinal and transverse effective masses of the electrons are different. Therefore, when an electric field is applied in one of these crystal directions ([100] in the Figure 1.2 (b)) the electron transport properties can differ regarding if the electrons are located in valleys longitudinal (in blue) or transverse (in red) to the electric field [Isberg, 2013]. This phenomenon occurs only in specific conditions (low temperatures and low electric fields) and is not observed at room temperature. This phenomenon is discussed with more details in Section 3.3.

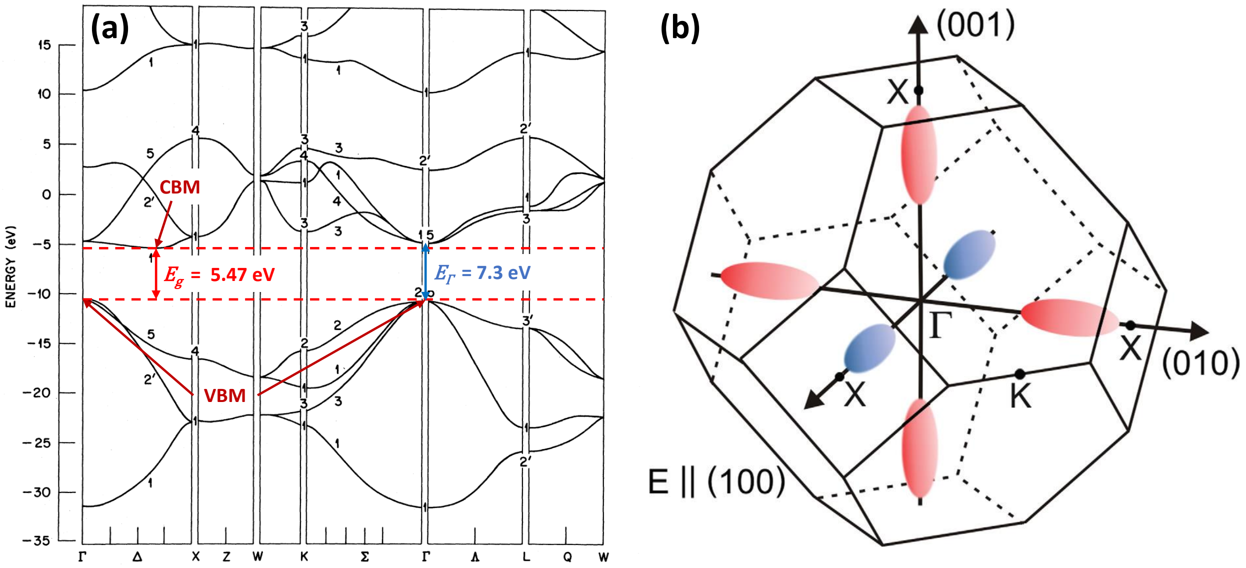

Figure 1.2: (a): Diamond band structure at 300 K from [Pomorski, 2008]. (b) first Brillouin zone for diamond with the six equivalent conduction band valleys are highlighted from [Isberg, 2012]. The (100) valleys in blue are orientated along the electric field.

---

[1] CB: Conduction Band | VB: Valence Band

1.1.3 Phonons in diamond

Phonons are lattice vibrations that occur at temperatures above 0 K. They can be induced by an optical excitation, stress relaxation in the medium or thermal excitation. Two types of phonons can be distinguished: the acoustic and the optical phonons. The first corresponds to coherent movements of lattice atoms out of their equilibrium positions, while the second corresponds to out-of-phase movements of lattice atoms and occur only in crystals with more than one atom per unit cell. The vibrations occurring along the propagation direction are called longitudinal phonons, the ones occurring in perpendicular planes are called transverse phonons. It is usual to use the following abbreviation: LA for Longitudinal Acoustic, TA for Transverse Acoustic, LO for Longitudinal Optic and TO for Transverse Optic. The dispersion relation of phonons in diamond is illustrated in Figure 1.3.

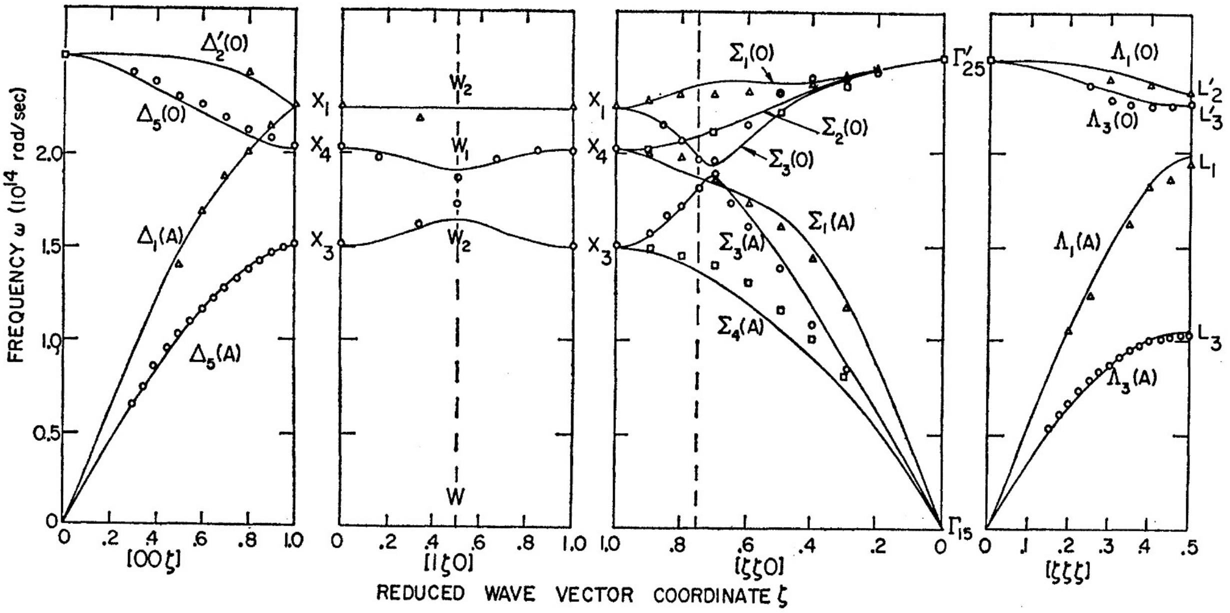

Figure 1.3: Phonon dispersion relation in diamond. The acoustic and optical branches are respectively indicated with a "(A)" and a "(O)". Extracted from [Warren, 1967].

In this figure, the branches indicated by "(A)" and "(O)" corresponds respectively to the acoustic and optical phonon dispersion curves. The acoustic phonons frequency is proportional to the coordinates of the wave vector around the Γ point, whereas the optical phonons appear only at relatively high frequencies (corresponding energy: ∼ 0.16 eV). This value explains the relatively high saturation drift velocities of charge carriers in diamonds [Ferry, 1975]. The phonon scattering have also a significant impact on the temperature dependence of the charge carrier low-field mobility (this phenomenon is discussed with more detailed in Subsection 3.3). Finally, the phonons are responsible of the impressive thermal conductivity of the diamond (20 W/(m·K), five time larger than the one of copper).

1.1.4 Main diamond parameters

The main characteristics of diamond are presented in the Table 1.1.

Table 1.1: Comparison of the Diamond, silicon (Si), germanium (Ge) and silicon carbide (4H-SiC) properties at 300 K. Table extracted from [Curtoni, 2020].

Properties	**Diamond**	**Si**	**Ge**	**4H-SiC**
Band gap [eV]	5.47	1.12	0.67	3.26
Resistivity [Ω·cm]	$> 10^{13}$	$2.3 \cdot 10^5$	50	$> 10^5$
Dielectric strength [V/cm]	10^7	$3 \cdot 10^5$	10^5	$5 \cdot 10^6$
Electron mobility [$cm^2/(V{\cdot}s)$]	2000*	1350	3900	1000
Hole mobility [$cm^2/(V{\cdot}s)$]	2300**	480	1900	115
Electron lifetime [ns]	$10^{-1} - 10^3$	$> 10^6$	$> 10^6$	500
Hole lifetime [ns]	$10^{-1} - 10^3$	10^6	$2 \cdot 10^6$	700
Saturation velocity [cm/s]	10^7	$1 \cdot 10^7$	$6 \cdot 10^6$	$3.3 \cdot 10^6$
Density [g/cm^3]	3.517	2.33	5.33	3.21
Average atomic number	6	14	32	10
Relative dielectric constant	5.72	11.9	16	9.7
Displacement energy [eV]	43	13 - 20	28	20 - 35
Thermal conductivity [W/(m·K)]	2000	150	60.2	120
Electron/hole pair creation energy [eV]	13.1†	3.62	2.96	7.8
Average number of electron-hole pairs created per MIP and per µm	36	89	249	51
Radiation length [cm]	12.2	9.36	2.3	8.7

* Common value. The measurements fluctuate between 1900 and 4500 $cm^2/(V{\cdot}s)$.

** Common value. The measurements fluctuate between 1800 and 3800 $cm^2/(V{\cdot}s)$

† Preponderant value. The measurements fluctuate between 11.6 and 16 eV

Compared to other materials commonly used to achieve particle detection, diamond has a high thermal conductivity (easy to evacuate the heat), a very good dielectric strength (high electric fields can be applied) and an impressive resistivity (low noise on signal acquisition). The charge carrier transport properties at room temperature (mobility and drift velocity) allowed to achieve very fast measurements. Finally, the relatively low dielectric constant induces a lower capacitance compared to other semiconductors, and allows fast time measurements.

1.1.5 Diamond classification

Diamond can be classified depending on their nitrogen concentrations. Diamond samples with nitrogen concentration measurable by infrared absorption spectroscopy ([N] $>$ 5 ppm; usually between 100 and 3000 ppm) are referred as type I. The other are classified as type II. The majority (98 %) of the natural diamond samples are classified as type I. Nevertheless, the type II diamonds are more suitable for particle detection (see discussion in Subsection 1.3.4). These diamonds are divided in two categories: type IIa and IIb. The purest diamonds are classified as type IIa. In these diamonds the nitrogen is the main impurity. In the type IIb diamonds, the boron is the main impurity. Depending on the boron concentration, these diamonds may have a blue color. Even some natural diamonds are type II, their cost (extraction and selection) is substantial. More their impurity concentrations and internal stress can vary from a sample to another and thus modify significantly their electric properties. Therefore, to reduce cost and control sample reproducibility, synthetic diamonds are preferred.

1.2 Synthetic Diamond Growth

There are two main techniques to produce synthetic diamonds: High Pressure, High Temperature (HPHT) and Chemical Vapor Deposition (CVD) techniques. Historically, HPHT was developed prior to diamond CVD, and allows to obtain samples with larger surfaces. Recent improvements in the CVD technique make it particularly interesting for applications in power electronics or particle detection. In the two following subsections, these techniques will be introduced and their benefits highlighted.

1.2.1 High Pressure, High Temperature growth technique

At atmospheric pressure and room temperature, the diamond is a metastable carbon atom arrangement (see carbon phase diagram represented in Figure 1.4). The natural diamonds were produced in the Earth's mantle under high temperature and high pressure conditions. The HPHT technique aims to reproduce these conditions. The temperatures and pressures involved are approximately between 600 to 1800 °C and 8 to 10 GPa, respectively. The use of a metallic solvent, called catalyst, allows to reduce the temperatures and pressures involved (see Figure 1.4).

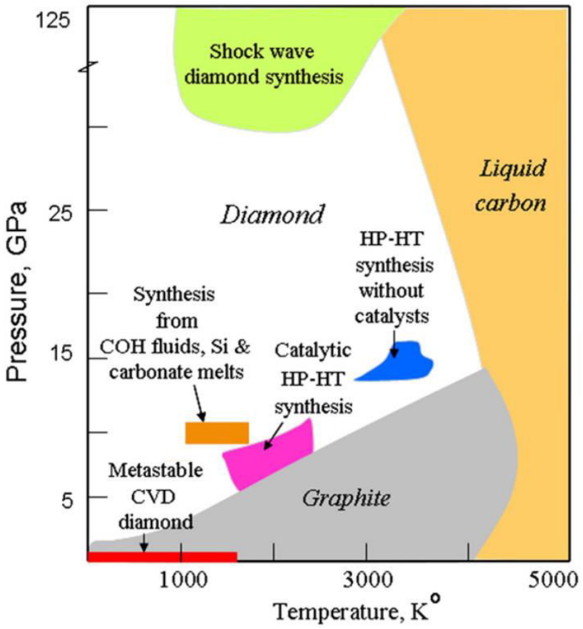

Figure 1.4: Carbon phase diagram [Dobrzhinetskaya, 2012].

Even if sample with large surfaces ($10 \times 10\,\mathrm{mm}^2$) can be made, the HPHT diamonds are generally not used for detection applications. Indeed, the nitrogen concentrations are relatively high (few ppm). Moreover, some metallic impurities due to the dissolution of the catalyst can be found. Finally, the crystalline orientations are not the same within a sample. These three elements can significantly degrade the electrical properties of HPHT diamonds.

1.2.2 Chemical Vapor Deposition growth technique

The CVD techniques consist in depositing thin films on a substrate from gaseous precursors. Regarding the growth of undoped diamond, the latter are generally methane (CH_4) and dihydrogen (H_2). The most commonly used technique consists in using a microwave-generated plasma to enhance the CVD; it is called Microwave Plasma Enhanced Chemical Vapor Deposition (MPCVD). The plasma generated in the reactor enable the activation of the carbon precursor (CH_4) which reacts with the surface of the substrate (see Figure 1.5). During the diamond growth, both diamond and graphic carbon phase are generated. However, the hydrogen present in the gas mixture leads to the preferential etching of the graphitic phases, thus favoring the diamond growth.

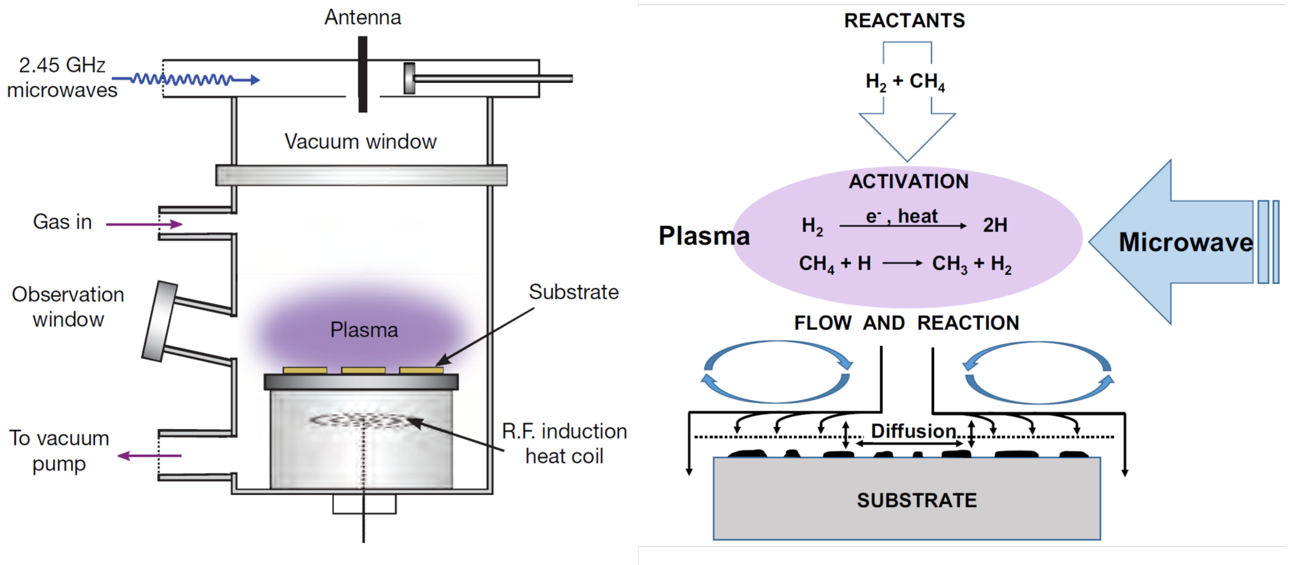

Figure 1.5: Left: scheme of a reactor used to achieve MPCVD diamond growth [Eaton-Magaña, 2012] Right: MPCVD growth scheme [Kasu, 2016]. Depending on the power of the microwave used, the substrate holder must be cooled.

The main advantage of the CVD technique over the HPHT technique is that the concentration of impurities can be precisely controlled and samples with nitrogen concentrations below 1 ppb can be obtained. Moreover, n-type and p-type doping can also be achieved by incorporating phosphorus and boron respectively.

1.2.3 Doping

The main dopants used for diamond devices are the boron for the p-type and, the nitrogen and the phosphorus for the n-type. Their position in the diamond bandgap are represented in Figure 1.6. The relatively high ionization energy of the dopants (0.38 eV for boron, 0.57 eV for phosphorus and 1.7 eV for nitrogen) leads to an incomplete ionization at RT.

In Figure 1.6, one can observed than the ionisation energy E_a of boron acceptors decreases with their concentration N_a. The parameter of the model developed in [Pearson, 1949] were fitted with experimental data for boron acceptors in diamond:

$$E_a = 0.38 - 4.7877 \times 10^{-8} \cdot N_a^{1/3} \quad (\text{with } N_a \text{ in cm}^{-3} \text{ and } E_a \text{ in eV}) \tag{1.1}$$

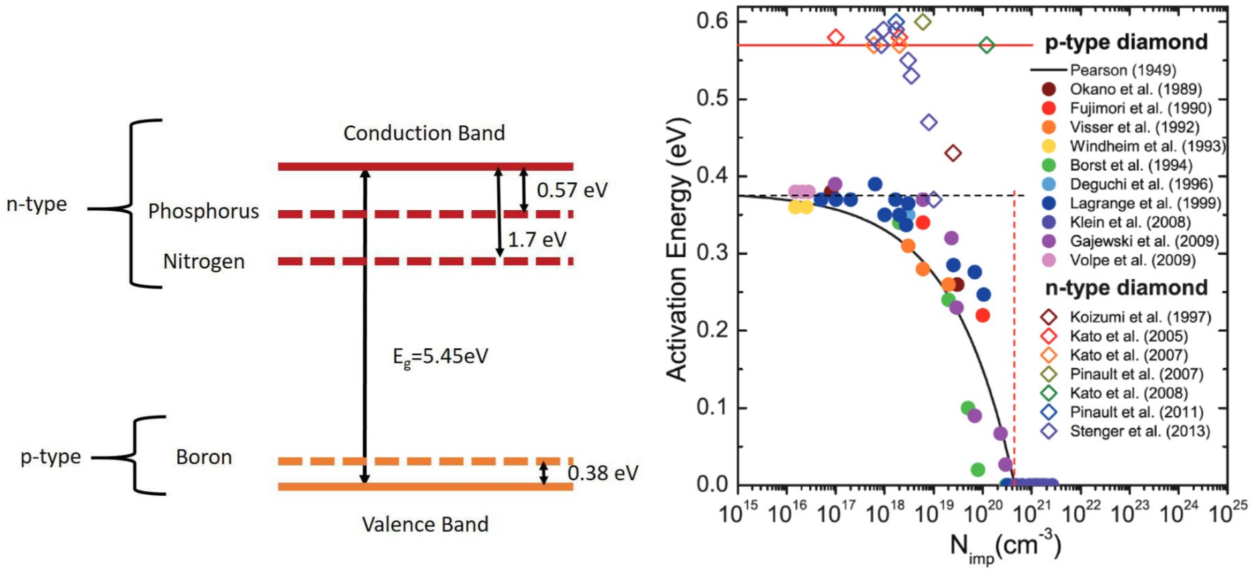

Figure 1.6: Left: ionization energies of the main dopant in diamond. Extracted from [Letellier, 2019]. Right: measurements of the activation energy of two dopants, phosphorus and boron, as a function of their concentrations. The data for boron are fitted with the Person model. Extracted from [Driche, 2018]

The fitted curve is represented with a solid black line in the figure. It can be noticed that for boron concentration approximately equal to $5 \times 10^{20}\,\mathrm{cm}^{-3}$, the ionization energy is null. For higher doping level, a metallic conduction occurs in boron-doped diamond.

The phosphorus doping was reported for the first time by Koizumi *et al.* in 1997 [Koizumi, 1997], and is now being studied by several groups [Kato, 2005, Kato, 2016, Temahuki, 2017, Pinault-Thaury, 2019]. Regarding the boron doping, it feasibility was shown in [Collins, 1971]. Several groups are currently working on it [Achard, 2011, Tallaire, 2017, Bogdanov, 2017, Teraji, 2017] and commercial solution are available[1].

1.2.4 Diamond crystalline quality

Depending on the seed used to perform the CVD growth, different cristalline quality can be achieved.

The single-crystal CVD (scCVD) diamonds are produced using a HPHT or CVD diamond seed (homoepitaxy). They are made of a single crystal and have only one crystal orientation. The commercially available scCVD samples have small active surfaces ($4.6 \times 4.6\,\mathrm{mm}^2$) and are relatively expensive. In the present work, only scCVD substrate from Element 6 were used. They have a <100> cristalline orientation and a low concentration of impurities ($[N] < 5$ ppb and $[B] < 1$ ppb).

The polycrystalline CVD (pcCVD) diamonds are obtained by heteroepitaxy (diamond grown on a different material). This technique permits to obtained sample with a greater surface (two-inch (50 mm) diameter diamond crystals commercially available [Kim, 2021]). Never-

---

[1] DiamFab website: `https://diamfab.com/fr/`

theless, pcCVD substrate have generally lower charge collection performances. This is largely due to their crystal structure: the growth of these samples generates a multi-column pattern separated by grain boundaries. The latter are generally composed of amorphous or graphitic carbon and constitute traps for charge carriers. Moreover, their nitrogen concentration is generally higher ($[\mathrm{N}] < 50\,\mathrm{ppb}$).

The Diamond-On-Iridium (DOI) are obtained by heteroepitaxy on an iridium substrate. They are mainly studied by two groups [Ohtsuka, 1996, Schreck, 1999]. They aim at obtaining samples with a large surfaces (a 90 mm diameter large dimond was reported in 2017 [Schreck, 2017]) and electronic properties similar to scCVD diamonds. Their electronic properties can be significantly affected by dislocations and a large divergence depending on the sample has been reported [Berdermann, 2019]. Recent studies in our group report: 1) good hole transport properties; 2) strongly degraded electron transport; and 3) severe charge collection inhomogeneities on the sample surface [Curtoni, 2020, Gallin-Martel, 2021a].

1.2.5 Metallic contacts

Before using a diamond sample for detection purposes, the latter has to be coated with metal. The metallic contacts thus realized allow to bias the samples and to drain the charge generated during the ionization while preventing the charges to diffuse in the detection volume. The nature of the metallic contacts can affect significantly the electronic properties of a sample. They can be characterized by:

- the Fermi level E_F;
- the metal work function Φ_m (ionization energy of the metal into vacuum level);
- the semiconductor work function Φ_s (energy difference between the semiconductor Fermi level E_F and the vacuum level);
- the electron affinity χ_s (energy difference between the CBM and the vacuum level).

Depending on the position of the metal Fermi level with respect to the conduction (n-type) or valence (p-type) band, two different types of contacts can be distinguished.

Ohmic contacts are characterized by a Fermi level higher than the conduction band (n-type, Figure 1.7 (D2)) or lower than the valence band (p-type, Figure 1.7 (B2)) at the semiconductor/metal interface. Therefore, the majority carriers (electrons for n-type and holes for p-type) will flow directly from the semiconductor to the metal. The I-V characteristic of such a device is then linear (follow the Ohm's law). Ohmic contacts are usually achieved by performing an annealing step after a titanium or chromium deposition in order to: 1) ensure metal adhesion and 2) induce carbide bounds at the metal-diamond interface allowing the ohmic nature of the contact.

Schottky contacts are characterized by a Fermi level lower than the conduction band (n-type, Figure 1.7 (C2)) or higher than the valence band (p-type, Figure 1.7 (A2)) at the semiconductor/metal interface. In this case a built-in potential Φ_{BP} appears. This is called the Fermi barrier. The I-V characteristic of such a device is non linear or asymmetric.

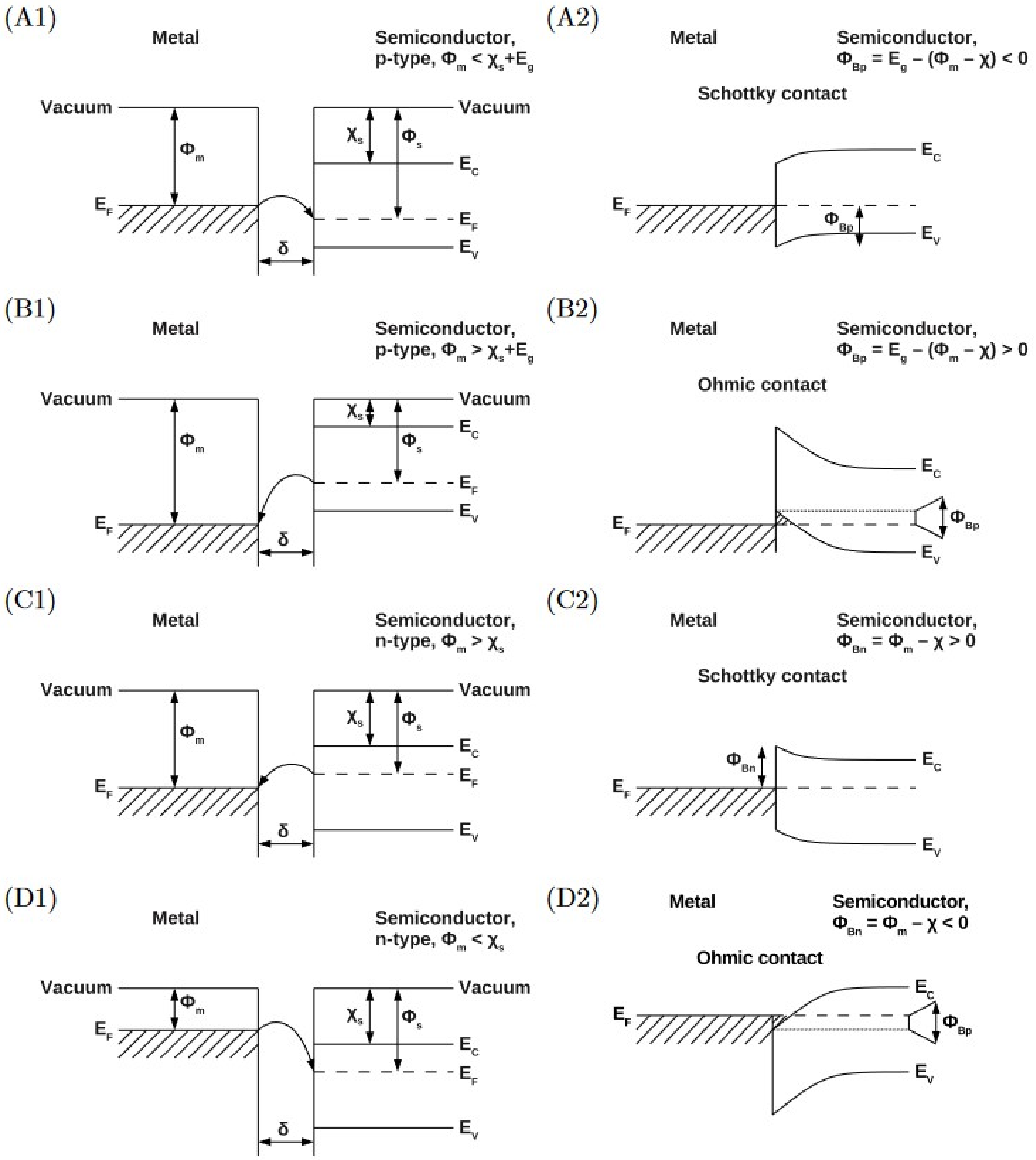

Figure 1.7: Band diagram of the metal/semiconductor interface for n-type (C and D) and p-type (A and B) semiconductors for different metal work functions. The left and right part of the figure represent respectively isolated systems (1) and systems at equilibrium (2). Extracted from [Jansen, 2013a].

The electronic grade scCVD diamond from Element 6 has a very low concentration of impurities ([N] $<$ 5 ppb and [B] $<$ 1 ppb). Therefore, the band bending effect occurs over relatively large distances[1]. On the contrary a metallic contact achieved on a highly boron-doped layer ([B] $> 5 \times 10^{20}\,\mathrm{cm}^{-3}$) will be ohmic due to the metallic conduction occurring in the layer. Indeed, in such a layer the Fermi level is below the VBM, thus a quantum tunnelling occurs at the metal-diamond interface.

In this section, I show that synthetic diamonds made by the scCVD technique have the adapted properties for particle detection applications. I have described the different dopants

---

[1] This distance is proportional to $1/\sqrt{N_{dop}}$ where N_{dop} is the doping density.

used to obtain n- and p-type diamonds, and the characteristics of the metal-diamond contacts. In the next section, I will describe the interaction of charged particle with matter and the use of diamond as a solid-state ionization chamber.

1.3 Diamond Detector

1.3.1 Interaction of the charged particle with matter

This subsection deals with the interactions of charged particles, mainly non-relativistic light ions and electrons, in matter. The interaction of photons in matter will not be discussed.

1.3.1.1 Heavy charged particles

A charged particle passing through matter mainly loose energy from its electromagnetic interaction with the atomic electrons of the medium. The stopping power of a charged particle (dE/dx) represents the energy loss per distance units. For a non-relativistic ($0.1 \lesssim \beta\gamma \lesssim 1000$) heavy charged particles (mass $M \gg m_e$), it is described by the Bethe-Bloch formula [Bethe, 1930, Bloch, 1933]:

$$-\left(\frac{dE}{dx}\right) = \left(4\pi N_A r_e^2 m_e c^2\right) \frac{\rho Z}{A} \cdot \frac{z^2}{\beta^2} \cdot \left[\frac{1}{2} \ln\left(\frac{2m_e c^2 \beta^2 \gamma^2 T_{max}}{I^2}\right) - \beta^2 - \frac{\delta}{2} - \frac{C}{Z}\right] \tag{1.2}$$

with $2\pi N_a r_e^2 m_e c^2 = 0.1535\,\text{MeV}\cdot\text{cm}^2/\text{g}$ is a **constant**, with:

- N_A the Avogadro constant ($6.022 \cdot 10^{23} 1/\text{mol}$),
- r_e the classical electron radius ($2.817 \cdot 10^{-13}\text{cm}$),
- m_e the electron's mass,
- c the speed of light.

$\rho Z/A$ characterizes the **absorber** with:

- ρ its density,
- Z its atomic number,
- A its mass number.

z^2/β^2 characterizes the **ionising particle** with:

- z its charge (in units of the elementary charge),
- $\beta = v/c$ with v its velocity.

The terms in the bracket are:

- $\gamma = 1/\sqrt{1-\beta^2}$ is the Lorentz factor of the ionizing particle;
- T_{max} is the maximum kinetic energy which can be transferred to a free electron in a single collision;
- I is the mean excitation energy of the absorber;
- δ is the correction term for the so-called density effect (significant at relativistic energies);

- C is he shell correction term (significant at low energies).

Figure 1.8 represents the stopping power of a charged particle versus $\beta\gamma$. The region described by the Bethe-Bloch formula is indicated as "Bethe". For low β, $\gamma \sim 1$ and, therefore, the energy loss is proportional to $1/\beta^2$. When the velocity v becomes close to c, $\beta \sim 1$ and the energy loss reaches a plateau. The energy loss is then proportional to $\ln(\beta\gamma)$. The particles with $\beta\gamma \approx 4$ are called Minimum Ionizing Particles (MIP).

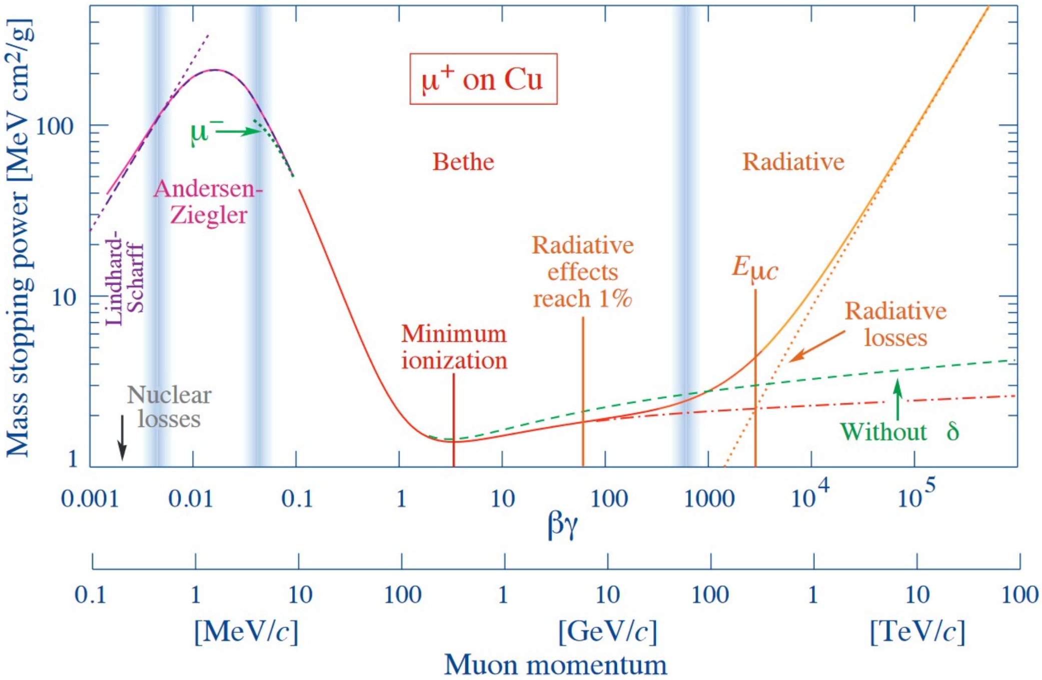

Figure 1.8: Stopping power (dE/dx) for positive muons in copper as a function of $\beta\gamma$. The region indicates as "Bethe" indicate the energy interval where the Bethe-Bloch formula is valid. Extracted from [Particle Data Group, 2022].

Regarding the energy deposit of the particles studied in this PhD, alpha particles emitted by the radioactive decay of a ^{241}Am source or 3 MeV protons, the corrective terms γ and C can be neglected. During the slowing down of such an ionizing particle, the energy deposit is characterized by, at first 1), a slow increase of the stopping power with distance followed by 2) a strong increase then decrease of the stopping power that matches the particle stopping. The range of a charged particle is the distance required for its energy to become approximately zero by ionization in matter. The energy deposited by a 5.486 MeV alpha particle was simulated thanks to the software **Stopping and Range of Ions in Matter** (SRIM[1]) and plotted in Figure 1.9. Such a particle has a 13.6 µm range. If the diamond thickness is thinner than the latter distance, the particle passes through the layer. The energy deposit is then proportional to z^2/v^2.

1.3.1.2 Electrons

When the electrons pass through matter, they loose energy by the electromagnetic interaction with the electron and the nucleus. Due to the small mass of the electron compared to the

---

[1] `http://www.srim.org/`

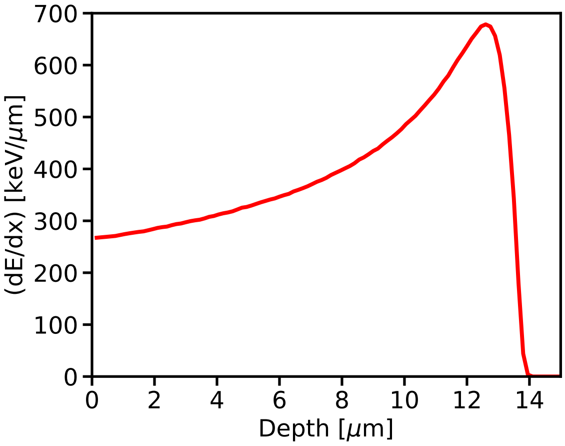

Figure 1.9: Energy deposits by a 5.486 MeV alpha particle in a diamond sample simulated with the SRIM software.

nucleus of the medium ($m_e = 0.511\,\text{MeV} \ll 938\,\text{MeV}$, the proton mass), the latter interaction may induce huge deviation. The energy loss of electron is thus less rectilinear. At high energy, electrons lose some of their energy through radiation (Bremsstrahlung). The total energy loss of an electron $(dE/dx)_{tot}$ can then be described by the addition of the energy loss per ionization $(dE/dx)_{ion}$ and the energy loss by radiation $(dE/dx)_{rad}$ as described by the following formula:

$$\left(\frac{dE}{dx}\right)_{tot} = \left(\frac{dE}{dx}\right)_{ion} + \left(\frac{dE}{dx}\right)_{rad} \tag{1.3}$$

The stopping power of electron in carbon is represented in Figure 1.10. In this PhD, only low energetic (from 5 to 30 keV) electrons have been used during the experiment. On this graph it can be noticed that the radiative losses are negligible for these energies. The particle with an energy around 1 MeV (for instance the beta particle emitted by a ^{90}Sr) are called MIP, and the energy where $(dE/dx)_{ion} = (dE/dx)_{rad}$ is called critical energy. The latter is around 100 MeV in diamond.

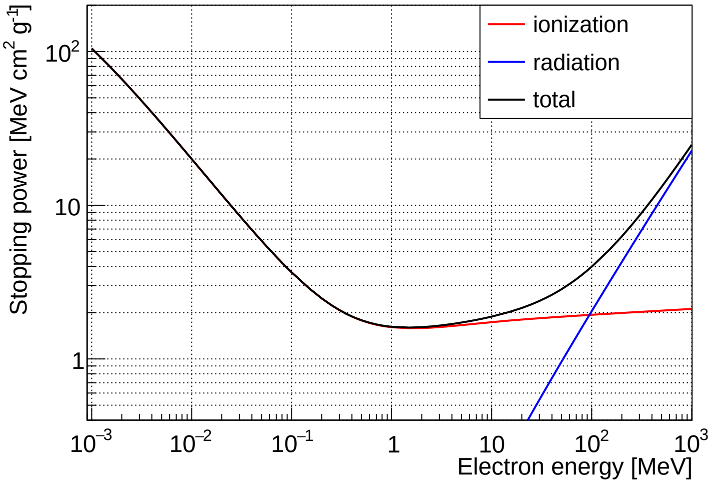

Figure 1.10: Stopping power of electrons in matter. Extracted from [Curtoni, 2020].

1.3.2 Solid-state ionization chamber principle

Diamond detectors can be used as solid-state ionization chambers. When a particle interacts within a medium, part or all its energy is transfered to the medium and ionize it by releasing free charge carriers. The quantity of free carrier is proportional to the energy loss of the particle in the medium. In the case where no electric field is applied, the carrier will recombined rapidly in the detector. When an electric field is applied, the charge carriers drift, depending of their charge, toward one or the other electrode. The drift of the charge carrier induces a current which can be measured with an adapted Read-Out Electronic. By analysing this signal, several parameter can be studied such as the energy deposited by the particle or the transport and charge property of the detector. In this process, there is no amplification of the signal during the drift. Figure 1.11 summarizes the principle of a solid-state ionization chamber principle in the case of a sandwish configuration (two parallel electrodes).

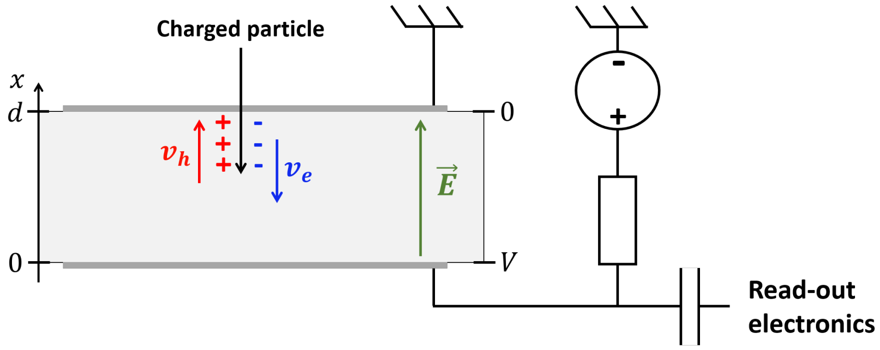

Figure 1.11: Principle of a solid-state ionization chamber. A particle impinging the detector is ionizing the medium and generating charge carriers which drift due to the applied electric field. x_0 represents the range of an ionizing particle which stopped within the detector.

1.3.3 The type of signals expected according to the nature of the incident particle

The induced signal can be described by the Shockley-Ramo theorem [Shockley, 1938, Ramo, 1939]. The current $I_{induced}$ and the charge $Q_{induced}$ induced by a free charge q drifting with a velocity $\overrightarrow{v_q}$ can be estimated by the following formula:

$$I_q = q\overrightarrow{v_q} \cdot \overrightarrow{E_w} \quad \text{and} \quad Q_{induced} = q\,\phi_w \tag{1.4}$$

with $\overrightarrow{E_w} = -\overrightarrow{\text{grad}}\,(\phi_w)$ the weighting field and ϕ_w weighting potential. The two latter parameters are the electric field and potential which would be induced considering a n-electrodes system in which one electrode is at the unity potential and the others at the ground. It is also assumed that no space charge is present within the volume delimited by the electrodes. In the case of sandwich configurations, the electric field becomes parallel to the direction of displacement of the charges. Its value is then constant and can be written as follows

$$\left\| \overrightarrow{E_w} \right\| = 1/d \tag{1.5}$$

with d the thickness of the sample.

1.3.3.1 Short range particles that stop in the detector

The current induced by a particle which is stopped in the detector at the position x_0 at the time $t = 0$ can be calculated. We assume, that this particle deposits its charge homogeneously and that the charge deposited does not modify locally the electric field (low injection regime). The recombination and carrier diffusion phenomena are also neglected in this simple model. In that ideal case, the hole induced current I_h and the electron induced current I_e can be written as follows:

$$|I_h| = \int_0^d \int_0^t \rho_h(x,t)\, dx\, dt \cdot \frac{v_h}{d} \tag{1.6}$$

$$|I_e| = \int_0^d \int_0^t \rho_e(x,t)\, dx\, dt \cdot \frac{v_e}{d} \tag{1.7}$$

with $\rho_{h/e}(x,t)$ the free charge linear distribution per time unit at dx and dt. The current induced in the case described in the Figure 1.11 will be estimated over time.

Hole current: in the case illustrated by Figure 1.11, the charges are deposited close to an electrode negatively biased. Therefore, the holes are collected from the time $t = 0$ to the time t_h when all the holes are collected. By considering that the charge Q_0 is deposited instantaneously at $t = 0$, $\rho_h(x,t)$ can be expressed as follows:

$$\int_0^d \int_0^t \rho_h(x,t)\, dx\, dt = \int_0^d \int_0^t \frac{Q_0}{d - x_0} \left(\delta(t)\, dx + \frac{dx}{dt} \right) dt \tag{1.8}$$

with $\delta(t)$ the Dirac function, $\delta(t)\, dx$ the charge generation at $t = 0$ and dx/dt the number of free holes collected on the electrode during the time dt. The second term can be assumed to be a negative constant equal to the hole drift velocity: $dx/dt = -v_h$. Therefore, the distribution of charge can be estimated at time t:

$$
\begin{aligned}
\int_0^d \int_0^t \rho_h(x,t)\,dx\,dt &= \int_0^d \int_0^t \frac{Q_0}{d-x_0}\ (\delta(t)\,dx - v_h)\,dt \\
&= \int_{x_0}^d \frac{Q_0}{d-x_0}\ (dx - v_h\,t) \quad \text{(charges created in the region } x_0 < x < d) \\
&= \frac{Q_0}{d-x_0}\ (d - x_0 - v_h\,t) \\
&= Q_0 \left(1 - \frac{v_h}{d-x_0}\,t\right) \\
&= Q_0 \left(1 - \frac{t}{t_h}\right)
\end{aligned}
\tag{1.9}
$$

As a result, the hole current can be estimated between the time $t = 0$ and $t_h = \frac{d-x_0}{v_h}$:

$$
|I_h| = \begin{cases} Q_0 \cdot \frac{v_h}{d} \left(1 - \frac{t}{t_h}\right) & \text{if } 0 \leq t \leq t_h \\ 0 & \text{otherwise} \end{cases}
\tag{1.10}
$$

Electron current: in contrast to holes, electrons are not collected before a given time $\widetilde{t_e}$ (see Figure 1.11). From the time $t = 0$ to $t = \widetilde{t_e}$, the charge are drifting with a constant velocity v_e and no charge are collected. Then, the charge are collected until the time t_e when no free electron remains in the bulk. From $t = 0$ to $t = \widetilde{t_e}$, $\rho_e(x,t)$ can be estimated as follows:

$$
\int_0^d \int_0^{\widetilde{t_e}} \rho_e(x,t)\,dx\,dt = \int_0^d \int_0^{\widetilde{t_e}} \frac{Q_0}{d-x_0}\,\delta(t)\,dxdt = \int_{x_0}^d \frac{Q_0}{d-x_0}\,dx = Q_0
\tag{1.11}
$$

Then, the free electrons are collected:

$$
\begin{aligned}
\int_0^d \int_{\widetilde{t_e}}^t \rho_e(x,t)\,dx\,dt &= \int_0^d \int_{\widetilde{t_e}}^t \frac{Q_0}{d-x_0}\ (\delta(t)\,dx - v_e)\,dt \\
&= \int_{x_0}^d \frac{Q_0}{d-x_0}\ \left(dx - v_e\ \left(t - \widetilde{t_e}\right)\right) \\
&= \frac{Q_0}{d-x_0}\ \left(d - x_0 - v_e\ \left(t - \widetilde{t_e}\right)\right) \\
&= Q_0 \left(1 - \frac{v_e}{d-x_0}\ \left(t - \widetilde{t_e}\right)\right) \\
&= Q_0 \left(1 - \frac{t - \widetilde{t_e}}{t_e - \widetilde{t_e}}\right)
\end{aligned}
\tag{1.12}
$$

As a result, the electron current can be estimated between the time $t = 0$ and $t = \widetilde{t_e} = \frac{x_0}{v_e}$ and between $t = \widetilde{t_e}$ and $t = t_e = \frac{d}{v_e}$:

$$|I_e| = \begin{cases} Q_0 \cdot \frac{v_e}{d} & \text{if } 0 \leq t \leq \widetilde{t_e} \\ Q_0 \cdot \frac{v_e}{d} \left(1 - \frac{t - \widetilde{t_e}}{t_e - \widetilde{t_e}}\right) & \text{if } \widetilde{t_e} \leq t \leq t_e \\ 0 & \text{otherwise} \end{cases} \tag{1.13}$$

Total current: Figure 1.12 summarizes the previous results and shows the shape of the induced current as a function of time. The red and blue curves represent the current induced by the drift of holes and electrons, respectively. On the graph, the time intervals are not represented with a realistic scale. Figure 1.13 gives a more accurate image of the induced current. This is typically the signal expected when an alpha of few MeV is impinging the surface of a 500 µm thick diamond sample. Depending of the bias voltage, one type of charge carrier is collected instantaneously and induced a short and sharp current peak. Whereas, the other type of charge carrier has to drift through the thickness of the sample and induces a long but less intense current pulse. Here, the time t_h, $\widetilde{t_e}$ and t_e correspond respectively to the drift time of the holes generated at the position x_0, of the electrons generated at the position x_0 and of the electron generated at the position d, respectively. It should be precised that, if the bias polarity is reversed (electric field in the other direction), equations similar to the Equation 1.10 and 1.13 can be obtained but with carrier inverted. In this case, the holes drift through the sample and then induce a long pulse and at the opposite the electrons are immediately collected.

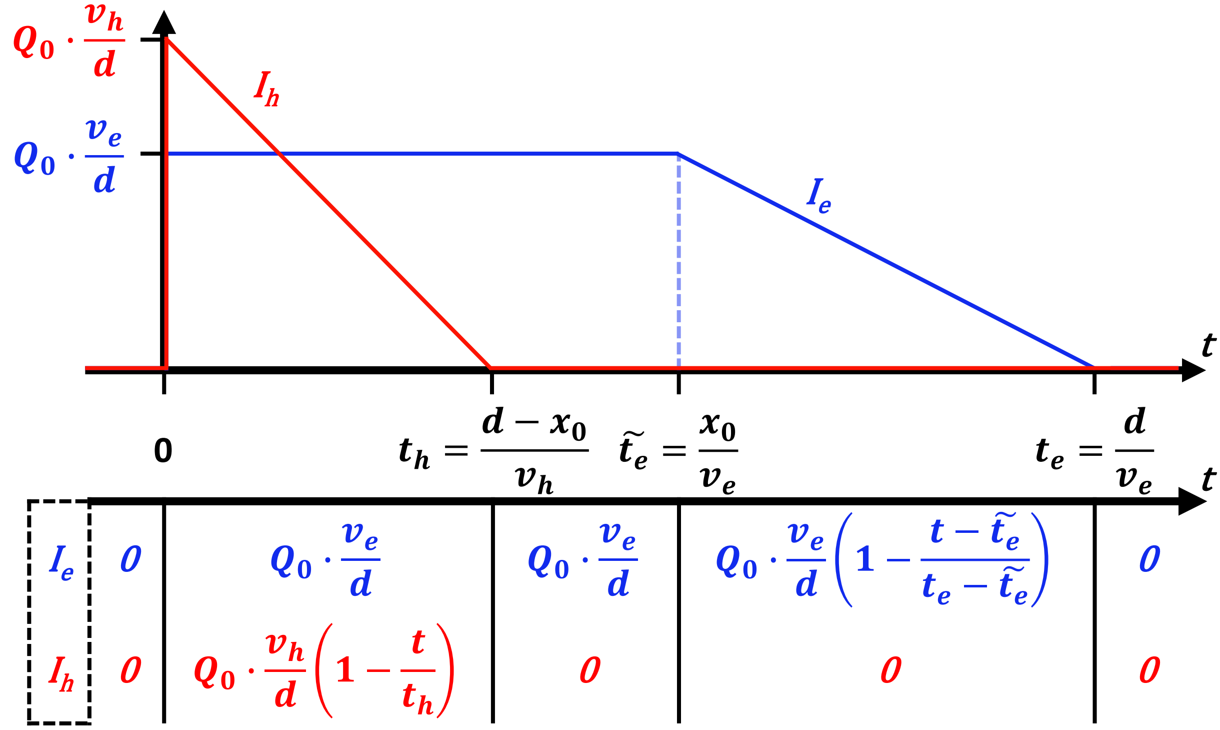

Figure 1.12: Charge carrier current verus time. The table summarizes the equations 1.10 and 1.13 while the graphic show a representation of the hole and electron currents over time. The time intervals are not represented with a realistic scale.

In Figure 1.13, the sum of hole and electron induced current is represented in green. The first part of the signal (i.e. the signal induced by the charge carrier which are collected by the closer electrode) cannot be observed due to the bandwidth of the ROE[1]. As a result, with particles which stop in the sample, it is possible to study separately the current by the electron drift and the current induced by the hole drift.

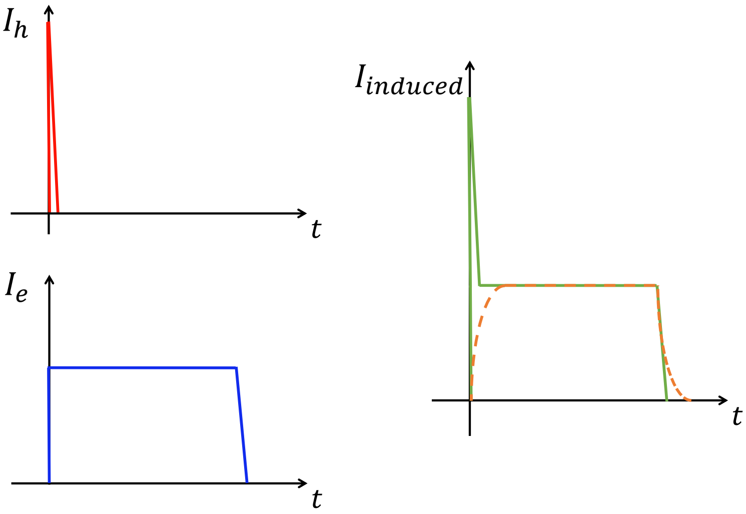

Figure 1.13: Hole (red curve) and electron (blue curve) induced currents. The total current is represented in green. The dash orange line shows the signal shaped by the ROE (bandwidth).

The approach developed in this part is quite simple but allows to give an idea of the induced current behavior while a low range particle is impinging a sample. In more deepened and complex studies, an accurate description of the signal induced by a UV laser pulse has been described [Gabrysch, 2010].

1.3.3.2 Particles which pass through the detector

The shape of the induced current is significantly different for particles which pass through the sample (theoretical equations described in [Curtoni, 2020]). In this case, charge carriers are created along the entire path of the particle. Thus, the current induced by both carrier types can be observed. These currents have a triangular shape due to the fact that some charge carriers are extracted from the time $t = 0$ (see Figure 1.14).

1.3.4 Trapping and related phenomena

1.3.4.1 Defects and carrier trapping centers

The semiconductor bulk countains some imperfections which can modify its electronic properties. These defects can be induced during the growth or after irradiation. These defects can be classified as followed:

---

[1] In specific experiments achieved with fast neutron [Weiss, 2016] or by two-phonon absorption [Dorfer, 2019], the contribution of both charge carrier was observed. In both cases, the charge carriers were created further from the electrodes.

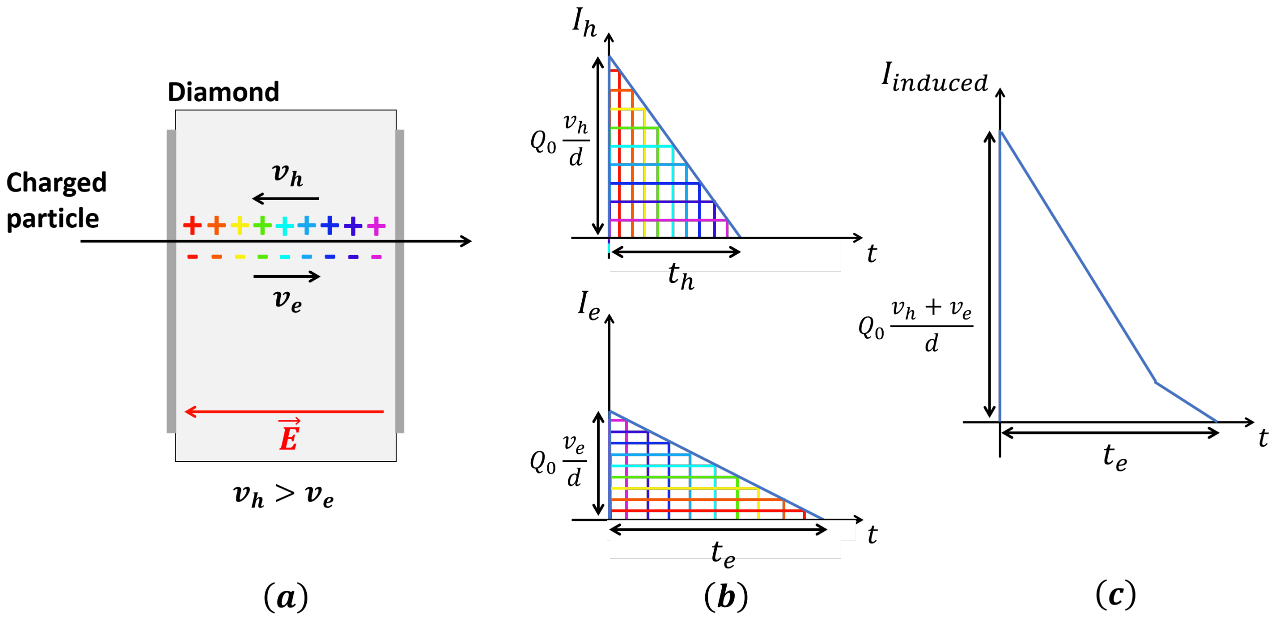

Figure 1.14: Current induced by a particle going trough the detector. (a): schematic of the detector setup. (b): current induced by both carriers. (c): total current induced. Figure extracted from [Curtoni, 2020].

- **zero-dimension defects** are attributed to vacancies, interstitial defects or impurities in the crystal. Hydrogen, boron and nitrogen are common impurities observed in diamond crystal. In particular, nitrogen is known to be a signal killer.
- **one-dimension defects** are mostly attributed to dislocations. More generally, these defects induce a rupture in the crystal symmetry.
- **two-dimension defects** are attributed to grain boundaries between two crystals with different orientations. These kind of defects are mostly observed in polycrystalline diamonds.
- **three-dimension defects** are attributed to cluster of defects (impurities, vacancies...).

These defects introduce energy levels in the forbidden band, thus modifying the band structure of the semiconductor. The energy level of different impurities commonly observed in diamond are represented in Figure 1.15 (left). An energy level close to the VBM, such as boron, is considered as a hole trap. On the contrary, an energy level close to the CBM, such as phosphorus, is considered as an electron trap. Finally, an energy level close to the the Fermi level E_f, such as vacancies, are considered as deep (electron or hole) traps.

Figure 1.15 (right) describes the impact of traps on the free charge carrier concentration. Traps can trap a charge carrier (1), reducing the amount of free carriers and so the signal intensity. A trapped charge carrier can either be re-emitted (1') or recombined by the capture of a charge carrier with an opposite charge (2). The probability of re-emission is proportional to $exp(-\frac{E_a}{kT})$, with E_a the activation energy defined as the energy difference between the trap energy level and the CBM (for electrons) or the VBM (for holes), k the Boltzmann constant and T the temperature. Therefore, the emission rate of a deep trap is very low ($E_a >> kT \sim 0.025\,\text{eV}$), hence the recombination phenomenon is predominant. Finally, the charge carriers can also be emitted by a deep trap (3).

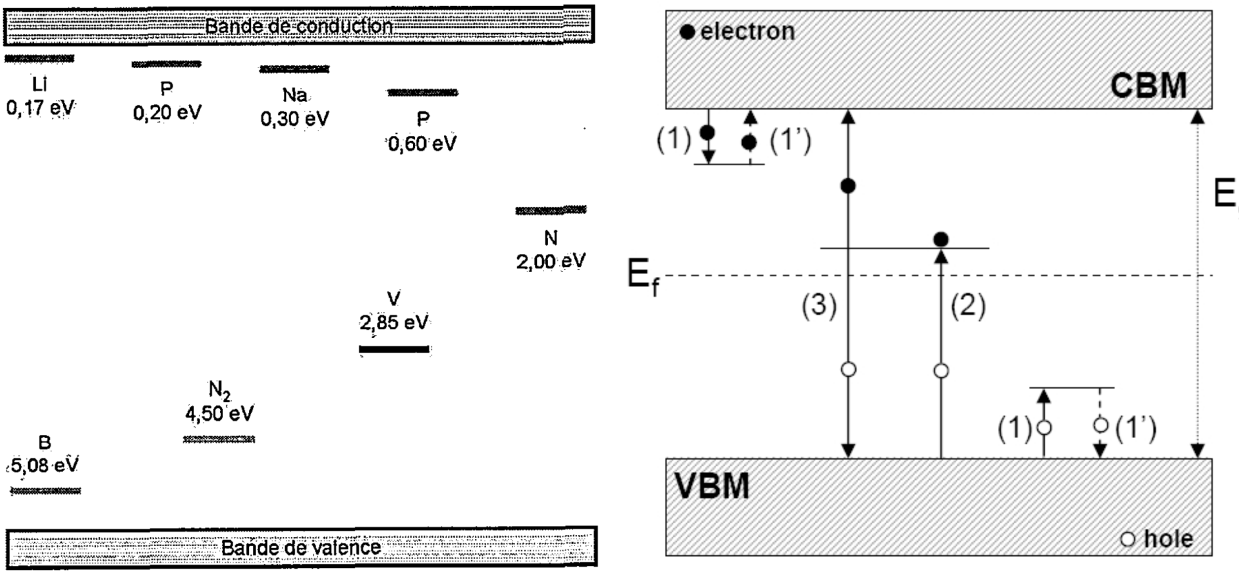

Figure 1.15: Left: energy levels of defects in diamond. Extracted from [Tranchant, 2008]. Right: simplify scheme of trapping (1), re-emission (1'), recombination (2) and generation (3). Extracted from [Pomorski, 2008].

1.3.4.2 Influence of the charge carrier trapping on the induced signal

If the concentration of traps is considered uniform in the bulk and constant over time, then, it is reasonable to consider that the recombination process is stationary and homogeneous. Thus, this phenomenon can be described by a constant $1/\tau_{h/e}$ equal to the probability of trapping a charge carrier during the time dt:

$$\begin{aligned} Q(t+dt) = Q(t) - \frac{1}{\tau_{h/e}} Q(t)\,dt \quad &\Longleftrightarrow \quad \frac{dQ}{dt} = -\frac{Q(t)}{\tau_{h/e}} \\ &\Longleftrightarrow \quad Q(t) = Q_0\, e^{-t/\tau_{h/e}} \end{aligned} \tag{1.14}$$

with $Q(t)$ the charge at the time t. In this equation, the generation and collection phenomena are not taken into account. By using the same approach as in the Subsection 1.3.3.1, the hole and electron induced currents (I_h and I_e) can be estimated, considering that the variation of the density of charge is described by Equation 1.15.

$$\int_0^d \int_0^t \rho_{h/e}(x,t)\,dx\,dt = \left[\int_0^d \int_0^t \frac{Q_0}{d-x_0} \left(\delta(t)\,dx - v_{h/e} \right) dt \right] e^{-t/\tau_{h/e}} \tag{1.15}$$

$$|I_h| = \begin{cases} Q_0 \cdot \frac{v_h}{d} \left(1 - \frac{t}{t_h}\right) e^{-t/\tau_h} & \text{if } 0 \leq t \leq t_h \\ 0 & \text{otherwise} \end{cases} \tag{1.16}$$

$$|I_e| = \begin{cases} Q_0 \cdot \frac{v_e}{d} \, e^{-t/\tau_e} & \text{if } 0 \leq t \leq \widetilde{t_e} \\ Q_0 \cdot \frac{v_e}{d} \left(1 - \frac{t-\widetilde{t_e}}{t_e-\widetilde{t_e}}\right) e^{-t/\tau_e} & \text{if } \widetilde{t_e} \leq t \leq t_e \\ 0 & \text{otherwise} \end{cases} \tag{1.17}$$

If Q is the charge collected over time, then:

$$Q = \frac{Q_0 v_h}{d} \left[\tau_h + \frac{\tau_h^2}{t_h} \left(e^{-t_h/\tau_h} - 1\right)\right] + \frac{Q_0 v_e}{d} \left[\tau_e + \frac{\tau_e^2}{t_e - \widetilde{t_e}} \left(e^{-(t_e-\widetilde{t_e})/\tau_e} - 1\right) e^{-\widetilde{t_e}/\tau_e}\right] \tag{1.18}$$

In the latter equation, the induced charge depends on t_h/τ_h and $\left(t_e - \widetilde{t_e}\right)/\tau_e$ ratios, showing clearly the competition between the drift and the trapping phenomena. The trapping phenomenon may affect significantly the transient current and the charge collection efficiency.

1.3.4.3 The polarization effect

Even in high quality (electronic grade) single crystal diamond sample, a phenomenon resulting of a non-uniform charge carrier trapping is regularly observed [Pernegger, 2005, Isberg, 2006, Sato, 2017, Naaranoja, 2019]. This effect is called polarization effect. It mainly appears when the charge carrier are not uniformly generated in the bulk or for high irradiation rate [Kassel, 2016].

In the case of short-range particles, one type of charge carrier is collected immediately while the other drifts through the whole thickness of the sample. The second type of charge carriers has therefore a higher probability to be trapped. The trapped charges induced an internal electric field with an opposite direction to the applied electric field. In Figure 1.16, the establishment of the resulting electric field is illustrated in the case where negative space charges are homogeneously distributed in the bulk.

The trapped charges lead to space charge in the bulk. When most of the trapped carrier are negatively (positively) charged, this phenomenon is referred to as negative (respectively positive) space charge. It was demonstrated that, depending on the charge carrier drifting in the bulk, it is possible to modify the space charge polarity [Rebai, 2016].

The polarization effect can considerably complicate the use of diamond as a radiation detector by inducing a partial or total loss of the primary signal. As observed in Figure 1.17, the shape of the induced currents is also significantly altered: the signals change from a rectangular to a rhombic shape.

Several procedure to limit this phenomenon were reported [Ramos, 2022].

- **Inverting regularly the bias**, by the transit of carriers of opposite charge, foster recombination phenomena and thus neutralize the space charge phenomenon [Guthoff, 2013, Valentin, 2015, Rebai, 2016, Holmes, 2019, Curtoni, 2020].

- **Switching on and off the bias** is an alternative way to induce the same phenomenon [Bergonzo, 2008, Gabrysch, 2011, Ibragimov, 2016].

- **A light excitation (optical or near infrared)** provide an energy sufficient to de-trap the charge carriers and recover the signal [Manfredotti, 2002, Bentele, 2016].

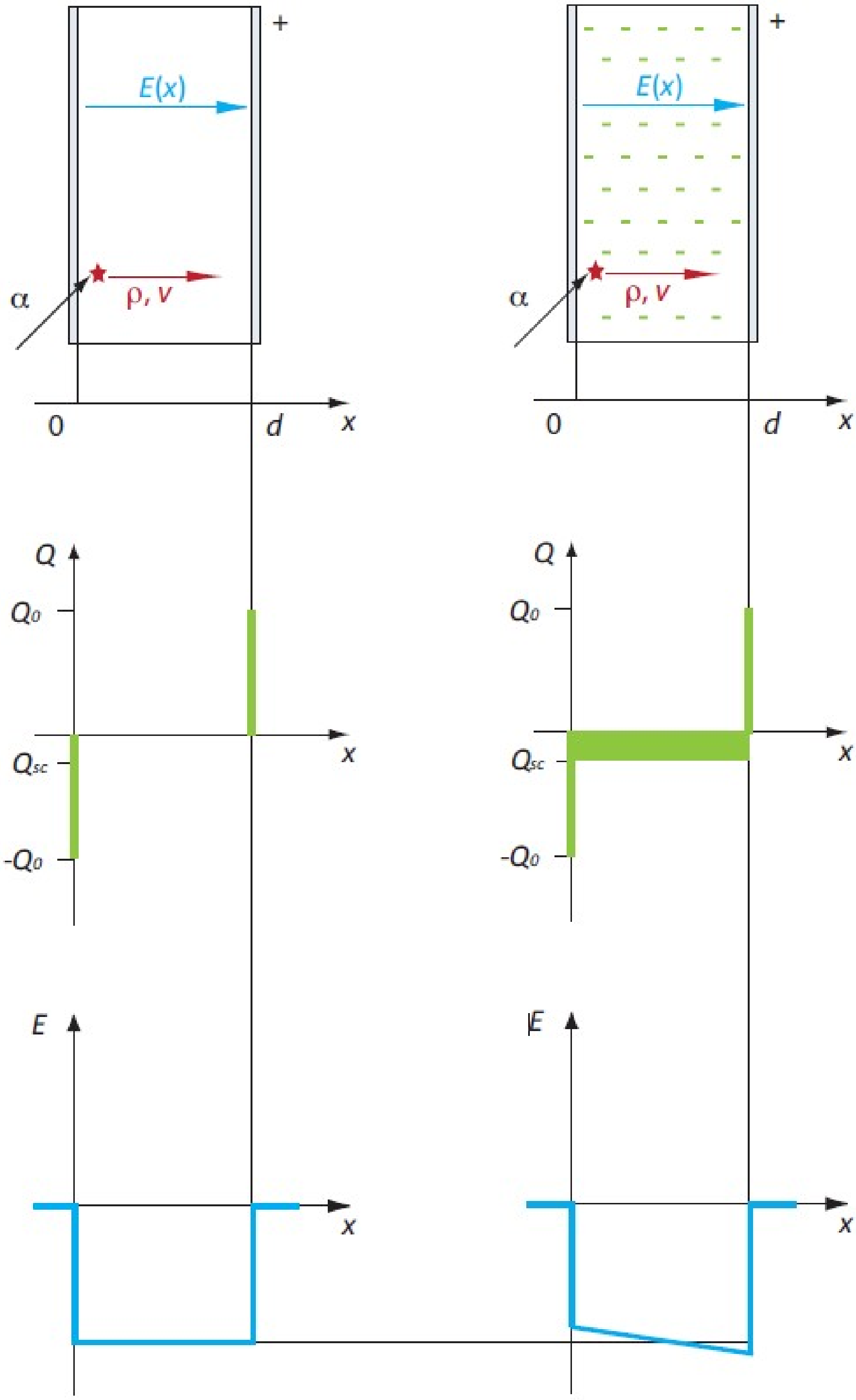

Figure 1.16: Electric field E induced in a diamond sample with a thickness d, without (left) and with (right) a homogeneous negative space charge Q_{sc}. Extracted from [Weiss, 2014].

- **Increasing the temperature** increases the thermal de-trapping of the charge carriers [Guerrero, 2006, Bergonzo, 2007, Angelone, 2019].

Nevertheless, some studies reported contradictory results, and it seems that these procedure are more or less efficient to recover the signal depending on the diamond sample and the experiment carried out.

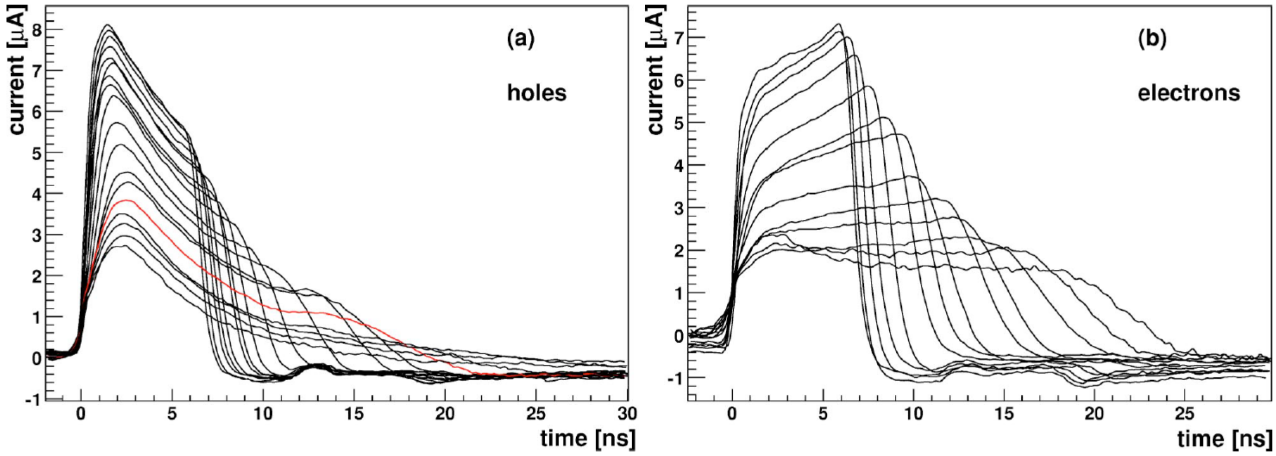

Figure 1.17: Currents induce by the transit of holes (a) and electrons (b) for increasing applied electric fields. The negative space charge in the diamond bulk modifies the shape of the induced current described in Figure 1.13. Extracted from [Pernegger, 2005].

1.3.4.4 The Priming effect

To avoid the trapping and polarization effects, filling homogeneously the deep traps - which take a long time to re-emit thermally the trapped charge carrier - before conducing an experiment can be interesting. Indeed, by saturating the traps, the free carriers have a lower probability to be trapped, and therefore their life time becomes longer. Moreover, due to the uniform filling of the traps, there is no internal electric field. The priming consisted in filling the traps homogeneously in order to enhance the signal obtained. The priming is commonly performed by irradiating the whole sample with particles with a low low energy transfer such as beta particles emitted by a ^{90}Sr radioactive source (MIP).

1.3.5 The Transient Current Technique Modelling of the charge drift: saturation velocity, low field mobilities

1.3.5.1 The Transient Current Technique

The Transient Current Technique (TCT) or Time-of-Flight (ToF) technique is a is very commonly used technique allowing to study the transport properties of a diamond sample [Canali, 1979, Isberg, 2002, Pernegger, 2005, Pomorski, 2006, Gkoumas, 2009, Gabrysch, 2011, Jansen, 2013b, Valentin, 2015, Majdi, 2016, Weiss, 2016, Berdermann, 2019, Dorfer, 2019]. This technique is exploiting the signal induced by short range particles which stopped close to the diamond surface (approximately 14 µm for 5.5 MeV alpha, see Figure 1.9). As discussed in the Subsection 1.3.3.1, it is then possible to study separately the drift of both charge carrier types. Moreover, the duration of the signal thus obtained depends directly of the drift time t_{drift} of the drifting charge carriers. The more accurate way to extract this time is to evaluate the duration of the signal at the half-amplitude (i.e., where the derivative is maximum, and so the timing resolution [Spieler, 1982]). Then, the drift velocity v_{drift} depending on the charge carrier studied and versus the electric field applied can be studied using the following formula:

$$v_{drift} = \frac{d}{t_{drift}} \tag{1.19}$$

In the next parts, the techniques used to extract the drift time and a description of the drift velocity versus the electric field will be presented.

1.3.5.2 Induced current fit functions and extraction of the drift time

To extract correctly the drift time, and so the drift velocity, a function that accurately describes the shape of the signal must be found. As discussed in Subsection 1.3.3.1, the current induced in a diamond sample by a short range particles can be described by a square shape function. For instance, the General Gaussian Distribution (GGD) has the desired characteristic to describe the induced current I over time t [Curtoni, 2020] (see Figure 1.18 (a)):

$$I(t) = I_0 \cdot exp\left[-\left(\frac{|t-\mu|}{\alpha}\right)^{\beta}\right] \tag{1.20}$$

with I_0 the maximum amplitude of the signal, μ a position parameter (position where $I = I_0$), α a scale parameter (sharpness of the signal slopes) and β a form parameter (form of the signal). Then, the drift time can be estimated with the following formula:

$$t_{drift} = 2\alpha \left[ln\left(2\right)\right]^{\beta} \tag{1.21}$$

The latter function describes accurately the signals measured at room temperature or at relative high electric fields where the diffusion phenomena, and thus the longitudinal extension of the charge carrier cloud, is limited. Moreover, due to the symmetry of the function, the number of parameters to adjust is limited and, as a result, the convergence is faster. Finally, the initial parameters do not influence significantly the fit convergence.

An alternative is to use the following function [Gabrysch, 2010,Majdi, 2012]. This equation is based on the work achieved in [Gabrysch, 2010], where the goal was to find an analytic formula to describe the signal induced in sandwich configuration by a UV pulse in a thick diamond sample.

$$I(t) = \alpha \cdot \left(1 + erf\left(\frac{t-t_0}{\sigma_0}\right)\right)\left(1 + erf\left(\frac{t_1-t}{\sigma_1}\right)\right) \times exp\left(\gamma t\right) \tag{1.22}$$

With α a parameter related to the maximum amplitude of the signal. To describe the rising and falling edge of the signal, Gauss error functions are used. The position parameter t_0 (respectively t_1) and the scale parameter σ_0 (respectively σ_1) represents the time at the half-amplitude and the sharpness of the rising (respectively falling) edge of the signal. The exponential $exp\left(\gamma t\right)$ is introduced to take into account a possible non uniformity of the electric field in the bulk. The drift time can then be estimated by the following equation:

$$t_{drift} = t_1 - t_0 \tag{1.23}$$

This function describes accurately the signal induced by the holes on the whole range of electric field and temperatures (see Figure 1.18 (b). Nevertheless, the higher number of parameters complicates the convergence and the initial parameters need to be carefully chosen to fit the signals.

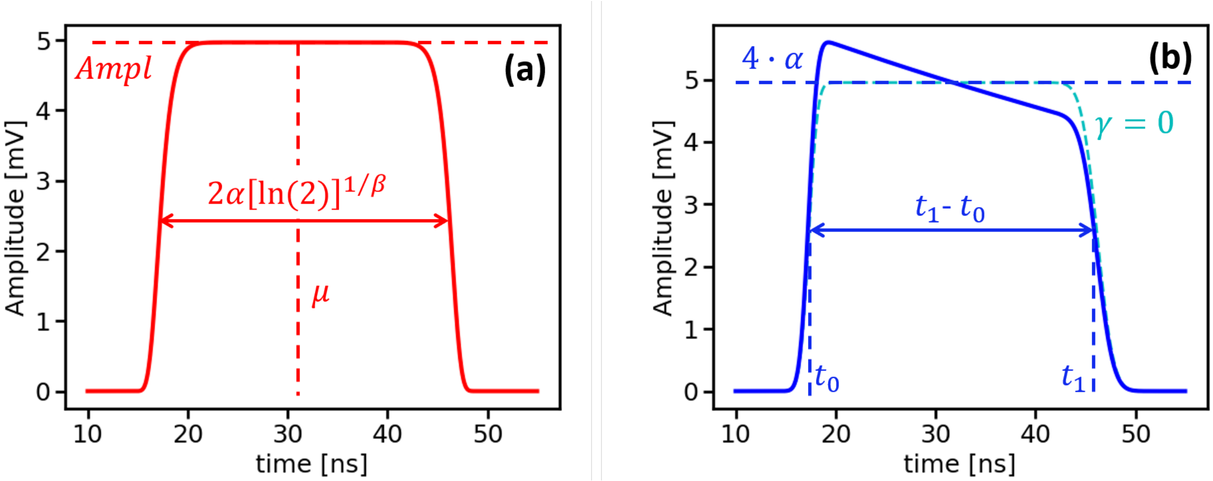

Figure 1.18: (a): GGD fit function. (b): Fit function described in function [Gabrysch, 2010]. The cyan curve is calculated for $\gamma = 0$.

1.3.5.3 Evolution of the drift velocity with the electric field

The drift velocity is directly dependent on the electric fields E. The mobility μ represents the ability of charged carriers to move through a semiconductor in response to an electric field (see Equation 1.24).

$$v_{drift} = \mu\left(E\right) \cdot E \tag{1.24}$$

At low electric field, the mobility is constant and so the drift velocity is directly proportional to the electric field. Whereas, at high electric field, the emission of optical phonons leads to a saturation of the drift velocity. A relative accurate model to describe the evolution of the drift velocity with the electric fields at room temperature is the Caughey-Thomas empirical model [Caughey, 1967]:

$$v_{drift}\left(E\right) = \frac{\mu_0 E}{1 + \frac{\mu_0 E}{v_{sat}}} \tag{1.25}$$

In this equation, μ_0 is the low field mobility and the v_{sat} is the saturation drift velocity. The asymptotic behavior of this function is the one expected: at low electric field, the mobility is equal to the low-field mobility, while at high electric field, a saturation of the drift velocity is observed (see Figure 1.19).

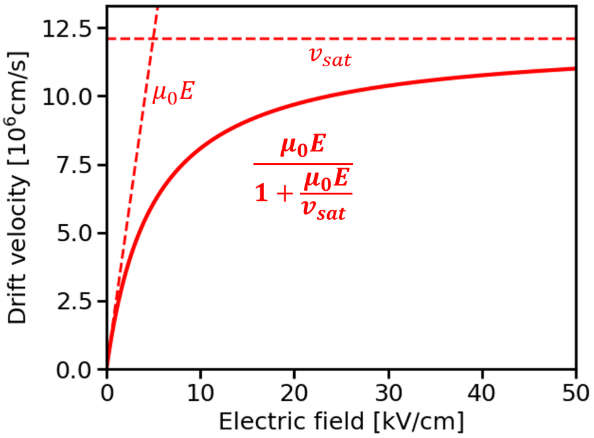

Figure 1.19: Drift velocity calculated from Equation 1.25 versus the electric field, for $\mu_0 = 2400\,\mathrm{cm}^2/(\mathrm{V{\cdot}s})$ and $v_{sat} = 12 \times 10^6\,\mathrm{cm/s}$.

1.4 Summary

In this chapter, the properties that make diamond suitable for fast counting and timing applications or for use in a harsh radiative environment were described. The advantages of CVD growth techniques for detection applications were highlighted and the difference between ohmic and Schottky contacts was presented. The impact of impurities on the signal induced by a diamond used as a solid state ionization chamber was discussed. In particular, the impact of polarization effects, which induces a modification of the electric field distribution in the bulk, was explained. Some techniques to limit these phenomena were introduced. Finally, the TCT, used to characterize the transport properties (low field mobility and saturation drift mobility), was presented.

2

Characterization of diamond samples in the laboratory

Contents

I mainly used the diamond as a solid state ionization chamber to estimate the energy loss of incident particles in the diamond bulk, and to study the intrinsic diamond charge collection and transport properties. In the first part of this chapter, the diamond sample main characteristics (batch name, dimension, metallic contacts) and their encapsulation (detector holder) are described as well as the Read-Out Electronic (ROE) they were connected to. Then, the different experiments carried out to quantify the diamond properties are presented.

The first one consisted in measuring the leakage current of the diamond at different biases. The I-V characteristics thus obtained gave information relative to the metalization quality. Afterwards, the Transient Current Technique (TCT) was a key to quantifying the transport properties of diamond. In particular, the carrier low-field mobility and drift velocity were estimated for each diamond and compared to the literature. Finally the charge collection properties, in particular Charge Collection Efficiency (CCE) was evaluated at different biases. To perform the two latter experiments, an alpha radioactive source of 241 Americium (^{241}Am) was used as a primary source of particles. Due to the small ranges of the alpha particles in the diamond samples, polarization effects were observed, this is a point I will emphasize in my analysis of the data.

2.1 Description of the detector design and of the read-out electronics

2.1.1 Sample preparation and encapsulation

In order to apply a homogeneous electric field in the [100] direction of the diamond crystal and to extract the induced current in the diamond bulk, the diamond samples are metallized. It means that electrical contacts are made by depositing thin metallic layers on the top of the sample. Different metals can be used to do so. In our case, three different metal combinations were investigated: aluminium, titanium+aluminium and titanium+aluminium with an annealing step before the aluminium deposition. The objective was to compare the impact of these three metallizations on the detector charge collection properties.

The Table 2.1 summarizes the different diamond samples tested. The diamonds are single crystal Chemical Vapor Deposition (scCVD) diamonds and are about $4.6 \times 4.6 \times 0.545$ mm^3. They were received at the same period of time (December 2019) from the same supplier: Element 6. This supplier was selected because of the very high purity of the diamonds they grow (impurities level concentration $[N] < 5$ ppb and $[B] < 1$ ppb).

The metallizations were performed by laser littography and metal evaporation on the NanoFab facility of the Institut Néel by the NanoFab staff.

Using a binocular magnifying glass, it is checked that: 1) the metallization is not too close to the edge of the diamond; and 2) that the metal layers on the two sides of the diamond are well aligned. On the Figure 2.1, two pictures are shown. On the left, the metallization is well centered and the two sides are aligned. Whereas, on the right, the metallization is too close of the left corner and the metallization of each side is not aligned: it can caused some sparkling effects when a bias is applied on the diamond and so damage the ROE. The leakage current is carefully evaluated and if its value is too high on the operating voltage range or if some sparkling effects are observed, the metallization is remade. Some diamonds are also metallized

Table 2.1: Diamond samples characterized at the laboratory.

Batch name	Diamond name	Thickness [µm]		Metalization	
		value	error	metal	thickness [nm]
GOT	Tyrion	545	5	Al	100
Star Wars	Han	545	5	Al	100
	Leia	545	5	Al	100
	Luke	545	5	Al	100
	Vador	545	5	Ti/Al + annealing	10/100
	Yoda	545	5	Al	100
Harry Potter	Albus	545.25	1.25	Ti/Al	10/100
	Harry	550.5	3.5	Ti/Al + annealing	10/100
	Hermione	550	1	Ti/Al	10/100
	Ron	546	3.5	Ti/Al	10/100
	Tom	548.25	1.75	Ti/Al	10/100
LOTR	Frodon	546.75	1.75	Ti/Al	10/100

by strips or pixels, the visual check is then useful to verify the shape of the pixels/strips or the inter-strip distance.

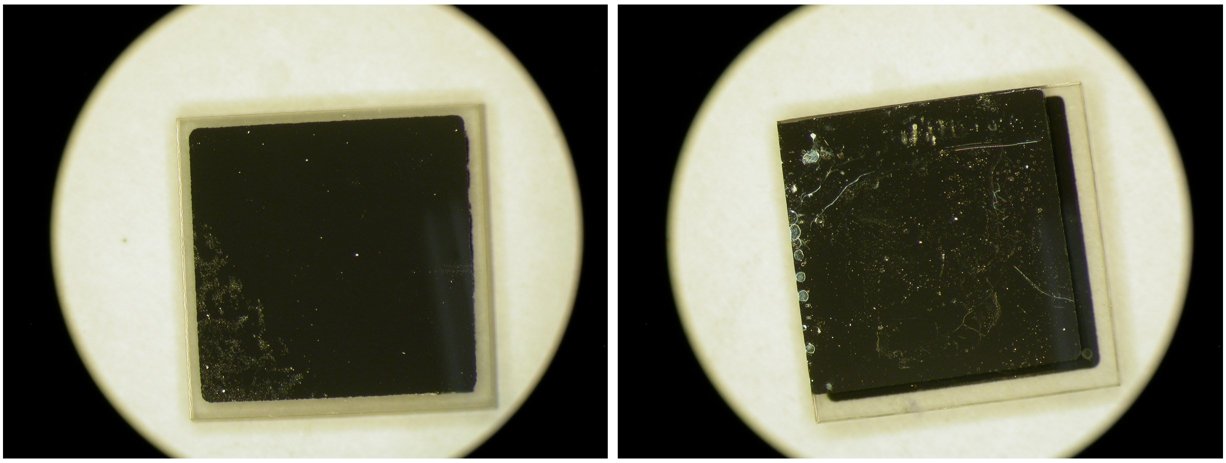

Figure 2.1: Picture captured using a binocular magnifying glass. On the left, the metallization of the diamond is centred and the two sides are well aligned contrary to the image on the right where the metallization is very close to the left edge and where the two faces are not aligned.

After this step, the diamonds are encapsulated in detector holders, designed at the LPSC, in order to use them as a solid ionization chamber, and so as a radiation detector. Two kinds of holders were fabricated.

With the first holders in Figure 2.2 (a) and (b), the diamond is in a "sandwich" configuration. It allows simplicity to mount and disassemble the diamonds and a certain robustness of the assembly. On the PCB, a circular hole is present at the center to allow the irradiation of the diamond. The electric contact is done thanks to a copper ring with gold coating. Those contacts are used to bias and collect the signal induced in the diamond during an irradiation. A 50 Ω adapted electric track is used to make the contact between the ring and the coaxial SMA termination allowing the transport of the high frequency signals with limited attenuation.

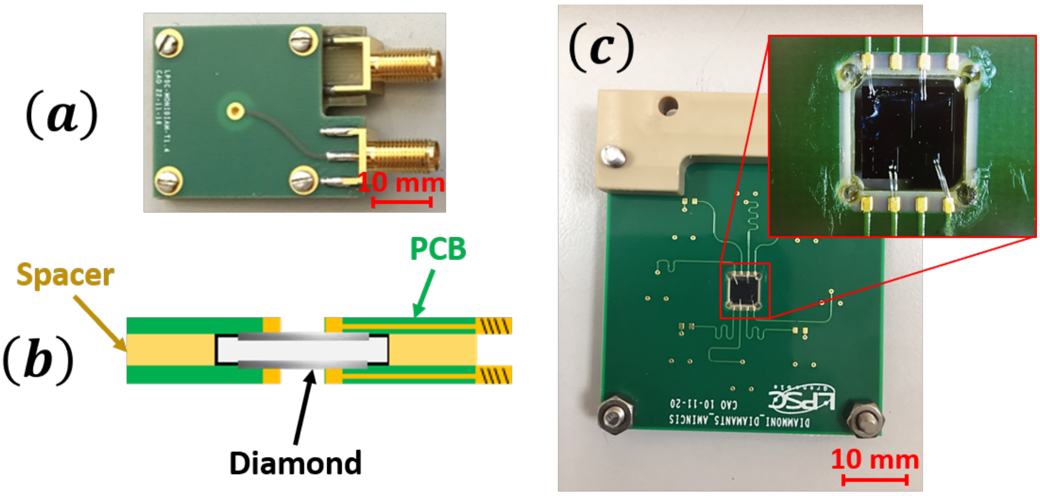

Figure 2.2: (a) picture and (b) and scheme of the first sample holder; those two images are extracted from [Curtoni, 2020]. (c) Photo of the second sample holder.

On this sample holder, it is not possible to correctly bias and read the signal of stripped or pixelated diamond because it is not possible to connect different pixels or strips.

The second sample holder in Figure 2.2 (c) was designed for that purpose. Here, the diamond is firstly glued to the sample holder at each corner. Then, aluminium bonding wires are used to connect each strip or pad to one of the 50 Ω adapted track (height possible on one side and one on the other side or four on both side). The tracks were designed to exhibit the same length. An SMA connector is also used as the termination of each track. As seen, on Figure 2.2 one face of the diamond can almost be entirely used during an irradiation, increasing consistently the working surface of the detector compared to the first sample holder. However, that kind of detectors are more difficult to mount (gluing, bonding wires...) and are also more fragile.

2.1.2 Read-Out Electronics used in the acquisition

In order to measure the current induced in the diamond sample, ROE needs to be used depending on the experiment. I used two different types of ROE: charge and current preamplifiers. For each of them, a commercial of CIVIDEC Instrumentation and a LPSC version were tested.

Regarding the current PA, the CIVIDEC C2-HV was chosen for its very good performances (see Table 2.2). In particular, its large bandwidth, its high gain and its low noise were key properties for signal acquisition. A current PA was also developed at the LPSC [Hoarau, 2021]. Although I did not have the opportunity to use this device in my personal work, recent improvements of the LPSC PA would make the device very interesting to use in future experiments. In particular, the LPSC PA has a higher gain and a larger bandwidth than the CIVIDEC C2-HV (see Table 2.2). The power consumption of the LPSC PA is also lower and can be reduced down to 4 V × 20 mA for specific applications. Regarding the spectroscopy measurements, the charge-sensitive LPSC PA was mainly used. Indeed, this device is adapted for the alpha spectroscopy measurements (see Subsection 2.4.1) and has the advantages to be already available at the laboratory. For some charge measurements, the CIVIDEC C6 was also used as a fast charge-sensitive PA. It has the advantage to be faster but only one input polarity is accepted. The performances of these devices are summarized in the Table 2.2.

Table 2.2: Characteristics of the Preamplifiers (PA) used during my PhD work.

	Current PA		**Charge PA**	
	CIVIDEC C2-HV [C2-HV]	**LPSC** [Hoarau, 2021]	**CIVIDEC C6** [C6]	**LPSC**
Bandwidth	1 MHz – 2 GHz	1 MHz – 3 GHz	/	/
Gain	40 dB	43 dB	/	/
Shaping time	/	/	10 ns	10 µs
Input polarity	Both	Both	Negative	Both
Inverting	False	False	True	True
Power supply	+12 V 100 mA	+12 V 40 mA	+12 V 30 mA	±12 V 40 mA

To acquire the signal (in particular in pulse mode), a Digital Sampling Oscilloscope (DSO) LeCroy HD09404 was used. The characteristics of this device are summarized in the following table. It can be noticed that the performances of this oscilloscope are more than satisfying for our measurements and that the main limitation are coming from the PA used (in particular about the bandwidth).

Table 2.3: Characteristics of the Oscilloscope LeCroy HDO9404 used during this PhD work.

Digital Sampling Oscilloscope (DSO) **LeCroy HDO9404** [WaveRunner 9000 Datasheet]		
Active analog channels	2	4
Sampling frequency	40 GS/s	20 GS/s
Analog bandwidth	4 GHz	
Vertical resolution	10 bits	
Dynamic range (at 50 Ω)	± 5 V	

2.2 Leakage current measurements

Measuring the leakage current is crucial to ensure that the detector can be used in further applications. Indeed, a too high leakage current might damage the ROE (in particular the PA) and, in general, highlights some metalization issues and/or structural defects. Otherwise, some information concerning the quality and the nature of the contacts can be extracted from the I-V characteristics. Moreover, the leakage current seams linked with the defect density [Pomorski, 2008]. Finally, the I-V characteristic gives information concerning the noise level when a bias is applied on the sample.

2.2.1 Equipment and methods

The leakage current setup was developed by a previous PhD Student who worked at LPSC [Curtoni, 2020]. The setup is illustrated in Figure 2.3. In this setup, the diamond is placed in a box to ensure the light and the electromagnetic isolation. Inside the box, a coaxial SMA cable is used to bias the diamond and another to measure the leakage current. The High Voltage (HV) supply is an ISEG NHQ 223M module which can apply a voltage up to ±3000 V. The current is measured thanks to a Keithley 6487 picoameter with a minimum resolution of 10 fA (for a 2 nA range). These two devices are linked to the box thanks to BNC coaxial cables and are controlled thanks to a computer.

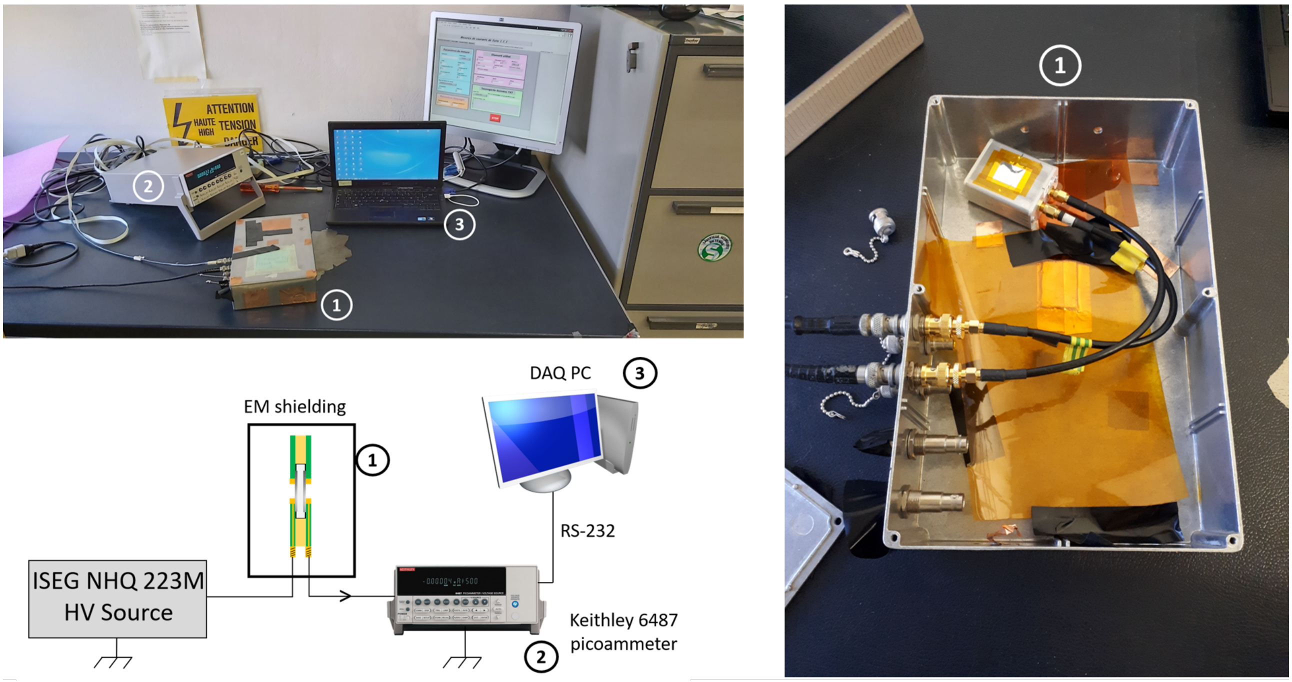

Figure 2.3: The leakage current setup at LPSC was developed by S. Curtoni; this image is extracted from his PhD manuscript [Curtoni, 2020]. The diamond is placed in a box (1) in order to have a Faraday shielding. The diamond is biased thanks to the ISEG NHQ 223 M and the current is measured thanks to a picoameter Keithley 6487 (2). (3) A software developed on LabVIEW was designed to synchronize the devices and generate the output files.

A LabVIEW program was developed in order to control the devices. With this program it is possible to control different parameters such as the voltage range, the voltage steps or the critical intensity above which the system goes into security mode (to avoid too high current induced by the sparkling effects). After each voltage variation, the system waits 60 s before starting the current measurement. Indeed, it was noticed that when the bias voltage is changing the leakage current increases sharply before decreasing slowly in time and reaching a steady value. This 60 s duration is sufficiently long, for the vast majority of samples, to reach the stable state of the system. In order to have an estimation of the leakage current, 100 measurements spaced by 1 s (the parameters can be modified by the user) are averaged and the standard deviation is taken as the current error. The different values were previously adjusted and are identical for all the sample presented in this work.

2.2.2 Experimental results

The different leakage current measurements are plotted in Figure 2.4. For those measurements a voltage range of ±1200 V with a 50 V voltage step was chosen to ensure that the system can safely be used in a large voltage range.

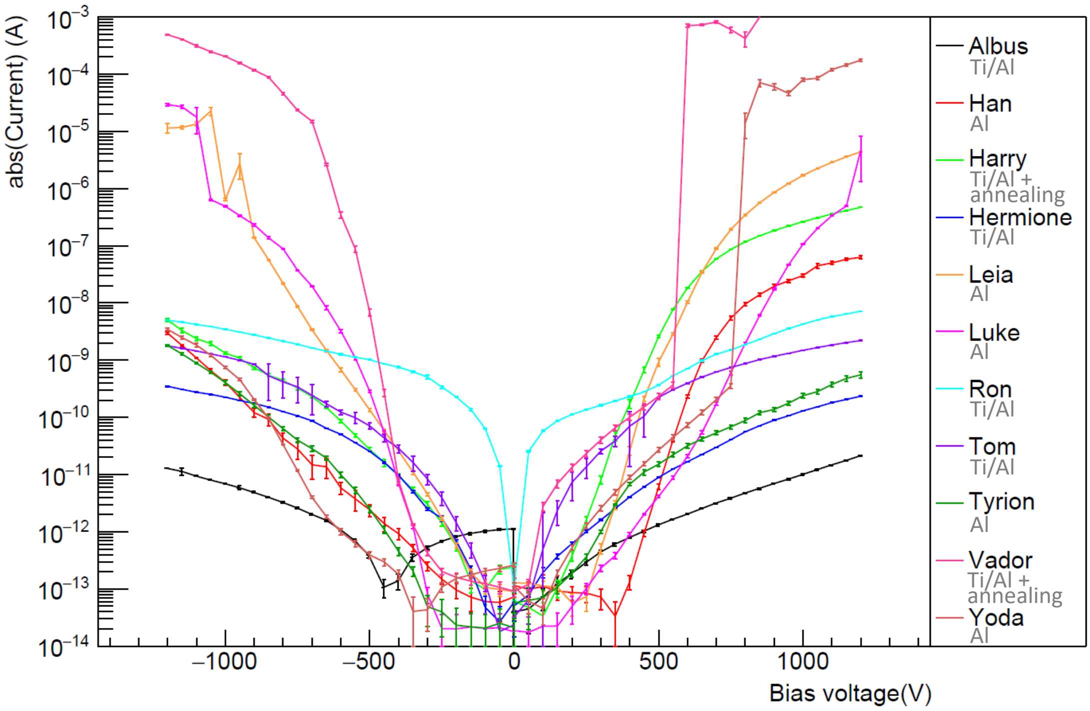

Figure 2.4: Leakage current measurements of the different diamonds presented in the Table 2.1

As it can be seen in the Figure 2.4, the leakage current characteristics vary a lot from one sample to another. That can be explained by the quality of the contacts (metallization and encapsulation), the exterior condition (temperature or other unidentified sources of noise) or the intrinsic quality of the diamonds. Only one diamond (Vador) reaches the limit of 1 mA. This diamond has some issues with the metallization, the titanium and aluminium layers of each side are not well aligned. It could be precised that it was the first diamond with such a metallization and that the deposit principle was later improved inducing lower leakage currents to be measured.

Some diamond samples have a quite symmetrical behavior and most of them have a leakage current below 10 nA over the entire voltage range. However, no difference of behavior between the aluminium and titanium+aluminium metallization was observed in this experiment.

2.2.3 Discussion and comments

Diamond leakage current was characterized prior to any other experiments. Some metallization issues were revealed (diamonds named VADOR in particular), but it seems that a bias of ±500 V (a little bit less than 10 kV/cm) can be reached for relatively limited leakage current ($<$ 10 nA). As a result, it should be possible to use those detectors on this bias range during an experiment.

Unfortunately those measurements are not done in the best possible conditions, which does not allowed an accurate quantification of the leakage current. Indeed, the measurements are not performed under vacuum and neither the temperature nor the humidity is controlled. Only the light and the electromagnetic isolation is ensured by a metallic box. Moreover, coaxial cable are not suitable to measure such low currents and triaxial cable should be considered to perform more accurate measurements. Nevertheless, it could be noticed that this setup is perfectly suitable to study the general evolution of the leakage current or to obtained a rough estimation of the leakage current. For instance, the same experiment was carried out few days apart on the diamond named RON (see the Figure 2.5), and some fluctuations can be observed. For instance, at 500 V, the leakage current measured on the 22^{nd} afternoon and 26^{th} of September is almost twice higher than the one measured on the 21^{st} of September. Moreover, the important increase of the leakage current at low biases seems to occur at different biases (between 700-900 V) depending of the measurement. Nevertheless, it can be noticed that the general behavior of the leakage current remains the same.

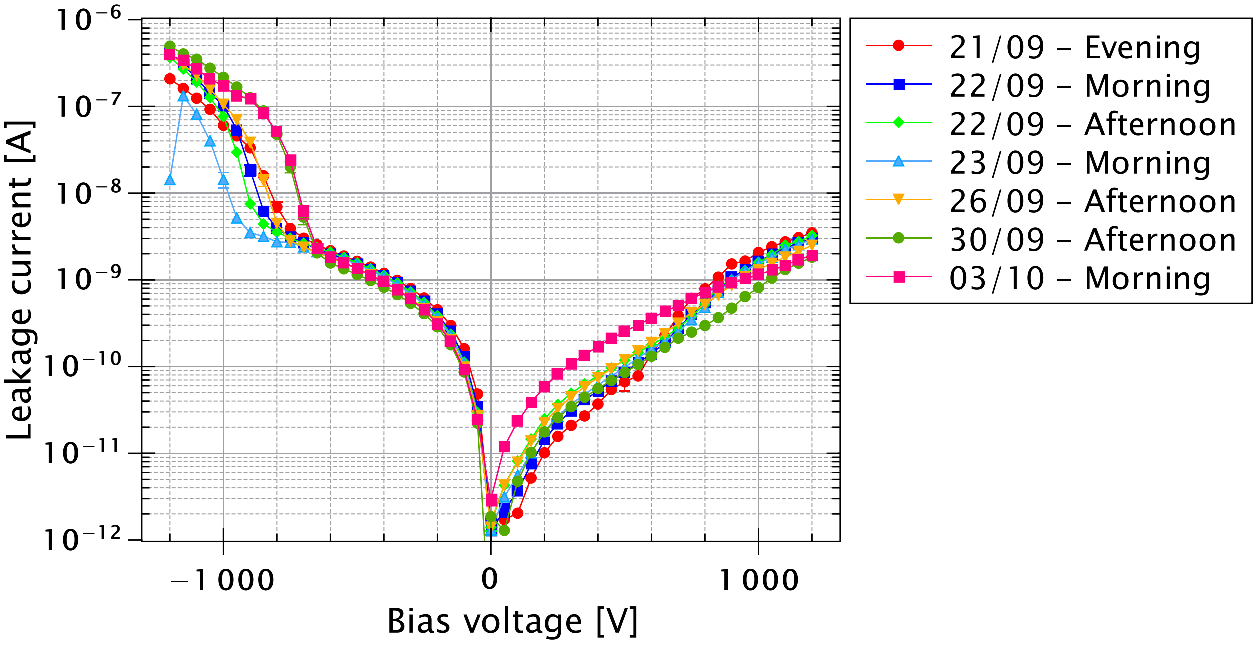

Figure 2.5: Leakage current measurements done on the diamond named RON few days appart.

2.3 Characterization of the charge carriers transport properties using the Transient Current Technique (TCT) with an alpha source test bench.

The charge transport properties of a given diamond sample are to be investigated if it is intended to be used as a detector. In particular, measuring the carrier drift velocity at various electric fields allows to estimate key parameters as 1) the carrier low-field mobility, and 2) the saturation drift velocity. Moreover, the shape of the current traces can reveal some polarization effects in the diamond samples [Pernegger, 2005]. As a result, optimal parameters and/or procedures can be studied and then implemented in the future measurements. To perform those characterizations, a test bench using an alpha source was developed. The α particles interacting in the detector are used as a primary excitation, and the Transient Current Technique described in the Subsection 1.3.5 is carried out in order to study separately the transit of holes and electrons. The different diamond of the Table 2.1 were then characterized using this method.

2.3.1 Equipment and methods

The Transient Current Technique (TCT) is described in details in the Subsection 1.3.5. To apply this technique, the charge carriers need to be generated very close to the electrode facing the excitation source. One of the simplest way to achieve that is to use an alpha radioactive source.

The 241 Americium (^{241}Am) is an alpha radioactive source with three main decay energies which are summarized in Tab 2.4 (data from NNDC - Brookhaven National Laboratory: `https://www.nndc.bnl.gov/`). A SRIM [Ziegler, 2010] simulation was proceed for those alpha energies in order to extract their ranges in diamond. For those energy levels, the alpha particles are stopped within 15 µm, which is negligible compared to the 545 µm thick diamond sample: it is then possible to carry out the TCT using an ^{241}Am source.

Table 2.4: Americium main alpha decay rays (>1%). The range of each alpha energy in diamond was calculated using the software SRIM.

Energy [MeV]	Intensity [%]	Range in diamond [µm]
5.388	1.66	13.2 ± 0.2
5.443	13.1	13.4 ± 0.2
5.486	84.8	13.6 ± 0.2

The Figure 2.6 illustrates the LPSC setup mounted to make TCT measurements. The diamond sample and the ^{241}Am source are placed in a vacuum chamber. The distance between the radioactive source and the diamond can be adjusted by moving the radioactive source. A first vacuum pump is used to reach pressures between 0.1 and 1 Pa. At those pressures, considering the relatively small distance between the source and the sample ($<$ 1 cm), the energy loss of the alpha particles is negligible. As a result, the particles interacting in the diamond sample deposit all their energy in this one and have, in average, a range of about 13.6 µm.

Each side of the diamond is connected thanks to small SMA cables to one CIVIDEC C2-HV wideband preamplifier located outside of the chamber. One of this CIVIDEC will be used

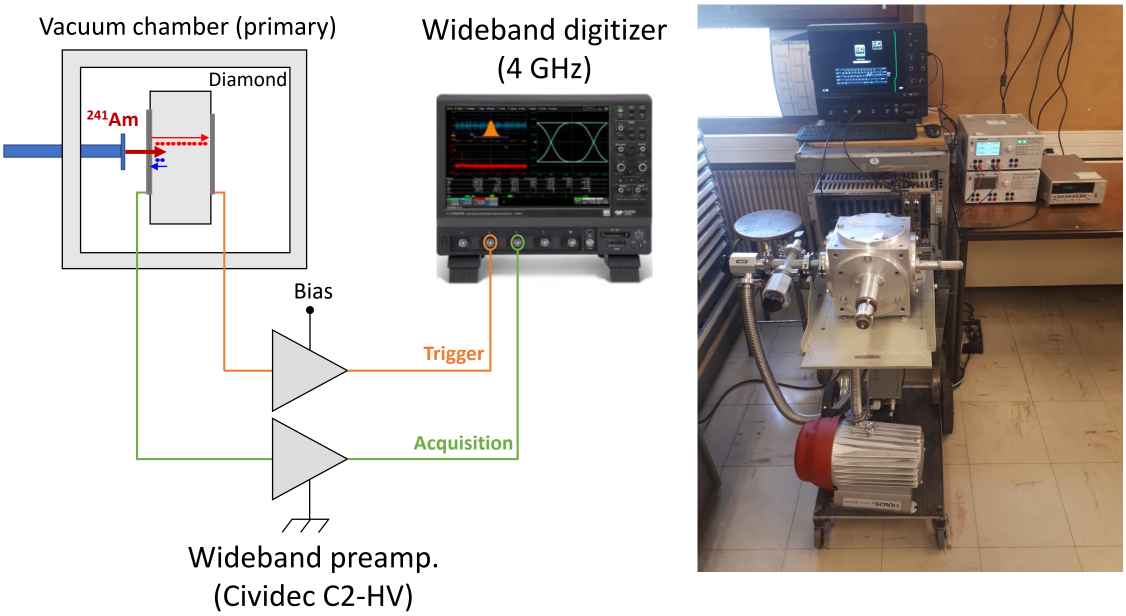

Figure 2.6: Setup used to perform transient current measurements at LPSC.

to apply a bias on the side not-facing the radioactive source, when the other is connected to the ground thanks to 50 Ω termination. The two signals are recorded by a wideband digitized sampling oscilloscope (DSO) LeCroy HDO9404. Even if, during the experiment, the two signals are recorded, one of them will be used as a trigger while the other one will be processed in order to extract the diamond sample characteristics. About 300 to 500 traces are individually saved for each channel.

Data processing is carried out as follows, the noisy traces, particularly numerous at low biases, are rejected using a charge threshold and the selected traces are fitted thanks to the GGD function described in Equation 2.1.

$$I(t) = I_0 \cdot exp\left[-\left(\frac{|t-\mu|}{\alpha}\right)^{\beta}\right] \tag{2.1}$$

In this equation, I is the intensity of the signal over time, t the time, I_0 the maximum amplitude of the signal, μ a position parameter (position where $I = I_0$), α a scale parameter (sharpness of the signal slopes) and β a form parameter (form of the signal). As explained in the Subsection 1.3.5, the equation 2.1 can be used to describe the TCT signals. This function has the advantage to converge quite easily, compared to more complex functions, while providing an accurate estimator (the FWHM of the function) of the signal drift time:

$$t_{drift} = 2\alpha\,[ln\,(2)]^{\beta} \tag{2.2}$$

During the fitting process, another signal selection is done: the traces with a fit reduced χ^2 superior to 3 are rejected and the drift times are not conserved. At the end of this step, a drift time distribution is obtained. Then, the mean and the standard deviation of the distribution are used as estimators of the drift time and its error for each specific bias. As discussed, in the Subsection 1.3.5, it is then possible to compute the drift velocity v_{drift} at each electric field by using the following formula:

$$v_{drift} = \frac{t_h}{t_{drift}} \tag{2.3}$$

with t_h the thickness of the diamond sample.

2.3.2 Experimental results

A large set of diamonds (see Table 2.1) were tested. This subsection will be divided in two parts. At first, the diamond Ron will be taken as a reference sample to illustrate an example of the results we can expect by using the TCT. Then, the mean parameters obtained for the whole diamond set will be presented.

2.3.2.1 Results obtained on one sample - example of the diamond named RON

The mean traces obtained for the diamond named RON for holes (electric fields from 549 to 9158 V/cm) and electrons (electric fields from 733 to 9158 V/cm) are presented in the Figure 2.7. It can be noticed that there is no polarization effects visible for this diamond confirming its good quality. The saturation of the drift velocity can also be observed for the highest fields (in particular for holes, see Figure 2.7 (left)).

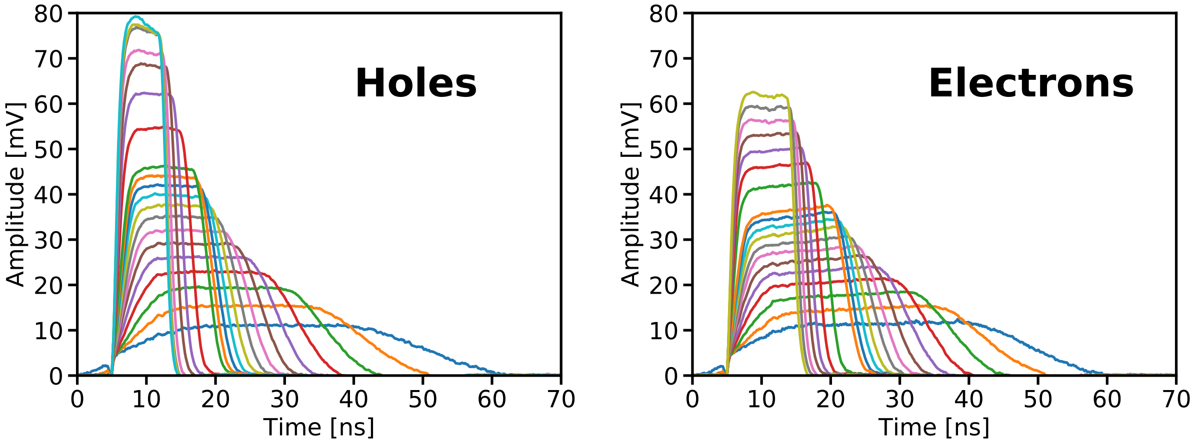

Figure 2.7: Mean traces obtained for the diamond named RON for holes (left, 549 to 9158 V/cm) and electrons (right, 733 to 9158 V/cm).

The drift velocities evaluated at various electric field for the diamond RON are shown on the Figure 2.8. The drift velocities obtained at a specific electric field for holes (left) are systematically higher than the one obtained for electrons (right). This phenomenon is consistent with most of the drift velocity measurements performed using the TCT on ultra-pure diamonds at room temperature [Pernegger, 2005,Pomorski, 2006,Gkoumas, 2009,Gabrysch, 2011,Jansen, 2013a].

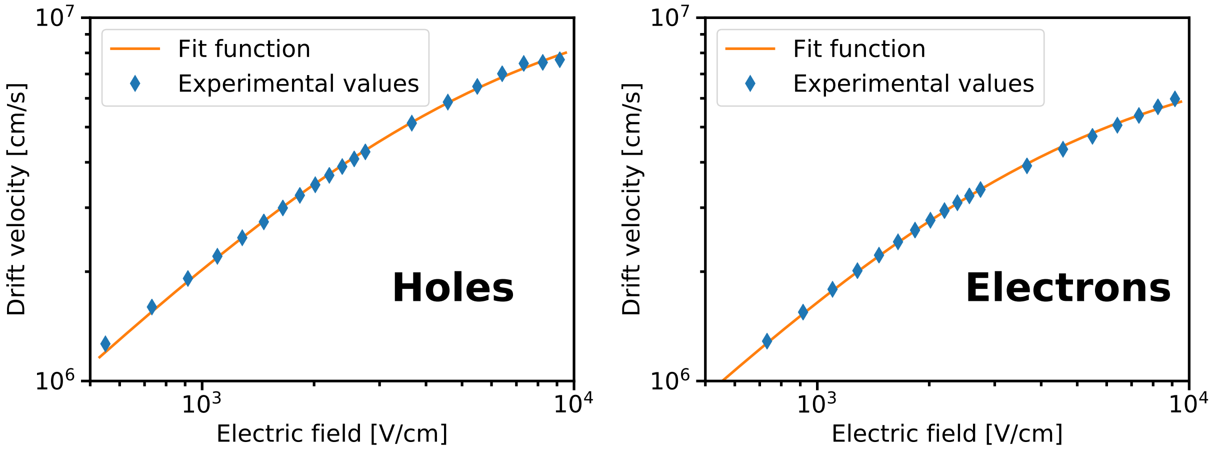

Figure 2.8: Drift velocities obtained at different electric fields for the diamond named RON for holes (left) and electrons (right).

The evolution of the drift velocity with the electric field can be described by the empirical model developed by Caughey and Thomas [Caughey, 1967]:

$$v_{drift}(E) = \frac{\mu_0 E}{1 + \frac{\mu_0 E}{v_{sat}}} \tag{2.4}$$

In this equation, v_{drift} is the drift velocity, E the electric field, μ_0 the low field mobility and v_{sat} the saturation drift velocity. Those two parameters give an important information on the rapidity of the detector and are critical parameters in other application such as diamond transistors [Donato, 2019]. By fitting the data with this function, the low field mobilities of electrons and holes were evaluated (see Table 2.5). The parameters presented are the average values between both side of the diamond. Those values are in a good agreement with the value found in the literature. For instance, values of hole (respectively electron) low field mobility around 2400 cm^2/(V·s) (resp. 2000 cm^2/(V·s))) were reported [Pomorski, 2006, Marsolat, 2014].

Table 2.5: Transport parameters obtained with the diamond named RON.

	Units	Holes	Electrons
Low field mobility	[cm^2/(V·s)]	2430 ± 10	2055 ± 15
Saturation drift velocity	[10^6 cm/s]	12.1 ± 0.2	8.4 ± 0.02

2.3.2.2 Parameters obtained for the diamond set

The same experiment was done for the whole diamond set. The Table 2.6 summarizes the parameters extracted from those measurements. Some fluctuations can be observed depending of the studied diamond. Those fluctuations can be caused by many factors such as the diamond and metallization quality (polarization effects, interface metal-diamond...), the external sources of noises during the acquisition (electromagnetic noises) or the way of performing the measurements. In present case, the measurements were done on a period of about one year (with an interruption due to Covid). The protocol evolved a little bit from the first to the last diamond tested: number of traces per bias, number of bias taken or procedures to avoid polarization effects (see Subsection 1.3.4.3). Furthermore, some CIVIDEC C2-HV can be more or less noisy and the quality of the cables were not systematically checked.

Table 2.6: Transport parameters obtained with the diamond set.

		Units	Holes	Electrons
Low field mobility	Mean	[cm^2/(V·s)]	2604	2202
	RMS		186	159
	Min		2360	1850
	Max		3170	2440
Saturation drift velocity	Mean	[10^6 cm/s]	12.57	8.22
	RMS		0.63	0.29
	Min		10.8	7.47
	Max		13.5	8.84

The temperature could also have an influence on the low field mobility estimation considering the time period of the measurements and that the experiment room is being badly isolated. On the Figure 2.9, it can be noticed that even if the low field mobility of the measurements done during the summer are slightly lower than the one taken during the winter, it is difficult to observe a clear influence of the temperature on the low field mobility.

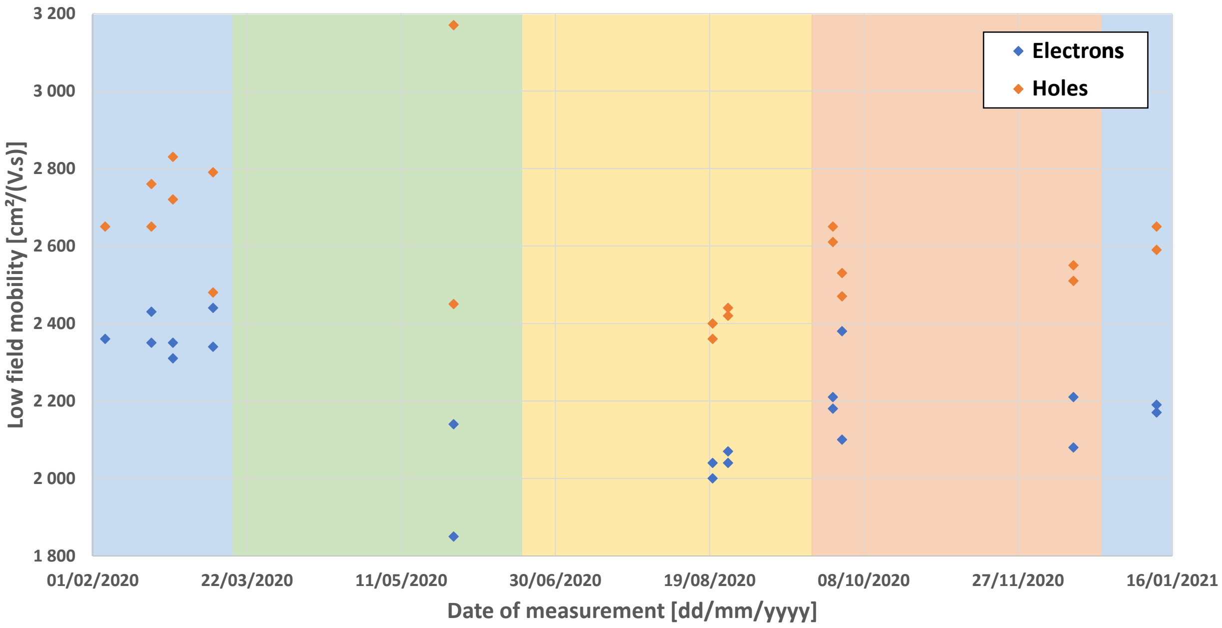

Figure 2.9: Electron and hole low field mobility evolution measured at different dates. The different colors on the graph represents the different seasons (blue: winter, green: spring, yellow: summer and orange: fall).

2.3.3 Discussion and comments

The alpha setup and the TCT were used to qualify and quantify the transport properties of the diamond set of Table 2.1. Those measurements highlighted the good crystalline quality of the diamond set (limited polarization effects). The low field mobility and the saturation drift velocity were computed for a whole diamond set. Thus, an average low field mobility of $(2600 \pm 190)\,\mathrm{cm^2/(V{\cdot}s)}$ and $(2200 \pm 160)\,\mathrm{cm^2/(V{\cdot}s)}$ were obtained for holes and electrons (respectively). Concerning the saturation drift velocity, values of $(12.60 \pm 0.63)\,\mathrm{V/cm}$ and $(8.22 \pm 0.29)\,\mathrm{V/cm}$ were extracted for holes and electrons (respectively). Some fluctuations were observed on those values probably caused by a procedure adaptation and external source of noises.

Those values are in a relatively good agreement with literature [Pomorski, 2006, Marsolat, 2014], confirming the procedure used to quantify the transport properties of the diamond samples. Nevertheless, this procedure could be improved by introducing a better strategy to avoid the polarization effects observed on few samples and a way to better control the external parameters such as carrying out the experiments in a temperature and humidity controlled environment. It can also been noticed that the fit function, does not perfectly describe the drift velocity. Even if the deviations are small, the errors are not randomly distributed around zero (see Figure 2.10).

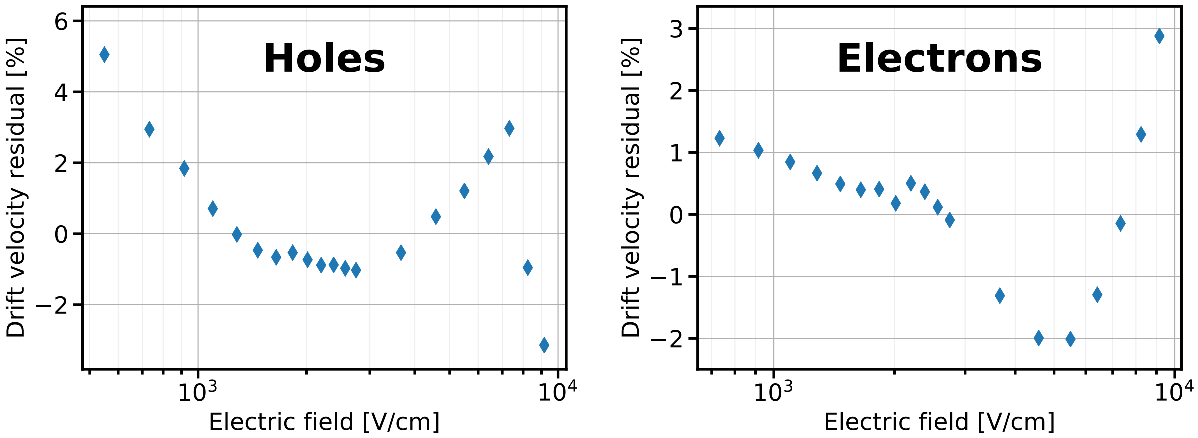

Figure 2.10: Drift velocities residual obtained for the diamond named RON for holes (left) and electrons (right).

2.4 Characterization of the charge collection of diamond detectors with an alpha source test bench.

The charge collection properties are key characteristics of radiation detectors. Indeed, those properties show how efficiently a detector can collect the charges generated by the incident particles or beam. If a detector cannot collect all the charges, this one cannot directly be used for spectroscopy applications and need, at least, a meticulous calibration phase.

2.4.1 Equipment and methods

To characterize the charge collection properties of diamond samples, the collected charge is studied at different external electric fields. The Charge Collection Efficiency (CCE) is defined by the following formula:

$$CCE(V_{bias}) = \frac{\text{Charge collected on the electrodes}}{\text{Charge generated by the ionization}} \tag{2.5}$$

If the charge collected is similar to the one created in the diamond by the slow down of the incident particle, then the CCE is maximum an equal to 100 %. As seen on Figure 2.11, the alpha setup is used to characterized the CCE of the diamond detectors. To be as much precise as possible, a different ROE is used. The signal is firstly amplified and integrated by a charge-sensitive preamplifier. Then, it is amplified and shaped by an amplifier-shaper Ortec 572 with a shaping time of 1 µs. Finally, the signal is digitized thanks to a 16-bit Multi-channel Analyzer (MCA) and the energy spectra is acquires and displayed on a computer. The gain of the amplifier-shaper was chosen in order to use the full dynamic range of the MCA (0 to 10 V).

The calibration of the ROE is done by using a pulse generator: a series of square signals of different amplitudes are injected in a test capacitance of 1 pF. The signal is amplified by the ROE chain described before. A spectra composed of different peaks as seen in Figure 2.12 (left) can be observed. As part of my work, I developed a program that could fit each of those peaks with a Gaussian function in order to extract and to make a relation between the mean of the distribution and the charge injected into the input capacitance (Figure 2.12 (right)). This relation should be linear on the range of interest. If it is not the case, the amplification gain of the Amplifier-shaper could be adapted.

In order to convert the charge collection spectra into an energy spectra, an average electron-hole pair creation energy of 13.1 eV is assumed [Kozlov, 1975, Canali, 1979, Kaneko, 1996, Shimaoka, 2016]. As a result, an average collected charge of 67 fC is expected in order to obtained a charge collection efficiency equal to 1, which is expected for single crystal CVD diamonds [Pomorski, 2008, Jansen, 2013a, Curtoni, 2020]. Nevertheless, it should be precised that the electron-hole pair creation energy value is not perfectly known yet, and some experiments are still ongoing [Keister, 2018].

The main limitation on this method is the uncertainty on the value of the entrance capacity. Indeed, capacities of about 1 pF are sold with an uncertainty of about 10 %. To avoid this problem, a silicon diode can be used as particle detector to achieve the calibration (see [Kozlov, 1975, Kaneko, 1996, Shimaoka, 2016, Skukan, 2019]).

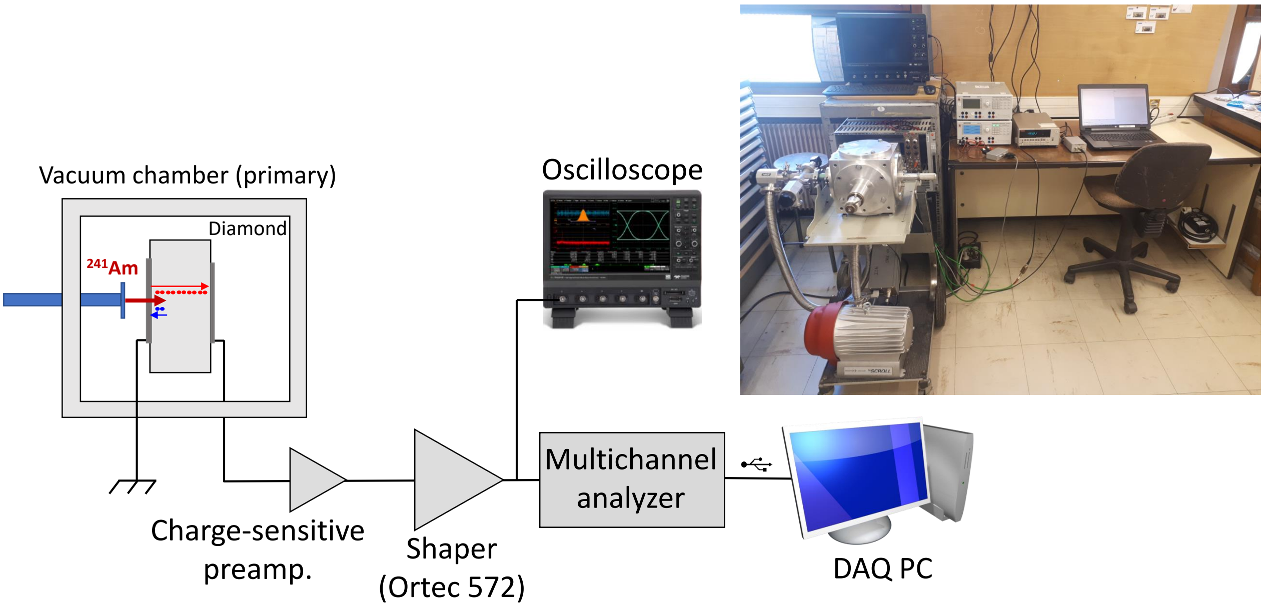

Figure 2.11: The alpha spectroscopy test bench at LPSC. The scheme is extracted from [Curtoni, 2020].

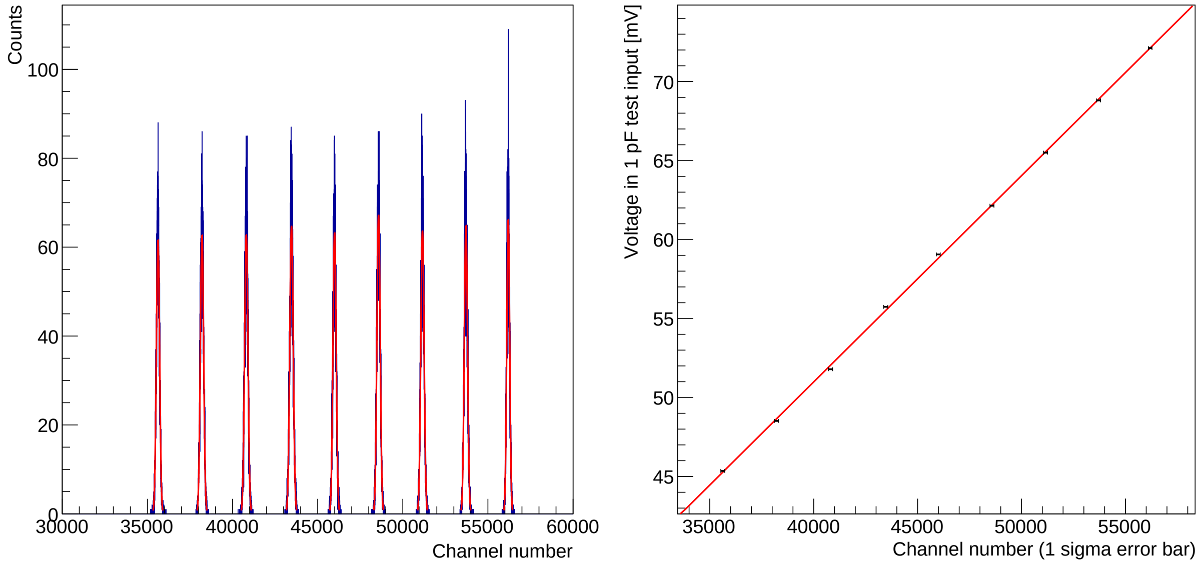

Figure 2.12: Calibration spectrum (left): each peak of this spectrum corresponds to a specific injected charge. A program was developed in order to localise the peaks and fit them with a Gaussian function. Calibration curve (right) used to calibrate the data of the diamond named RON.

2.4.2 Experimental results

I had tested many diamonds (see Table 2.1) on this test bench. As for the subsection 2.3.2, this subsection will be divided in two parts: the result obtained on the diamond named RON will be presented at first, before dealing with the whole diamond set.

2.4.2.1 Results obtained on one sample - example of the diamond named RON

The hole and electron spectra obtained at different biases are presented on the Figure 2.13. Each acquisition was 20 min long, except the one performed at 500 V which was acquired during a longer time to check the stability of the response 50 min long). One can expect to have a peak for each different alpha rays (see Table 2.4), however, whatever the charge carrier and the bias considered, the resolution of the diamond detector is not good enough to distinguish them. Indeed, even for the highest biases, only one more or less broad peak can be observed. Moreover, a large dispersion on the energy collected can be observed for the lower biases. This phenomenon is attributed to the carrier recombinations and the polarization effects.

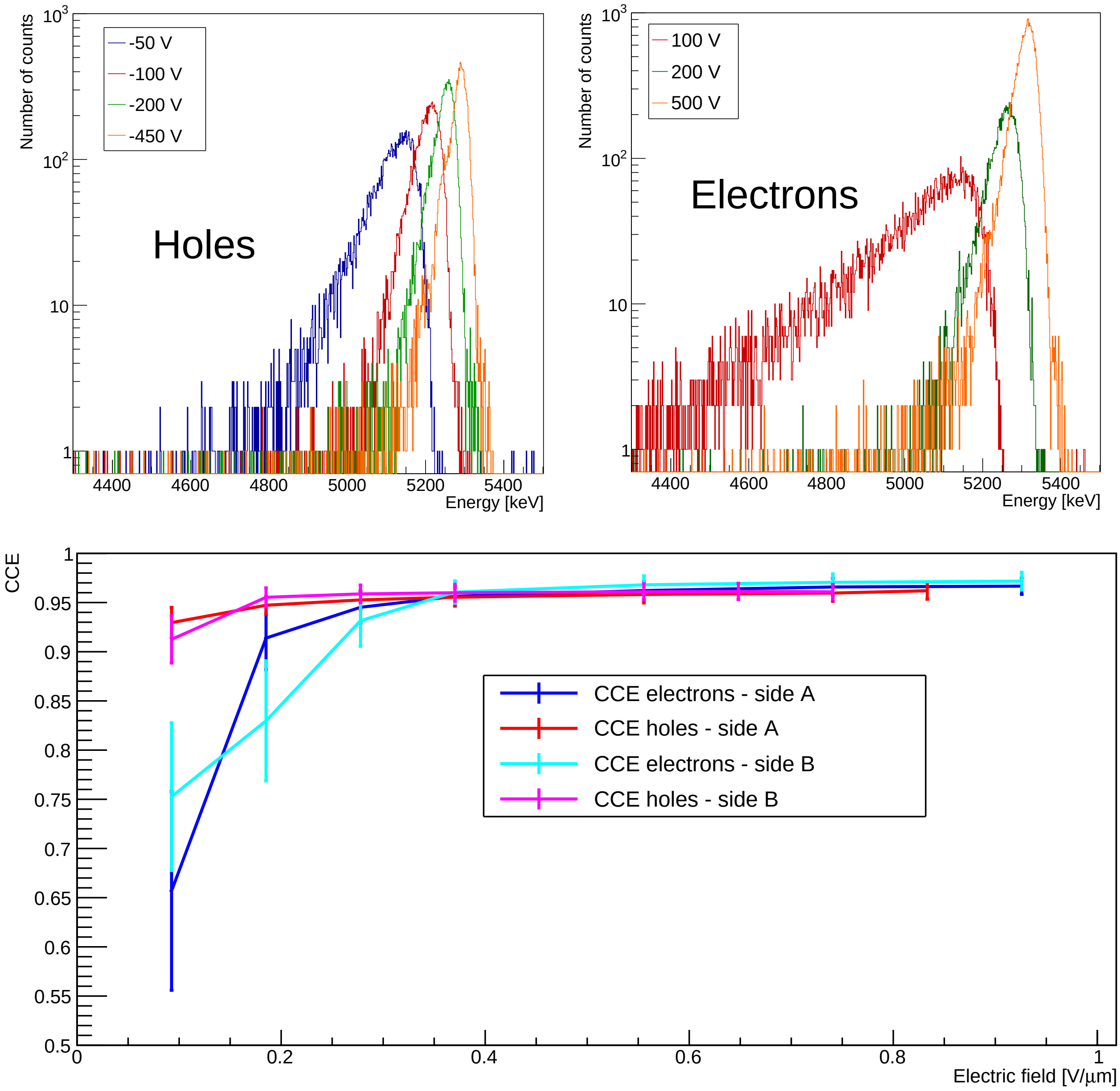

Figure 2.13: Alpha spectrum obtained with the diamond named RON for holes (left) and electrons (right). Each acquisition was about 20 min long, except the one performed at 500 V (about 50 min long). Bottom: CCE obtained for electrons and holes

For this sample, it was not possible to acquire a spectrum at −500 V (holes). The reason is that the noise was too high for the MCA, but it was decided that it was not suitable to modify the amplification parameters just for one acquisition.

In this figure, it can also be noticed that the charge collection is incomplete for lower biases (in particular for electrons) and that a saturation around 95 % is observed for higher biases. The incomplete charge collection at low biases and the important dispersion of the energy collected show the necessity to work at high biases for spectroscopy purposes. For higher biases, the incomplete charge collection can be explained by the uncertainty on the value of the input capacitance. Indeed, on the bottom graph of the Figure 2.13, the error bars do not take into account this effect.

At low biases, strong polarization effects are observed as shown in the Figure 2.14. In this, figure, it may be observed that the charge collection remains constant over time for biases higher than 200 V leading to a constant value for the energy. However for 100 V and in particular for 50 V, the charge collection decreases with time. As a result, in less than 20 min the mean of the energy distribution was divided by a factor greater than 3. In Figure 2.14 right, the peak corresponding to the CCE at 50 V without polarization effects is gradually shifted to the low energies. The dispersion becomes significantly higher, in particular for times intervals between 8 and 14 min. Finally, after about 15 min a new peak can be observed at low energy close to the noise level. As described in Subsection 1.3.4.3, this phenomenon can be avoided by, for instance, inverting regularly the bias value, as it was demonstrated with the same setup in [Curtoni, 2020].

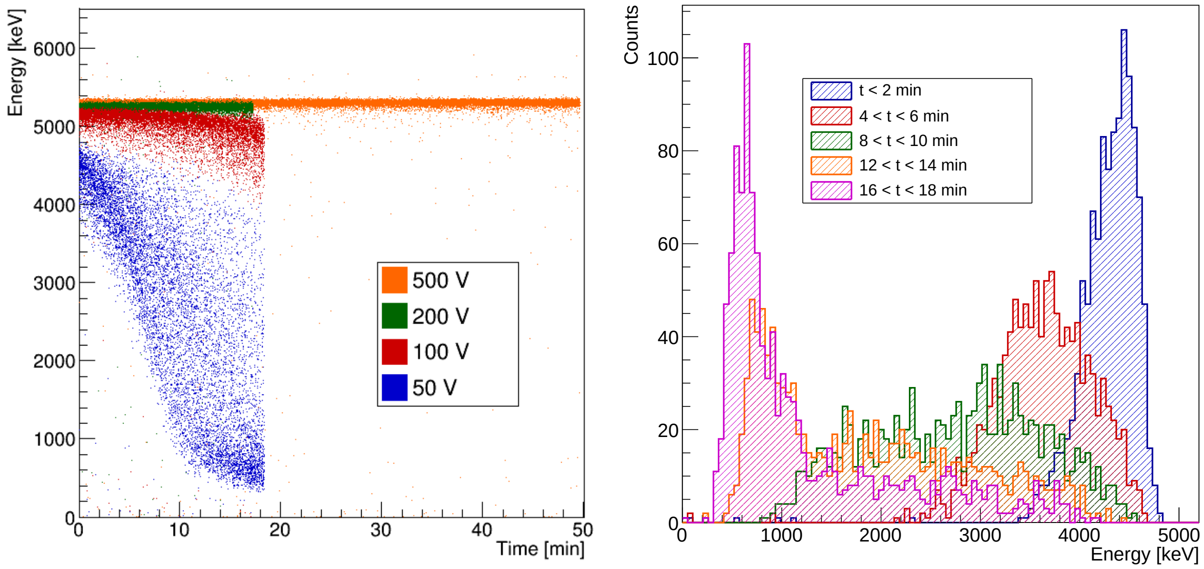

Figure 2.14: Left: Energy collected over time at various biases obtained for the diamond named RON for an electron drift. Right: Spectrum obtained at 50 V (electrons) for the diamond named RON on different time ranges.

2.4.2.2 Parameters obtained for the diamond set

The maximum CCE reached for each diamond of the set (see the Table 2.1) was extracted and, the average of the values thus obtained for electrons and holes are presented in Table 2.7.

In some experiments, it was not possible to compute the CCE for electric fields higher than 0.37 V/µm; in particular because of too important noise fluctuations. These diamonds were not taken into account for this analysis. Indeed, as it can be seen with the example of the diamond named RON on the Figure 2.13, the saturation of the CCE is not reach for electrons for field values below 0.37 V/µm.

A mean value of 96 % (respectively 97 %) is reached for holes (resp. electrons). It has already been explained that the slight difference between those values and a full CCE can be explained by the uncertainties on the value of the input capacitance. Small fluctuations are also observed between the samples. Those fluctuations could be explained by the difference between intrinsic quality of the diamond (dislocations and defaults in particular), the quality of the metallization and the calibration used. Indeed, for time saving issues, the calibration was not done before or after each spectroscopy studies. As a results, if a small modification of the parameters occured, it could not be possible to correct it.

Table 2.7: Maximum CCE obtained for the diamond set.

		Holes	Electrons
CCE	Mean	0.96	0.97
	RMS	0.01	0.01
	Min	0.94	0.95
	Max	0.99	1.00

In general, the results obtained for the diamond set are satisfying knowing that a CCE very close to 1 was obtained as expected for a single crystal diamond. Therefore, those diamond can be used as a solid state ionization chambers for particle detection purposes.

2.4.3 Discussion and comments

A procedure to quantify the charge collection properties of the diamond sample was established using an alpha test bench. Thus, the CCE of the whole diamond set was quantified, and satisfying results were observed. Indeed, it seems that most of the sample reaches a CCE very close to 1 (in average, $(96 \pm 1)\,\%$ for holes and $(97 \pm 1)\,\%$ for electrons). Some polarization effects leading to a decreasing charge collection over time were also highlighted for the lowest electric fields. At 50 V (0.09 V/µm), the charge collected is divided by a factor grater than 3 in less than 15 min. These observation put forward the necessity to have a strategy to compensate this phenomenon for measurements at low electric fields.

Another properties that could be interesting to study is the linearity of the charge response of the detector depending on the energy of the incident particles. With this setup is can theoretically been studied by changing the pressure of the chamber and so by reducing the energy of the alpha particles interacting in the detector. Nevertheless, to perform this experiment it is necessary to control precisely the pressure of the vacuum chamber and the distance between the source and the diamond; which is not possible on the LPSC setup. The ideal way to carry out this study would be to control perfectly the incident energy of the incident particles. Then, a suitable way to perform this experiment, would be to use the Ion Beam Induced Current (IBIC) technique. Indeed, with this method, the initial energy of the ions can be controlled.

2.5 Conclusion

Different methods are used for the characterisation of the diamonds detectors. The metallizations are systematically visually checked thanks to a binocular magnifying glass in order to detect the potential defaults. Then the leakage current is controlled and the few samples whose leakage current is too high are set aside for re-metallization. After this measurement, the sample properties are studied. In particular, the TCT is used to extract the low field mobility and the saturation drift velocity of the samples and the CCE of the sample is evaluated. Thus, those measurements allowed to estimate keys properties of the diamond detectors.

A large set of diamond were studied which permited to extract some parameters of interest. An average low field mobility of $(2600 \pm 190)\,\mathrm{cm}^2/(\mathrm{V{\cdot}s})$ and $(2200 \pm 160)\,\mathrm{cm}^2/(\mathrm{V{\cdot}s})$ were obtained for holes and electrons respectively for a set of 11 diamonds. Moreover, a CCE very close to 1, for both charge carriers, was found for almost all of the diamond samples. The polarization effects were also observed and study at low electric fields. It was noticed that, for an electric field of $0.09\,\mathrm{V/\mu m}$, the charge is divided by more than 3 in about 15 min. These measurements have motivated the development of a compact (compared to IBIC) and innovative in-laboratory-experimental-setup which allows the characterization of diamond properties in terms of transport and charge collection without being affected by polarization effects on a wide temperature and applied electric field ranges.

3

Implementation of a new electron beam characterization technique: the Time-of-Flight electron Beam Induced Current (ToF-eBIC)

Contents

The Time-of-Flight (ToF) technique, also called Transient Current Technique (TCT) is commonly used to study the charges transport properties in diamond. Generally, it relies on alpha particles that deposit their energy near the surface of the diamond [Canali, 1979, Pernegger, 2005, Pomorski, 2006, Nesladek, 2008, Gkoumas, 2009, Jansen, 2013b]. Nevertheless, some experiments based on pulse X-rays [Pan, 1993], pulsed UV light [Gabrysch, 2011, Isberg, 2013, Majdi, 2021, Djurberg, 2022] or accelerated pulsed electrons [Quaranta, 1970, Reggiani, 1981] were reported. The use of such techniques has enabled drift velocity measurements at cryogenic temperatures [Reggiani, 1981, Pan, 1993, Nesladek, 2008, Gkoumas, 2009, Gabrysch, 2011, Isberg, 2012, Jansen, 2013b, Isberg, 2013, Majdi, 2013, Majdi, 2016]. Some measurements have shown a saturation of the hole low-field mobility of approximately $10^4\,\mathrm{cm^2/(V{\cdot}s)}$ at 2 K [Jansen, 2013b], while other experiments concluded that, to measure the hole low-field mobility below ∼80 K, one should reach extremely low electric fields [Majdi, 2013]. The highest hole low-field mobility reported using the TCT is between 1 and $2 \times 10^4\,\mathrm{cm^2/(V{\cdot}s)}$ [Reggiani, 1981, Gabrysch, 2011] at about 80 K.

During my PhD, I contributed to the development of a technique using electron pulses generated by a Scanning Electron Microscope (SEM) to characterize diamond samples (setup described in Section 3.1). This technique, called ToF - electron Beam Induced Current (ToF-eBIC) was developed to perform drift velocity studies through large electric and temperature ranges. A similar experiment was developed by Quaranta *et al.* [Quaranta, 1970] and used to study hole transport properties at various temperatures [Reggiani, 1981]. Nevertheless, the present ToF-eBIC technique allowed us to monitor multiple parameters independently and simultaneously (in-depth distribution of electron-hole, amount of electron-hole pairs generated and lateral distribution of charge carriers within a pulse and during all the acquisition), thus limiting polarization effects (Section 3.2). As a results, it enabled the measurement of the drift velocity for electric fields as low as 1.5 V/cm for holes and 18 V/cm for electrons. This achievement allowed us to assess the hole low-field mobility down to 13 K (Section 3.3).

Finally, we used this setup to map the collected charge in a diamond device at the micrometer scale (Section 3.4). Multiple applications, such as the characterization of defects generated by the growth of the diamond or its exposure to ionizing radiation, are discussed.

3.1 Material and Methods

The setup used for the work presented in this chapter is based on a Scanning Electron Microscope (SEM) FEI Inspect F50. One particularity of this microscope is that the electron beam is generated thanks to a field emission gun, which enables measurements at a nanometric resolution. As a result, the electron beam diameter can be as small as 0.8 to 3 nm, depending on the excitation conditions (see `http://sernia.ru/upload/pdf_files/Inspect%20F50%20DS0019_09-11.pdf`). The acceleration voltage can vary from 200 V to 30 kV, and the intensity up to 200 nA. The SEM offers the possibility to obtain very precise pictures of the samples through the detection of the secondary electrons and the opportunity to perform electron Beam Induced Current (eBIC) measurements [Donatini, 2016, Umezawa, 2016].

My PhD aimed to develop a method for characterizing diamond samples while working in pulse mode. To this end, a fast beam blanker was added to the SEM structure. The beam blanker is a conical metallic piece with a gap allowing the electron beam to pass through it.

Three gap sizes can be used in the experiments: 100, 200 and 300 µm. It is important to specify that before each use, the gap of the beam blanker needed to be precisely aligned with the electron beam so as not to degrade the instrument's performance. This gap can be biased in order to deflect the electrons and thus shut down the beam. If this operation is done sufficiently quickly, it is then possible to create short pulses of electrons and thus to work in a pulse mode.

In order to control the beam blanker, the Pulse Rider PG-1072 from Active Technology was used. This device can switch from 0 to 5 V (and reversely) with a rise and fall time of 70 ps and a repetition rate of 800 MHz. It was observed experimentally that by applying 5 V on the 100 µm gap, an electron beam with an energy of up to 30 keV could be deflected. As a result, 1 ns pulses of electrons can be generated (pulse mode). Moreover, it is possible to use this device to trigger the signal acquisition.

The scheme of the ToF-eBIC setup is presented in the Figure 3.1. The diamond is placed in the SEM vacuum chamber (10^{-7} mbar). In order to read out the signal induced by the electron pulses, current to voltage fast preamplifiers (CIVIDEC C2-HV), and a Digital Sampling Oscilloscope (DSO LeCroy HDO9404), are used (see Subsection 2.1.2). The diamond is biased with a Keithley 6487. All these devices were interfaced to the computer connected to the SEM to automatize the setup (see Subsection 3.2.1).

Another feature of this SEM is its helium liquid cryogenic stage (Gatan CF302[1]). Since the diamond is mounted on the cryogenic stage, the sample can theoretically be cooled to 5 K. In order to perform these measurements, a specific sample holder was designed, and thermal shields were added to limit the thermal losses.

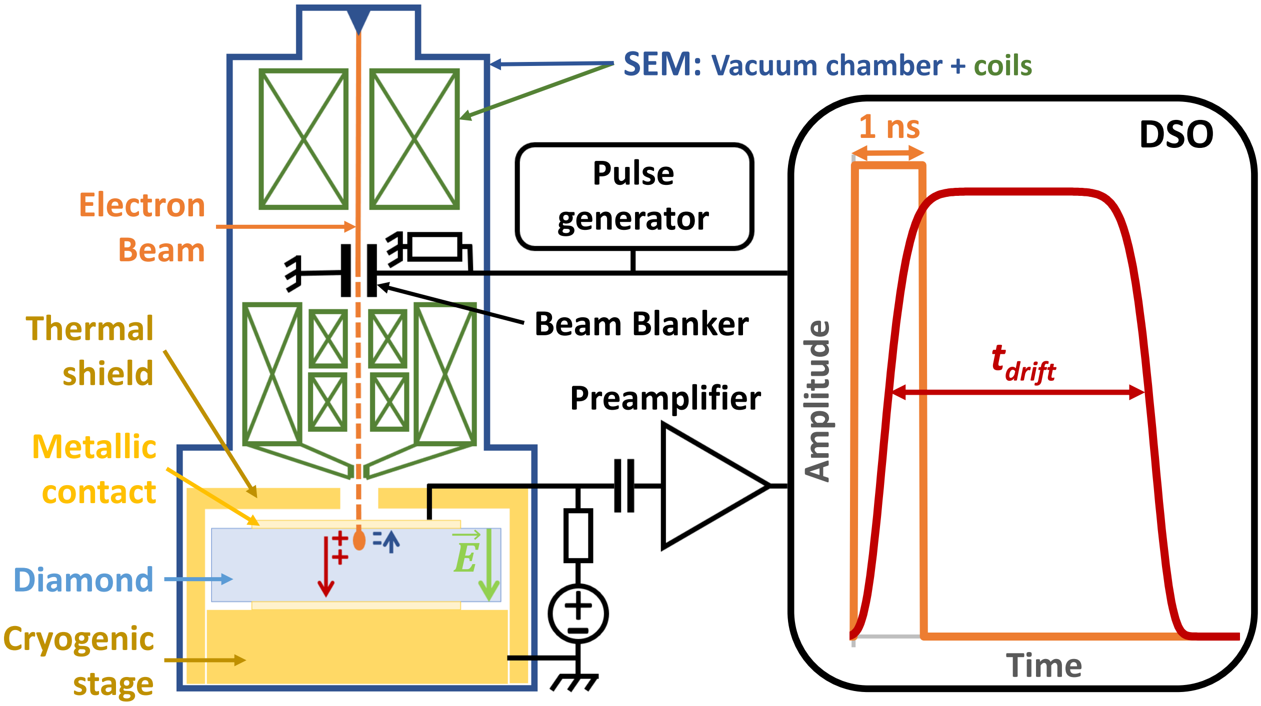

Figure 3.1: Scheme of the setup used to conduct experiments using the ToF-eBIC technique.

---

[1] Gatan website: https://www.gatan.com/products/sem-specimen-stages/cooling-stages

3.2 Measurements of the drift velocity and the mobility of the charge carriers

One of the main objectives is to study the drift velocity of the charge carriers in different conditions (field, temperature...). To achieve this objective, one crucial step consisted to find the optimal parameters to perform those measurements.

The first parameter I studied was the electron beam energy since the electron range, in the material, depends on it. I performed some Monte-Carlo simulations using the software CASINO[1] (version 2.51) [Drouin, 2007]. The energy deposit distribution was extracted for different primary electron energies (Figure 3.2). Up to 30 keV, the electrons are stopped within 6 µm which is negligible compared to the diamond thickness of 545 µm. Therefore, the TCT method can be used. In order to maximize the energy deposited in the diamond, a beam energy of 30 keV per electrons was chosen. Under these conditions, the maximum energy deposit density is 4.7×10^{-2} keV per electron for a volume of $7.0 \times 10^{5}\,\text{nm}^{3}$ which lead to a peak carrier concentration of $5.1 \times 10^{15}/\text{cm}^{3}$.

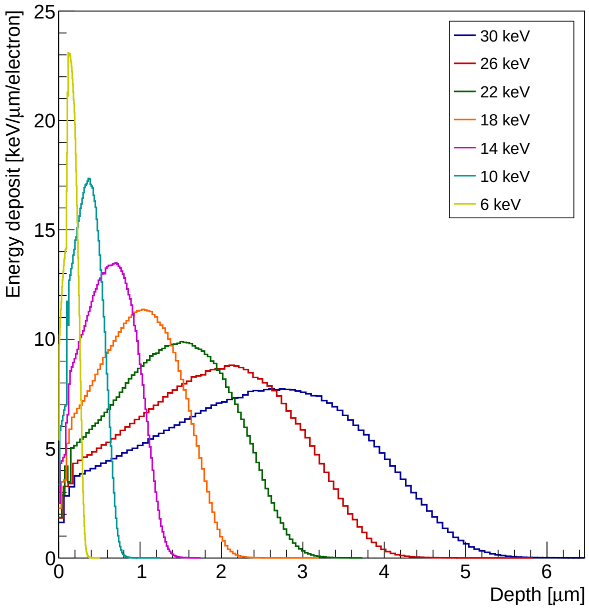

Figure 3.2: Simulated energy deposit for electron with different energies. The simulations were done with the CASINO software. The binning is different for each curve.

In order to reach the higher Signal over Noise Ratio (SNR) defined in the Equation 3.1, a beam intensity from 3 to 6 µA in continuous mode, corresponding to the maximum current of the SEM, was selected. As a result, between 20 to 40 electrons were impinging the diamond surface.

$$SNR = \frac{\text{Signal amplitude}}{\text{Noise rms}} \tag{3.1}$$

---

[1] CASINO: monte CArlo SImulation of electroN trajectory in sOlids https://www.gegi.usherbrooke.ca/casino/What.html

To perform accurate measurements of the diamond charge collection and transport properties, it is necessary to have a signal stable over time. However, it has been observed experimentally that the signal amplitude slowly decreases with time. This phenomenon reflects the polarization effects (see Subsection 1.3.4.3). Furthermore, to evaluate precisely the carrier transport properties, the carrier concentration must be limited. Indeed, a too high carrier concentration induces, among other things, electric field screening and carrier-carrier scattering interactions. To avoid these phenomena, the charge injection must be carefully monitored and specific procedures, relying on inverting regularly the bias, had to be implemented. The implementation of these procedures, the automation of measurements, and the influence of charge injection on polarization effects are the topics of the next subsections.

3.2.1 Influence of bias voltage cycling on polarization effects

3.2.1.1 Experimental observations

As discussed in the Subsection 1.3.4.3, various strategies have been studied and reported in the literature to prevent the polarization phenomenon in diamond samples. Changing the temperature [Guerrero, 2006, Bergonzo, 2007, Angelone, 2019, Ramos, 2022], switching on and off the bias [Bergonzo, 2008, Gabrysch, 2011, Ibragimov, 2016, Ramos, 2022], inverting regularly the bias [Guthoff, 2013, Valentin, 2015, Rebai, 2016, Holmes, 2019, Curtoni, 2020, Ramos, 2022] or using a light excitation [Manfredotti, 2002, Bentele, 2016, Ramos, 2022] have proven to reduce or avoid completely the polarization effects. However, some contradictory results were reported, highlighting the necessity to develop procedures adapted to each specific experiment. Regarding, the ToF-eBIC measurements, a suitable way to limit this phenomenon consisted in inverting regularly the bias. The following experiment was designed to demonstrate the efficiency of this procedure.

Experimental procedure: the beam was focused on a small area ($< 1\,\mu m^2$) on the diamond surface. An external electric field of 5.5×10^3 V/cm was applied in the [100] direction of the diamond crystal. The drift of holes through a 545 µm diamond was studied. Every 100 electron pulses, an averaged waveform was computed and recorded. In one cases (a) the acquisition was not stopped and continued until 20 averaged waveforms were recorded. In the other case (b), the bias was inverted during 1 s before continuing the acquisition. As a result, the signal evolution could be studied with and without inverting the bias. After a baseline correction, the charge was computed by integrating the signal on a time window of 25 ns.

Experimental results: the averaged waveforms acquired without (a) and with (b) bias inversion are shown in Figure 3.3. In the Figure 3.3 (a), the amplitude of the signal was found to rapidly decreased with the acquisition number. Indeed, on the 8th acquisition, the signal induced by the transit of the holes is no longer visible. At the opposite, on the Figure 3.3 (b), the 20 averaged traces are plotted and no significant difference is visible. Regarding the charge collected, on the case where any bias inversion is done (Figure 3.3 (c)), the charge decreased sharply before reaching the noise level after the 5th acquisition. On the contrary, when the bias is regularly inverted (Figure 3.3 (d)), the charge collected remained constant.

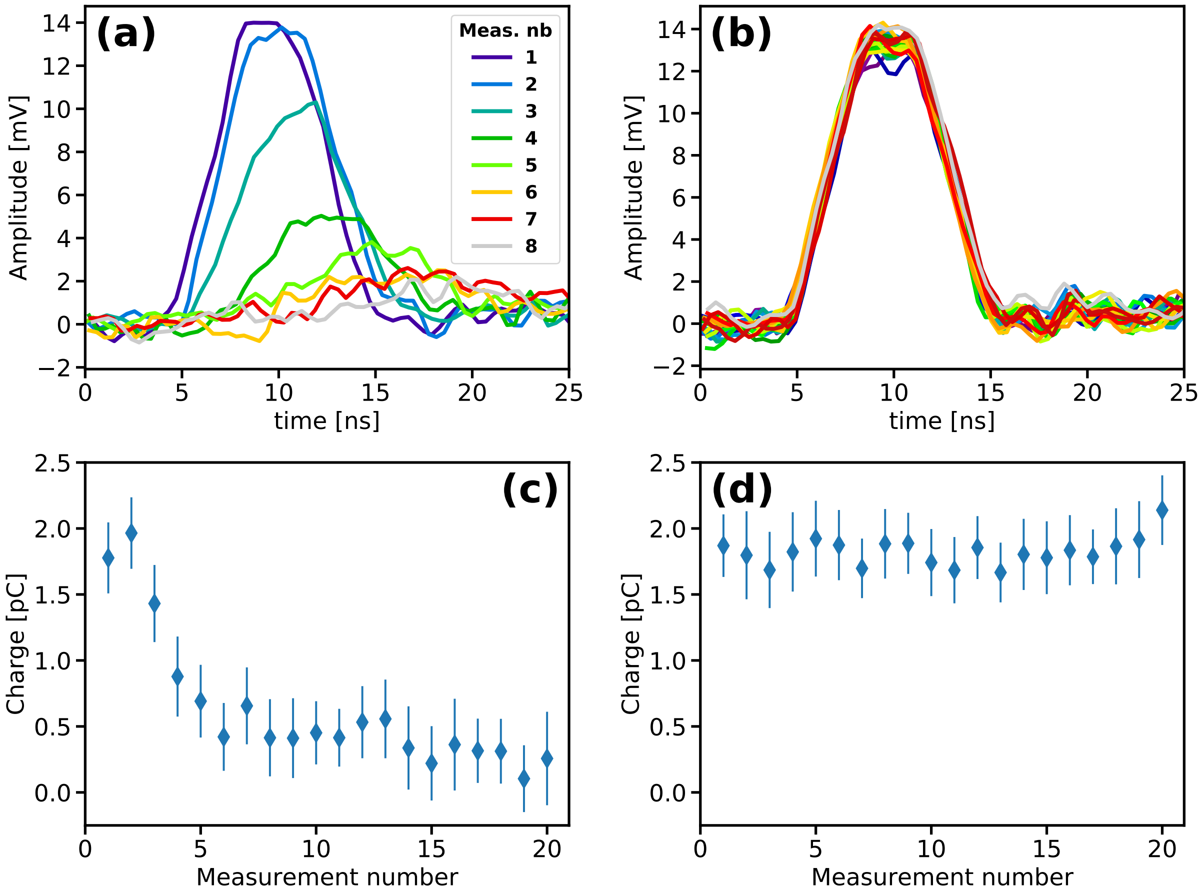

Figure 3.3: Averaged traces (100 signals) obtained for hole transits at an electric field of 5.5×10^3 V/cm without (a) and with (b) performing regular bias inversions. In (a), the first eight traces are shown, whereas in (b), the twenty traces are plotted. (c) and (d): charge collected computed by integrating the traces (a) and (b), respectively, over a 25 ns window.

Inverting regularly the bias is thus a suitable way to avoid polarization effects. Indeed, inverting the bias during 1 s after 100 pulses is sufficient to get a stable hole induced current at an electric field of 5.5×10^3 V/cm. This procedure of inverting regularly the bias will be referred to as "cycling" in the rest of this chapter. For repeatability and time efficiency reasons a slow control was developed to perform this cycling procedure and record the data.

3.2.1.2 Slow control and data acquisition

The scheme of the slow control is described on the Figure 3.4. The pulse generator (Pulse Rider PG-1072 from Active Technology) is used to generate pulses of electron, and as an external trigger for the oscilloscope (LeCroy HDO9404). The oscilloscope and the HV power supply are interfaced with a computer using GPIB[1] communication. The slow control is performed using a dedicated LabVIEW interface. An input table provides the instructions at each step of the cycling procedure. Thus, for each measurement (corresponding to one line in the table), seven parameters need to be given. The seven input parameters are listed below.

- **Working bias** (V_{bias}) corresponds to the bias applied during the measurement.

---

[1] General Purpose Interface Bus (IEEE-488 standard)

- **Number of traces per cycle** (N_{WF}) corresponds to the number of traces averaged by the oscilloscope between two bias inversions. The resulting waveform is then imported on LabVIEW and added to the traces previously acquired during the ongoing measurement. As a results, the waveform obtained at the end of each measurement corresponds to the sum of the imported traces.

- **Number of cycles** (N_{cycl}) corresponds to the number of cycles done per working bias. The total number of traces averaged is equal to the number of traces per cycle multiplied by the number of cycles ($N_{tot} = N_{WF} \times N_{cycl}$).

- **Voltage step** (V_{step})**:** the slow voltage transitions are performed by steps to avoid too abrupt voltage variations. The number of steps is an integer; thus, the voltage step need to be divisor of ($V_{bias} - V_{cycl}$).

- **Waiting time** (t_{step}) corresponds to the time between two consecutive steps.

- **Cycling time** (t_{cycl}) corresponds to the time spent at the cycling bias.

- **Cycling bias** (V_{cycl})**:** value of the "inverse voltage" to be reached. In most experiment, the cycling bias equals to the opposite of the working bias ($V_{cycl} = -V_{bias}$). However, this parameter can be adapted by the user to study its influence.

For each working bias, an averaged waveform is saved in a text file.

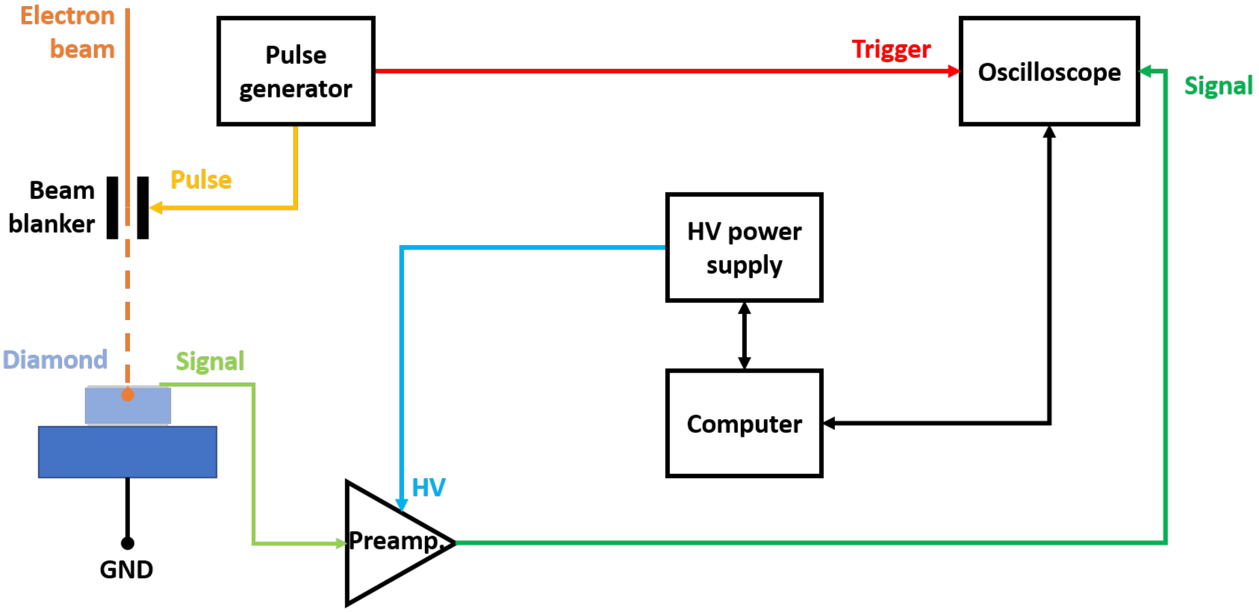

Figure 3.4: Scheme representing the connection between the different instruments. Each colored line represents an SMA cable, the black line delimited by two arrows are GPIB connections and, the GND is simply done by putting in contact the back side of the diamond with the metallic sample holder.

The cycling procedure is illustrated on the Figure 3.5. In this figure, the time starting from the working bias to the cycling bias is exaggerated in order to highlight the different steps of the procedure. It can also been noticed, in this particular example, that the cycling bias is the

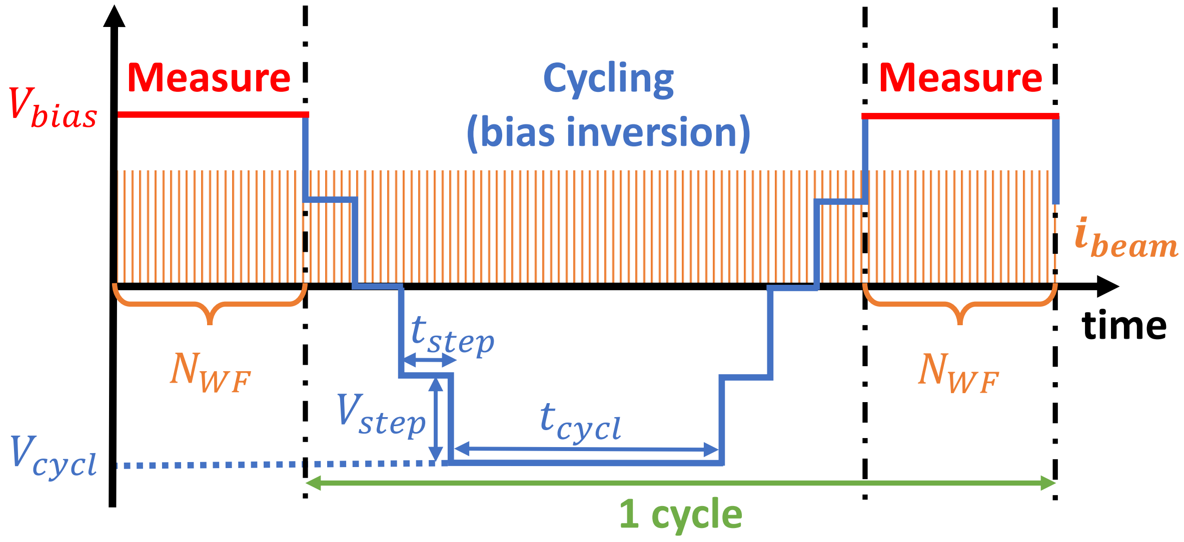

Figure 3.5: Cycling procedure used to minimize the polarization effects.

opposite of the working bias ($V_{cycl} = -V_{bias}$). Another specificity is that the cycle starts by a cycling step before starting the measurement.

Typical values of these parameters are listed in the table below. They illustrate cycling procedures performed at 5, 50 and 500 V. The higher the *bias voltage*, the lower the *number of traces per cycle* and the greater the *voltage step*. Indeed, for higher biases, the SNR is better and polarization effects are less visible; it is therefore possible to invert the bias less often and thus to reduce the measurement time. To not damage the ROE, it was chosen to limit the *voltage step* to 50 V. Regarding the *waiting time* and the *cycling time*, they were generally fixed at the beginning of the experiment and not changed. Finally, the *cycling bias* was the opposite of the *bias voltage*. These parameters must be adapted according to the charge carrier, the temperature or the diamond sample.

Table 3.1: Example of cycling parameters for three different voltages.

Parameters	Symbol	Procedure at		
		5 V	50 V	500 V
Working bias [V]	V_{bias}	5	50	500
Number of traces per cycle	N_{WF}	25	100	100
Number of cycles	N_{cycl}	50	10	10
Voltage step [V]	V_{step}	5	10	50
Waiting time [ms]	t_{step}	30	30	30
Cycling time [ms]	t_{cycl}	1000	1000	1000
Cycling bias [V]	V_{cycl}	-5	-50	-500

3.2.1.3 Relevance of the method and challenges to be met

In this subsection, I evidenced that the amplitude of the signal and the charge collected slowly decreased after successive measurements if any precaution is taken during the ToF-eBIC measurements. This effect caused by the polarization effect, could be avoided by inverting regularly the bias applied on the diamond sample. A slow control was then developed to automatize this cycling procedure. Thus, the slow control allowed to perform measurements with a good repeatability and a thorough control of the cycling parameters.

Other methods to avoid polarization effects mentioned in literature were also tested [Ramos, 2022]. As a result, it seems that switching on and off the bias and using a light excitation did not allowed to limit the polarization effect as efficiently as the procedure described above. The strategy of changing the temperature was not tested because one goal of this experiment was to study the temperature dependence of the transport parameters in diamond sample.

As seen in Section 2.4, the polarization effects are particularly important at low electric fields (less than $\sim 1 \times 10^3$ V/cm at 300 K). As a result, it could be very difficult to measure accurately the drift velocity even while performing several bias inversion. Unfortunately, estimating the drift velocity at low electric fields is crucial to estimate accurately the low field mobility. It is therefore very important to study this phenomenon in depth in order to find ways to limit it as much as possible. Thus, after studying the temporal evolution of the signals, the next step was to study the spatial impact of polarization effects.

It should be precised that the polarization effects are also existing at higher field (in particular for holes) but the dynamic is slower. In particular, it was noticed that after 1000 pulses the electron signal at 9.2×10^3 V/cm was not significantly affected by polarization effects. Electron transits at such an electric field are then a suitable way to study the polarization effects.

3.2.2 Spatial extension of the polarization effects

To discuss about the spatial influence of polarization effects, the SEM specificities must be detailed. The SEM can work in two different modes:

- **spot mode:** a beam diameter spot can be moved by the experimenter to study some local effect;
- **scan mode:** the SEM is scanning an area of 1024 × 884 pixels from top to bottom and left to right. The size of the scanned area can be adjusted by using the magnetic lenses but the number of pixels in the image remains the same.

In order to study some very local effects with the best spatial resolution, it is necessary to work in spot mode. As a result, first experiments were carried out in this mode.

3.2.2.1 Influence of charge injection during measurements

This experiment aimed to study the spatial influence of the polarization effect for optimizing the charge injection during the acquisitions.

Experimental procedure: the experimental procedure is described in Figure 3.6 (a). It consisted in irradiating one spot on the surface of a 545 µm thick diamond sample for about 1 min (step 2 and 4) before doing a measure in another spot at a given distance from the initial spot (step 3 and 5). After that, a bias inversion was performed (illustrated between step 3 and 4) in order to reset the electric field distribution in the diamond sample. Then, the same procedure was repeated by irradiating the same point and measuring the signal shape at a new position. Using this procedure, the impact of polarization effects on the current waveforms was studied as a function of the distance between the irradiated position and the measurement positions. The irradiations and the measurements were carried out using 1 ns pulses of 30 keV electrons. Before starting the experiment, current waveforms were recorded at each position (step 1). During this step, the bias is inverted manually before each measurement. The resulting traces are considered as the reference measurements. In this experiment, the cycling procedure could not be used; considering that performing a bias inversion is resetting the charge state of the diamond sample. Therefore, to limit the temporal evolution of the signals, it was chosen to work with electrons and an electric field of 9.2×10^3 V/cm (optimal condition with respect to polarization effects).

Experimental results: the Figure 3.6 summarized the experiment protocol and the main results. In the plot (b), the averaged waveform (1000) obtained after irradiation (blue line) is compared to the reference measurement (black line). Both these measurements were done at 12 µm from the irradiation spot. The polarization effects are clearly visible: the rising and falling edges are less sharp, and the charge collected (integral of the traces) is significantly lower after the irradiation. Nevertheless, it was noticed that as the distance from the irradiated spot position increases, the sharpness of the rising and falling edges and the charge are recovered. Indeed, that phenomenon can be observed on the plot (c), where averaged traces obtained after the irradiation at different distances are compared. For distances higher than approximately 50 µm, the sharpness of the rising edge is recovered. On the plot (d) the charge collected at different positions for the control case and the post-irradiation cases are compared. For distances greater than 100 µm, the amount of charge collected after irradiation is similar to that measured for the reference data.

The results of this experiment shows that an easy way to limit the polarization effects is to do two successive measures spaced by more than ∼100 µm. This conclusion is particularly relevant for measurements at low electric fields, where the polarization effects are highly significant. As a result, it was chosen to work using the SEM scan mode to limit this phenomenon. Since most of our measurements focused on studying the drift velocity versus the electric field on the whole surface of the diamonds, this was not an issue. Nevertheless, when it comes to map the diamond properties or perform some micro-metric studies, it was necessary to work with high electric fields to limit the polarization effects and measured signal in spot mode.

3.2.2.2 Influence of the size of the scanned area

To complete the results of the previous experiment, some measurements were carried out to study the influence of the size of the scanned area. It can be assumed that the larger the scanned area, the less significant the polarization effects.

Experimental procedure: in this experiment, measurements at different electric fields (±1.8, ±3.7, ±5.5, ±7.3 and ±9.2 kV/cm) are firstly performed on a large area of the metallized diamond surface. Then, three zooms are successively performed, and for each, the same measurements are carried out. A bias inversion is performed before each measurements. As in the previous experiment, a diamond with a thickness of 545 µm and an averaging over 1000 traces were used.

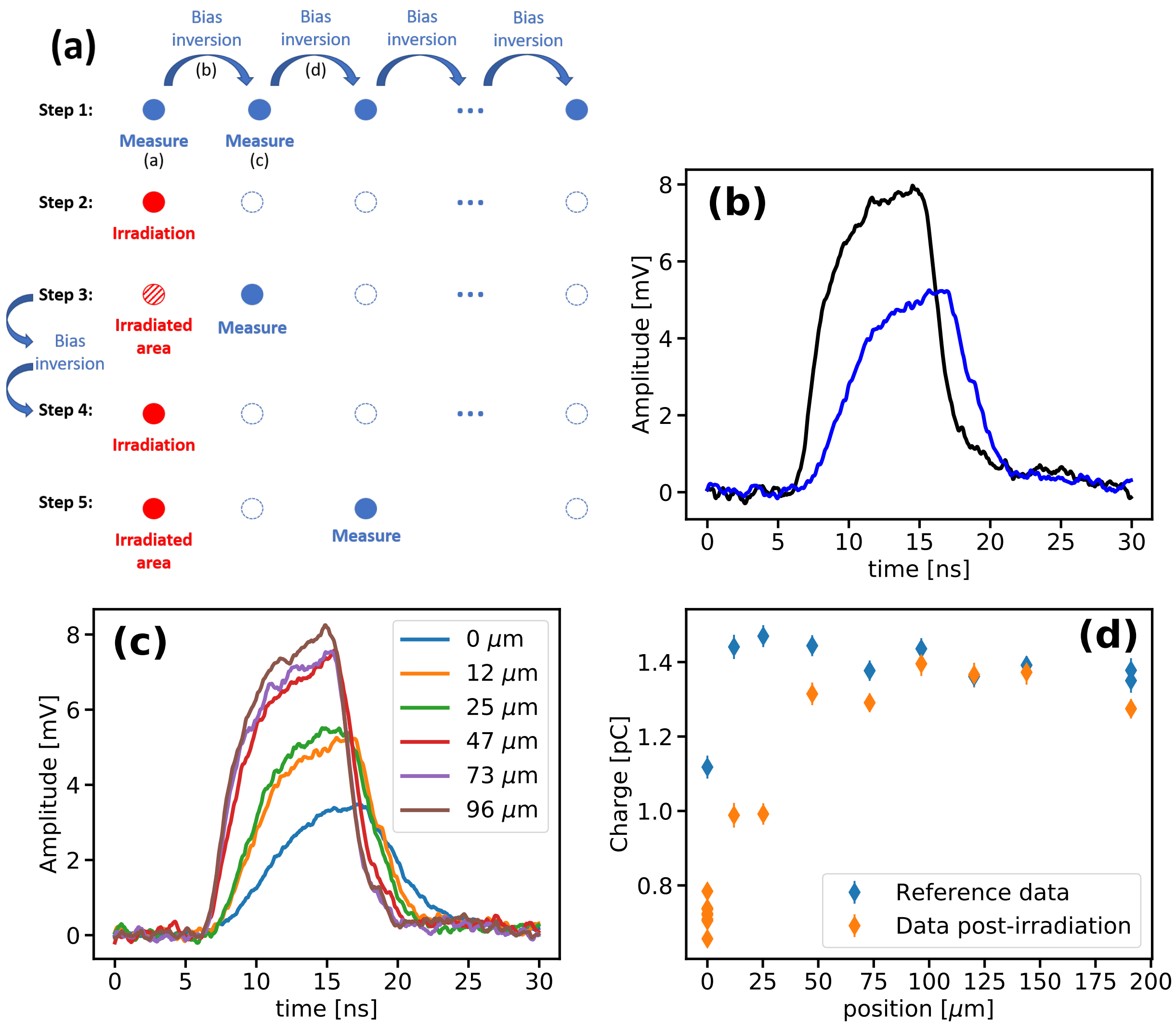

Figure 3.6: (a) Experimental procedure scheme. First the different control measurements are carried out and a bias inversion is done between two measurements (Step 1). Then the irradiation is performed for about 1 min (Step 2), and just after a measurement is achieved followed by a bias inversion (Step 3). This last step is then repeated for each position (Step 4 and 5). On the last position, a measurement is performed after the bias inversion and the resulting signal is compared to the reference waveform. In this experiment, only the electron transit is studied because it seems more stable over time. 1000 traces are averaged for each measurement. (b) Comparison between the reference waveform (black line) and the waveform recorded after irradiation (blue line). Both acquisitions were performed at 12 µm from the irradiation position. (c) Averaged traces obtained after irradiation at different positions. (d) Charge measured at different positions for the reference data (blue point) and the data recorded after irradiation (orange). The values were not corrected for the amplification gain.

Experimental results: the averaged traces obtained for electrons and holes for the different electric fields at each scanned area size are presented in Figure 3.7. By decreasing the surface area, the holes signal are deteriorating (shape and charge collected). This effect is gradual, at first only the signal obtained at low electric fields are affected (1.8 and 3.7 kV/cm), then, for surface smaller than $100\times100\,\mu\text{m}^2$, the signal obtained at higher electric fields are affected (3.7

and 5.5 kV/cm). For electrons, the effects are less visible, but it should be noticed that those curves were acquired for high electric field. At lower fields, even for the electrons, the effect was experimentally evidenced. As a results, to study the drift velocity of the charge carriers at low electric fields, we must work in scan mode on a large area.

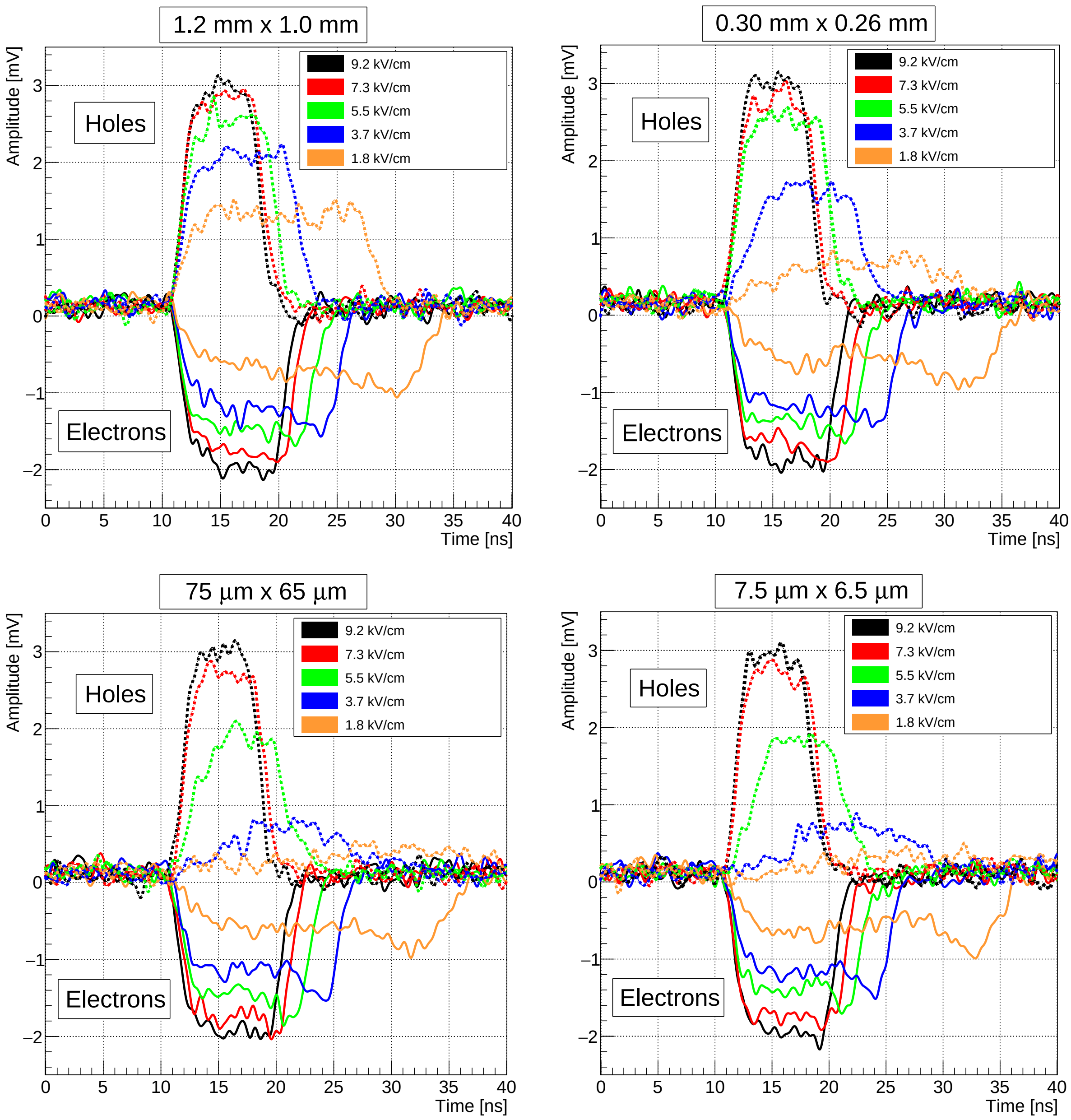

Figure 3.7: Holes and electrons averaged traces (1000 traces) obtained for five electric field values and four different scanned surfaces.

3.2.3 Influence of the charge injection density on polarization effects

3.2.3.1 The SEM beam focusing: a key parameter

In normal operating mode, the electron beam of the SEM should be carefully focused on the sample to obtained the sharpest image. Nevertheless, being out of focus, can be interesting to modify the electron-hole pair density in the sample. Indeed, the primary electrons of an unfocus beam will interact on a larger surface. During the experiment described in Appendix A.1, it was shown that 60 µm diameter spots can improve significantly the shape of the measured signal.

The scheme of the Figure 3.8 illustrates this phenomenon. For a focused beam, the charge carriers are created, for each pulse, in a relatively small interaction volume (4 µm diameter in the lateral directions and a depth of about 5 µm). Whereas, by working out of the beam focus, the different impacts are relatively spaced and so, locally, the charge carrier density decreases considerably. Indeed, if an averaged charge deposited of 11 fC is assumed (around 30 primary electrons impinging the diamond surface with an energy of 30 keV) each primary electron of a single pulse interacts in its own volume (considering a 60 µm diameter unfocused spot). The scheme of the Figure 3.8 considered a uniform distribution of the primary electrons in the beam. This assumption is rough, a Gaussian distribution of the sample is probably more realistic. Nevertheless, the conclusions remain the same, especially since an unfocused spot of 300 µm in diameter was mainly used in the experiments.

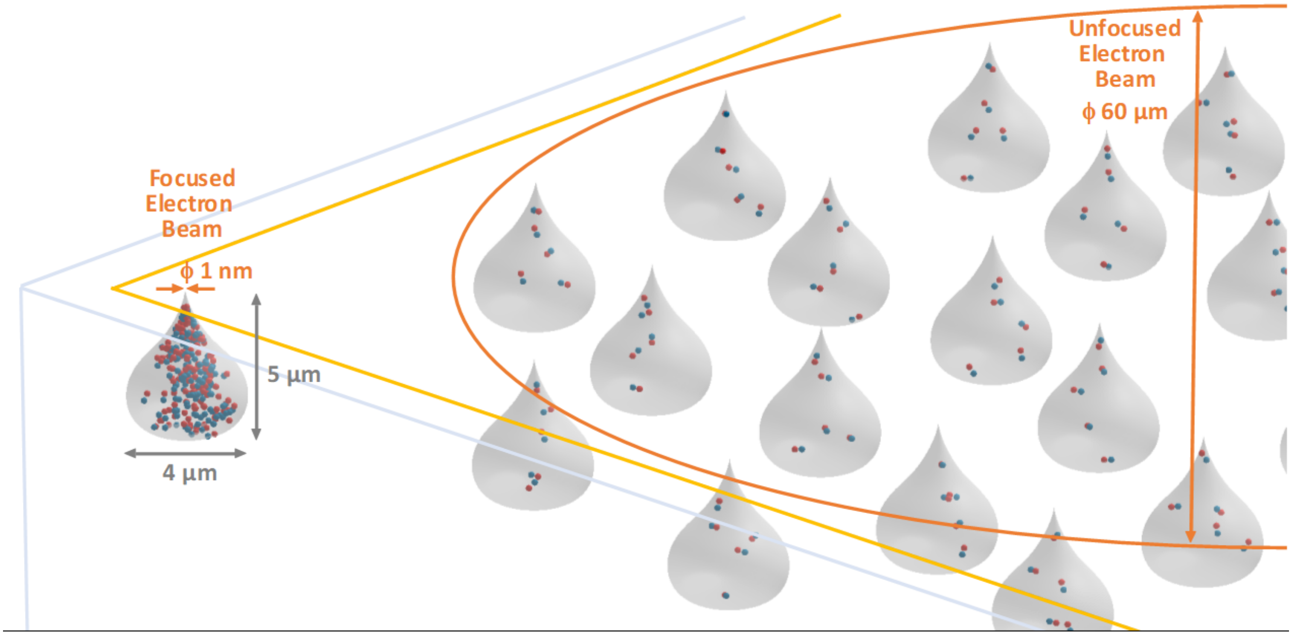

Figure 3.8: Electron-hole pairs distribution created within a focused electron beam and an unfocused electron beam. The orange line delineates the lateral size of the unfocused beam and the yellow line the outer limit of the metallic contact through which the beam excites the electron-hole pairs in diamond.

By decreasing the electron-hole pair density, the electromagnetic screening should be reduced and, as a result, it should be easier to perform measurements at lower fields. Therefore, an assumption was made: by being out of focus, it should be possible to obtained a more intense signal at low electric fields and a similar one at high fields. A dedicated experiment was set up to check this hypothesis.

3.2.3.2 Charge injection density and screening effects

Experimental procedure: in this experiment, signals obtained with the SEM completely out of focus and carefully focused were compared in the same experimental conditions. This experiment was done two times, one at very low electric field (18 V/cm) and one at high electric fields (9.2×10^3 V/cm) in order to check if the assumption previously made is correct.

To observe a signal at 18 V/cm, the measurement were performed at low temperature ∼25 K. For both measurements, the cycling procedure described in the Subsection 3.2.1 is used with $V_{cycl} = -V_{bias}$.

Experimental results: the Figure 3.9 shows the traces obtained on focus (blue curves) and out of focus (orange curves) at low (left) and high (right) electric field. In a few words, defocusing the SEM allows to get a signal at very low electric fields (plot on the left) without modifying the results obtained at higher fields (plot on the right). The assumption previously made is verified. Using unfocused beam is a key issue to study charge transport at low field and low temperature.

Experimentally, no significant impact were observed for electric fields greater than 183 V/cm, showing that this effect is only occurring at low electric fields. To better understand the screening effect generated within a pulse, a future experiment could be set up to study more thoroughly the impact of the excitation density as a function of the electric field.

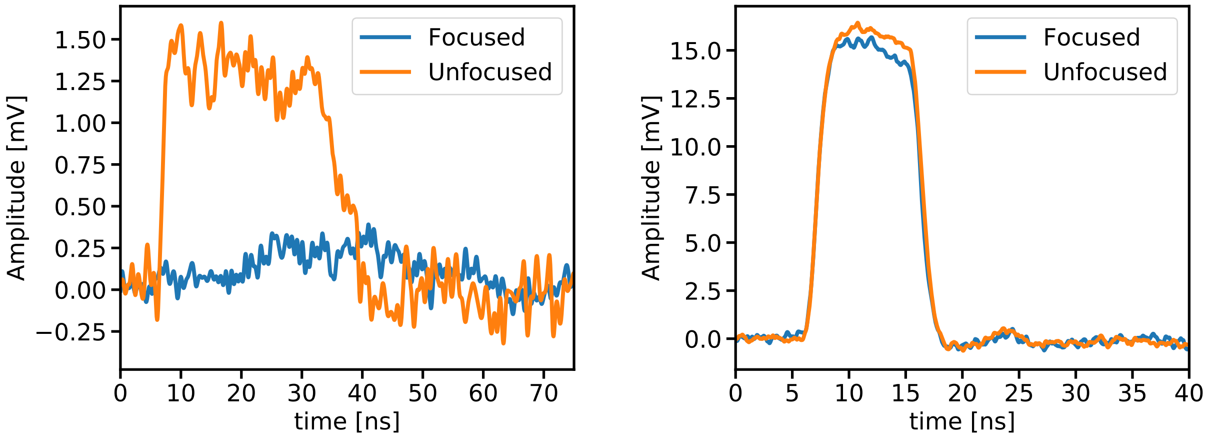

Figure 3.9: Left: hole traces obtained for an electric field of 18 V/cm at ∼25 K. Right: electron traces obtained for an electric field of 9.2×10^3 V/cm at 300 K.

3.2.3.3 Challenges of low temperature measurements

An excitons is a quasiparticle composed of en electron and a hole bind by the electrostatic Coulomb force. They are considered as a neutral particle with a binding energy of $Ex = (80.0 \pm 0.5)$ meV [Dean, 1965].

After a high energy irradiation (e.g. using the ToF-eBIC technique), a mixture of excitons and free-carriers is generated. Thus, it is possible to define the fraction of excitons n_{ex}/n and the fraction of electron-hole pairs n_{eh}/n in the mixture, considering that $n = n_{ex} + n_{eh}$ is the total number of excitons and electron-hole pairs at equilibrium. These fractions depend on the temperature T according to the law of mass-action [Konishi, 2020a]:

$$\frac{n_{eh}^2}{n_{ex}} = AT^{3/2} \cdot exp\left(-\frac{E_{ex}}{k_B T}\right) \tag{3.2}$$

with k_B the Boltzmann constant, $A = \left(\mu k_B / \left(2\pi\hbar^2\right)\right)^{3/2}$, μ the exciton reduced mass, E_{ex} the exciton binding energy and k_b the Boltzmann constant. Using this equation Konishi *et al.* [Konishi, 2020a] showed that, due to the large binding energy of excitons in diamond, the fraction of excitons of the mixture at equilibrium is almost equal to one at low temperatures.

At the opposite of the free charge carriers, the excitons are neutral particles and thus, are not impacted by the electric field. It can then be expected that the ToF-eBIC technique cannot be used at low temperatures. Nevertheless, by applying an external electric field, the electrons and the holes are drifting in opposite directions and can thus be separated prior to the formation of excitons. This effect is limited when the excitation density is high (focused electron beam) due to the difficulty of separating the charge carriers in a large and dense cloud of electrons and holes. At the opposite, for low carrier density (unfocused electron beam), this phenomenon is sufficient to decrease significantly the quantity of excitons generated.

As a result, using an unfocused beam allowed to increase the charge collected at low temperatures and so the SNR. Combined with aforementioned effects at low electric fields, unfocusing the electron beam is a key to perform measurements at low electric fields. In the following, the experiment were performed using 300 µm diameter spots.

3.2.4 Drift velocity measurements at room temperature

Thanks to the optimizations mentioned above, drift velocity measurements were carried out at Room Temperature (RT). These measurements were used to compare the results obtained with the ToF-eBIC setup and the ones obtained previously with the alpha source setup (see Section 2.3). As a result, the experimental protocol is similar to the one described to evaluate the transport parameters with the alpha setup except that the bias cycling procedure and the slow control were used here.

3.2.4.1 Results obtained on the diamond RON using the ToF-eBIC technique

The mean waveforms obtained for the diamond RON for holes (electric fields from 183 to 9158 V/cm) and electrons (electric fields from 366 to 9158 V/cm) are presented in the Figure 3.10 (top). No polarization effects are visible for holes (waveform shape). Regarding the electrons, a little positive space charge effects can be observed below 1100 V/cm. Although the cycling parameters could be optimized to avoid this effect, this phenomenon is not an issue to estimate the electron drift time. Furthermore, for holes and electrons, measurements could be conducted at electric fields three and two times lower, respectively, than previously with the alpha test bench. This can be explained by the use of an external trigger and the optimization of the ToF-eBIC technique (bias cycling procedure, pulse spatially separated and low concentration of the charge carriers).

Using the same procedure described in the Section 2.3.2, the drift velocity was extracted and fitted using the equation 2.4. The drift velocity evaluated for both charge carriers and the fitted function are presented in the Figure 3.10 (bottom). The results are similar to the ones obtained using the TCT with alpha particles. The low field mobility and the saturation drift velocity were then extracted.

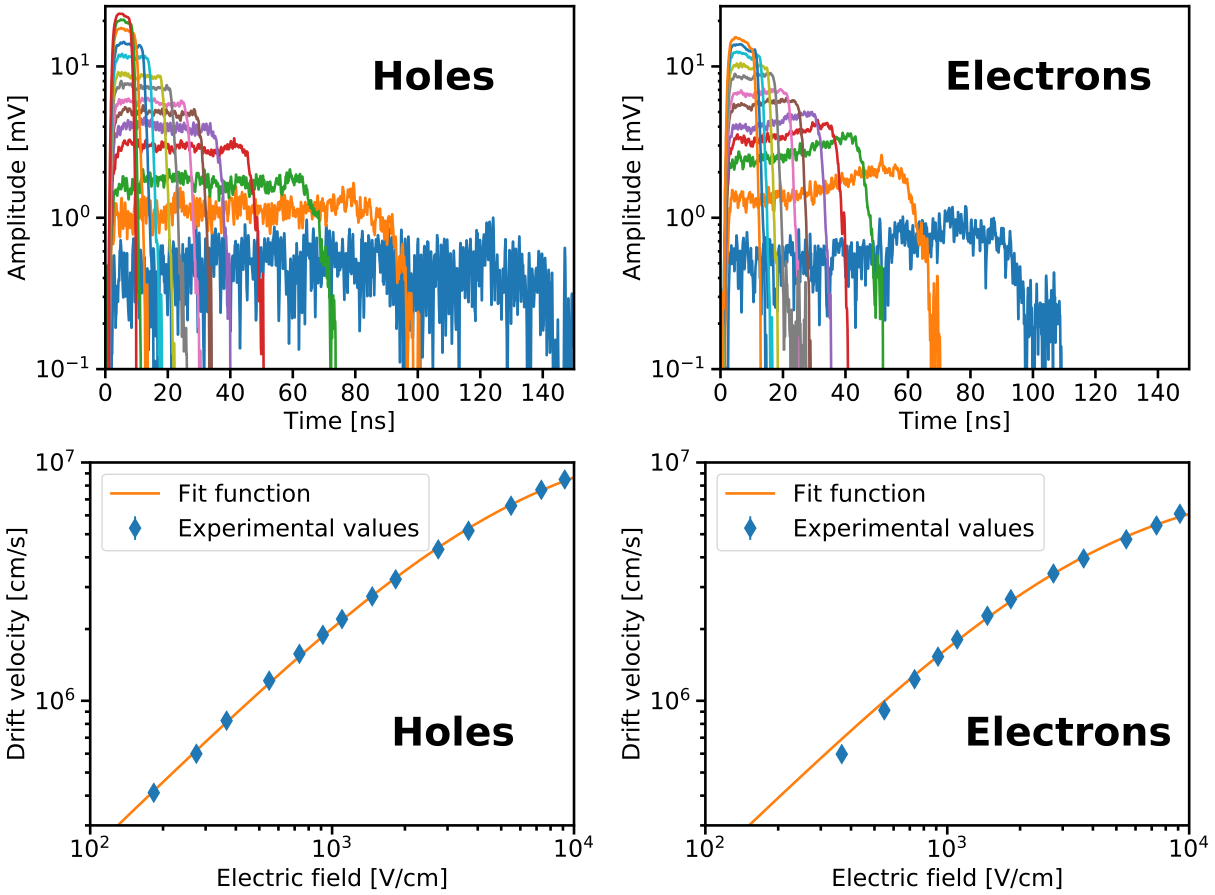

Figure 3.10: Top: mean traces obtained for the diamond named RON for holes (183 to 9158 V/cm) and electrons (366 to 9158 V/cm.) Bottom: drift velocities obtained at different electric fields for the diamond named RON for holes and electrons.

3.2.4.2 Comparison of the transport parameters obtained using the ToF-eBIC and the TCT with alpha particles

The low field mobility and the saturation drift velocity obtained on the diamond named RON with the alpha TCT and the ToF-eBIC technique are compared in Table 3.2. A very good agreement was found between those data (in particular for electrons). Nevertheless, it was possible to perform measurements at lower electric fields using the ToF-eBIC technique but not with the alpha TCT. As a result, the numerous developments have made the ToF-eBIC more suitable for performing low-field measurements on scCVD diamond samples, and thus for studying the low-field mobility of charge carriers accurately.

3.2.5 Conclusion

The polarization phenomenon is the main limitation when studying the drift velocity of diamond samples. In particular, it results in time evolution and deformation of the traces. Moreover, this effect is also significantly stronger at low electric fields, which poses a problem when evaluating mobility at low fields. Therefore, an adapted strategy is required to limit its effect.

Table 3.2: Low field mobility and saturation drift velocity obtained at RT for holes and electrons using the diamond named RON on the ToF-eBIC setup and on the alpha setup.

Holes			
Primary particles (nb)	Energy deposit [MeV]	Low field mobility [cm^2/(V.s)]	Saturation drift velocity [10^6 cm/s]
Electron pulses (20 to 40)	0.60 to 1.2	2330 ± 30	13.0 ± 0.5
Alpha particle (1)	5.479	2430 ± 20	12.1 ± 0.2

Electrons			
Primary particles (nb)	Energy deposit [MeV]	Low field mobility [cm^2/(V.s)]	Saturation drift velocity [10^6 cm/s]
Electron pulses (20 to 40)	0.60 to 1.2	2070 ± 40	8.62 ± 0.02
Alpha particle (1)	5.479	2060 ± 15	8.40 ± 0.02

To limit the polarization effects, we decided to implement a cycling procedure - consisting of inverting regularly the bias voltage - in order to reset the charge polarization effects in the diamond. However, this cycling process is time consuming. Fortunately, the polarization effect is quite local ($\sim$ 100 µm impact area). Therefore, we choose to work in scan mode (not in spot mode) to limit these effects. Indeed, in scan mode, the SEM is scanning a surface more or less broad divided into 1024 × 884 pixels while in spot mode the electron pulses interact in a sub-micrometer area (beam focused). We pointed out that the larger the scanned surface, the better the resulting signal. As a result, for drift velocity studied, the experiments were conducted in scan mode on a large area using a cycling procedure. Subsequently, we demonstrated that to obtain a more intense signal at low electric field, we must defocus the SEM, and thus dilute the charges injected at each pulse. Table 3.3 summarize the procedure implemented.

Table 3.3: Procedures achieved to limit the polarization effects.

Experimental issues	**Physical reasons**	**Experimental solutions**
Evolution of the transient current along an acquisition	Space charge generated in the bulk $\Longrightarrow$ electric field no longer uniform *Polarization effect*	Invert the bias voltage regularly to reset the space state in the bulk. *Cycling procedure*
Cycling procedure works only for two spatially distant acquisitions	Polarization effect is a local phenomenon: 100 µm impact area	Work in scan mode on large areas to space two consecutive pulses.
Not possible to measure the transient current at low electric fields.	Screening of the applied electric field within the charge cloud.	Defocus the beam to dilute the impacts within a same pulse.

A LabVIEW slow control was set up to automatize the measurements and the cycling procedure. This development allowed the implementation of theses advanced cycling procedures and a better repeatability of the experiments.

Thanks to the developments and experiments described along this section, it was then possible to carry out drift velocity studies on larger electric field ranges that the one previously obtained in the laboratory with the alpha source. The transport parameter obtained are similar confirming the possibility to use this setup to do rapid and precise characterization of diamond sample. These key properties motivated the sample characterization at lower temperature and the study of the drift velocity on large temperature and electric field ranges.

3.3 Influence of the temperature on the drift velocity measurements

The low-filed mobility is a key parameter for many applications, such as particle detection [Canali, 1979], power electronics [Donato, 2019] and valleytronics [Isberg, 2013, Suntornwipat, 2021]. Electron and hole low field mobilities were deeply investigated during the last four decades in ultra-pure diamond by different ToF techniques [Nava, 1980, Reggiani, 1981, Isberg, 2002, Pomorski, 2006, Tranchant, 2007, Nesladek, 2008, Gabrysch, 2011, Isberg, 2012, Majdi, 2013, Jansen, 2013b, Isberg, 2013, Majdi, 2016] and by Time Resolved and Continuous-Wave Cyclotron Resonance (TRCR [Akimoto, 2014, Konishi, 2020b] and CWCR [Konishi, 2022]). Even if very high electron low-field mobility was reported by both TCT [Majdi, 2016] and cyclotron resonance techniques [Akimoto, 2014, Konishi, 2020b, Konishi, 2022], the low-field mobility of holes has never been measured using the TCT at temperatures below 80 K. Regarding the TRCR technique, hole low-field mobility of $6.4 \times 10^5\,\mathrm{cm}^2/(\mathrm{V{\cdot}s})$ at 10 K was reported in [Akimoto, 2014]. However, no hole values have been reported since 2014, while some improvement in the technique made it possible to reach higher low field mobilities for electrons. Indeed, an electron low-field mobility of $100 \times 10^6\,\mathrm{cm}^2/(\mathrm{V{\cdot}s})$ at 3 K was reported in 2022 in [Konishi, 2022] by performing CWCR measurements. This value is one decade higher than the previous TRCR reported values [Konishi, 2020b].

Several of these values are compared in Figure 3.11. For both charge carriers, a $T^{-3/2}$ dependency can be identified at low temperatures ($T \lesssim 300\,\mathrm{K}$). This phenomenon is induced by the carrier scattering caused by the acoustic phonon. Indeed, recent studies [Majdi, 2021] have demonstrated that this phenomenon is the dominant scattering mechanism in this temperature range[1]. At higher temperatures, both acoustical and optical phonon are responsible for the carrier scattering and thus, the carrier low-field mobility follows a T^{α} rule, with α greater than 2. A deviation of the $T^{-3/2}$ dependency of the electron low field mobility was highlighted in [Majdi, 2016, Konishi, 2020b, Konishi, 2022]. On the contrary, some groups [Jansen, 2013a, Konishi, 2020b] have reported a saturation of the carrier low-field, probably due to impurity scattering at low temperature.

A dispersion can also be noticed. The highest mobilities were systematically measured using the CWCR or the TRCR technique. According to the authors, the reason is that these cyclotron techniques can only explore the movement of carriers confined to high quality regions of the order of 100 nm in radius. Conversely, TCT techniques enable the measurement of carrier drift over the entire thickness of the sample.

The low-field mobility is also directly dependant on the effective doping level. Indeed, at 300 K, the low-field mobility can be estimated based on the impurity density N_{imp} using the following formula [Pernot, 2008, Volpe, 2009]:

$$\mu\left(300, N_{imp}\right) = \mu^{min} + \frac{\mu^{max} - \mu^{min}}{1 + \left(\frac{N_{imp}}{N_{\mu}}\right)^{\gamma_{\mu}}} \tag{3.3}$$

---

[1] Except for electrons between 100 K and 200 K, where the authors were not able to form a conclusion.

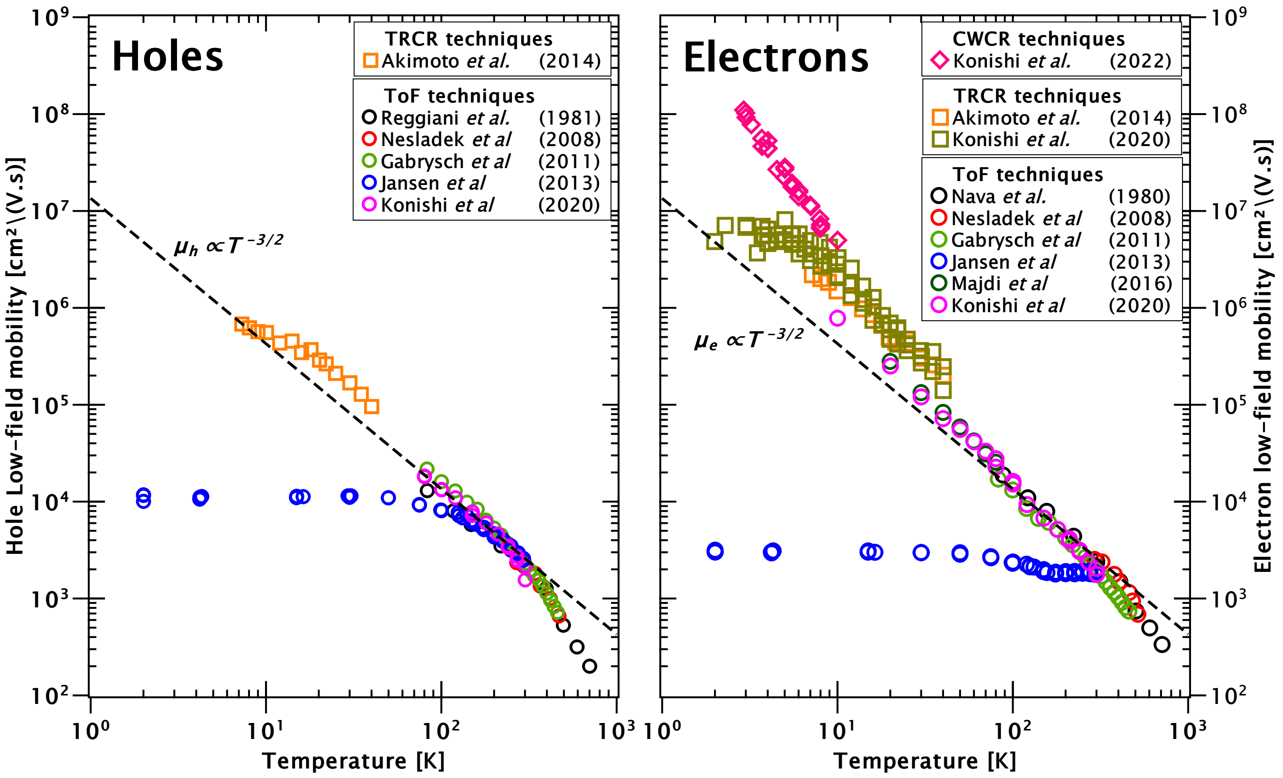

Figure 3.11: Hole (left) and electron (right) low-field mobility versus temperature reported in the literature. These values were obtained using the ToF, the TRCR ot the CWCR techniques. A $T^{-3/2}$ dependence of the carrier low-field mobility has been added on both plots (dash-black line).

with μ^{max} the mobility of pure material, μ^{min} the mobility of highly doped material. For both electrons and holes, the parameters N_μ and γ_μ were determined by fitting experimental data at 300 K. In this model, it can be noticed that as N_{imp} increases, the low-field mobility decreases. This effect was expected due to the greater contribution of the ionized and neutral impurity scattering on the mobility.

During my PhD, I had the opportunity to perform measurements using the ToF-eBIC technique at very low temperatures. The objective was to characterize intrinsic diamond properties - in particular the hole low field mobility - at very low temperatures (theoretically down to 4 K). To achieve this, we used a very pure sample: $[\mathrm{N}] < 9 \times 10^{14}\,\mathrm{cm}^{-3}$ and $[\mathrm{B}] < 2 \times 10^{14}\,\mathrm{cm}^{-3}$. The diamond named RON (see Table 2.1) was chosen. It was selected because of its good charge and transport properties.

3.3.1 Equipment and temperature calibration

3.3.1.1 Sample holder

One of the greatest challenges for performing measurements at low temperatures is the difficulty of limiting the thermal leakage to ensure that the sample is at the desired temperature. Indeed, since the sample was connected to the ROE, at RT, via an SMA cable, it was impossible to accurately study its properties below ∼ 40 K. It was therefore necessary to adapt the design of the sample holder.

Some pictures of the design used to carry out the experiments on large temperature ranges are presented in the Figure 3.12. In this configuration, the diamond is directly fixed onto the cryogenic stage using silver paste. An enamelled copper wire is connected to the diamond with silver paste and sandwiched between the cryogenic stage and a piece of gold foil in order to thermalize the cable before it reaches the diamond. The other part of the wire was previously welded to an SMA termination. This SMA connector is part of a tungsten holder which is fixed to the cryogenic stage using two screws. This tungsten block is connected to the ground via the SMA cable, and thus, the glued side of the diamond is grounded. This holder is also used to apply pressure on the gold foil and ensure the cooling of the enamelled wire used to read the signal and bias the sample. Then, two thermal shields, one connected to the cryogenic stage and the other connected to the metallic part surrounding it, are added to avoid radiative losses.

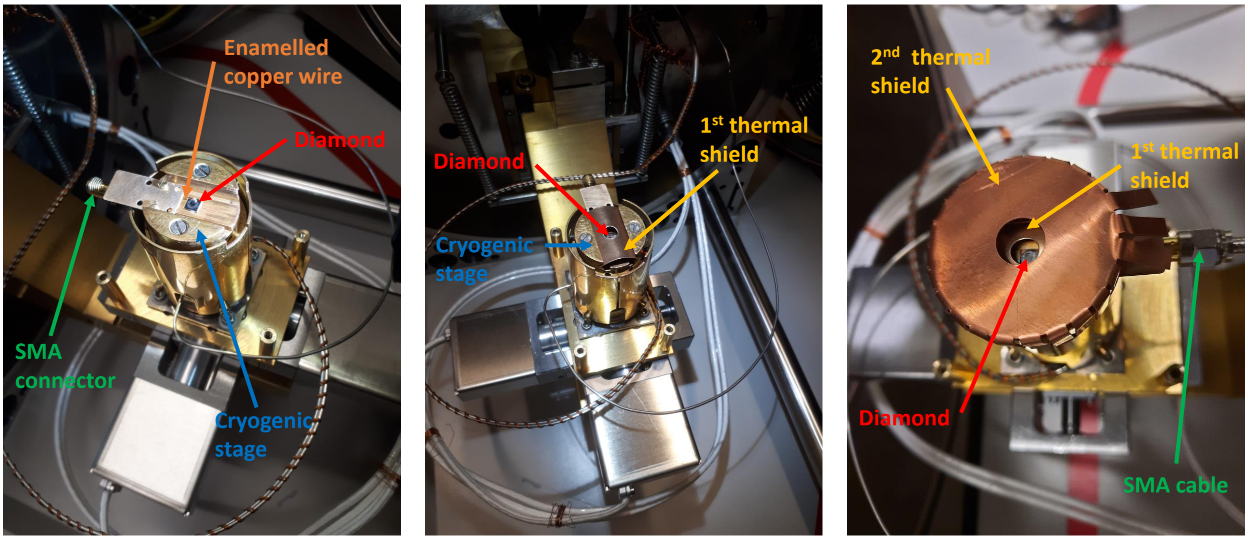

Figure 3.12: Sample holder used to perform measurements at low temperatures. First, the diamond is attached to the cryogenic stage using silver paste. An enamelled copper wire is then connected to the diamond and sandwiched between the cryogenic stage and a piece of gold foil in order to thermalize the cable before it reaches the diamond. The other part of the wire was welded beforehand to an SMA termination. Then, two copper thermal shields are set up in order to avoid radiative losses.

Temperatures down to 13 K were reached with this setup. Unfortunately, drift velocity was not measurable at lower temperatures because the SNR was too low.

3.3.1.2 Temperature calibration

The temperature calibration was performed using a CERNOX CX-1070-S-HT-4L sensor [1]. This cryogenic temperature sensor has a wide temperature range, from 3.8 to 300 K, adapted to this experiment. Using silver paste, the sensor was fixed to the cryogenic stage close to the diamond sample, and the cable used to measure the resistivity of the sensor was thermalized in a similar way to the sample. The sensor was biased at ±2 V and the resistivity was measured

---

[1] CERNOX cryogenic temperature sensors (website): https://www.lakeshore.com/products/categories/overview/temperature-products/cryogenic-temperature-sensors/cernox

thanks to a Keithley 2611B. At each temperature, the resistivity was measured at 2 and −2 V, and the average value was used to evaluate the temperature of the sample using the calibration curve given by the supplier. During the experiment, the temperature was stabilized before each measurement. Then the resistivity value was saved and controlled during the signal acquisition.

A comparison between the sensor calibration curve and the resistivity measured during the experiments is plotted in Figure 3.13. In this figure, the X-axis corresponds to the temperature of the cryogenic stage. This temperature is measured at the heat exchanger using a cryogenic rhodium-iron temperature sensor placed just below the removable sample holder. The Y-axis corresponds to the resistivity of the CERNOX sensor expected at this temperature ("Calibration curve") and the resistivity experimentally measured ("Measurements"). For temperatures lower than 30 K, a saturation of the measured temperatures can be clearly observed. As a result, it appears impossible to reach temperatures lower than ∼13 K with this setup. This phenomenon was already highlighted by cathodoluminescense measurements performed with similar equipment [Sakr, 2015].

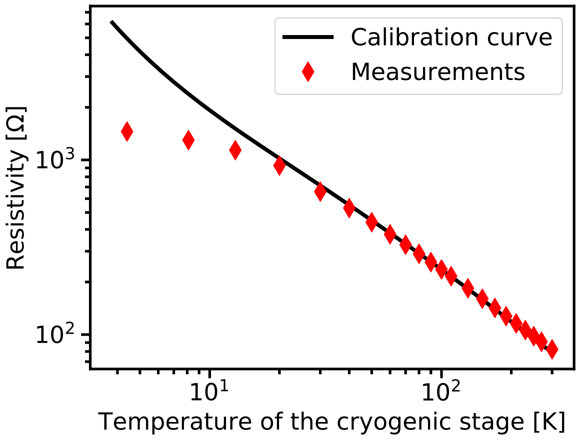

Figure 3.13: Comparison between the measurements performed with the CERNOX sensors close to the diamond sample and the calibration curve given by the provider.

The uncertainty of the temperatures was estimated to be lower than 5 % for the entire temperature range.

3.3.2 Experimental results

The measurements were taken with the following cycling procedure:

- for electric fields higher than 18 V/cm, 100 traces were averaged at each cycle. At each cycle, the opposite electric field was applied during the cycling step. 10 cycles were done. The instructions were therefore:
  - if $V_{bias} \geq 10\,\mathrm{V}$, $N_{WF} = 100$, $N_{cycl} = 10$ and $V_{cycl} = -V_{bias}$
- for lower electric fields, a similar cycling procedure was performed. The main difference was that the 1000 waveforms were acquired in 40 cycles (25 waveforms per cycles). For very low electric fields (less than ∼1.8 V/cm)[1], more cycles were achieved to increase the SNR. The instructions were therefore:

---

[1] this value was different depending on the the temperature

- if $V_{bias} \leq 10\,\mathrm{V}$, $N_{WF} = 25$, $N_{cycl} \geq 40$ and $V_{cycl} = -V_{bias}$

A different cycling procedure was carried out at low electric fields, because, as previously mentioned, polarization effects are stronger at low electric fields. To ensure that the two procedures produced similar results at higher fields, the signal at $V_{bias} = \pm 10\,\mathrm{V}$ was recorded with both cycling procedures.

3.3.2.1 Traces and drift time extraction

The average traces obtained at 13, 32, 90 and 300 K are shown in Figure 3.14. As observed previously, the signals obtained for holes are shorter (and thus the drift velocity is higher) than the signals obtained for electrons. In general, for a specific electric field, the signals are shorter at low temperatures.

On these curves, it may be observed that the polarization effects are relatively limited, in particular for the hole traces (i.e., top of the curve is flat) showing the efficiency of the cycling procedure.

At low temperatures and low electric fields, two contributions can be distinguished in the electron signals. This phenomenon was first observed and described in a diamond sample by Isberg *et al.* in 2013 [Isberg, 2013] and is known as valley polarized electrons. This phenomenon is explained by the particular band structure of diamond. As seen in Section 1.1, in the conduction band-structure of diamond, six energy minima are observed for different positions in the $k-$space. Moreover, the electrons in these valleys have different longitudinal and transverse effective masses ($1.56 \pm 0.02\ m_0$ and $0.280 \pm 0.002\ m_0$ respectively [Naka, 2013]). As a result, by applying an electric field in the [100] direction, an anisotropy is induced: the electron effective mass in the (100) valleys (longitudinal valleys to the electric field) is significantly higher than the one in the (010) and (001) valleys (transverse valleys), leading to different transport properties (drift velocities). As described by Isberg *et al.* [Isberg, 2013], this effect can be observed only because *"the scattering between valleys on orthogonal axes, requiring an interaction with a LA or TO phonon modes close to the K-point at the Brillouin zone boundary, require the interaction with a phonon with a very high energy of about 120 meV"*. Indeed, under the effect of the electric field, the electrons in the transverse valleys reach higher energies (they are heated more), and therefore, they reach the energy thresholds for LA and TO phonon emissions faster. It is then common to talk about cool (longitudinal polarized) and hot (transverse polarized) electrons. As a result, at high temperatures or high electric fields the electrons populating the hot valleys are scattered in the cool valleys: this is why this contribution is only observed at relatively low temperatures ($\leq 90\,\mathrm{K}$) and low electric fields (lower than ~400 V·cm). Recent studies [Djurberg, 2022] have described this phenomenon by performing Monte Carlo simulations based on anisotropic deformation potential.

The traces without valley polarized effects were fitted with the following formula extracted from [Gabrysch, 2010, Majdi, 2012]:

$$I(t) = \alpha \cdot \left(1 + erf\left(\frac{t - t_0}{\sigma_0}\right)\right)\left(1 + erf\left(\frac{t_1 - t}{\sigma_1}\right)\right) \times exp\left(\gamma t\right) \tag{3.4}$$

where I is the current induced in the diamond, t the time and α a parameter proportional to the amplitude of the signal. To describe the signal, Gauss error functions were used with

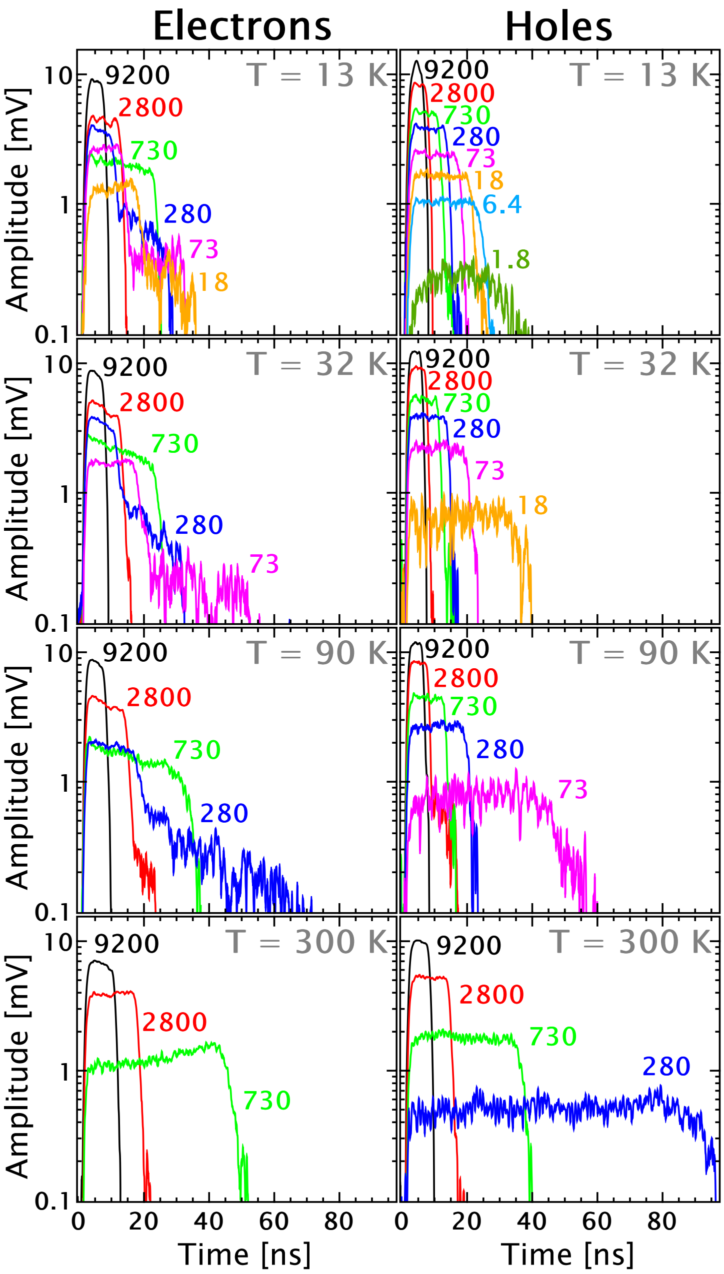

Figure 3.14: Mean traces obtained at 13, 32, 90 and 300 K for electric fields from 18 to 9200 V/cm. The electric field is expressed in V/cm and is specified in a label next to each curve. On these traces, the electric noise was subtracted for readability reasons, and the traces obtained at 13 K were filtered to remove some high frequency parasitic noise oscillations induced by the preamplifier (0.35 to 0.40 GHz and 1.15 to 1.35 GHz).

position parameter t_0 (respectively t_1), and scale parameter σ_0 (respectively σ_1) for the rising (respectively falling) edge of the signal. As a result, the time t_{drift} can be easily estimated by subtracting t_1 by t_0:

$$t_{drift} = t_1 - t_0 \tag{3.5}$$

The experimental uncertainties on the drift time are mainly dependent on the ability to detect the rising edge of the signal, which is directly correlated to the SNR. Then, the error on the drift time can be estimated by computing the ratio of the noise standard deviation by the local value of the rate of change evaluated at t_0 and t_1 (see [Spieler, 1982]). In our case, that can be approximated to be equal to the ratio of the noise standard deviation by the slope of the signal edges [Jansen, 2013a, Jansen, 2013b] as described in Equation 3.6. Using the parameters of the fit function, the slope can be approximated as the ratio of the maximum amplitude 4α to the scale parameter σ_i. As a result, the time resolution can be estimated by the Equation 3.7.

$$\sigma_{t_{drift}} = \sqrt{\left[\frac{\sigma_{noise}}{\left(\frac{dV}{dt}\right)_{t_0}}\right]^2 + \left[\frac{\sigma_{noise}}{\left(\frac{dV}{dt}\right)_{t_1}}\right]^2} \approx \sigma_{noise} \cdot \sqrt{\left[\frac{1}{slope_{RE}}\right]^2 + \left[\frac{1}{slope_{FE}}\right]^2} \tag{3.6}$$

$$slope_{RE} \approx \frac{4\alpha}{\sigma_0} \approx \frac{\sigma_1}{\sigma_0} \cdot slope_{FE} \qquad \Longrightarrow \qquad \sigma_{t_{drift}} \approx \frac{\sigma_{noise}}{4\alpha} \cdot \sqrt{\sigma_0^2 + \sigma_1^2} \tag{3.7}$$

with $slope_{RE}$ (respectively $slope_{FE}$) corresponding to the slope of the rising (respectively falling) edge of the signal.

Compared to the General Gaussian Distribution (GGD) function (Equation 2.1), this function is directly resulting from a physical analysis of the signal done in [Gabrysch, 2010], and can accurately fit a waveform with unsymmetrical edges. It is then perfectly adapted to fit the signal at low electric fields which can be strongly asymmetrical due to the long time transit of the carriers and the scattering phenomena. Regarding the valley-polarized currents, the signals were fitted using a sum of two GGD. Nevertheless, with 8 free parameters there is almost no chance to obtain a fit of the hot and cool currents: the baseline fluctuations can lead to an incorrect fit and it is difficult to have a cool electron signal starting at the same time as the hot electron signal; they are often shifted in time. To solve this issue, and improve the fit convergence (and so processing time), a relation between the parameters must be found. The relation needs to take into account that the cool electron signals start at the same time as the hot electron signals; or in another words, that both cool and hot electrons start drifting at the same time. The selected relation is the following one:

$$t\left(I_{2,RE}(t) = I_{0,2}/2\right) = t\left(I_{1,RE}(t) = I_{0,2}/2\right) \tag{3.8}$$

with $I_{2,RE}(t)$ the amplitude over time of the cool electron rising edge current, $I_{0,2}$ the maximum amplitude of the cool electron current and $I_{1,RE}$ the amplitude over time of the hot electron rising edge current. In a few words, this relation requires that the time corresponding of the half-amplitude of the rising edge of the cool electron signal is equal to the one corresponding, at this same amplitude, on the rising edge of the hot electron signal. This relation can be expressed with the parameters of the double GGD function:

$$(3.8) \qquad \Longleftrightarrow \qquad \mu_2 - \alpha_2 \log(2)^{1/\beta_2} = \mu_1 - \alpha_1 \log\left(\frac{2I_{0,1}}{I_{0,2}}\right)^{1/\beta_1} \tag{3.9}$$

with, $I_{0,i}$ the maximum amplitude of the signal, μ_i a position parameter, α_i a scale parameter and β_i a form parameter; with the index 1 corresponding to the hot electrons and 2 to the cool electrons. As a result, the fit function used to fit the electron polarized current is the following:

$$I(t) = I_{0,1} \cdot exp\left[-\left(\frac{|t-\mu_1|}{\alpha_1}\right)^{\beta_1}\right] + I_{0,2} \cdot exp\left[-\left(\frac{|t-\mu_2|}{\alpha_2}\right)^{\beta_2}\right]$$

$$\text{with, } \mu_2 = \mu_1 - \alpha_1 \log\left(\frac{2I_{0,1}}{I_{0,2}}\right)^{1/\beta_1} + \alpha_2 \log(2)^{1/\beta_2} \tag{3.10}$$

This fit function lies on the fact that any better description of the signal was developed during the time of this PhD and that the results obtained with this description are sufficiently accurate to study the electron drift velocities. Indeed, as seen on the Figure 3.15 - where two signals (at 18 V/cm (left) and 180 V/cm (right)) are fitted with the fit function of Equation 3.10 - the signal of hot and cool electrons is well reproduced by the fit function even if 1) the SNR is not very good; and, 2) important noise fluctuations are observed.

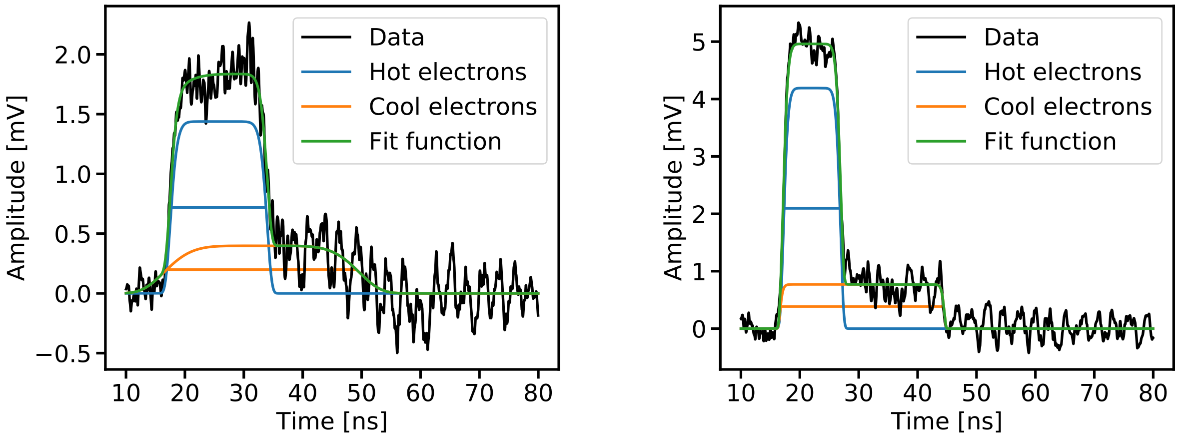

Figure 3.15: Electron signals obtained at 13 K at 18 V/cm (left) and 180 V/cm (right). The data were fitted by the fit function of Equation 3.10 (green curve). The contribution of hot (blue) and cool electron (orange) are also plotted. The horizontal lines represent the drift time estimated at half amplitude.

3.3.2.2 Drift velocity versus electric field

The drift velocity v_{drift} can be easily estimated by computing the ratio of the diamond thickness t_h by the drift time t_{drift} (see Equation 2.3). On the diamond named RON, the diamond thickness is (546 ± 4) µm, leading to an uncertainty lower than 1 % on the diamond thickness. For the valley polarized current, the two drift times are computed using the same equation.

The drift velocity measured at different electric fields E and temperatures for holes and electrons is shown in Figure 3.16. For the temperatures lower than 90 K, it is possible to extract the drift velocities for the cool (a) and the hot electrons (b). The hot electron drift velocity can only be computed at low electric fields (up to ∼275 V/cm). Indeed, as explained previously, the hot electron transits can not be observed because of the repopulation phenomena. For the same reasons the hot electron transits cannot be studied at higher temperatures. It was then chosen to plot the electron drift velocity obtained at higher temperatures in another graph (Figure 3.16 (c)). On this plot, the drift velocity evolution with the electric field can be studied at four different temperatures (120, 150, 200 and 300 K). In particular, it can be noticed that at 120 K, the electron drift velocity decreases between 360 and 550 V/cm. This phenomenon is called negative differential mobility and, it was observed for the first time in diamond sample by Isberg *et al.* in 2012 [Isberg, 2012]. This phenomenon is also a consequence of the electron scattering in orthogonal valleys. Our measurements accurately reproduce the results obtained by Isberg *et al.* [Isberg, 2012] at 120 K, demonstrating the reliability of our method.

Regarding the holes, the effect of the temperature on the drift velocity evolution with the electric field is clearly visible: the hole curves are deformed as described by Majdi *et al.* [Majdi, 2013]. It is then not possible to fit the data with the fit function of Equation 3.11 used to extract the transport parameters at RT. As a result, the low field mobility μ_0 was evaluated, for both carriers, by fitting the slope of the drift velocity at low electric fields (see Equation 3.12). These results also show the necessity of being able to perform measurements at very low electric fields to extract the low field mobility.

$$v_{drift}(E) = \frac{\mu_0 E}{1 + \frac{\mu_0 E}{v_{sat}}} \tag{3.11}$$

$$v_{drift}(E) = \mu_0 E \qquad \text{in the linear region at low electric fields} \tag{3.12}$$

In these measurements the saturation drift velocity v_{sat} was not particularly studied, but it does not seem to depend too much on the temperature. In particular for the lowest temperatures ($\leq 90\,\mathrm{K}$), it seems to remain constant, supporting the assumption of Majdi *et al.* [Majdi, 2013].

Those curves seems to reproduce pretty well the data obtained by Isberg and Majdi *et al.* [Isberg, 2012, Isberg, 2013, Majdi, 2013]. Nevertheless, we measured hole transit at lower electric fields with the ToF-eBIC technique and thus evaluate the hole low-field mobility. As discussed at the beginning of this section, this parameter is a key for plenty of applications and the data were never evaluated using the TCT at temperatures lower than 77 K.

Unfortunately for electrons, the extraction of the low field mobility is more difficult, in particular for temperatures lower than 30 K. As a result, only the low field mobility obtained for temperatures higher than 32 K were extracted.

3.3.2.3 Influence of the temperature on the low field mobility

Thanks to the Equation 3.12, the low field mobility of holes, cool and hot electrons was extracted. The Figure 3.17 represents the temperature dependence of the low field mobility obtained during this work (blue points). The results obtained can be compared with the ToF data reported by Konishi *et al.* [Konishi, 2020b] (open points). A very good agreement is obtained for temperatures higher than 77 K. In order to compare our data at lower temperature, a red dashed line representing the theoretical low field mobility expected for holes was added. Those data were computed using the model described by Pernot *et al.* [Pernot, 2010]. In this model, the deformation potential scattering was assumed to be elastic. That assumption is no longer

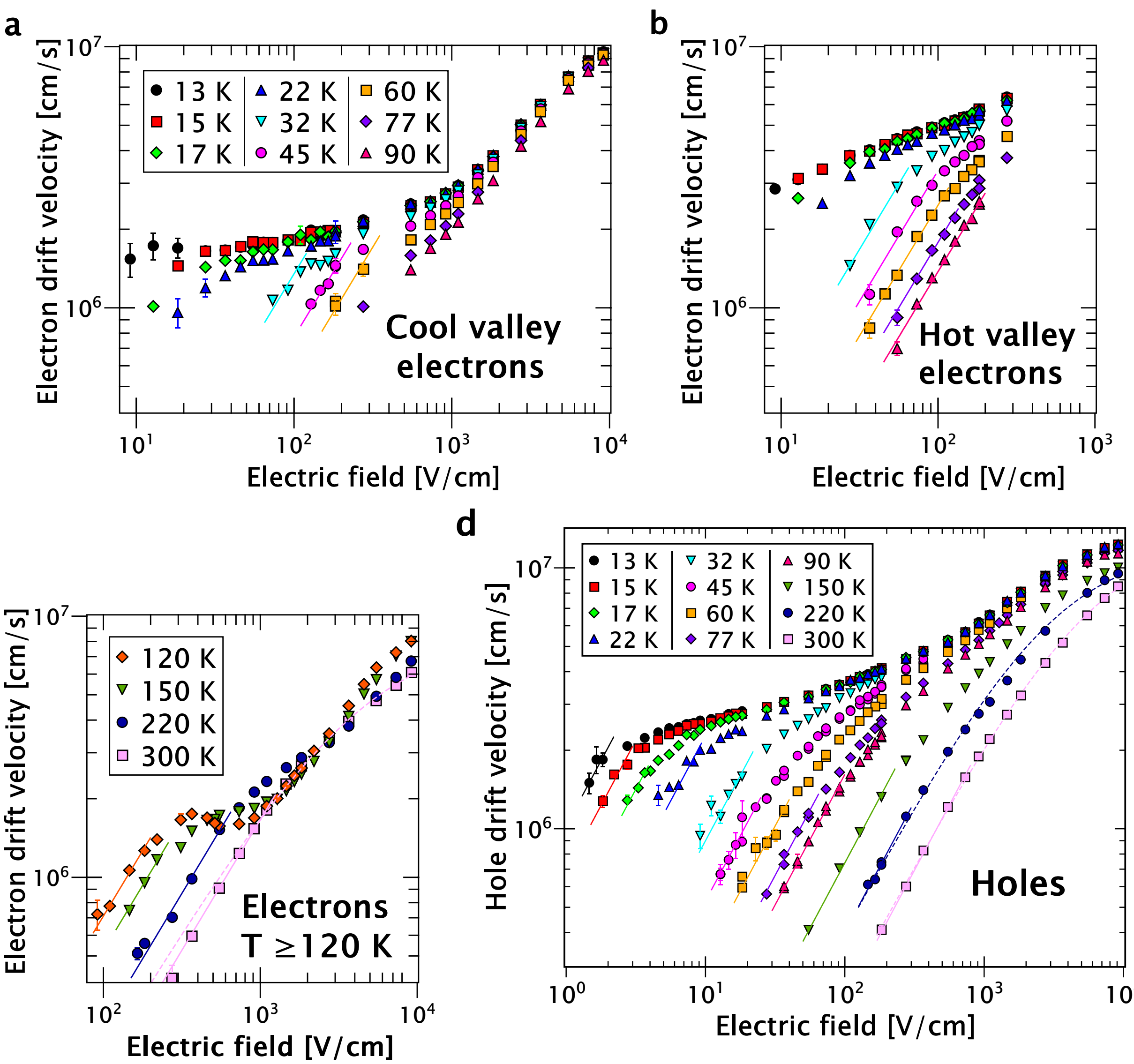

Figure 3.16: Electron and hole drift velocities and low-field mobilities. Cool valley (a) and hot valley (b) electron drift velocity versus electric field at various temperatures. (c): electron drift velocity versus electric field measured at 150 and 300 K. (d): hole drift velocity versus electric field at various temperatures. The solid lines show the linear fit at low electric fields used to extract the low-field mobility. A fit on the entire electric field range was also performed using formula 3.11 at 220 and 300 K (dashed line).

valid at low temperatures where the energy lost occurring during a phonon scattering process is not negligible. Indeed, it was recently shown that the electron low field mobility increases significantly at very low temperature [Majdi, 2016,Konishi, 2022] and that the evolution can be described by considering inelastic scattering. Unfortunately, it was not possible to implement a simulation during the duration of this PhD.

Nevertheless, regarding the hot and cool electrons, a lower low field mobility was extracted (except at RT). Such difference is difficult to explain without considering that the intrinsic properties of the samples are different. Indeed, if the method used to extract the low field mobility is not perfect, it seems difficult that it could induce such a difference. In particular, this method should allow an accurate extraction of the hot electrons due to the good SNR

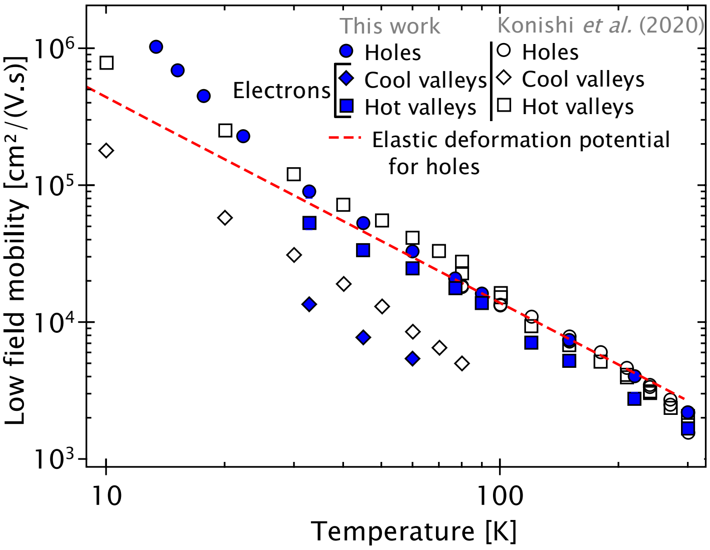

Figure 3.17: Hole and electron low field mobility versus temperature. The blue points correspond to the value extracted during this work and the open symbols to the value of Konishi *et al.* [Konishi, 2020b]. The red dashed line, represent the theoretical low field mobility expected for holes considering an elastic deformation potential based on calculations from Pernot *et al.* [Pernot, 2010].

on this part of the signal. Regarding the measurement itself, it seems surprising to obtain a good agreement for holes data and not for electrons. A possible explanation could be the chosen procedure chosen minimizes polarization effects: in our case a procedure consisting of inverting regularly the bias was chosen when Isberg *et al.* have chosen to apply the bias by pulses of 50 µs during the measurements [Isberg, 2005, Isberg, 2009, Gabrysch, 2011, Isberg, 2012, Majdi, 2013, Isberg, 2013, Majdi, 2016, Djurberg, 2021]. Nevertheless, in order to explain this difference, it seems interesting to perform ToF-eBIC experiments with the diamond sample they used during their experiments. This would allow us to understand whether the origin of this difference is due to the intrinsic quality of the diamond sample or to the technique itself.

3.3.2.4 Temperature dependence of the charge collection

During these experiments, the charge collected at high biases (±150, ±200, ±300, ±400, and ±500 V) is almost constant before it suddenly decreases between 80 and 120 K (between 14 % to 22 %). In Figure 3.18, it can be noticed that this phenomenon occurs for holes (left) and electrons (right) at approximately 120 K.

This phenomenon was already highlighted in previous experiments using protons, helium, lithium and carbon ions [Jansen, 2013a, Cosic, 2022]. However, the charge collection drop with 30 keV electron pulses is less important than the drop observed previously with heavier particles. This assumption goes in the same direction as the previous observations done by Cosic *et al.* [Cosic, 2022] which noticed a smaller drop for less energetic lighter particles.

According to Cosic *et al.* [Cosic, 2022], this phenomenon can be explained by the screening process of the external electric field applied inside of the electron-hole pairs cloud leading to a slower charge separation and therefore increasing the probability of exciton formation. Moreover, according to the law of mass action [Konishi, 2022], there is an equilibrium between the density of excitons and the one of electron-hole pairs and for low temperature, only exciton

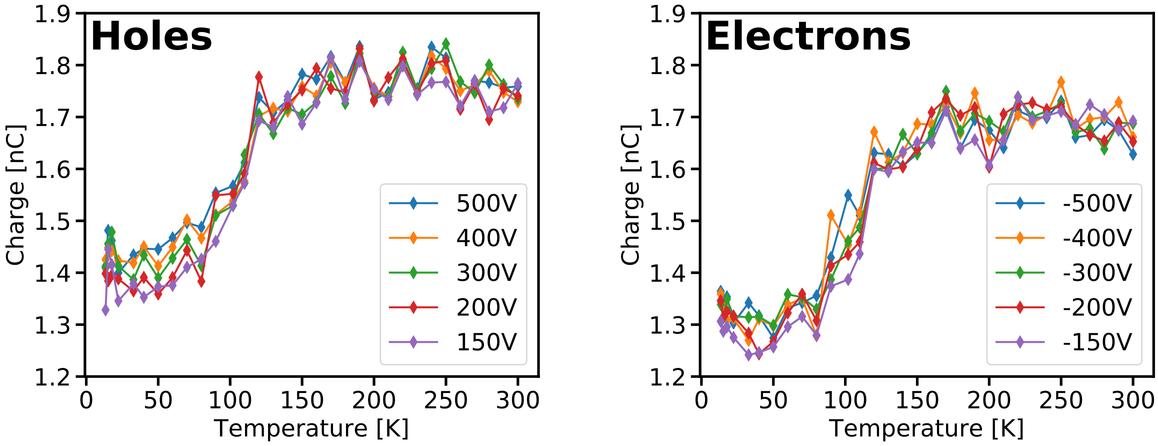

Figure 3.18: Charge collection versus temperature for holes (left) and electrons (right). The charge collected after amplification by the CIVIDEC is plotted.

should exist. The exciton being a neutral particle, they should not contribute to the signal (at least for field lower than the exciton ionisation critical field). As a result, if the fraction of excitons is increasing, there is less electron or holes drifting toward the electrodes, and so a lower charge is collected.

Nevertheless, the model developed by Jansen *et al.* [Jansen, 2013a] - which describes the temperature dependence of the collected charge - and used by Cosic *et al.* [Cosic, 2022] to explain this phenomenon does not applied in our case. Indeed, first, this model was made and adapted to explain the resulting signals after the interaction of a light ions (and not low energetic electrons) in diamond and, secondly it was also made to explain some deformed waveform observed by Jansen for temperatures between 75 to 150 K and no waveform following this behavior was experimentally observed in the present study.

3.3.3 Discussion and comments

Thanks to the ToF-eBIC technique and the development of a sample holder to work at low temperatures, it was possible to study the hole and electron transits depending on the temperature. Valley-polarized currents were observed in diamond sample for the first time since their first observation by Isberg *et al.* [Isberg, 2013] in 2013. The drift velocities of electrons and holes were computed by fitting the average waveform obtained at various electric fields and temperatures. It was reported that the drift velocity was increasing versus temperatures at a specific electric field confirming some previous observations done in other experiments [Reggiani, 1981, Gkoumas, 2009, Gabrysch, 2011, Majdi, 2013, Jansen, 2013b]. Thanks to the work done to limit the polarization and screening effects, it was possible to reach very low electric field and to evaluate the low field mobility of hot and cool electrons and of holes down to 13 K. It is the first time that the low field mobility of holes was experimentally extracted at temperatures below 80 K. The hole low field mobility seems to be in a good agreements with the literature (see Figure 3.19) for temperature higher than 80 K and with the model computing by Pernot *et al.* [Pernot, 2010] down to 30 K. Below this temperature, it is mandatory to take into account the inelastic scattering of the charge carriers. Regarding the electrons, the values obtained with our technique are slightly lower than the one obtained by Konishi *et al.* [Konishi, 2020b]. These differences are probably due to the diamond sample intrinsic properties (impurities, dislocation concentration...). Indeed, a very interesting fact is that Isberg *et al.* mentioned that *"successive* ***hole*** *transits do not appreciably affect the electric field distribution within the sample."* [Isberg, 2006], whereas it seems that, in our experiments, a similar phenomenon is observed with **electrons**. To check this hypothesis, it would be interesting to test their sample using the ToF-eBIC technique.

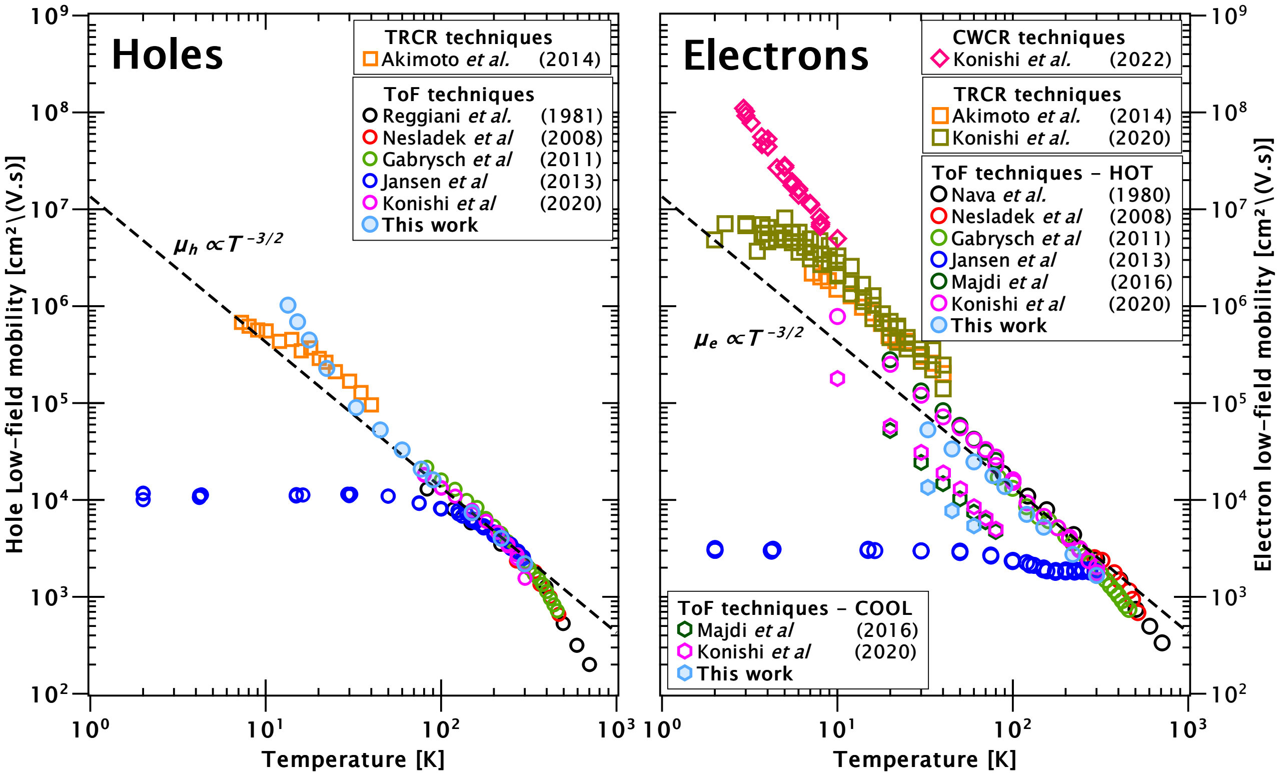

Figure 3.19: Hole (left) and electron (right) low-field mobility versus temperature reported in the literature and computed in this work. These values were obtained using the ToF, the TRCR ot the CWCR techniques. A $T^{-3/2}$ dependence of the carrier low-field mobility has been added on both plots (dash-black line).

3.4 Two-dimensional charge collection mapping of a diamond substrate

The crystalline inhomogeneities (local defaults, dislocations, impurities...) can affect significantly the properties of a sample. In particular, for particle detectors, homogeneous charge collection properties are crucial to achieve high energy resolution. For instance, pcCVD diamonds have a poor energy resolution compared to scCVD diamonds [Curtoni, 2020]. In a SEM, the electron beam position can be controlled at the nanometer scale. Also, mapping of the charge collection properties at the micrometer scale[1] of a sample can be achieved.

Therefore, one of the main motivations was to perform precise mapping of diamond samples using the ToF-eBIC technique. Indeed, studying the homogeneity of the charge collection properties of scCVD diamond detectors is necessary to assess their performances or to investigate the cross-talk and the charge sharing phenomena in stripped and padded diamond samples. Moreover, there is also a need to map local properties of diamond detectors to better understand the charge collection process e.g in DOI and polycrystalline diamond samples - which exhibit both structural defects - or on diamond damaged under high irradiation doses.

This technique is complementary to the experiments performed at the ESRF (the European Synchrotron Radiation Facility), where diamond samples were already mapped using 8.5 keV X-ray photon micro-bunch beam [Gallin-Martel, 2021a, Curtoni, 2020]. Indeed, contrary to the experiment carried out with X-rays, in the ToF-eBIC mapping, the particles are stopped within the diamond bulk close to one electrode. It is then possible to study separately the drift of electrons and holes and compare the charge collection properties depending on the charge carrier.

3.4.1 Equipment and methods

Two techniques were implemented to perform the mapping of the diamond sample's charge properties. The fist one was designed to map large surfaces (from $100\times100\,\mu m^2$ to $4.5\times4.5\,mm^2$). The second one enables mapping at the micrometer scale. Both will be presented in the next subsections.

3.4.1.1 Mapping of the diamond homogeneity

To study the homogeneity of charge collection or transport properties over the entire surface of a scCVD diamond sample (about $4.5\times4.5\,mm^2$), a resolution of approximately 100 µm is sufficient. Therefore, the spot mode should be avoided to minimize polarization effects.

Thus, the first mapping was carried out using the SEM scan mode with a cycling procedure similar to the one described in the subsection 3.2.1. To save time, we performed a single cycle at each position. During these measurements, we had to find a balance between the spatial resolution that we wanted to achieve and our willing to limit the effects of polarization:

- on the one hand, too low a spatial resolution does not allow to identify inhomogeneities in the charge collection. Therefore, relatively small pixels[2] are required.

---

[1] The interaction volume of 30 keV electrons is approximately 4 µm large in the lateral directions (see Figure 3.8).

[2] The pixels must be less than ∼400 µm wide to have ten pixels along the length of the diamond

- on the other hand, the polarization effects are stronger for the small scanned areas, here the pixel surfaces (see Subsection 3.2.2.2).

Consequently, we decided to map the charge properties of the sample using electron transits at high electric fields, typically 5.5 to 10 kV/cm, because the resulting waveforms are more stable over time.

The mapping procedure is described in Figure 3.20. To map the diamond properties on a 4.5×4.5 mm^2 area (sample surfaces) with 100 µm long pixels, 45×52 pixels are required. These pixels correspond to scanned areas where typically 1000 traces are averaged. For each scanned area, the beam can take 1024 horizontal positions and 884 vertical positions. Consequently, with a scanning time of 100 ns an inter-pulse time of approximatly 3 ms, two successive pulses are at least 13 µm apart, which is not sufficient to completely avoid polarization effects.

Figure 3.20: Mapping procedure used to scan large areas. To map a surface of 4.5×4.5 mm^2 with 100 µm pixels long, 45×52 pixels are necessary. Each pixel corresponds to a scanning area where the beam sweeps 1024 horizontal positions × 884 vertical positions.

This technique does not allow mapping of small areas at low electric fields. For example, to map a sample with hole transit at an electric field of 5.5 kV/cm, the surfaces should be greater than ∼100×100 µm^2. Thus, another mapping procedure, more flexible on these aspects, was developed.

3.4.1.2 Mapping at the micrometer scale

The highest spatial resolution of the SEM is reached by working with the spot mode. However, it was not possible to reach satisfying results in a reasonable time with the standard cycling procedure while using the spot mode. Therefore, we developed an alternative version of the cycling procedure .

As described in Figure 3.22, this procedure was designed to achieve a measurement during the first electron pulse and to invert the bias during the next pulse (reset electric field distribution). The Keithkey 6487 has a rise time of 4.5 ms for the high voltage range (> 50 V), and thus cannot reverse bias fast enough. Therefore, three Keithleys with a rise time shorter than 1 ms were plugged in parallel(Keithley 2601A, 2636A and 2611B) to provide the bias voltage up to 80 V. As described on the scheme of Figure 3.21, the Keithley and the oscilloscope were triggered with the second channel of the pulse generator. This channel has been set at half the frequency, so that every other pulse is triggered. Then, A Stanford Research Systems DG535 was used to delay the bias inversion so that the voltage is not reversed when the primary electrons interact in the diamond. The Keithley HV supply and the oscilloscope were connected to a computer thanks to GPIB connectors. The slow control was achieved using LabVIEW, and managed the HV applied on the diamond sample and the signal acquisitions. On this program, the experimenter can fix the:

- **working bias V_{bias}:** bias applied during the measurement (maximum ±80 V due to hardware limitation).
- **cycling bias V_{cycl}:** bias used to reset the diamond. Generally, $V_{cycl} = -V_{bias}$ (maximum ∓80 V due to hardware limitation).
- **working time Δt_{bias}:** time spent at the working bias (typically 1.5 ms).
- **cycling time Δt_{cycl}:** the time spent at the cycling bias, is then equal to $2T - \Delta t_{bias}$; with T the time between two impacts (typically 1.5 ms).
- **number of traces per cycle N_{WF}:** number of traces averaged at each position; the averaging is tune by the oscilloscope (typically 1000 traces).

A program was developed to perform line mapping, but it can be adapted to different kind of surfaces.

For an electric field of 1.5 kV/cm, the charge collected using this method was significantly lower than that obtained using the methods described in Subsection 3.2.1. As described in Appendix A.1, working with an unfocus beam, to reduce the density of electron-hole pairs, cancels this discrepancy. However, such a method does not allow mapping of charge collection at the micrometer scale (the beam must have a 60 µm diameter to recover the CCE). Considering that the bias voltage was limited to ±80 V by the hardware, we chose to work with a 150 µm sample in order to reach higher electric fields (5.3 kV/cm, 3.6 times higher than the maximum electric field achievable with the diamond named RON used previously) and thus avoid a decrease in charge collection.

3.4.1.3 Pad detector used for mapping

The mapping was carried out on different diamond substrates, but in the following, only the results obtained on the pad detector of the Figure 3.23 will been presented. This sample is a 150 µm thick scCVD diamond from Element 6 which was metalized by the platform NanoFab of Institut Néel. On the top side of this sample, the metallization consisted of four 100 nm thick aluminium pads with different surfaces (0.5×0.5, 1×1, 1.5×1.5 and 2×2 mm^2). On the back side, only one 100 nm thick aluminium pad of 4×4 mm^2 was made. This sample was placed

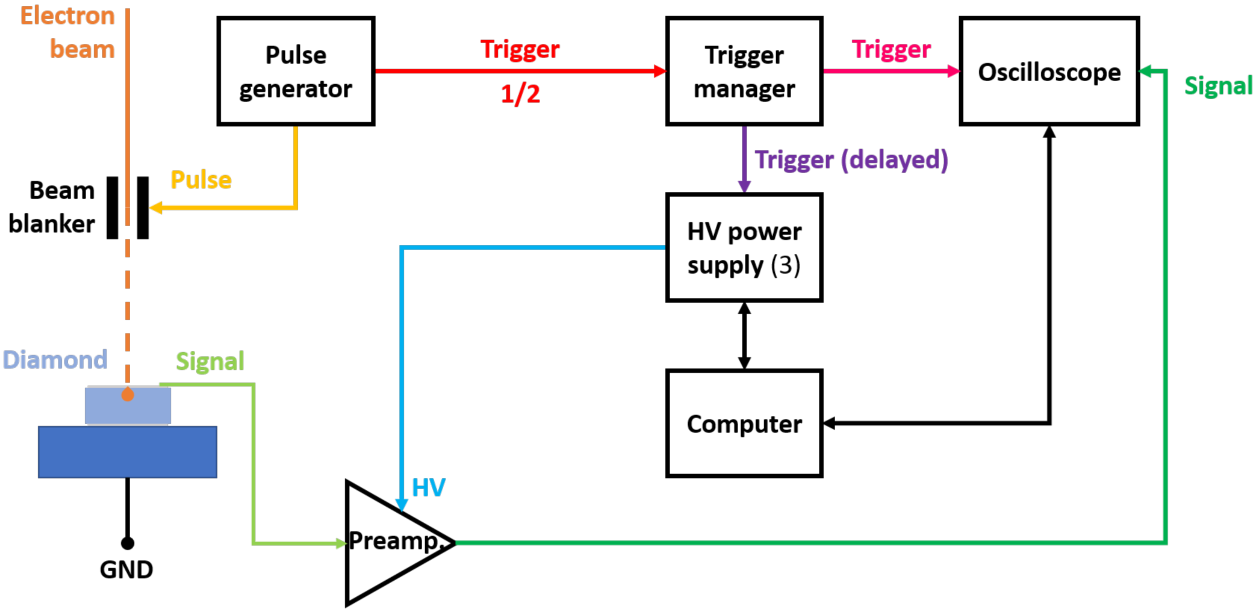

Figure 3.21: Scheme representing the connections between the different instruments during the mapping experiments. Each color line represents an SMA cable, the two double black arrows are GPIB connections and, the GND is simply done by putting in contact the back side of the diamond with the metallic sample holder or by using end-caps. This scheme can be compared to the one of Figure 3.4 used for drift velocity studies.

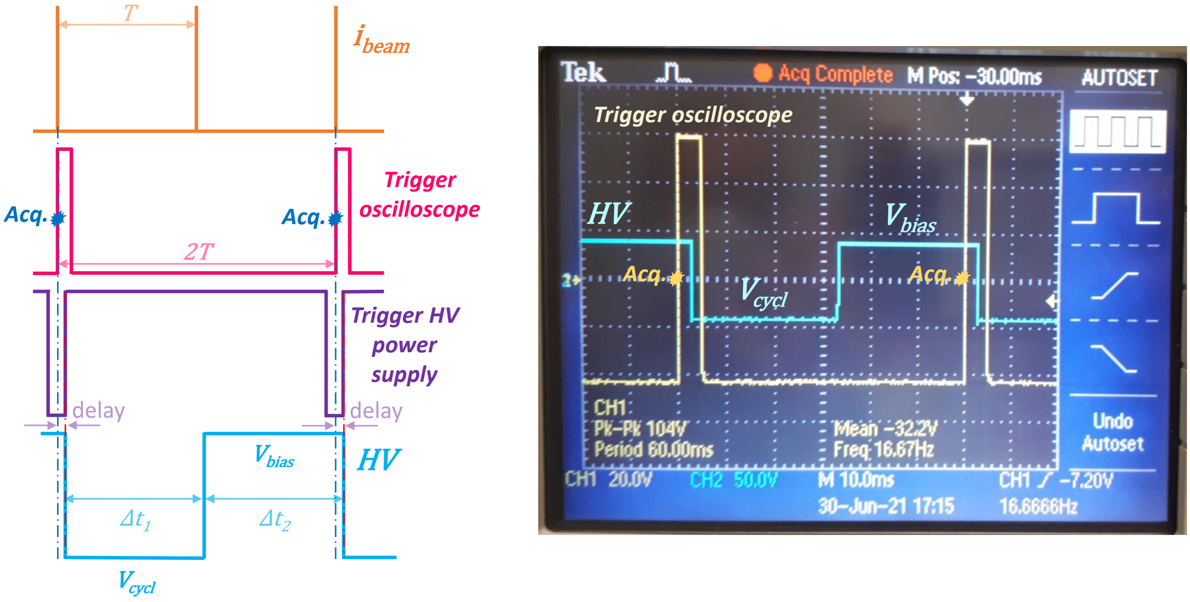

Figure 3.22: Cycling procedure used to minimize the polarization effects during sample mapping. In this scheme $\Delta t_{bias} = \Delta t_{cycl} = T$. This cycling procedure can be compared to the one of Figure 3.5 used for drift velocity studies.

in the sample holder presented in the Figure 2.2 (c). Bonding wires were used to connect the pads to the read-out tracks. Thus, it was possible to bias and study the signal of each pad individually. To perform the mappings, the top side (with the four metallized pads) was facing the electron source; this side will be called A side in the following. At the opposite, the other side will be named B side.

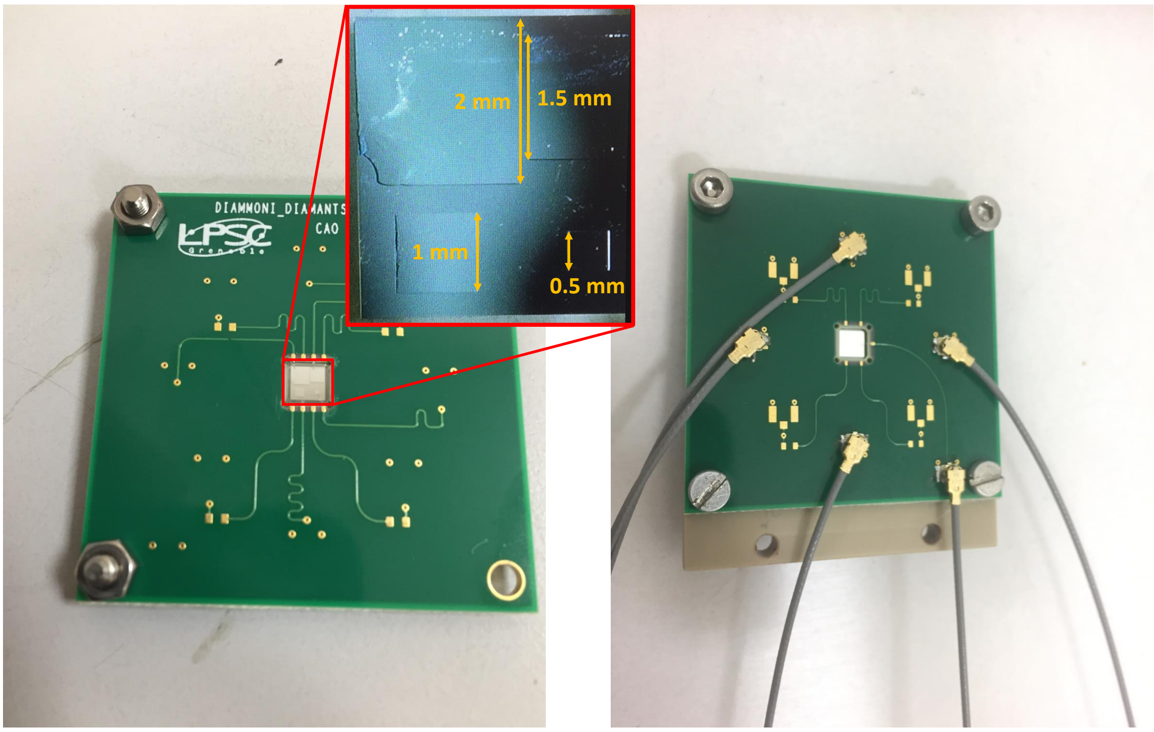

Figure 3.23: Pad detector used for mapping. On one side, the metallization consisted of four aluminium pads of different sizes 0.5×0.5, 1×1, 1.5×1.5 and 2×2 mm^2 and of a pad of about 4×4 mm^2 on the other side.

No quantitative drift velocity measurements can be performed on this sample. Indeed, due to its relatively small thickness (150 µm), short signals were obtained at high electric fields (see Figure 3.27). Then, the capacitance and the electronic contribution on the rise and fall time were not negligible. Therefore, triangular shaped signals were obtained and the estimation of the drift time was not possible.

3.4.2 Experimental results

3.4.2.1 Mapping of the diamond homogeneity

A charge mapping of the pad detector was performed to study the charge collection homogeneity 1) on each pad and 2) in the gap between the pads. A SEM image (Figure 3.24 (a)) was recorded at the same time as the charge mapping (Figure 3.24 (b)). The charge mapping was achieved by biasing the B side (4×4 mm^2 pad) and applying an electric field of 10 kV/cm. In this experiment, only the drift of electrons was studied. The size of the pixels (mapping) is about 70×80 µm^2 and at each pixels 1000 traces were averaged. In this configuration, the signal was stable over time.

The bonding wires used to bias the pixels and the five pads can be identified. The four of them facing the beam correspond to the four yellow squares, while the one in the other side to the lighter blue area. A better charge collection at the level of the pads of the side A is

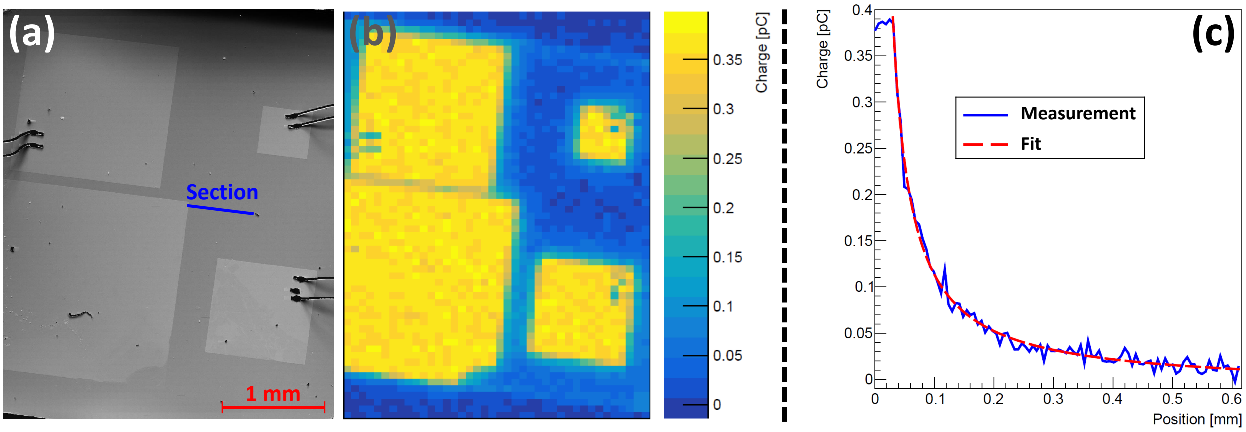

Figure 3.24: (a): SEM image of the pad detector. (b): Corresponding charge mapping at 10 kV/cm of the pad detector. (c): Charge collection evolution when the beam is moving away from the edge of the pad (see blue section on the image (a)). The data were fitted using a $1/x$ law (red curve); for more details about it see Appendix A.2. The origin of the position corresponds to the position of the first pixel of the line scan.

observed. To explain this, a simulation was performed with COMSOL Multiphysics[1] in two dimensions (see Figure 3.25). Under these pads, the electric field lines are parallel to each other in the [100] direction, which induces a drift of electrons towards the pad on the B side. As the electron beam moves away from the edges of the pads, the electric field lines are no longer aligned in the [100] direction and the electric field strength decreases significantly. (see Figure 3.25). Therefore, the charge carriers produced in such a region hardly drift towards the electrodes, they recombine, and thus, the amount of collected charge decreases sharply. As a

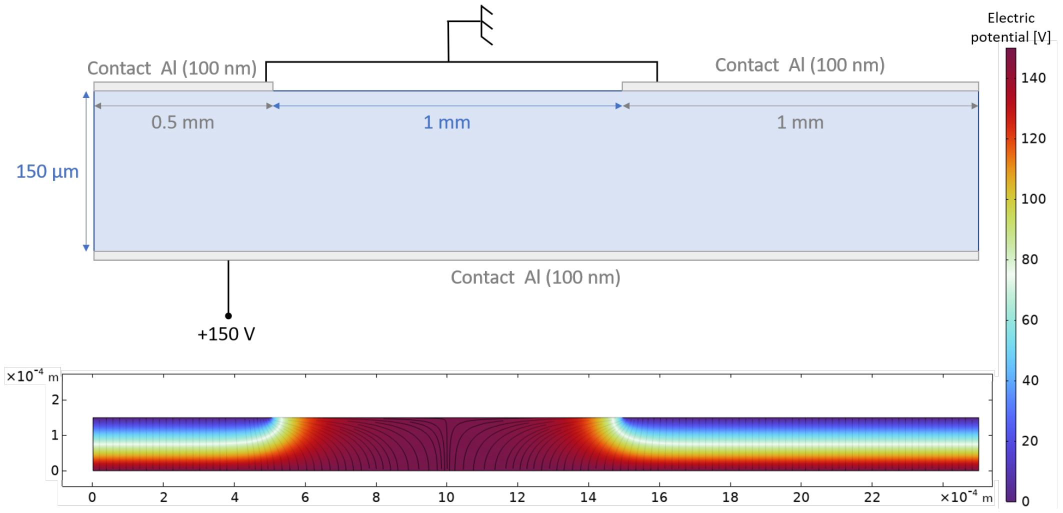

Figure 3.25: COMSOL simulations of the potential and the electric field applied on the diamond sample. The architecture used to achieve these simulation is plotted above the COMSOL results. In these figures, the 0.5×0.5 and 1×1 mm^2 are represented. The distance between the pad is assumed to be approximately 1 mm.

---

[1] https://www.comsol.fr/

result, the farther the charges are generated from a pad, the lower the collected charge. A similar phenomenon was already observed and reported in [Marsolat, 2015].

On the A side, the charge collection homogeneity was evaluated on the larger pad. A charge collected of approximatly (0.36 ± 0.01) pC after amplification was estimated on an area of 20×25 pixels (500 entries in total for a surface of $1.4\times2\,\mathrm{mm}^2$). The decrease of the charge collection when the electron pulses were moving away from the edge of a pad was also studied (Figure 3.24 (c)). In Figure 3.24 (a), the section (or line) mapped is represented. This mapping is composed of 100 positions; at the beginning the electron pulses are focused on the pad (corresponds to the stable part on the graph (c)) while the next ones are interacting more and more further away from the pad edge. The collected charge decreasing slope seems to follow a $1/x$ law (with x the distance from the edge of the pad). This dependency is probably due to the form of the field line. As a results, some theoretical models are currently under development to confirm this tendency [Molle, 2022]. We also noticed that the initial charge is divided by 4 after $\sim$50 µm from the edge of the pixel and by 10 after $\sim$200 µm.

3.4.2.2 Mapping at the micrometer scale

The charge mappings achieved with the second method were performed on a small area close to the edge on the smallest metallic pad ($0.5\times0.5\,\mathrm{mm}^2$) indicated by a green square on the Figure 3.26 (left). A linear mapping, from the metal to the diamond surface, was performed for electrons and holes. It is indicated by the red horizontal line in Figure 3.26 (right). On this image, the border of the metallic pad is indicated by a blue line. The origin of the position of the mapping is taken at the intersection of the two lines.

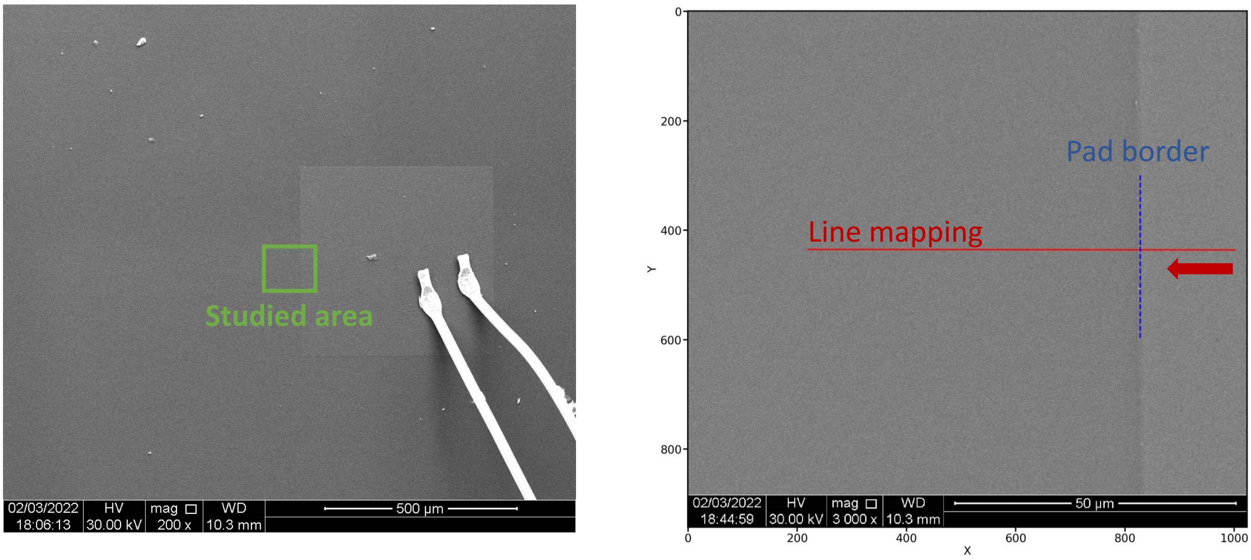

Figure 3.26: On the left, a SEM image taken with a small magnification shows the smallest metallic pad ($0.5\times0.5\,\mathrm{mm}^2$). A green rectangle shows the area where the measurements were performed. The latter corresponds to the SEM image on the right. On this image, a red line on which about 600 to 800 measurements were taken is plotted. The mapping is done from right to left and starts on the metallic pad. The pad limit is indicated by a blue line.

In this study, the 0.5×0.5 mm^2 pad was biased and the others were grounded. Considering that the small pad is at least 0.9 mm away from all the pad of the side A and that the diamond is 0.15 mm thick, the charge transit occurred between the two sides of the diamond sample. As a result, an electric field of 5.3 kV/cm is imposed between the area under the small pad and the pad of the B side. As the mapping on the diamond surface is only 60 µm, it is assumed that the transit of the carrier will only occur between the small pad and the pad on the B side.

For the two mappings, 1000 traces were acquired at each position and the traces were directly averaged by the DSO LeCroy HDO9404. The distance between two successive positions was about 100 nm. However, considering that the lateral diffusion of the secondary electrons is approximately 4 µm of diameter, the spatial resolution is lower.

In Figure 3.27 (a) and (b), it can be noticed that when the beam is moving away from the edge of the pad, the waveform are more and more deformed and the amplitude is decreasings. At about 60 µm (see Figure 3.27 (c)), a residual signal is still existing leading to a charge collected slightly superior to the noise level. It can also be noticed that the charge collected by electron and hole transits follows a similar behaviour. After 50 µm, the charge is divided by a factor 4 which is in agreement with the measurements using the other mapping procedure. For the position close to the edge of the pixel, where the waveform of the traces are not too deformed, the drift time was estimated using GGD fits (see Equation 2.1). Here, the idea is not to extract quantitative values of the drift time, but to study its position dependence for electrons and holes. In Figure 3.27 (d), when the beam is moving away from the pad, the electron and hole drift time increases respectively by a factor 1.2 and 1.6. It was expected considering that the charge carrier must drift a longer distance to reach the pad on the B side and that the norm of the apparent electric field is weaker (see Figure 3.25).

3.4.3 Discussion and comments

Two procedures were developed to map the charge properties of diamond samples: one to study large area and the other to study local phenomena at the micrometer scale. The first mapping procedures had proven to be efficient to study charge collection homogeneity on a 150 µm thick diamond sample. The charge was found relatively homogeneous on all the metallization surfaces. The two procedures were also used to study the charge collection evolution when the beam is moving away from a pixel and found similar results: the charge collected is divided by 4 after about 50 µm. This observation promises that the ToF-eBIC technique can be very useful to design and study pad and stripped detectors, for instance to optimize the inter-pad or inter-strip distance or to study the cross talk phenomenon. The second procedure is also an opportunity to study micrometric structures such as the grain boundaries in polycristaline diamond or eventually irradiation damages.

However, these techniques are time consuming. Unfortunately, in the short term it appears difficult to improve the acquisition duration. A way to do it would be, for the first procedure, to improve the cycling procedure based on the work done on the ToF-eBIC drift velocity studies, and for the second procedure, to increase the maximum achievable bias. By doing so, it might be possible, in a close future, to do local (down to the micrometer scale) drift velocity studies and to check the homogeneity of the carrier low field mobility and the saturation drift velocity at different temperatures.

3.5 Conclusion

During my work, I participated to make a setup which can achieve measurements using the ToF-eBIC technique. This technique consists in using electron pulses generated by a SEM to induce a transient current in diamond samples. The advantages of this technique are numerous, the setup offers an accurate control of the:

- incident energy deposited (energy - 0.2 to 30 keV - and number of primary electrons - up to 40 primary electrons per nanosecond);

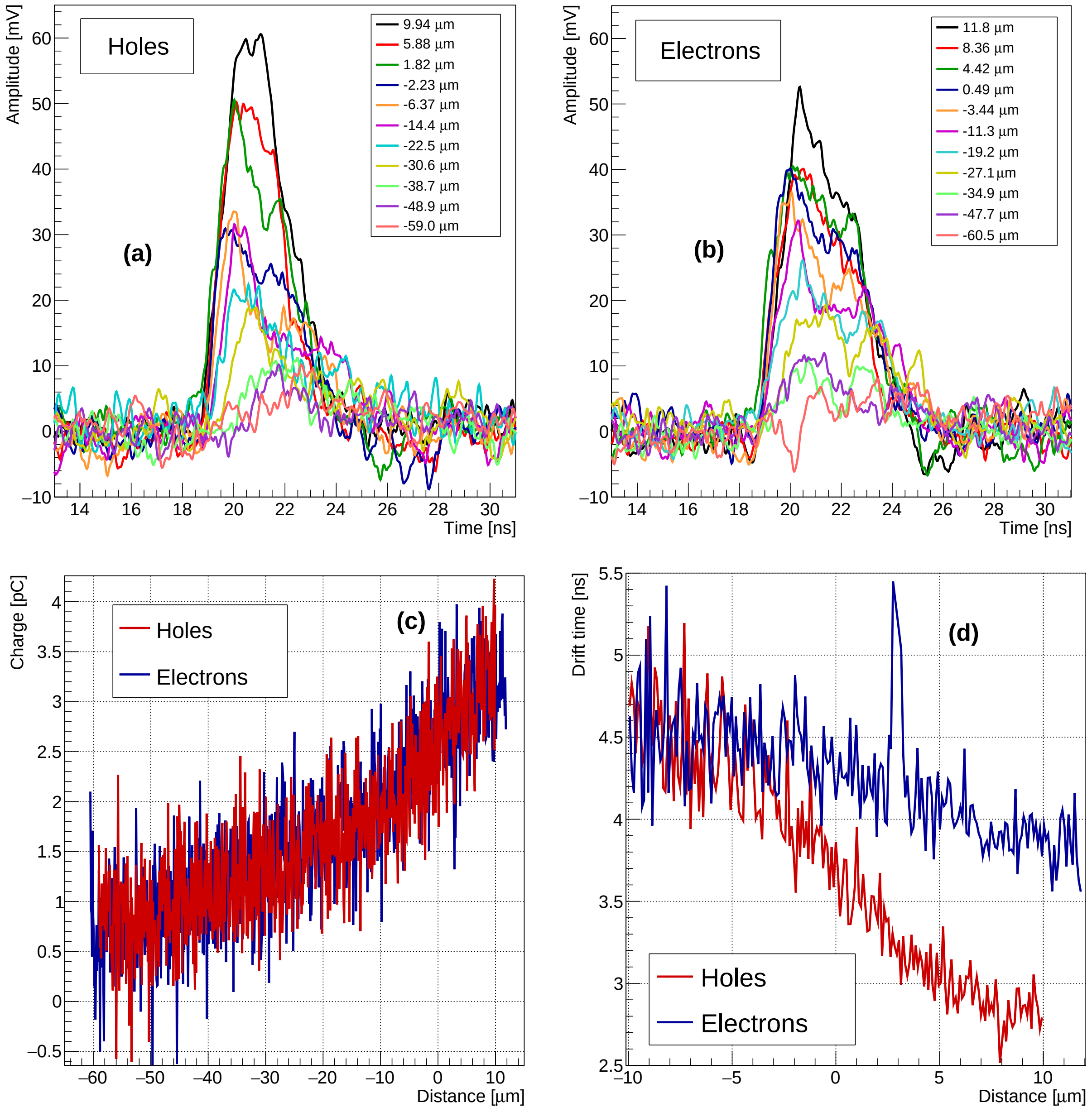

Figure 3.27: Average traces (1000 traces were acquired for each position) obtained at different positions for holes (a) and electrons (b) for an electric field of 5.3 kV/cm. (c): charge after amplification for holes and electrons depending of the position (the position are not exactly the same for holes and electrons). (d): drift time versus the position close to the pixel border.

- area studied (very precise beam positioning at nanometer scale);
- excitation density (by defocusing the electron beam);
- temperature (300 to 13 K with a precision below 5 %).

To carry out drift velocity measurements, it was necessary to optimize the parameters of the SEM. Bunches of about 20 to 40 electrons of 30 keV were used to maximize the SNR. An advance cycling procedure consisting of inverting regularly the bias was implemented to avoid polarization effects. To perform this cycling procedure, the HV power supply and the oscilloscope were interfaced with LabVIEW. The slow control was also managing the acquisitions and the saving of the averaged traces.

Polarization effects were studied and delimited in space (∼100 µm area of influence). During the drift velocity measurements, the goal was to study the global properties of the charge carriers. Then, to limit the polarization effects, the scan mode of the SEM was used. In this mode the beam is scanning a (1024×884 pixels) surface. The polarization effects on the waveform decrease with the size of the scan area. Thus, it was decided to work on the larger surface achievable. By scanning the entire surface of a sample (4.6×4.6 mm^2), it is then possible to space each impact by at least 200 µm. However, due to screening effects, it was not possible to acquire signal at very low electric fields (lower than 183 V/cm). This was an issue to study the drift velocity at low electric field and so to evaluate the low field mobility, in particular for low temperature. The solution was to work out of focus to decrease the excitation density and thus the density of charge carriers and the screening effects. Moreover, for a low density of electron-hole pairs, the free charge carriers are separated by drift before the exciton formation. As a result, more charges were collected at low temperatures. The drift velocity at RT and the transport parameters were compared to the one extracted using the alpha setup. The low field mobility and the drift velocity for electrons and holes were in a good agreement, confirming the good functioning of the setup.

A specific sample holder was designed to study the transport properties of diamond at low temperatures. Our goal was to study the low field mobility of electrons and holes down to cryogenic temperatures. In particular, the holes low field have never been investigated using the TCT at temperatures lower than 80 K with extremely pure and high quality samples. The previous attempts were limited by neutral impurities [Jansen, 2013b] or highlighted the necessity to reach very low electric fields to compute it [Majdi, 2013]. In this study measurements down to 13 K were achieved. During these experiments, valley-polarized electrons were observed for the first time since the publication of Isberg *et al.* in 2013 [Isberg, 2013]. To extract the hole low field mobility, the drift velocity was investigated down to 9 V/cm. Then, a linear fit was performed to compute the low field mobility for holes and electrons. Our data was then compared to the low field mobility published by Konishi *et al.* [Konishi, 2020b]: the hole low field mobility is in a good agreement down to 70 K. At lower temperature, the hole low field mobility was compared to the theoretical model developed by Pernot *et al.* [Pernot, 2010]. Unfortunately, this model only considered elastic deformation potential which is a valid hypothesis at high temperature but which is started to be inaccurate at temperature lower than 30 K where the energy loss is not negligible anymore. As a result, our data are in a good agreement down to about 30 K. For the lowest temperatures a behavior similar to the one observed by [Majdi, 2016, Konishi, 2022] is observed highlighting the necessity to implement a model considering the inelastic scattering.

At 13 K, a hole low-field mobility of $(1.03 \pm 0.04) \times 10^6\,\mathrm{cm}^2/(\mathrm{V{\cdot}s})$ was measured. This value is the highest hole low-field mobility measured in a bulk semiconductor and is approaching the low-field mobility measured in 2D gas systems [Chung, 2022] and in graphene [Banszerus, 2016]. The extracted electron low field mobility is a little bit smaller than the data published by Konishi *et al.* [Konishi, 2020b] probably because the diamond samples may have different intrinsic properties. A way to check this hypothesis would be to test the sample used by Isberg *et al.* with our ToF-eBIC technique.

During these experiments, the charge collected by hole and electron transits was also studied versus the temperature. A drop of the charge collection is observed between 80 and 120 K. This observation is in agreement with previous experiments done with light ions [Jansen, 2013b, Cosic, 2022].

The ToF-eBIC technique was also used to map the transport and charge properties of diamond samples. To do so, two dedicated mapping procedures were developed: one to map large surfaces and one to map local effects (micrometric scale). These two procedures were used to map the charge properties of a pad detector. A good homogeneity was observed on the surface of the pads (more or less 3 % RMS) using the first mapping procedure. The decrease of the charge collected when the beam is moving away from the pixel edges was also studied with the two techniques. It was observed with both procedures that at a distance of 50 µm from the edge of the metallization the collected charge is divided by a factor of 4. These mappings are complementary to those performed at the ESRF [Bergonzo, 2003, Gallin-Martel, 2021a] with X-rays. Indeed, in the case of X-rays, the particles are crossing the sample whereas the electrons are stopping in the first micrometer below the surface, allowing a study depending of the charge carrier (electrons or holes).

In the future, it would be interesting to develop models to describe the polarized electron currents to better asses the electron drift velocity at low temperature and low electric fields. Some experiments could also been conducted to better understand polarization effects or to improve the procedure used in this work. More rapid mapping of charge collection would allow systematic characterization of samples. In particular, grain boundaries in polycrystalline diamond or irradiation damaged in monocrystalline diamonds could be studied. Finally, the transport properties of diamond sample could be map at different temperatures.

4

Two innovative diamond devices for short range particle detection: a monolithic ΔE-E telescope and a *pn* junction

Contents

This chapter presents a technique commonly used for short-range particle identification in nuclear physics: the ΔE-E (telescope) technique. The interest in developing a monolithic diamond telescope to be used in a highly radiative environment is undeniable. It is part of the objectives that we have set ourselves in the framework of the DIATEL project in which this research work is included. We have designed a first prototype. The steps of its fabrication - growth of the different layers, etching and metallization - will be explained in detail as well as its electrical characterization and its packaging. I will also comment on the study of its performance in eBIC, ToF-eBIC and alpha spectroscopy experiments. Finally, an alternative solution to the ΔE-E technique, based on a *pn* diamond diode fabricated by the National Institute for Materials Science (NIMS) of Tsukuba (Japan) will be discussed.

4.1 Principle of operation and review of diamond-based compact ΔE-E telescopes

4.1.1 Principle of operation of the ΔE-E telescopes

The ΔE-E telescopes are widely used in nuclear physics to perform particle identification. Indeed, they are the main instrument for detecting fragments in the study of nuclear reaction mechanisms. When they are in coincidence with other detectors, they allow to measure the time of flight (and thus the velocity) or the lifetime of unstable nuclei.

These telescopes are composed of two stages: the ΔE stage in which the particles pass through and the E stage in which the particles stop and deposit their residual energy. The average energy loss of a non relativistic charged particle in the ΔE stage can be accurately evaluated by the Bethe-Bloch (see Subsection 1.3.1.1) formula and is proportional to Q^2/v^2[1] [Badalà, 2022]. The total energy deposited in the two layers is equal to the kinetic energy of the particle, and so proportional to $A \cdot v^2$. Consequently, the comparison of the ΔE and E energy deposits permits the identification of the particle. The two stages can use different types of detector technologies (gaseous, scintillator [Gunzert-Marx, 2008] or semiconductor) or a mix of different technologies [Carboni, 2012, Ciampi, 2019]. Recently, there has been a real challenge to have compact detectors which exhibit a very good energy resolution. As a result, significant research are currently done on semiconductor ΔE-E telescopes [Goulding, 1964, Seamster, 1977, Kim, 1984, Kordyasz, 2004, Matsumoto, 2005, Topkar, 2011, Singh, 2015, Carboni, 2012, Ciampi, 2019, Cesaroni, 2019, Verona, 2022].

As discussed by Ciampi *et al.*, the *"new experiments are being planned exploiting high beam intensities in order to study very rare events or measure very low cross sections"*. Therefore, *"they all require radiation-hard detectors with excellent performance in terms of stability, energy resolution, timing and insensitivity to visible light"* [Ciampi, 2019]. Then, (ultra) wide-bandgap semiconductors such as SiC, and in particular diamond, exhibit very interesting properties (discussed in Chapter 1) in order to meet these requirements.

Recently, some groups, such as the FAZIA collaboration, have also developed an alternative way to perform particle identification. In particular, the pulse shape analysis technique applied in silicon and silicon-carbide detectors gave very promising results [Carboni, 2012, Ciampi, 2019]. This technique is exploiting the correlation between two parameters related to the shape of the

---

[1] Q, A and v are the charge, mass and velocity of the incident particle, respectively.

signal (for instance charge collected and maximum transient current [Carboni, 2012]) induced in one detector. The main advantage of this technique is to reduce the detection thresholds with respect to the ΔE-E telescope technique [Badalà, 2022]. Thanks to this technique, the FAZIA collaboration, was able to identify the incident particle charges on the whole charge range available in their experiment [Carboni, 2012].

However, it seems difficult to use this technique for some nuclear physics experiments such as the identification of heavy Fission Fragments (FF). These experiments are of primary interest to better understand the fission reaction. Unfortunately, for these kinds of particles, an incomplete charge collection was highlighted: the so-called pulse height defect [Singh, 2015, Gallin-Martel, 2021b]. This effect is mainly caused by the high ionization density of the FF which induces a zone around the ion track, with high density positive ions and electrons, the displacement of which screens the applied electric field and leads to numerous in situ recombinations. Thus, a careful procedure should be conducted to calibrate the spectrum obtained [Singh, 2015]. This effect probably has a significant impact on the rise time or the maximum current reached which could complicate the PSA. As a result, it seems more convenient to use a ΔE-E telescope to carry out these measurements. In particular, such a telescope could be used at the Institut Laue Langevin (ILL) facility in Grenoble to perform FF identifications [Singh, 2015, Gallin-Martel, 2021b].

4.1.2 Review of diamond-based compact solutions

In order to achieve the most compact detector, monolithic ΔE-E telescopes are of prime interest. Such devices have already been reported and tested [Kordyasz, 2004, Topkar, 2011, Singh, 2015, Cesaroni, 2019, Verona, 2022]. Especially, a diamond monolithic telescope was made [Cesaroni, 2019] and used to identify He, Li, C and O ions at several low energies [Verona, 2022]. In Figure 4.1 (left) the architecture of such a diamond ΔE-E telescope is exhibited. According to the authors, the ΔE stage is about 2.5 µm thick and the diamond electrode (highly boron doped layer), used to bias the two stages of the telescope, is 1.8 µm thick. The latter is relatively thick considering that it is a dead area of detection, and thus, could limit the performance of the device. However, the accurate ion identification of this detector should be highlighted. In Figure 4.1 (right), the parabolas corresponding to each ion (He, Li, C and O) can be clearly separated, and a good agreement with the Monte Carlo simulations can be observed. Their measurements showed also a good homogeneity of the charge collection on the whole sensitive area of the ΔE stage (about 7 %) and a good linearity with the linear energy transfer of the incident ions. Despite these interesting results, a significant cross-talk effect in the ΔE stage of the telescope was also observed. Even if this effect was successfully corrected by fitting their data with an exponential function [Verona, 2022], the causes of this phenomenon are still under investigation. Finally, the spectrum acquired in coincidence between both stages of the detectors are in relatively good agreement with their simulations.

4.1.3 Scientific and technological objectives of the present project

Scientifc objectives: the ΔE-E telescope is to be used, at first, to study light ions, such as alpha particles emitted during the nuclear decay of heavy radioactive elements (^{241}Am). However, this ΔE-E telescope should be considered as a demonstrator for future applications

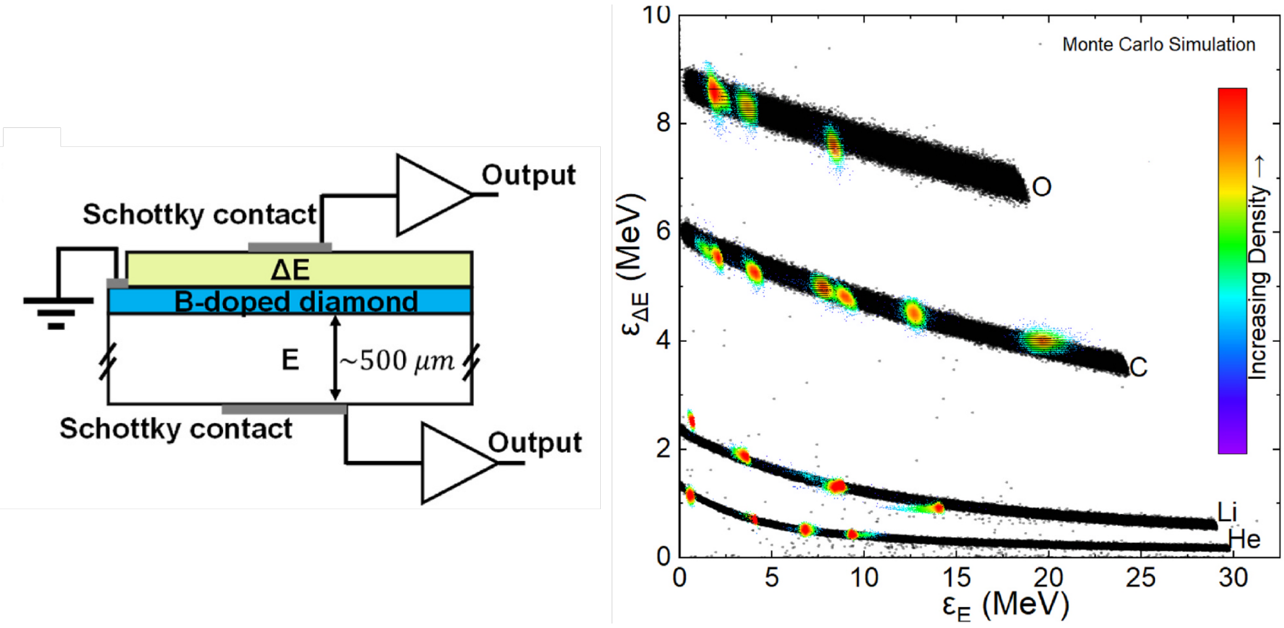

Figure 4.1: Left: Structure of the ΔE-E tested in [Verona, 2022]. Right: ΔE-E histogram obtained by performing IBIC measurements with different ions at the Ruder Boskovic Institute (RBI) at Zagreb [Verona, 2022]. The black dots correspond to the results of Monte Carlo simulations.

in FF identification at the ILL facility. Therefore, it must be made and characterized on several test benches.

Technical objectives: considering the principle of operation of the ΔE-E, the design of a compact monolithic detector that I will describe in this chapter is obviously close to the architecture shown on Figure 4.1 from [Verona, 2022]. Moreover, the project DIATEL funded by the University Grenoble Alpes (UGA), in which my PhD is involved, was submitted before the first publications of the authors of [Cesaroni, 2019]. Thus, my work mainly consisted in proposing improvements to the concept. In particular, I pointed out two key aspects on which we focused: the thickness of the intermediate electrode and the quality of the epitaxial growths. We aimed to improve the performance in terms of energy resolution, homogeneity and identification capability. A thinner highly boron-doped diamond middle electrode (less than 1 μm) will reduce the energy losses in this dead layer. Furthermore, a high crystalline quality of the ΔE layer will permit to limit the number of dislocations, impurities concentration and will improve the charge collection efficiency.

The next three sections will discuss: 1) design considerations; 2) fabrication steps; and 3) experiments performed on a first ΔE-E sample.

4.2 Specifications and designing phases

4.2.1 Key aspects of the design

In order to design a detector, the objectives and the project framework must be clearly defined. The main objectives of the project were to develop a detector which can be used to study the energy deposited by light ions generated by nuclear decays (alpha particles) or accelerated light ion beams. In particular, this detector should allow to measure the energy deposited by an incident particle and identify its atomic number.

The structure of the monolithic diamond ΔE-E telescope is described in the Figure 4.2. This detector is composed of three layers. The first and third diamond layers are directly used to measure the energy deposited by the incident particle, while the middle layer is used to bias the two other layers.

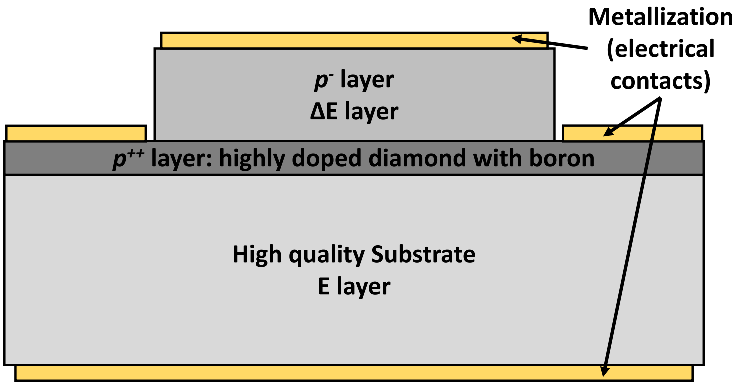

Figure 4.2: Structure of the ΔE-E sensor.

The challenge of this project lies in the design of a diamond electrode made of a highly boron-doped diamond layer. Indeed, the thickness of the different layers need to be adapted to the incident particle energy deposition. Therefore, we will first examine the requirements of each layer (the substrate, the p^{++} layer and the p^- layer) in order to establish the specifications of a ΔE-E telescope adapted to our needs. Then, some SRIM simulations achieved to design properly the p^- layer of the detector will be explained and discussed. As a result, a ΔE-E design will be presented. The fabrication steps of the detector (diamond layer epitaxial growth, etching, metallization and encapsulation) will be described in the next section and, the first ΔE-E sample will be then reported.

4.2.1.1 High quality and thick diamond substrate

It is crucial to choose carefully the diamond substrate since the quality of the epitaxially grown layer on it is the key factor for charge collection efficiency. Indeed, it has been shown [Tallaire, 2008] that the crystalline quality of a grown layer, in terms of dislocations, is directly dependent on the quality of the substrate. Furthermore, a small amount of impurities is required in order to reach a CCE close to 100 % and avoid the polarization effects.

In order to meet these requirements, a 550 µm thick Element 6 (electronic grade) diamond, produced by the CVD technique, was chosen as a substrate. Indeed, a 550 µm thick diamond layer allows to stop 12 MeV protons, and thus to study light ions in the targeted energy range.

Moreover, the low level of impurities ($[N] < 9 \times 10^{14}\,\mathrm{cm}^{-3}$ and $[B] < 2 \times 10^{14}\,\mathrm{cm}^{-3}$) of the Element 6 diamonds is very interesting in terms of charge collection properties.

4.2.1.2 The sandwished p^{++} layer

The p^{++} layer is used as an intermediate electrode connected to the ground and used to bias the p^- layer and the substrate thanks to complementary top and bottom metallic electrode, respectively. Therefore, the layer needs to be highly doped to be conductive. As seen in Subsection 1.2.3, for a diamond layer to be conductive, a doping of at least $10^{20}\,\mathrm{cm}^{-3}$ is needed.

This layer is a dead volume for the detection. On this point of view, it should be as thin as possible. Moreover, the growth of this layer can induce the appearance of dislocations whose density increases with the thickness of the layer, which is even more critical [Letellier, 2019]. Nevertheless, realizing a too thin doped layer can complicate the next steps of the fabrication. Indeed, in some areas, the p^- layer will be etched entirely to realize a contact on the p^{++} layer. The p^- layer is several micrometers thick, thus it may be difficult to etch it completely and stop the etching within a too thin p^{++} layer. The error bar on the etching rate could lead to a too thick etching depth down to the substrate. Therefore, a p^{++} layer with a thickness of at least 200 nm was targeted.

4.2.1.3 The top p^- layer

The thickness of the p^- layer defines, for each ion, the energy range that can be studied with a ΔE-E detector. Indeed, the energy deposited by an incident particle needs to be shared between the two detection layers (the p^- and the substrate) in a way that it is possible to measure the charge deposited precisely enough in both. Then, the p^- layer has to be sized to handle a 1 MeV energy deposit ($E_{dep}^{p^-}$) arising from a 5.5 MeV (E_{init}) alpha particles (^{241}Am) impinging the detector. Moreover, the p^- and p^{++} layers must be thin enough so that the energy that the particle will deposit in the substrate (E_{dep}^{Sub}) is greater than 50 % of its initial energy. These two energy values were chosen accordingly to previous experimental results (ToF-eBIC measurements: see Section 3.2, alpha spectroscopy: see Subsubsection 4.5.3). As a last requirement, to achieve measurements with a CCE close to 100 %, the p^- layer must not be intentionally doped (to avoid recombination centers).

4.2.1.4 Specification list and technical solutions

The various requirements discussed for each layer are summarized in the Table 4.1.

To meet these specifications, a $4.5 \times 4.5 \times 0.55\,\mathrm{mm}^3$ electronic grade Element 6 diamond was chosen for the substrate. Then, DIAMFAB[1], a startup from Institut Néel, CNRS, was in charge of the growth of the p^- and p^{++} layers. The p^{++} layer is relatively thin (between 0.5 and 1 µm) and highly boron-doped (more than $10^{20}\,\mathrm{cm}^{-3}$). On the contrary, the p^- layer is not intentionally doped and its thickness implies to conduct SRIM simulations to satisfy the detector specification list.

---

[1] DIAMFAB website: `https://DIAMFAB.com/fr/`

Table 4.1: Specifications for the monolithic ΔE-E telescope.

Layer	**Param.**	**Criteria**	**Requirements**	**Growth method**
p^- layer	Thickness	$E_{dep}^{p^-}$ E_{dep}^{Sub} Leakage current	> 1 MeV $> E_{init}/2$ < 1 nA	MPCVD Microwave Plasma enhanced Chemical Vapor Deposition
	Doping	Non intentionally doped	$[\mathrm{B}] < 5 \times 10^{15}\,\mathrm{cm}^{-3}$	
p^{++} layer	Thickness	Dead area of detection Fabrication requirements	$< 1\,\mu\mathrm{m}$ $> 0.2\,\mu\mathrm{m}$	
	Doping	Conductive layer	$[\mathrm{B}] > 10^{20}\ \mathrm{cm}^{-3}$	
Substrate	Thickness	Stop the incident particles Commercially available	$550\,\mu\mathrm{m}$	single crystal MPCVD
	Doping	Intrinsic	$[\mathrm{N}] < 9 \times 10^{14}\,\mathrm{cm}^{-3}$ $[\mathrm{B}] < 2 \times 10^{14}\,\mathrm{cm}^{-3}$	

4.2.2 SRIM simulations

4.2.2.1 Design and methods

The simulations consisted in studying the energy loss in the different layers of the sensor for various p^- layer thicknesses and for several ion species and energies. To perform them, it was chosen to use the python package pysrim which allows the automation of the SRIM calculations.

The first step of the computing consists of reproducing the architecture of the detector. The substrate and the p^- layer were considered to be carbon layers with a density of $3.52\,\mathrm{g/cm^3}$ (diamond density), an average displacement energy of 43 eV [Koike, 1992], a lattice binding energy of 7.1 eV, and a surface binding energy of 7.4 eV [Yin, 1981]. In the following, a layer with these characteristics will be referred as a "diamond layer." Regarding the p^{++} layer, the simulations proved that, as expected, the doping ($< 1\,\%$) does not significantly affect the energy deposit. As a result, the p^{++} layer was simulated as a simple diamond layer.

In the first simulation, the thickness of the p^{++} layer was arbitrarily set to 500 nm. After the growth of the p^{++} layer by DIAMFAB, the measured thickness of this layer (845 nm) was used to constrain the following simulations.

Various isotopes of hydrogen ($^1_1$H, $^2_1$D and $^3_1$T) and helium were studied ($^3_2$He and $^4_2$He) for energies ranging from 0.5 to 10 MeV and for p^- layer thicknesses ranging from 1 to 8 µm. The values used in the simulations are summarized in Table 4.2.

Table 4.2: p^- thicknesses and initial ion energies simulated used in the SRIM simulations.

	p^- Thicknesses [µm]		
	Infimum	Supremum	Step
Range 1	1	2	0.5
Range 2	2.5	6.5	0.25
Range 3	7	8	0.5

	Initial ion energies [MeV]		
	Infimum	Supremum	Step
Range A	0.5	1	0.5
Range B	1.5	7.5	0.25
Range C	8	10	0.5

For each isotope, initial ion energy and p^- layer thickness, two simulations were conducted.

- A first simulation including only the p^- layer was performed to determine the corresponding energy loss.
- A second simulation including, that time, the p^- and the p^{++} layer, was performed to determine the energy loss in the p^{++} layer and in the substrate.

In these simulations, the energy of the ions which pass through the layer(s) is averaged using the information extracted from the "TRANSMIT.txt" file. The uncertainty is estimated to be the standard deviation (rms).

4.2.2.2 Results

In Figure 4.3 (left), the average energy loss in the p^- layer was estimated for various isotopes at different energies. All parabolic curves are well separated considering the uncertainties. Therefore, the ion which interacts in the p^- layer can be easily identified. The various noise contributions (electronic noise in particular) were not taken into account.

The results obtained with ${}^4_2$He ions are shown for different initial ion energies and p^- layer thicknesses in Figure 4.3 (right). In this graph different parabola branches can be observed for each different thickness. As expected, the energy deposit increases with the thickness of the p^- layer.

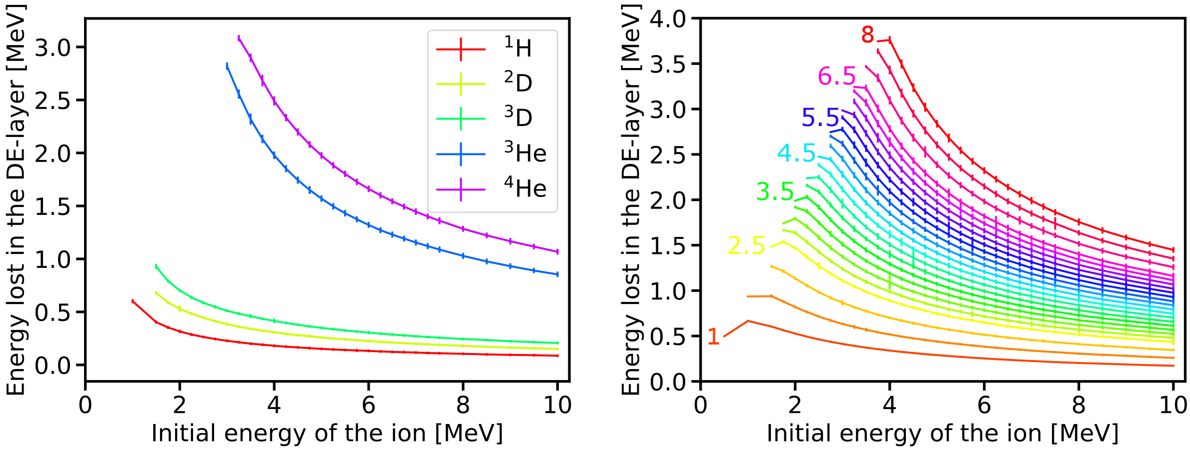

Figure 4.3: Left: energy loss of ${}^1_1$H, ${}^2_1$D, ${}^3_1$T, ${}^3_2$He and ${}^4_2$He particles in a 6 µm p^- layer depending on the initial energy of the ions (SRIM simulations). Right: energy loss of ${}^4_2$He particles for different p^- thicknesses depending on the initial energy of the ion (SRIM simulations). The thicknesses indicated next to the data are in micrometer.

As discussed in the first part of this section, the first version of the ΔE-E telescope was designed to satisfy the detection of the alpha particles emitted by a ^{241}Am radioactive source. To meet the specifications summarized in Table 4.1, the p^- layer should be thicker than 3.5 µm. Considering a p^{++} layer of 845 nm, the p^- layer must be thinner than 7.5 µm to fulfill the condition $E_{dep}^{Sub} > E_{init}/2$ in Table 4.1. Therefore, a thickness of 5 µm has been targeted for the p^- layer.

4.2.3 Specifications for the fabrication of the ΔE-E detector

The technical scheme of the monolithic diamond ΔE-E telescope demonstrator is presented in Figure 4.4.

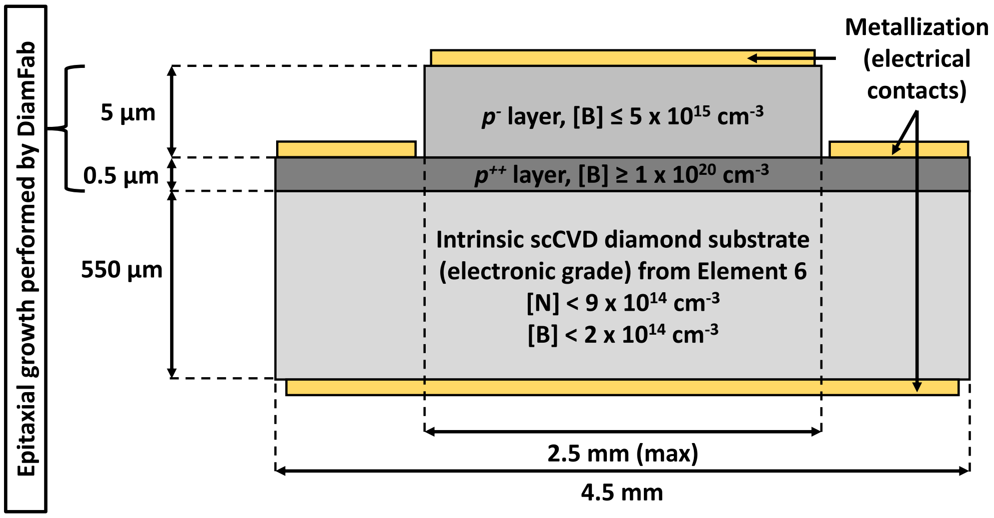

Figure 4.4: Technical details of the monolithic diamond ΔE-E telescope for DIAMFAB fabrication.

This design is well suited to study light ions (based on 5.5 MeV alpha particles). It exhibits the following characteristics.

- The p^- layer is non-intentionally doped, and its thickness should be between 3.5 and 7.5 µm. A targeted doping level of $[B] < 5 \times 10^{15}\,\mathrm{cm}^{-3}$ and a thickness of 5 µm was addressed to DIAMFAB.

- The p^{++} layer is a highly boron doped layer ($[B] \geq 10^{20}\,\mathrm{cm}^{-3}$), and its thickness should range between 0.2 and 1 µm. A targeted thickness of 0.5 µm and boron doping of $10^{20}\,\mathrm{cm}^{-3}$ were addressed to DIAMFAB.

- The substrate is a single crystal detector grade Element 6 diamond. This diamond is 550 µm thick, and the datasheet of the provider specify that: $[N] < 9 \times 10^{14}\,\mathrm{cm}^{-3}$ $[B] < 2 \times 10^{14}\,\mathrm{cm}^{-3}$. Such a diamond sample meets the specification list of the project and was supplied to DIAMFAB.

4.3 Fabrication and electrical characterization

4.3.1 Growth of the p^- and p^{++} layer by DIAMFAB

4.3.1.1 Growth technique

The epitaxial growth of the p^{++} and p^- layers were performed by DIAMFAB using the Microwaves Plasma enhanced Chemical Vapor Deposition (MPCVD) technique (see Subsection 1.2.2). The growth conditions were based on the work achieved in [Bousquet, 2015].

To measure the thickness of both layers and the doping level of the p^{++} layer, ellipsometry measurements were carried out. In this technique the polarization between the incident beam - with a linear polarization - and the reflective beam from the sample - with a ellipsoid polarization - are measured, compared and fitted [Bousquet, 2015, Letellier, 2019]. Therefore, the thickness of the grown layers can be given with a resolution of about 5 nm.

As a result, a thickness of (845 ± 5) nm and a doping level of $(9 \pm 2) \times 10^{20}\,\mathrm{cm}^{-3}$ were measured for the p^{++} layer. Regarding the p^- layer, a thickness of (6160 ± 5) nm was estimated. The Figure 4.5 summarizes the sample architecture.

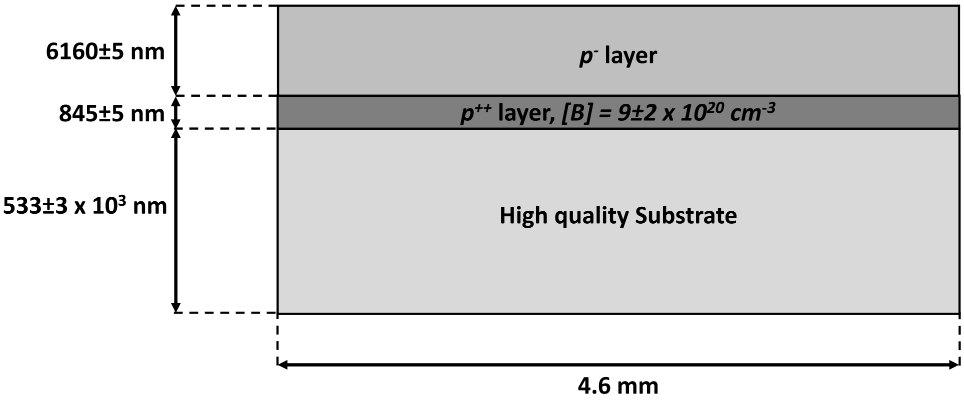

Figure 4.5: Scheme of the ΔE-E architecture after the growths.

4.3.1.2 Growth defects

On the Figure 4.6 (left), an image of the p^- upper surface observed with an optical microscope is shown. On this image, some defects which usually appear after the HPHT [Kanda, 1996] and CVD [Wang, 2000, Tallaire, 2008, Khomich, 2019] diamond growths can be identified: hillocks with flat top, pyramidal hillocks and unepitaxial crystals. According to Tallaire *et al*, the first two faults originate from extended crystallographic defects and stacking defaults; here dislocations in the p^{++} layer; whereas the other do not have any apparent relation with the crystalline quality [Tallaire, 2008]. Therefore, the density of dislocations in the <100> crystalline direction was estimated by DIAMFAB to be $3 \times 10^3\,\mathrm{cm}^{-2}$.

An optical profilometry was performed by DIAMFAB in order to evaluate the roughness of the sample and the size of the hillocks. Peak to peak, the roughness was estimated to be 1.4 µm. Both the hillocks and the unepitaxial crystals are about 2 µm height.

These defaults are responsible of dielectric breakdown effects and current leakage [Khomich, 2019]. Their relatively important thickness could also deteriorate the charge collection performance of the ΔE-E sample. Indeed, by passing through the hillocks, the incident particles

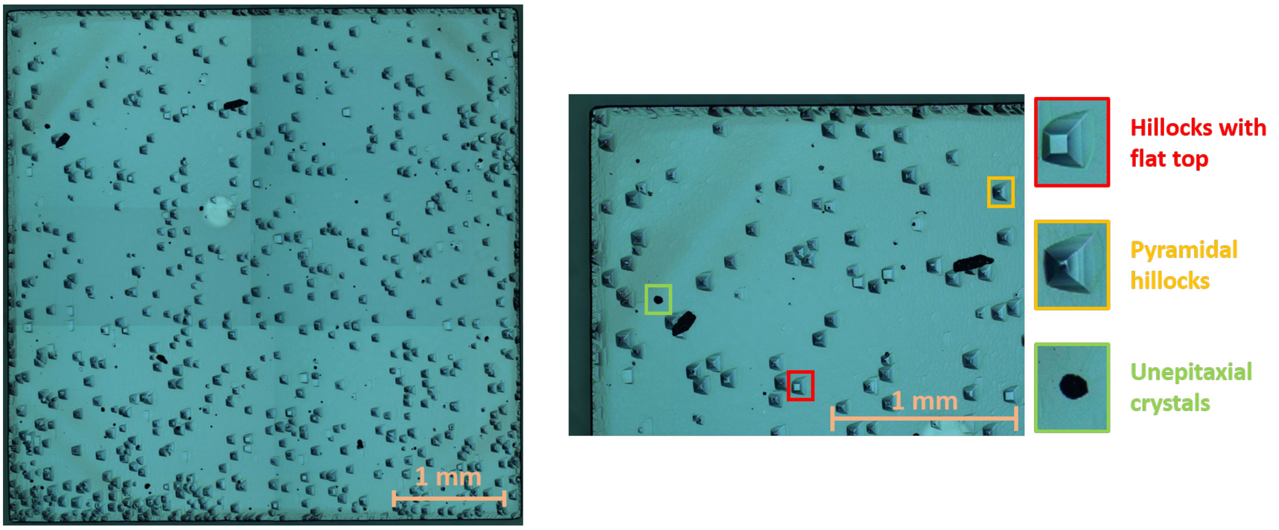

Figure 4.6: Left: images of the ΔE-E sample after the two epitaxial growths. Right: zoom on the upper left part of the sample and identification of three common growth defects: hillocks with flat top, pyramidal hillocks and unepitaxial crystals.

will loose more energy (thicker diamond layer) in the p^- layer. Consequently, a significant dispersion can be expected on the energy spectra of this ΔE-E sample.

A concentration of defects (hillocks in particular) is observed in the corners of the sample. X-ray topography performed at beamline BM05 at ESRF showed that similar diamond substrates had different growth orientations in the corners (<111> in the corners and <100> in the center). For the next prototypes, we plan to etch the substrate in order to remove these areas before the growth of the epitaxial layers. Furthermore, the substrate we used is a commercial one with polished faces. The surface micro-defects induced by the polishing may also contribute to growth defects observed in the epitaxial layers. For a next prototype, we may have to consider this issue to improve the crystalline quality of the device.

4.3.2 Manufacturing in clean room and detector packaging

4.3.2.1 Etching

To bias the two stages of the ΔE-E telescope (p^- layer and the substrate), the electric potential of the p^{++} layer must be controlled. This layer is buried under the p^- layer. Furthermore, it was proven that the p^- layer suffers from lateral growth. Consequently, the p^{++} cannot be electrically connected on the detector lateral side. As a result, an etching of the p^- layer was achieved. An alternative to the etching would have been to perform a selective growth. In this technique, a mask is used to achieve the growth only in the uncovered area. Nevertheless, as explained by Letellier [Letellier, 2019], it is not possible to perform a selective growth up to 6 µm using a metallic mask (a too thick metal layer, few microns, would be necessary and it could contaminate the growth chamber) and, the growth performed using a hard mask would lead to a low crystalline quality p^- upper surface.

As described in Figure 4.7, the etching process is divided in several steps. I realized all these stages of fabrication of the future detector at the platform NanoFab of the Institut Néel.

Lithography: at the beginning a UV sensitive resist is coated on one side of the diamond. To have a homogeneous coating (no border effect[1]), a specific sample holder was developed [Letellier, 2019] and a spin coater was used. Then, the resist was locally exposed to UV light and developed in order to be removed later creating a mask through which the metal will be deposited. The positive resist S1818 was chosen because it is adapted to the thickness of the metallic mask in the *"Evaporation and lift-off"* step (resist at least 1 µm thick). Furthermore, this type of resist is more suitable to achieve the geometry of the desired etching (to be developed only in the center of the sample). The exposure was performed using laser lithography.

Evaporation and lift-off: the metallic mask consists in covering with a Ti/Ni layer the surface which will not be etched. The thin titanium layer (about 10 nm) ensured the good adhesion of the mask while the thick nickel one (between 300-350 nm) would protect the p^- area during the *Etching* phase. The remaining resist is finally dissolved in acetone.

Etching: it consisted in using the Reactive Ion Etching (RIE) device. It was achieved using a CF_4-O_2 mixture (7 sccm of CF_4 and 40 sccm of O_2). This "recipe" is based on the know-how of SC2G team (Institut Néel), DIAMFAB and NanoFab teams. The etching rate was about 80 nm/min. At the end of the process, the metallic mask was removed using a hot Aqua Regia mixture (3 HNO_3 : 1 HCl ratio).

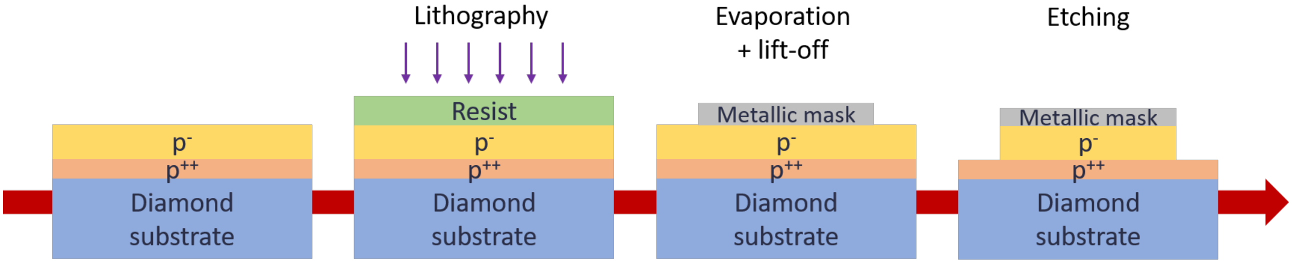

Figure 4.7: Main steps of the etching process done at NanoFab.

Due to technical issues, the etching phase was performed in two steps (Figure 4.8). The first step consisted in etching 3 µm of the p^- layer, while in the second step 3.5 µm were etched in order to finally reach the p^{++} layer. A 100 µm lateral margin between the two etchings was implemented in order to clearly distinguish them. On the right side of the sample, a 400 µm margin was taken to study later on the ΔE-E sensor not only with the alpha particles (^{241}Am) but using as well the eBIC technique. As discussed previously, the maximum range of 30 keV electrons (maximum reachable energy with a SEM) is shorter than 6.5 µm which implies to work on a thinner p^- layer. The apparent part of the p^{++} layer (area etched twice) represents a 300 µm wide frame. This value is a reasonable trade-off for maximizing the active area (p^- surface) and have a contact on the p^{++} level large enough to achieve the wire bonding during the detector encapsulation. Some images of the diamond, taken during the etching process with an optical microscope, can be found in Appendix A.3.

---

[1] The border effect reflects the difficulty to develop the resist in the borders of a sample because the resist layer is thicker. A thicker resist implies a higher exposure dose which, if applied, would deteriorate the lithography resolution in the center of the sample. Hence the non-development of the edges in "normal" condition.

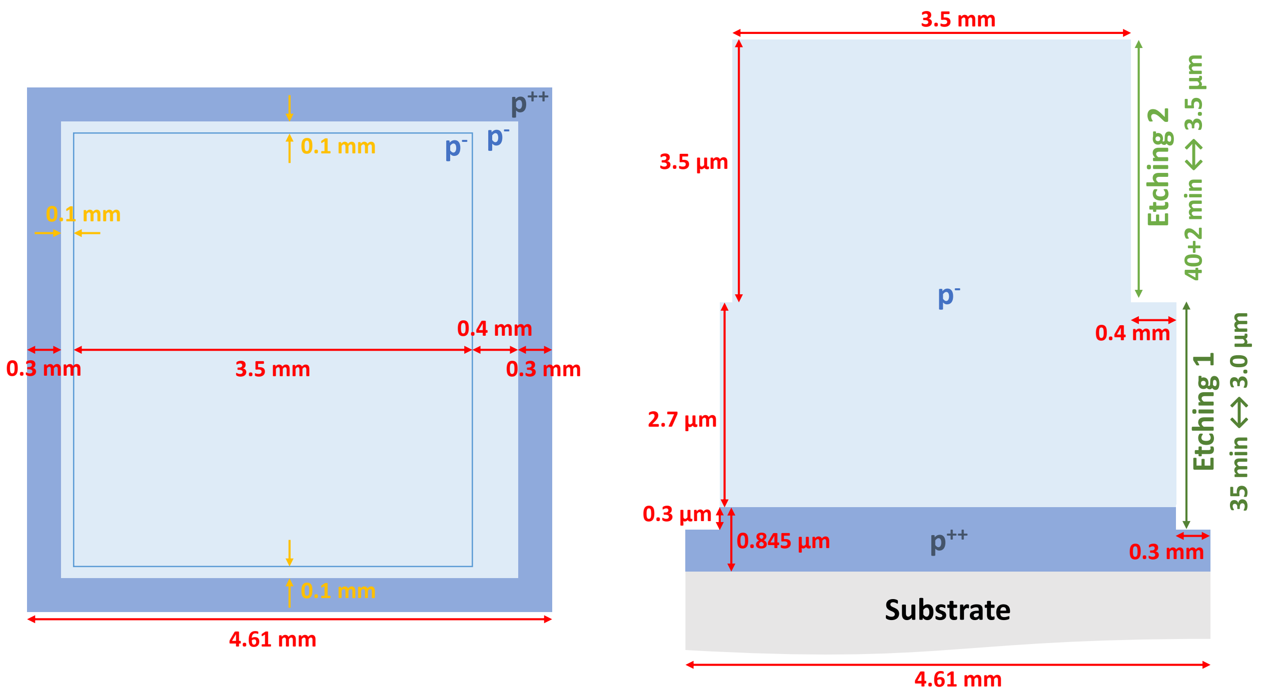

Figure 4.8: Focus on the two etching steps performed to get the ΔE-E telescope.

To check the etching depth, mechanical profilomery measurements were performed using a DektakXT[1] profilometer in the NanoFab clean room. Nine measurements were thus performed, allowing to evaluate the two etching depths, respectively of $(3.00 \pm 0.02)\,\mu\text{m}$, and $(3.47 \pm 0.05)\,\mu\text{m}$. The uncertainties are induced by the surface roughness of the sample (in particular the hillocks) which makes the measurements less reliable.

4.3.2.2 Metallization

Nature of the contacts: it was chosen to perform a 100 nm thick aluminium metallization on both sides of the sample. Such a process is easy to set-up and has proven its efficiency in the past for particles detection [Curtoni, 2020].

Geometry of the contacts: the metallic pad design is described in the Figure 4.9. The metallization consists in six large pads on the p^- layer, three smaller pads on the p^- layer etched once, and two sectors on the p^{++} layer. For the three smaller pads on the p^- layer and the two sectors on the p^{++} layer, the side margins are 50 µm large. For the six large pads on the p^- layer, the side margins are 100 µm large in the horizontal direction and 50 µm large in the vertical direction.

The metallization steps are achieved using the lithography and metal deposition techniques already described for the etching process. To metallize the back side of the sample (substrate), the p^- side was attached to a silicon wafer with a PMMA resist. I chose to metallize the substrate afterwards because metallization on both p^- and p^{++} layers was more complicated and required to control the border effects.

---

[1] `https://www.bruker.com/fr/products-and-solutions/test-and-measurement/stylus-profilometers/dektakxt.html`

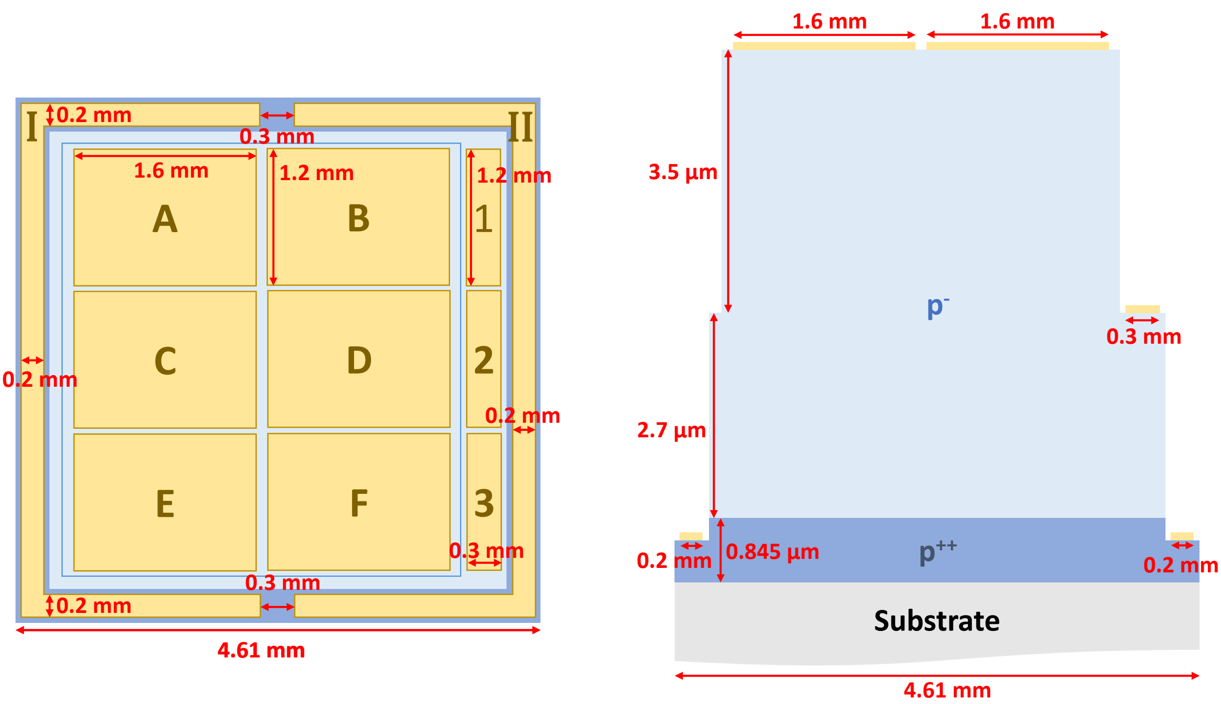

Figure 4.9: Metallization achieved on the top side of the ΔE-E sample. The contacts are 100 nm thick aluminium pads. The numbering of the metallic contacts was also added on each pad.

In the Figure 4.10, two images acquired with an optical microscope are presented. On these images, the border effect is visible. Indeed, the resist was not sufficiently exposed on the

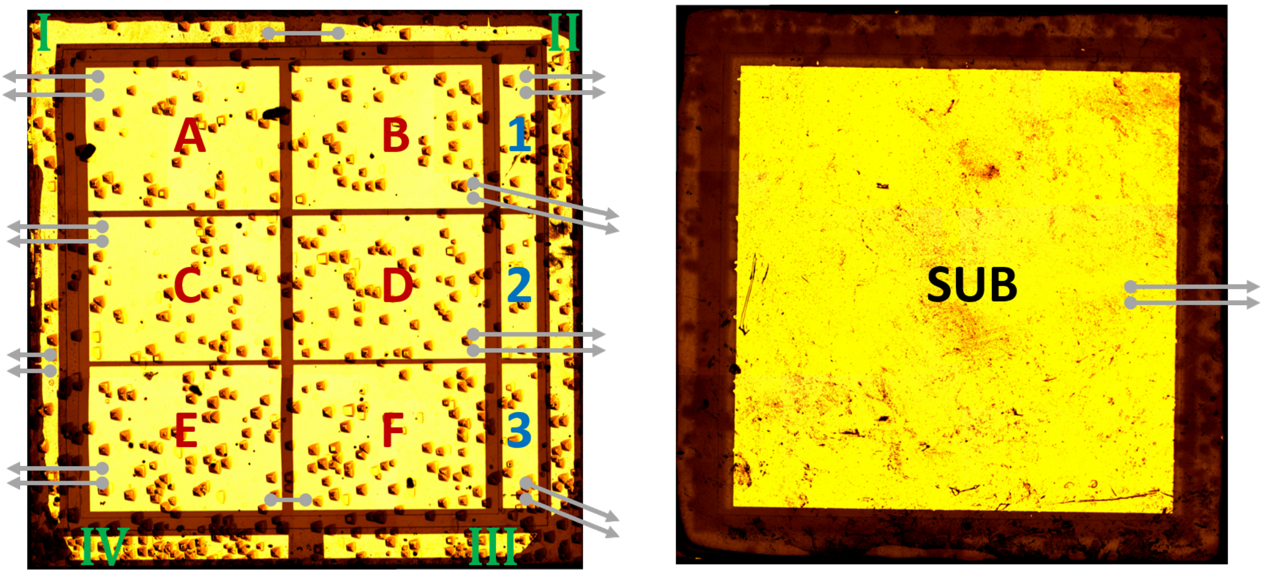

Figure 4.10: Front (left) and back (right) contacts of the ΔE-E detector. On this image, the grey lines represent the bonding wires. When a grey line is terminated by a arrow, it means that the bonding wire is connected to a RO track. The numbering of the metallic contacts was also added on each pad, "SUB" stands for "substrate contact".

two bottom corners of the sample and on the exterior edges. As a result, the shape of the metallization on the p^{++} layer is not exactly the one expected.

4.3.3 Sample I-V characterization and encapsulation

4.3.3.1 I-V characteristics

Before the encapsulation of the detector, the different contacts were electrically tested using two probes:

- the first one was positioned on a p^{-} contact (A to F or 1 to 3 in Figure 4.10) and connected to high voltage output of a Keithley 2636A;
- the second one was positioned on the p^{++} layer (I to IV) and was connected to the low voltage output.

The I-V characterization of the sample using different pads are presented in Figure 4.11. On this image, one can notice that most of the contacts had a Schottky behavior due to the contact Aluminium/p^{-} layer.

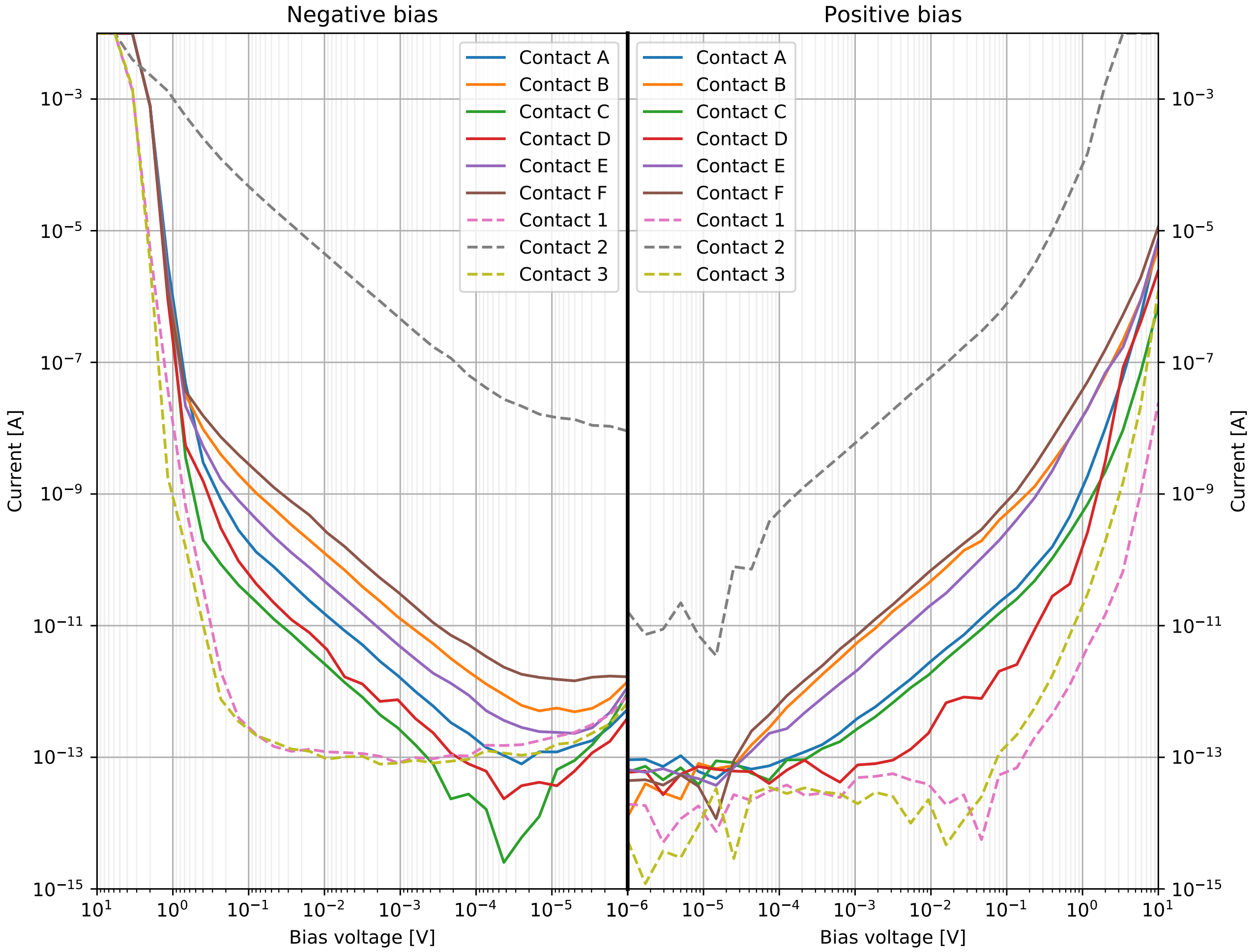

Figure 4.11: I-V characteristics on the thick (solid lines) and the thin (dash lines) p^{-} layer.

Thick p^- layer (pads A to F): in the forward regime (negative biases), the currents were above 10 mA when −3 V or more were applied on the contacts. In the reverse regime, the current values measured at 10 V were between 0.74 (pad C) and 12 µA (pad F). These contacts have a Schottky nature.

Thin p^- layer (pads 1 to 3): in forward regime, the I-V characteristics of the pad 1 and 3 are similar to the ones of the pads A to F. Even if the layer is thinner, the currents measured under 1 V are lower. At 10 V, a current of 24 nA and 1.2 µA were measured for contact 1 and 3, respectively. In forward regime, I-V characteristics of pad 1 and 3 are different from the ones of pads A to F: the currents of both pads are below 1 pA for absolute bias voltages lower 0.1 V, and for greater negative biases, the currents increase sharply. The contact 2 exhibits a different behavior: whatever the polarity of the applied bias the current was at least one decade above the current measure on the other pads. It was then decided to not use it in the following experiments.

In the experiments which will be described in the next section, the p^- layer will be only biased in the reverse regime, in order to limit the leakage current to less than 10 µA. Some C-V measurements are aimed to be carried out to better understand the characteristics of the p^- layer. In particular, the doping level and the built in potential of the p^- layer should be extracted.

4.3.3.2 Packaging

After being metallized, the diamond sample was mounted in the LPSC sample holder presented in the Figure 2.2 (c). Drops of UV sensitive glue were deposited at the four corners of the sample. Then, the sample was bonded with aluminium wires to the PCB Read-Out (RO) tracks. Figure 4.12, shows the ΔE-E with the bonding wires in its PCB sample holder.

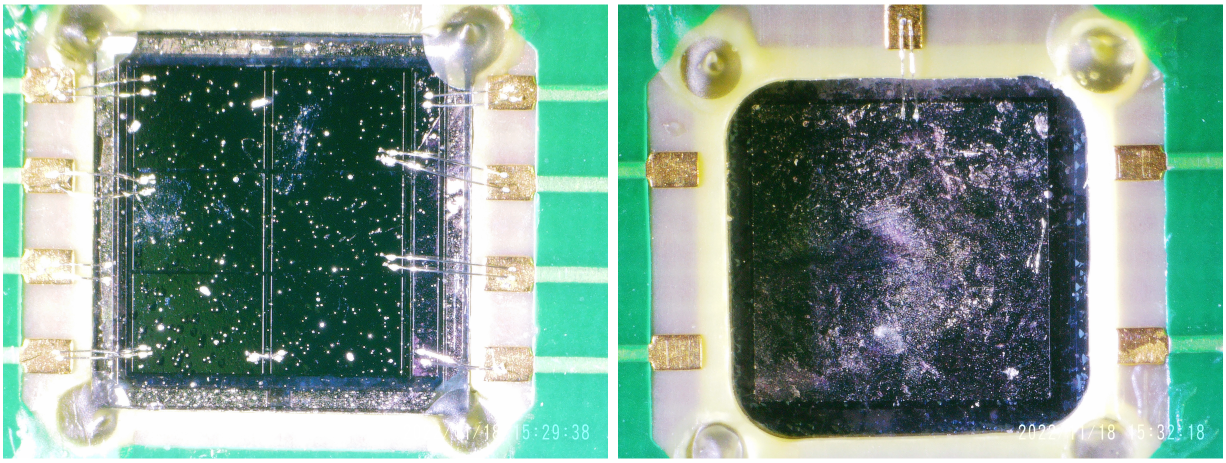

Figure 4.12: Photos of the front (left) and back (right) side of the ΔE-E detector. The contacts and the bonding wires can be clearly identify.

As described in the Figure 4.10, not all the pads were connected to the RO tracks. Indeed, there are only height RO tracks available for the front side of the sample. Therefore, few pads were connected together: the pads E and F; the pads I and II. The pads III and IV were not connected to I and II to avoid to have too many bonding wires in the bottom edges. In Figure 4.10, the bonding wires are represented by grey lines.

4.4 Characterization with eBIC, ToF-eBIC and alpha spectroscopy techniques

In this section the various measurements performed with low range charged particles will be presented. The first experiments were performed at the Neel institute using the setup described in Section 3.1. A continuous electron beam was used to investigate the charge collection properties in a steady state. Then, the ToF-eBIC technique was performed. In this experiment, the goal was to study the signal induced in the different layers of the sample depending of the beam position. Finally, the sample was tested using 5.5 MeV alpha particles on the setup described in Subsection 2.4. All these results were compared to simulations performed with the CASINO and SRIM softwares.

4.4.1 eBIC measurements

4.4.1.1 Experimental procedure

The first experiments performed on the ΔE-E sample consisted in studying the current induced by a continuous electron beam for various primary electron beam energies and applied electric fields in the p^- layer and in the substrate. The electron beam was scanning the whole surface of the sample. The electron beam energy was fixed either at 10 keV (penetration depth: ∼1 µm) to study only the thin p^- layer (2.8 µm thick) or at 30 keV (penetration depth: ∼6 µm) to study both the p^- layer and the substrate.

The setup used during these experiments is described in Figure 4.13. The sample was placed on a copper holder electrically connected to the back contact of the sample (substrate). A Keitley 2636A and 2611B were used to bias the p^- layer and the substrate respectively. A Keithley 6485 picoammeter was connected to the p^{++} layer and used to measure the induced current.

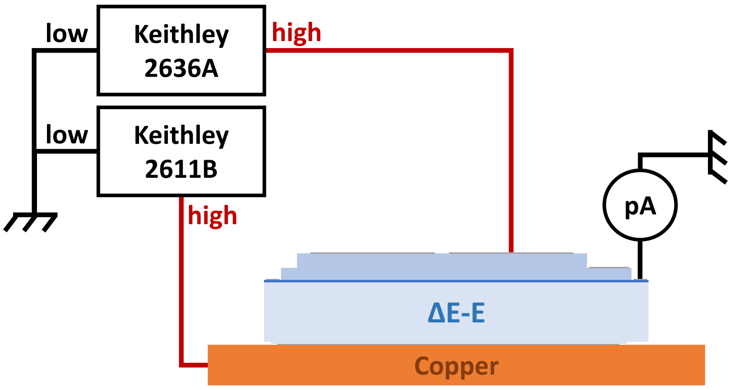

Figure 4.13: Scheme of the setup.

4.4.1.2 Results

The experimental results will be presented in two parts. At first, I will comment on the intensity level of the induced current in the p^- layer, through the analysis of eBIC maps. Then, the influence of the applied electric field on the current induced in the substrate, will be discussed.

Current induced in the thin p^- layer: the first eBIC measurements was performed with a primary electron energy of 10 keV. Thus, the primary electrons are stopped in the thin p^- layer (see CASINO simulations in Appendix A.4). The contact 1, the p^{++} layer and the substrate were grounded, while the other contacts were not connected. On the induced current map in Figure 4.14 (left), it can be noticed that, even if the applied electric field is null, some current is measured (white area). This means that an internal electric field is making the charge carrier drifting under the contact: the Schottky behavior of the contact is confirmed. It is then possible to modify the applied electric field between the contact 1 and the p^{++} layer to compensate the observed internal electric field (white area vanished). This procedure allowed to estimate, experimentally, the Schottky barrier value to be (1.70 ± 0.05) V.

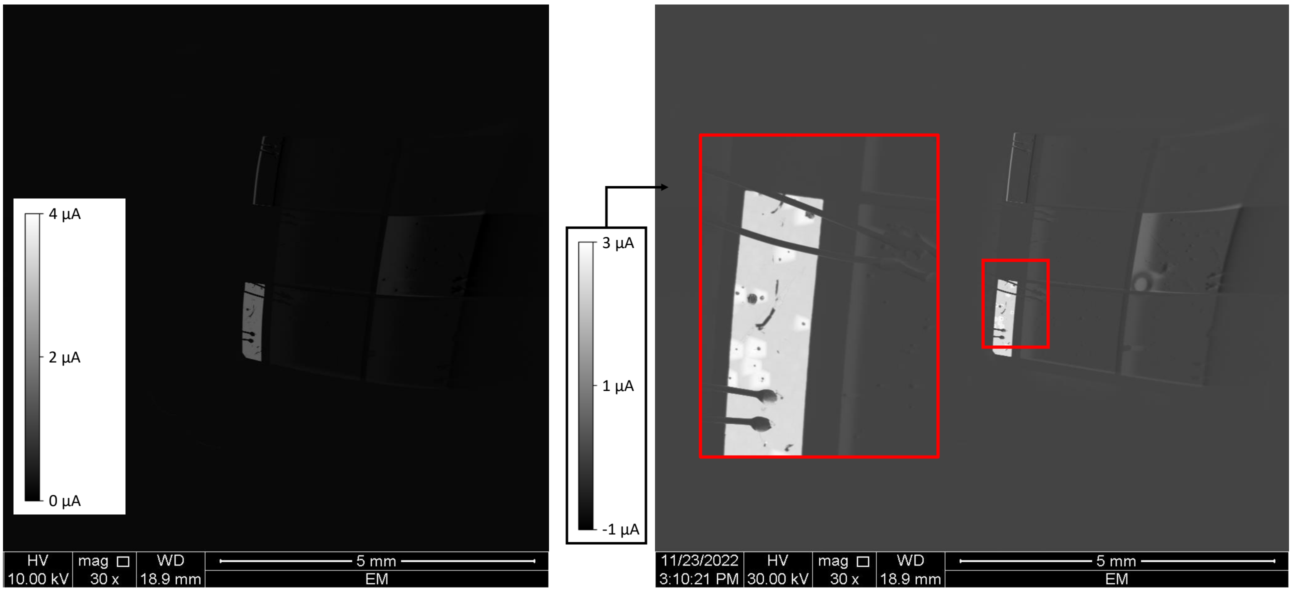

Figure 4.14: eBIC maps performed on the ΔE-E sample for an electron beam energy of 10 keV (left) and 30 keV (right). On both images the contact 1 and the p^{++} layer were grounded, while the other contacts were at floating biases. On the right image, an eBIC map performed with a higher magnification was added in an insert.

Then, the same measurement was carried out using 30 keV primary electrons. At this energy, the electrons passed through the thin p^- layer and stopped in the substrate. The results are shown on Figure 4.14 (right). A small insert of the same image, taken with a higher magnification, was added. In these pictures, the hillocks are clearly visible. Indeed, at the hillocks locations, the p^- layer is thicker (up to 2 µm thicker), and thus the 30 keV primary electrons deposit more energy. In contrast, at the unepitaxial crystal locations, no current was measured whatever the applied electric field. At these locations, the charge carriers were trapped and could not drift through the p^- layer.

Current induced in the substrate: the same eBIC map was recorded for ±10 V applied on the substrate (see Figure 4.15). Doing so, a bright white spot, corresponding to a high induced current (greater than 3 µA in some locations) can be observed under the metallic contact on the p^{++} layer (bottom of the eBIC image). Over time, the size of the white area increased and some additional areas became white. For higher positive biases, the induced current even became much higher than the maximum current expected: some avalanche phenomena occurred. These observations could be explained by a runaway phenomenon that occurs when holes are collected in the p^{++} layer. Experiments are being conducted to understand this phenomenon.

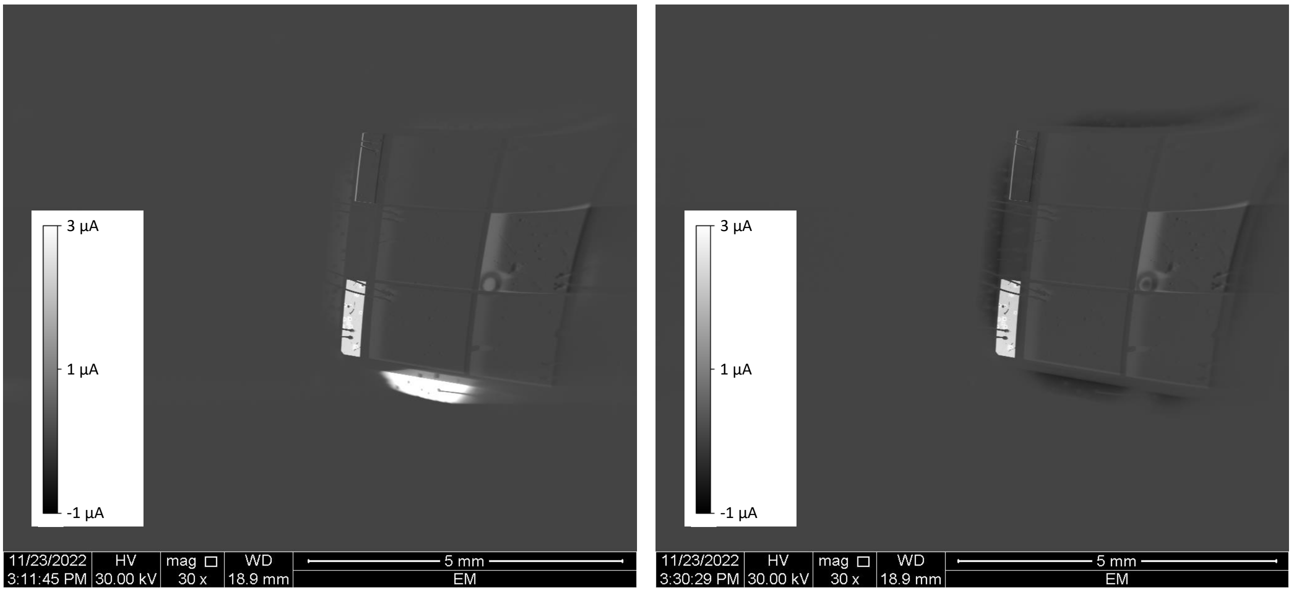

Figure 4.15: eBIC maps performed on the ΔE-E sample for an electron beam energy of 30 keV. Left: 10 V is applied on the substrate. Right: −10 V is applied on the substrate.

This phenomenon was not observed when negative biases were applied. Therefore, in the next experiments, the substrate will be biased with a negative bias polarity.

The electron beam was also used in beam spots to study the current induced depending of the beam position for various beam energies ranging from 10 to 30 keV. Nevertheless, due to current instabilities, significant systematic uncertainties on the measured current complicate the analysis of the results. The result of this latter experiment is discussed in Appendix A.4.

4.4.2 ToF-eBIC measurements

4.4.2.1 Experimental procedure

Some measurements were performed using pulses of electrons. In these experiments, the charge collected in the thin p^- layer and the substrate were recorded using two house-made LPSC charge preamplifiers. The primary electron energy was 30 keV and the pulses were 10 or 100 ns long. The primary beam current was 1.9 nA (in average 12 electrons per nanosecond). The Keithley 2636A and 2611B were used to bias, respectively, the p^- layer (contact 1) and the substrate (see Figure 4.16). 10 V was applied on the thin p^- layer (electric field: ∼37 kV/cm), and −200 V on the substrate (electric field: ∼3.8 kV/cm). The p^{++} layer was grounded. The other contacts were floating. The measurements were performed in spot mode without a beam defocusing and without a bias voltage cycling procedure (described in Section 3.2). Indeed, these experiments were carried out at RT for relatively high electric fields and a charge preamplifier was used instead of a current to voltage one. Even if the charge collected decreased slightly over time, it was still possible, by inverting the applied bias on the substrate before the measurements, to obtain a stable signal during several seconds: the polarization effects are relatively limited.

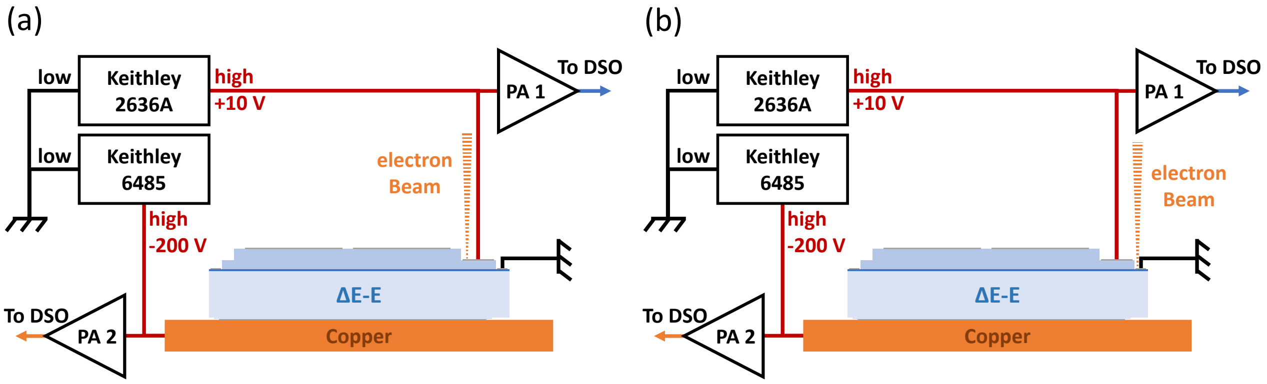

Figure 4.16: Scheme of the setup used during the ToF-eBIC experiments. The beam was focused, at first, on the thin p^- layer (a), and then, on the p^{++} layer (b).

4.4.2.2 Preamplifier calibration

In order to compute the absolute charge collected, the charge preamplifier were calibrated. The calibration procedure was similar to the one described in the Section 2.4. The setup used is represented on the Figure 4.17 (left). As described in the scheme, voltage pulses with an amplitude V_{in} were injected in the PA test capacitor channels and the output amplitude V_{out}, corresponding to a known charge Q_{in}, was measured using an oscilloscope. This procedure was repeated for different values of V_{in}. A Keysight 33600A waveform generator was used to generate the voltage pulses and the oscilloscope LeCroy HDO9404 was used to measure V_{in} and V_{out}.

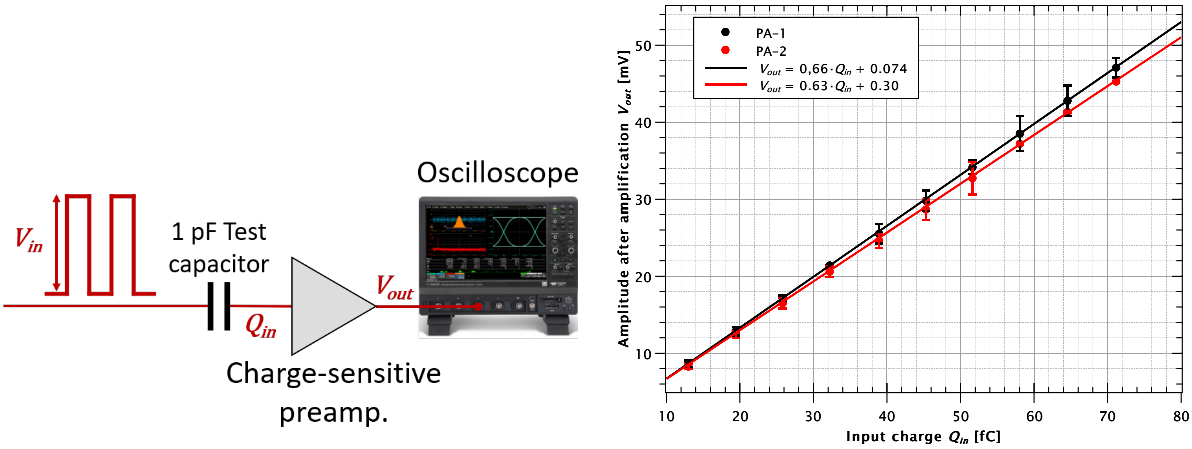

Figure 4.17: Left: Scheme of the calibration setup. Right: amplitude measured after amplification for the two PA in function of the input charge (close circles). The data were fitted using a linear fit function (solid line).

The distribution of V_{out} versus Q_{in} is plotted, for two different PA, on the Figure 4.17 (right). On the range of Q_{in} studied, the responses of the two PA are linear. The data were fitted using a linear fit function (solid line), and the calibration function is indicated in the legend of the figure.

4.4.2.3 Results

The main ToF-eBIC results are presented in Figure 4.18. Figure 4.18 (d) is a SEM image of the top left edge of the sample taken at 30 keV. The two red crosses indicate the beam positions where the measurements were performed. The first two measurements were carried out on the contact number 1 of the thin p^- layer at the same position (cross (a) and (b) of Figure 4.18 (d)). The third experiment experiment was conducted on the contact II of the p^{++} layer (cross (c) of Figure 4.18 (d)).

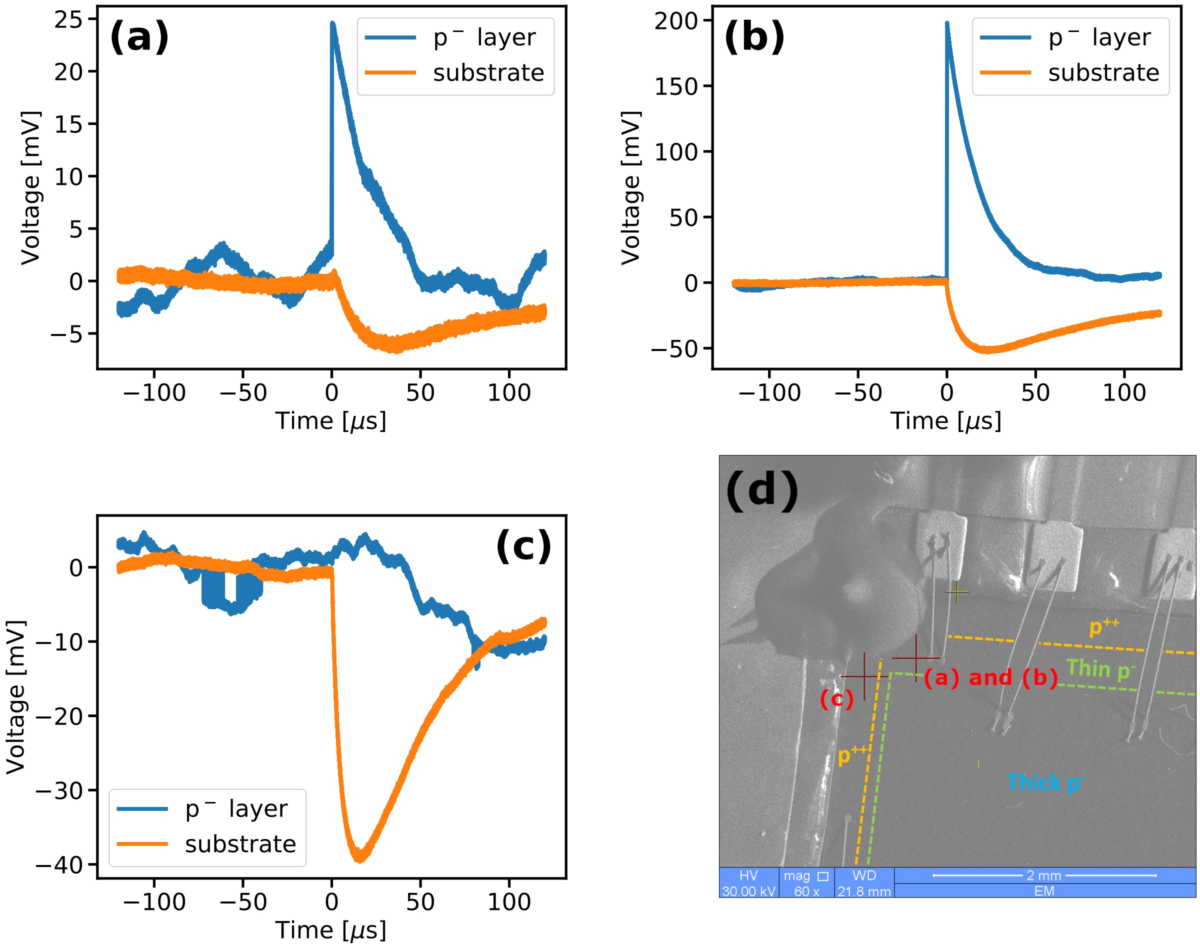

Figure 4.18: (a) and (b): charge preamplifier output voltage (integrated voltage) measured in the p^- layer and in the substrate versus time for the beam focused on the contact 1 of the thin p^- layer. (c): charge preamplifier output voltage (integrated voltage) measured in the p^- layer and in the substrate versus time for the beam focused on the contact II of the thin p^{++} layer. The pulse durations were 10 ns for (a) and (c), and 100 ns for (b). (d): SEM image of the top left edge of the sample. The crosses represent the beam positions during the experiment (a), (b) and (c).

The integrated current induced in the thin p^- layer and in the substrate for the beam positioned on the contact number 1 are plotted in Figure 4.18 (a) and (b). The measurements were performed for different pulse durations: 10 ns for (a) and 100 ns for (b). For each plotted curve, the noise level (calculated on the 120 µs prior to the peak) was subtracted. Then, the fluctuations of the noise and the maximum amplitude of the signal were computed. In the following, the uncertainties stand for the noise rms values. Nevertheless, it should be precised that the roughness of the sample could also significantly impacts the energy deposition in the different layers, and thus, is also a major source of uncertainties.

By using the calibration fit function of the PA, the ratio between the charge collected in the substrate versus the p^- layer was calculated. In Table 4.3 (left), the experimental ratios were compared to the ones obtained thanks to the CASINO simulations. For a pulse duration of 10 ns, the experimental ratio (0.30 ± 0.03) is compatible with the theoretical values (0.30). However, even if the ratio obtained for longer pulses is close to the theoretical value (0.28 ± 0.01), the results are not compatible (this is done without considering the roughness of the sample, nor a systematic error related to the injection). Moreover, it can be noticed that, whatever the layer studied, a factor 10, which came from the time difference between the two pulse durations, is not observed in the amount of charge collected, as it should be. One explanation is that charge recombinations was occurring for longer pulses. However, up to now, it was not possible to confirm this latter assumption. The total charge collected in the layers was found to be superior to the charge generated in the sample[1] (in case (a), 37.1 fC (p^-) + 11.2 fC (Sub) > 43.5 fC (injected charge)). The beam current was measured at the end of the experiment; therefore, the most probable explanation to this phenomenon is that the alignment between the beam and the beam blanker shifted over time. As a result, it was not possible to accurately quantify the CCE.

Table 4.3: Comparison of experimental ((a) and (b)) and theoretical (CASINO simulations) charge collected ratios.

Substrate/p^- layer		
pulse duration [ns]	Expected value	Experimental value
10	0.30	0.30 ± 0.03
100	0.30	0.28 ± 0.01

Pulse duration 100 ns / 10 ns		
Layer	Expected value	Experimental value
p^- layer	10	8.1 ± 0.6
Substrate	10	7.5 ± 0.5

Then, the beam spot was focused on the contact II (cross (c) on Figure 4.18 (d)). The current induced in the p^- layer and in the substrate at this position are plotted in Figure 4.18 (c). As expected, no current was measured in the p^- layer (the p^- layer was etched at this position), while a large peak was observed in the substrate. Thanks to a CASINO simulation, it was estimated that the charge collected in the substrate at this position is supposed to be 1.20 times higher than the charge collected at the position (b). Experimentally, the charge collected in the substrate was (63.1 ± 1.3) fC which is compatible with (58.2 ± 3.9) fC[2]. These results confirm the proper functioning of the ΔE-E sample in these experimental conditions.

Nevertheless, the characterizations of the ΔE-E sample were carried out at the end of my PhD, and thus the influence of various parameters was not investigated. For example, the impact of the applied electric field on the charge collection efficiency (in the p^- layer and in the substrate) was not studied. Moreover, only one of the p^- contacts was extensively examined. Experiments are already planned to complete these results.

---

[1] More than 20 % of the injected charge was also deposited in the p^{++} layer (CASINO simulations). Therefore, the total charge measured is significantly higher than expected

[2] $58.2 = 1.20 \times (37.1 + 11.2) = 1.20 \times$ the charge measured in (a)

4.4.3 Alpha spectroscopy

Due to the Covid 19 pandemic, the fabrication phases of the ΔE-E were impacted and as a consequence its study under different types of irradiation could not be conducted as initially planned in the PhD schedule. The results obtained during alpha spectroscopy measurement are still ongoing. Therefore, in this subsection, only a preview of the experimental results will be discussed.

4.4.3.1 Experimental setup

To assess the performance of the detector for light ion detection, the setup describes in Section 2.4 was used. The experiments were divided in two steps: in a first time, the substrate (back side) was facing the alpha source. The goal was to check its charge collection properties. In a second time, the p^- layer (front side) was facing the radioactive source, that time, to evaluate the performance of the telescope. As described in Figure 4.19, the measurements were achieved using two LPSC charge PA, two amplifier-shaper Ortec 572. Two acquisition systems were used: the oscilloscope LeCroy HDO9404 and the 16 bits MCA. The sample was biased thanks to two Keithley 6487. Several p^- pads were tested (C, 1 and 3), they all exhibit similar behavior. In the following, in order to compare the results obtained using the alpha setup and the ToF-eBIC technique, only the ones obtained with the pad 1 will be discussed. The p^{++} contact was grounded. Measurements were carried out with the unused pads either not connected or at ground potential with no difference in the results.

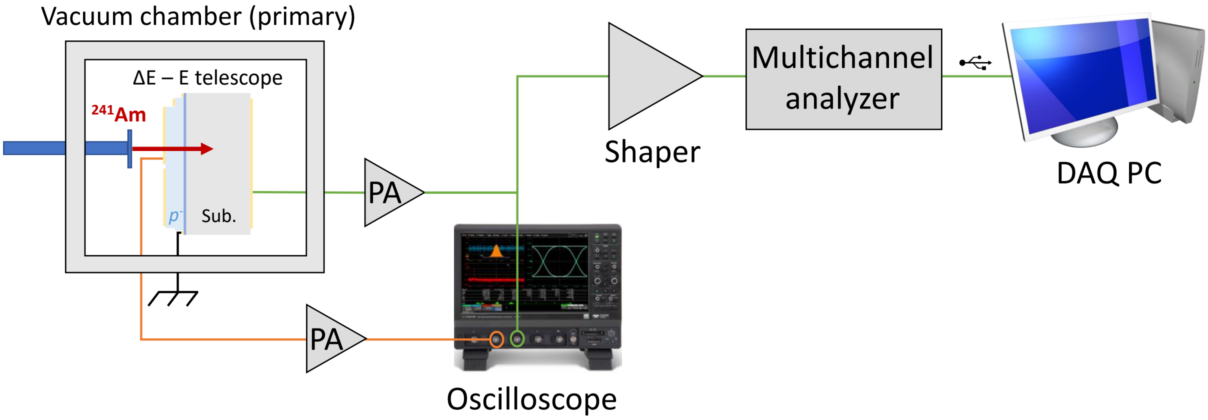

Figure 4.19: Setup used during the alpha spectroscopy experiments. In this configuration, the alpha are impinging in the p^- layer and are stopped in the substrate.

4.4.3.2 Experimental results

The results obtained while the substrate was facing the alpha source are similar to the ones described in Section 2.4. In Figure 4.20 (a), two energy spectra taken at ±100 V are plotted. The peaks at (5.5 ± 0.1) MeV, respectively (5.2 ± 0.2) MeV), attest the relatively good hole (CCE of (100 ± 2) %), respectively electron (CCe of (95 ± 4) %), collection properties of the substrate. The significant energy dispersion can be attributed to the relatively low electric field (about 1.9 kV/cm) which was applied on the substrate.

However, when the detector was used as a telescope, some issues that we have not yet fully understood have arisen (alpha source facing ΔE stage, see Figure 4.19).

- The signal in the p^- layer remained identical whatever the bias applied in the range $[-1\,\mathrm{V}; 2\,\mathrm{V}]$. For higher biases (in absolute values), the amplitudes of the noise fluctuation were too high. This is probably evidence of a relatively high built-in potential. In this experiment it was then not possible to compensate it. These results are not in agreement with the results obtained using the ToF-eBIC technique. Indeed, with this technique, induced current were measured in the p^- layer while 10 V were applied on the same contact.

- When a negative bias (up to −300 V) was applied on the back side of the substrate (hole transit through the substrate), almost no signal was collected. This is also not consistent with the ToF-eBIC measurement.

- When a positive bias was applied on the back side of the substrate (electron transit through the substrate), some signal were measured (configuration not tested during ToF-eBIC measurements due to the "avalanche phenomenon" observed in eBIC). In Figure 4.20 (b), an energy spectrum resulting from the charge collection in the substrate was recorded, with the following experimental conditions: p^- layer bias at 0 V and substrate bias at 100 V. Three peaks (indicated by the red arrows) can be observed. They may be attributed respectively to the alpha passing through: 1) the thick p^-, 2) the thin p^- and 3) the p^{++} layers. The positions of these peaks were extracted and compared to simulations performed with the SRIM software (see Table 4.4). The experimental values are systematically lower than the simulated ones, highlighting an incomplete charge collection. Indeed, for each peak, a CCE of approximately 80 % was found with a 1σ precision. This seems to confirm the attribution of the peaks. Although peak assignment is achievable, the CCE is significantly lower when the particle interacts from the front side (p^- or p^{++} layer) than when the particle interacts from the back side (directly into the substrate). Indeed, a CCE of (95 ± 4) % was obtained in the latter configuration.

Table 4.4: Comparison between the experimental peak positions and the energy values obtained by SRIM simulations.

Peak number	Experimental value [MeV]	SRIM value [MeV]	CCE [%]
1	2.7 ± 0.2	3.32 ± 0.05	81 ± 6
2	3.5 ± 0.4	4.46 ± 0.02	78 ± 9
3	4.1 ± 0.1	5.32 ± 0.01	77 ± 2

I just compared the alpha and ToF-eBIC measurements and noticed in my analysis that there were inconsistencies in the results. There is a major difference between the two techniques. In one case, ToF-eBIC, a beam can be focused precisely on the sample. In the other case, the alpha particles emitted by the radioactive source have no ballistic precision. In the ToF-eBIC experiments, we took care to focus the beam in a region where the defect density was lower. This could explain in part the discrepancies observed between the two experiments.

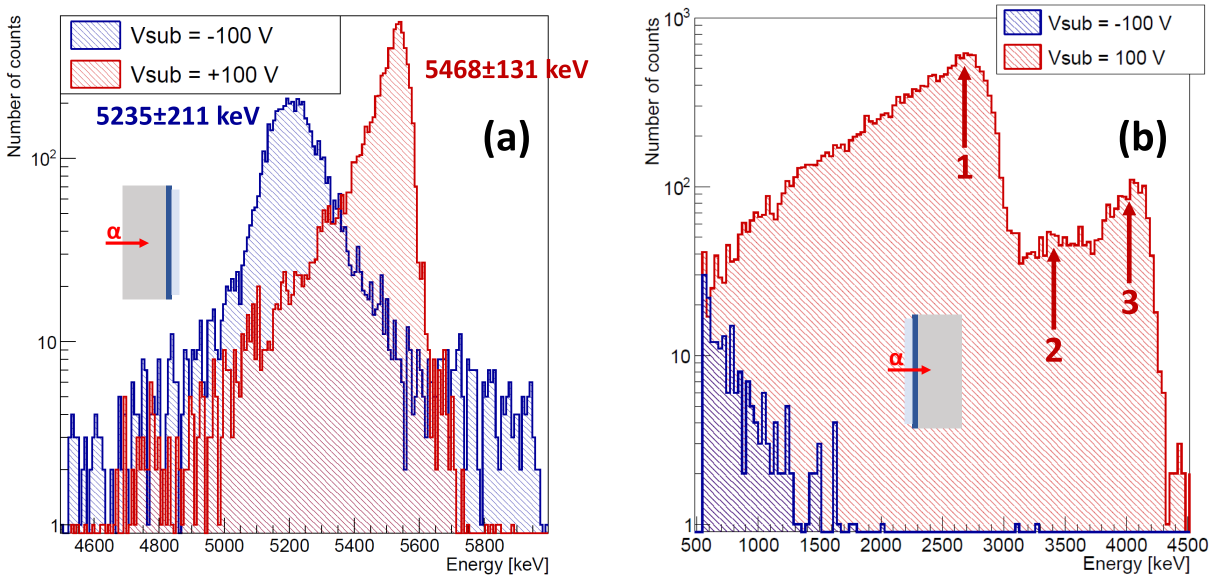

Figure 4.20: Energy spectrum measured in the substrate when the alphas were impinging the detector through the substrate (left) and through the p^- layer (right). For each case the spectrum were recorded at 100 V and −100 V.

A second version of the setup is under development in order to measure in time coincidence the energy deposited in the p^- layer and in the substrate. We will use a module Uctm2 developed at the LPSC. Thanks to these future measurements, we aimed to even better understand the whole behavior of the detector and find complementary explanations.

These experiments will be conducted as a continuation of my PhD work. A systematic study using the ToF-eBIC technique will also be implemented. It offers the possibility to use a beam (surface positioning, beam stamps) and will undoubtedly be of great interest for the development of the future prototypes.

4.5 Characterization of an alternative solution based on *pn* junctions

As an alternative of ΔE-E telescopes, *pn* junctions and Schottky diodes are promising for high-performance detectors, enabling their use with low bias voltage, increased charge carrier collection efficiency, and charge amplification (Schottky). This section will deal with the characterization of a diamond *pn* junction at laboratory and at a light ions beams at AIFIRA in the context of a collaboration between Grenoble and Tsukuba laboratories in order to exchange skills and experience, and promote the development of innovative diamond detectors. A particular focus will be given on the elaboration of *pn* and Schottky diode detectors, their instrumentation with electronic readout, and first tests at radiation sources and accelerators.

4.5.1 *pn* junction

As part of the collaboration PRC CNRS and JSPS & TYL IN2P3, the performances regarding particle detection of a *pn* junction made at the National Institute for Materials Science (NIMS) in Tsukuba were investigated. This sensor was designed to work in harsh radiative environment [Shimaoka, 2018]. A pseudo-vertical diamond *pn* diode with a very thin active area of 1 µm was chosen in order to meet these requirements. As shown in Figure 4.21, this *pn* junction was made of four successive homoepitaxial growths on a IB diamond substrate with a (111) orientation: a 1.6 µm p^+ layer, a 0.1 µm p^- layer, a 0.9 µm n^- layer and a 0.3 µm n^+ layer as shown in Figure 4.21. Ohmic contact were achieved by electronic beam deposition of Ti/Mo/Au layers.

In order to perform experiments on this sensor, the *pn* junction was glued on a half LPSC sample holder (b) described in Figure 2.2. The goal was to bias and read the signal on the existing LPSC setup without any other adaptation. Even if several *pn* junctions were made on the same diamond substrate, only one of them was tested ((c) and (d)). On this sensor, the p^+ metallic contact is connected thanks to a bonding wire to the ground while n^+ contact is biased. As a result, by applying a positive bias voltage, the *pn* junction can be used in reverse mode as a radiation detector.

4.5.2 eBIC measurements

Shimaoka *et al.* [Shimaoka, 2020] already reported on eBIC measurements at the Institut Néel on some *pn* junctions with a ∼2 µm active area. I performed complementary measurements that will be described in the following subsection.

4.5.2.1 Experimental procedure

In this experiment, the goal was to study the eBIC current by the diode versus the electron beam energy, the applied bias voltage and the beam impact location on the sample. To do so, the sensor was placed in the SEM setup presented in Section 3.1.

Two studies were achieved:

- in scan mode, an eBIC mapping was performed at 0 V for two different electron accelerating voltages. The goal was to study the influence of the penetration depth of the primary electrons on the induced current.

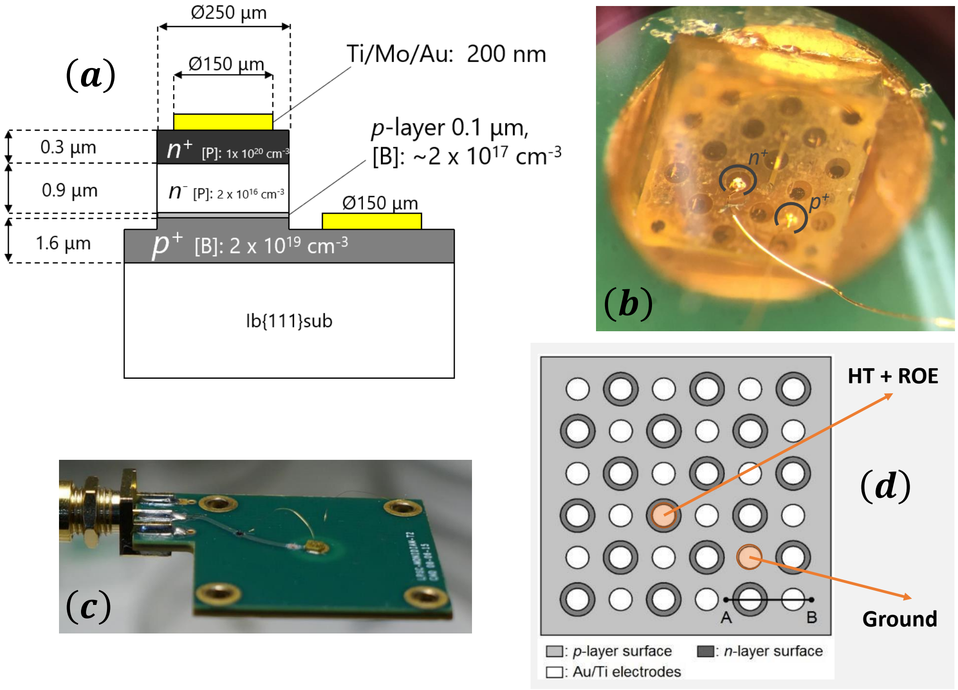

Figure 4.21: (a): Schematic cross section of the PN junction from [Shimaoka, 2018]. The active area is about 1 µm. (b): Optical picture of the sample. On this image, the different n type growth recovered with metallic contact and the bonding wires used to bias and read the signals of one of these junctions can be distinguished. (c): Optical picture of the sample glued on a LPSC sample holder. The position of the contacts used during the experiments is indicated in gray. (d): Schematic top view of the device. The orange arrows represent the bonding wires.

- in spot mode, the induced current of the diode was investigated versus: 1) the applied voltage; and 2) the primary electron energy. The goal was to compare the experimental current with CASINO simulations.

4.5.2.2 CASINO simulations

To evaluate the maximum depth and the energy deposited by the electrons in the *pn* junction, some simulations were achieved using the software CASINO. At first, the metallization was not taken into account and the different layers were considered as intrinsic diamond layers. The Figure 4.22 (a) shows the simulated energy deposited depending on the depth for six different primary electron energies. The n^+ layer, the n^- and p^- layers (active layer), the p^+ layer and the substrate are represented respectively by the red, blue, green and white areas. On this graph, it may be noticed that 5 keV electrons are stopped within less than 0.3 µm and do not deposit any energy in the active area of the diode (blue area). For higher energies, the energy deposited in the active area can vary up to 11 keV per electron for a 15 keV primary electron energy.

Then, a 200 nm thick Au-Mo-Ti metallic contact with an average density of 11.26 g/cm^3, three time higher than the one of diamond (see Figure 4.22 (b)) was added to the detector scheme in the simulation. In this case, for the energies considered, the electrons lost a significant part of their energy in the metallic contact. Indeed, the energy deposit distribution is peaked in the

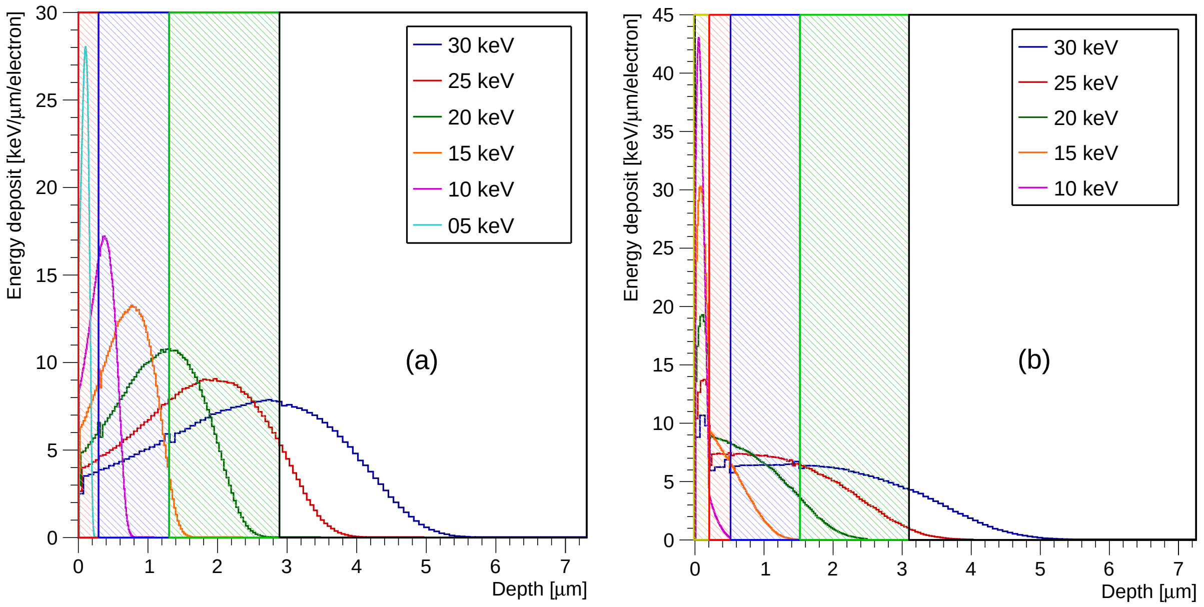

Figure 4.22: Energy deposited in the different layers of the *pn* junction: in red, the n^+ layer; in blue, the active area (n^- and p^- layer); in blue, the p^+ layer; and in white the substrate. To obtained these graphs, two simulations were achieved with the software CASINO: one without considering the metallic contact (a) and one considering a metallic contact (yellow area) with a density of 11.26 g/cm^3 and a thickness of 200 nm (b).

metallization. As a result, 10 keV electrons do not deposit any energy in the active area and the maximum energy deposit is reached around 25 keV. However, in both simulations, electrons with an energy higher than 20 keV go through the active layer.

4.5.2.3 Results

On the SEM picture displayed in Figure 4.23, the n^+ layer is circled in blue, the metallic contact in orange, the weld connected to the bonding wire in yellow. The remaining part corresponds to the p^+ layer (green).

Induced current mappings: the two eBIC maps are presented in the Figure 4.24. A grey scale represents the eBIC current intensity. As expected from the simulation:

- the 10 keV electrons induced a significantly lower current in the metallized region ((2.44 ± 0.04) nA) than in the unmetallized region ((11.8 ± 0.2) nA). As suggested in [Shimaoka, 2018], a diffusion of some charge carriers from the n^+ layer may explain the signal in the metallized region (primary electrons stopped in n^+ layer).

- the 30 keV electrons induced a higher current in the metallized region ((46.0 ± 0.1) nA) than in the unmetallized region ((41.1 ± 0.1) nA).

Some black spots (areas where the induced current is lower) are observed in both maps. Others are only visible on the mapping performed with 10 keV electrons. Among them, some were already visible on the SEM image (see Figure 4.23); these spots were circled in red. This

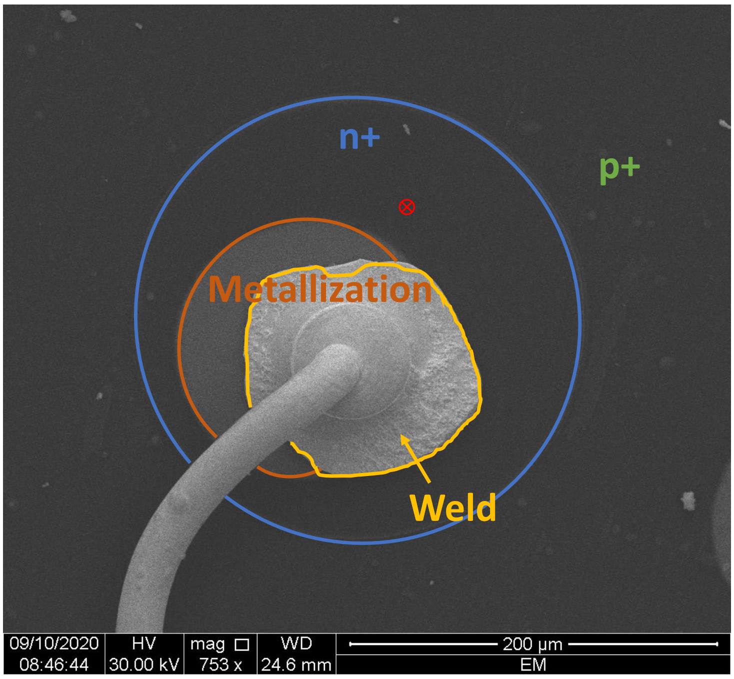

Figure 4.23: SEM picture of the *pn* junction. The different elements are indicated on this picture: the n^+ layer (blue), the metallic contact (orange), the weld and the bonding wire (yellow) and in the background the p^+layer. A circled red cross has been placed to indicate the localisation of the beam during the second experiment.

is probably due to dust on the surface of the sample. On the contrary, other black spots are not visible on the SEM picture and, that time, could be attributed to inner defects.

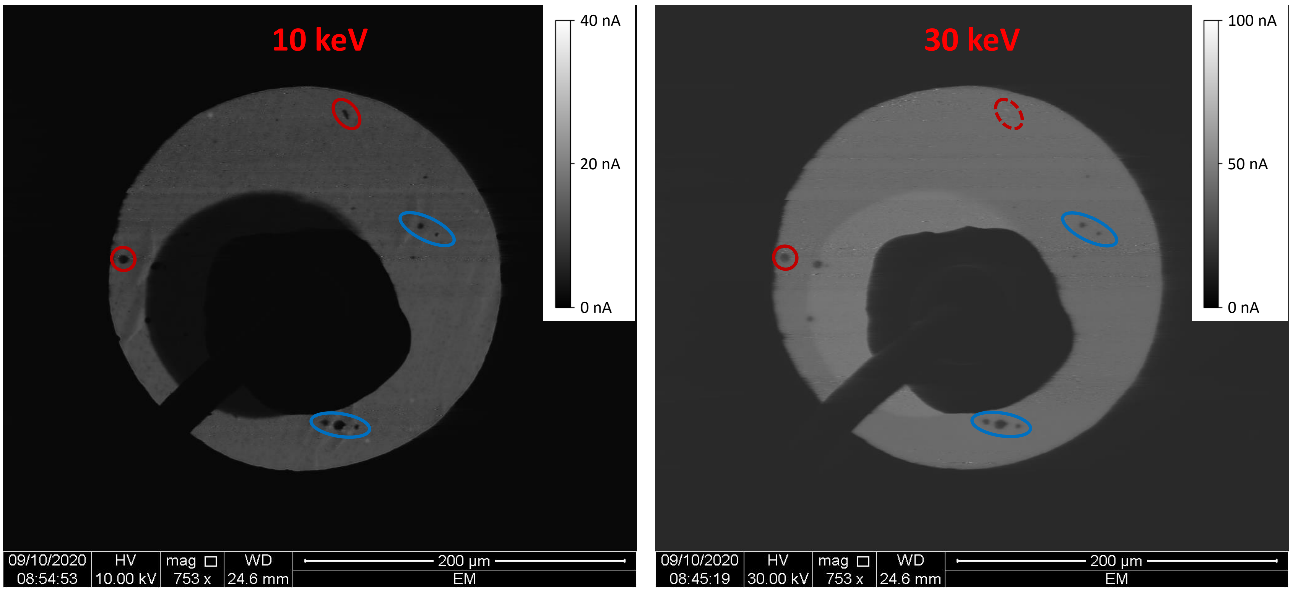

Figure 4.24: eBIC mapping performed on the *pn* junction at 0 V for an electron beam energy of 10 keV (left) and 30 keV (right). On both pictures the same area was scanned, and a grey scale is representing the intensity of the current measured. Some dark spot were circled: the red ones are visible on the SEM image (see Figure 4.23) (dust on the surface), the blue ones are not (inner defects).

Current induced depending on the primary electron energy: in the second experiment, the beam was focused on an unmetalised area indicated by a circled red cross on the Figure 4.23. The normalized induced current (I_{norm}) depending on: 1) the bias voltage (V_{bias}) applied on the *pn* junction; and 2) the primary beam electron energy (E_{e^-}) of the beam; is plotted in Figure 4.25. The normalization was performed by: 1) subtracting the measured current I_{eBIC} by the leakage current I_{lc}; and 2) dividing the result by the theoretical current I_{th} induced in the sample:

$$I_{norm}(V_{bias}, E_{e^-}) = \frac{I_{eBIC} - I_{lc}}{I_{th}}, \text{ with } \quad I_{th}(E_{e^-}) = \frac{I_{beam} \times E_{e^-}}{\sigma_{eh}} \tag{4.1}$$

with I_{beam} the beam current measured with a Faraday cage and $\sigma_{eh} = 13.1\,\text{eV}$ (see Table 1.1) the energy necessary to create an electron-hole pair. One can notice that the back-scattered electrons are not taken into account in the calculation of the theoretical current. This means that the theoretical current is in reality slightly overestimated.

In Figure 4.25, the induced current increases with the reverse voltage applied on the n^+ contact. This is probably the consequences of two effects: a better CCE at higher biases (transit time shorter) and an extension of the depletion region (and so of the active volume). This effect is stronger for the low primary electron energies. This could be a sign of an extension of the depletion region in the n^+ area. Indeed, such a phenomenon would lead to a higher induced current at lower primary electron energies without modifying significantly the current induced for more energetic primary electrons (see Figure 4.22). Whatever the bias voltage applied, the normalized induced current increases from 3 to 15 keV before decreasing for higher primary

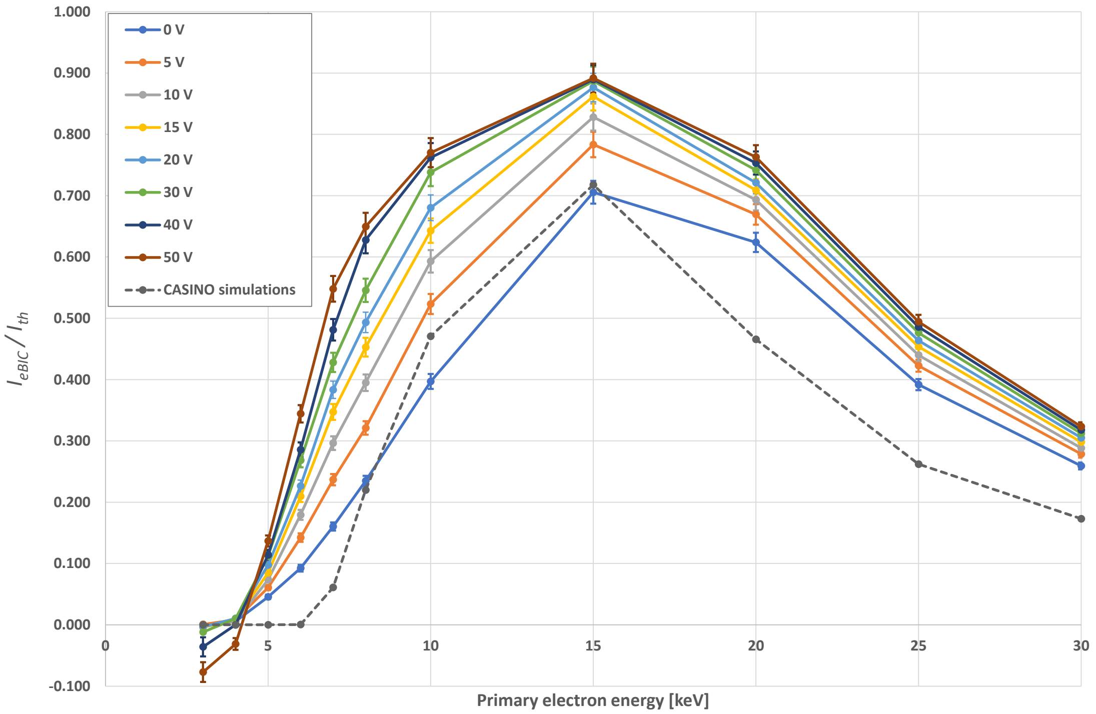

Figure 4.25: Normalized induced current depending on the energy of the primary electrons. The measurements (solid lines) were carried out for various applied voltages on the n^+ contact and are compared to the CASINO simulations (dash line).

electron energies. This observation is consistent with the CASINO simulation results (dash line).

The CASINO normalized current curve consisted, for each energy, in 1) calculating the mean energy deposited in the active layer; and 2) by normalizing it by the initial energy of the electrons. The simulated currents describe well the behavior of the experimental data at 0 V. In particular the normalized current peak for both simulated and experimental data is 0.7 at 15 keV. Nevertheless, few differences between the experimental and simulated data are observed for primary electron energies above 20 keV. This could be due to a thicker active area. Indeed, a thicker active area only induces a higher energy deposition for high energy beams (more than 15 keV). One explanation could be that the layer is thicker than expected.

4.5.3 Alpha spectroscopy

4.5.3.1 Experimental procedure

The *pn* junction was characterized with the setup described in Figure 2.11. The diode was biased in reverse (50 V applied on the n^+ contact).

4.5.3.2 Results

Figure 4.26 (left) represents the charge collection histogram of the *pn* junction. The distribution has a broad peak at approximately 7.5 fC. A Gaussian function (red curve) was used as a fit and estimated a mean value of (7.44 ± 0.01) fC and a rms of (0.91 ± 0.01) fC. Due to the low amount of charge collected, the SNR is low, which explains the dispersion observed around the mean value.

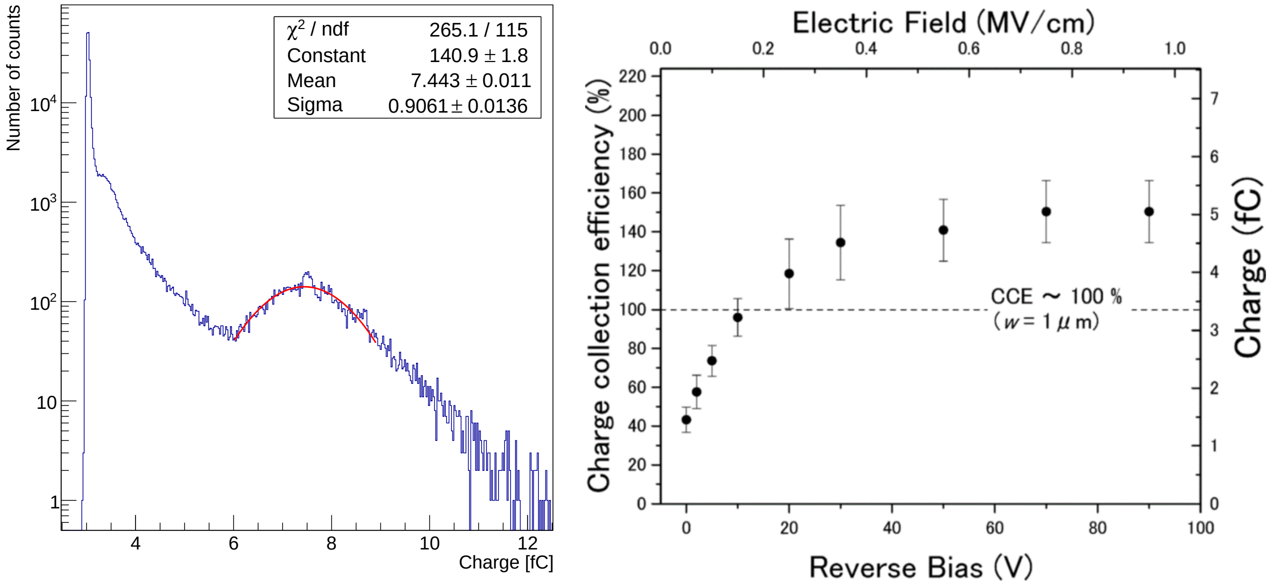

Figure 4.26: Left: charge spectrum recorded in the alpha setup when 50 V were applied on the *pn* junction. Right: CCE versus the reverse bias performed by [Shimaoka, 2018]

Figure 4.26 (right) represents the CCE versus the reverse bias of a similar junction reported by [Shimaoka, 2018]. During this study, charges were collected at 0 V. Our experimental observation confirms their statement. This properties is particularly interesting for plenty of applications such as radioactivity monitoring (dosimeter) or energy storage (betavoltaic cell). On such a device, a CCE equals to 1 is expected around 3.4 fC. Nevertheless, for high reverse biases, the CCE is 30 % greater. According to the authors, this phenomenon can be explained by charge diffusion from the n^+ and the p^+ regions.

The amount of charge collected in Figure 4.26 (left) is compatible at 3σ with the results reported in Figure 4.26 (right) (amount of charge collected: (4.7 ± 0.5) fC). However, to explain such a difference: 1) the two experiments were probably not performed on the same junction; 2) the size of the depletion region might have changed in the meantime.

These first results validate the *pn* junction assembly on the LPSC sample holder. In order to study its performances as a detector, we performed measurements on the AIFIRA platform. Therefore, the charge collection of the device was mapped with ion micro-beams.

4.5.4 Characterization of the *pn* junction under light ions beams at AIFIRA

4.5.4.1 The experimental set-up at AIFIRA

Applications Interdisciplinaires de Faisceaux d'Ions en Région Aquitaine[1] (AIFIRA) is a LP2i[2] facility providing light ion ($^1_1$H, $^2_1$H and $^4_2$H) beams in the MeV range (between 0.7 and 3 MeV). The accelerator provides high brightness (20 A/(m^2·rad^2·eV)) and high energy stability ($\Delta E/E = 10^{-5}$) beams in five different beam lines dedicated to specific analysis [Barberet, 2021]. In particular, some IBIC (Ion Beam Induced Current) mappings can be conducted using sub-micrometer beam spots [Barberet, 2011, Barberet, 2021] at the AIFIRA microbeam line.

To generate the ion beam, two electrodes are used to ionize a gas and generate a plasma in a bulb. Three permanent magnets allow to confine this plasma. The ions are extracted by a channel and are accelerated to the desired energy (up to 3.5 MeV) in the Singletron accelerator. Then, a 90° spectroscopy magnet enables to obtain a mono-energetic and mono-charged ion beam. Finally, two stabilisation slits are used to monitor the possible slight energy deviations.

To achieve the high-resolution beam scans, a two stage magnetic quadrupole quintuplet focusing system combined with electrostatic deflections plates and a flexible beam control system were developed [Barberet, 2011, Daudin, 2013]. A XYZ motorized stage coupled with video cameras ensures a micrometric positioning of the sample in the vacuum chamber [Barberet, 2021]. The latter is also equipped with a surface-barrier, two Si(Li) and a secondary electron detectors to achieve various characterizations.

During the IBIC experiment, the samples were attached on the motorized stage in the vacuum chamber, and connected to the LPSC charge preampifiers by SMA cables and connectors. After verifying the beam properties, the sample was aligned with the beam using the motorized stage. The ROE was composed of one LPSC charge preampifier, an Amplifier-Shaper Ortec 572 and an analog-to-digital converter 7072 Dual ADC.

---

[1] Interdisciplinary Ion Beam Applications in the Aquitaine Region

[2] LP2i: Laboratoire de Physique des Deux Infinis de Bordeaux | Laboratory of Physics of the Two Infinities of Bordeaux (France)

4.5.4.2 Method and experiment description

The sample was placed in a vacuum chamber (secondary vacuum) positioned in the micro-beam line (see Figure 4.27). A LPSC charge sensitive PA permits to read-out the signals. It is connected to a shaper Ortec 572. A multi-parameter data acquisition system digitized the charge and the X-Y positions. The charge collection spectra versus the position is then recorded and plotted thanks to a graphical user interface. During these experiments 50 V were applied on the junction. The experiment consisted in scanning the *pn* junction with a ${}^{4}_{2}$He micro-beam in order to study the charge collection (distribution and homogeneity). 3 MeV ${}^{4}_{2}$He ions were used to induce the signal in the diode. At this energy, the ${}^{4}_{2}$He ions have a range of 5.8 µm in diamond: the ${}^{4}_{2}$He ions pass through the junction and stop in the substrate.

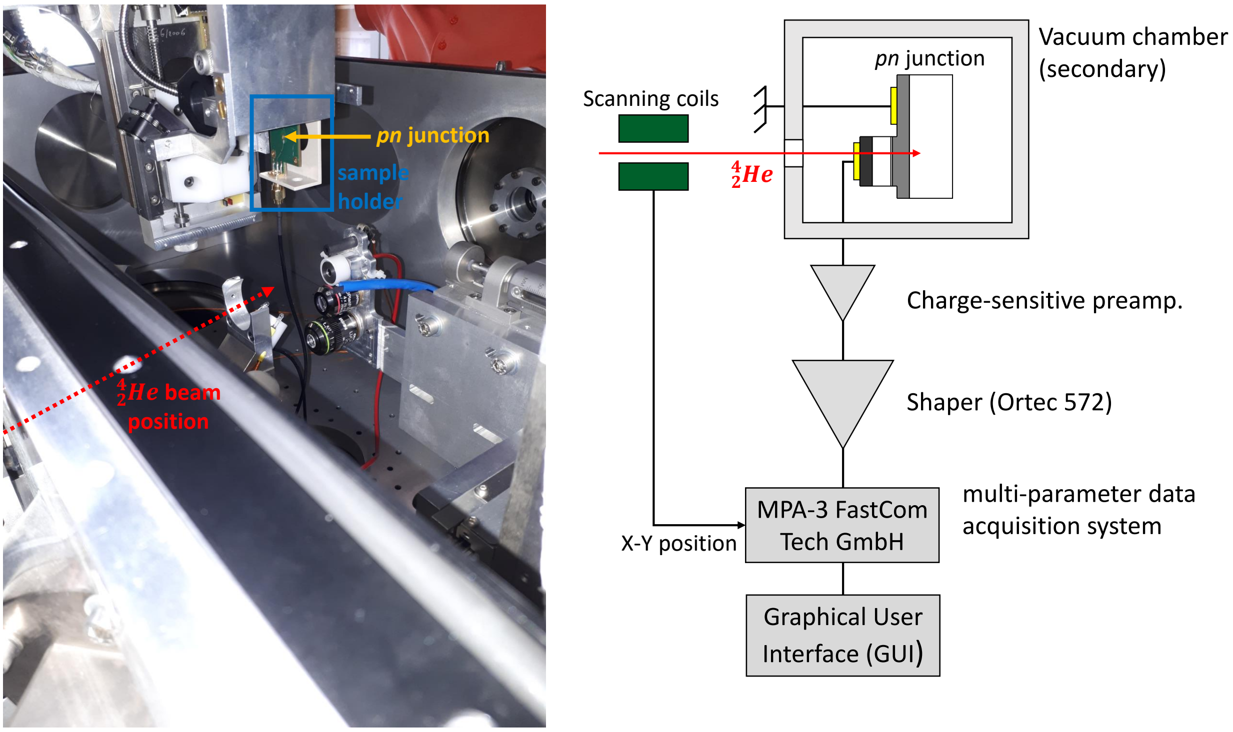

Figure 4.27: Left: picture of the *pn* junction in the AIFIRA vacuum chamber. Right: scheme of the setup.

Some SRIM simulations were performed assuming a depletion region of 1 µm thick. The energy deposited versus the ion initial energy were extracted for metallized and unmetallized areas (see Figure 4.28 left). Under the assumption previously made, 3 MeV ${}^{4}_{2}$He ions are depositing approximately 423 keV (respectively 435 keV) in the active area for unmetallized area (respectively metallized area). This 12 keV difference is explained by the ion energy loss in the metallization layer.

4.5.4.3 Results

The main results are summarized in the Figure 4.29. In the plot (a) and (c), the x-axis is in ADC channels because it was not technically possible to do an in-situ calibration to convert the ADC units in energy ones.

In the energy spectra (top left) obtained on the scanned area, it is possible to distinguish three contributions: at low energy, the electric noise; between 90 to 170 ADC, the peak corresponding

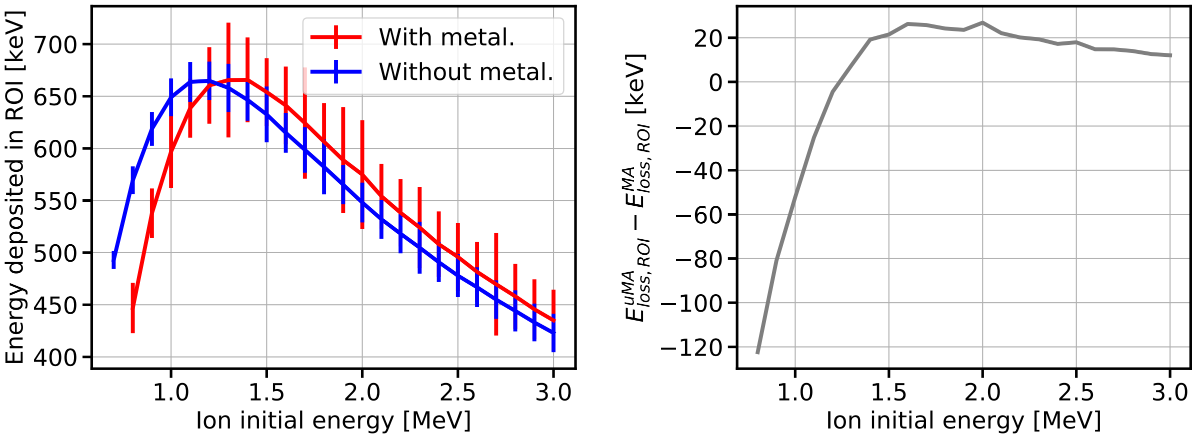

Figure 4.28: Results of the SRIM simulations considering the *pn* junction architecture described by Shimaoka *et al.* [Shimaoka, 2018]. Left: Energy deposited in the active region for metallized and unmetallized area. Right: comparison between the energy loss in the unmetallized area ($E^{uMA}_{loss,ROI}$) and the energy loss in the metallized area ($E^{MA}_{loss,ROI}$).

to the detection of the $^4_2$He ions; at higher energy (around 240 ADC), a small contribution due to the pile up effect. The latter corresponds to the detection of two $^4_2$He ions which interact at the same time in the detector.

In Figure 4.29 (top right), the average energy collected on the surface of the diode was calculated. This plot was obtained by performing two energy cuts: one at 90 ADC units to remove the electric noise and one at 165 ADC units to exclude the pile up effect and have a color scale adapted to study the homogeneity of the energy collected by the junction. On this map, it is possible to observe that two areas stand out: 1) the larger green-blue area, where less energy is collected, corresponds to the unmetallized area; and 2) the green-yellow area, where the average energy collected is a little higher, corresponds to the metallized surface. The energy spectrum was extracted (bottom) for two areas, one on the metallization (blue square) and one on the unmetallized area. The two resulting distributions are clearly distinguished and can be fitted by Gaussian distribution (red and blue line). The parameters of the Gaussian fit are summarized in the Table 4.5. According to the fit results, the two distributions can be identified at 1σ and an energy resolution of 6 % can be achieved.

We can conclude that this *pn* junction is suitable for the detection of short-range charged particle. The work I have just presented is a feasibility study of the *pn* junction concept for particle detection, it is now time to think about the structure itself (layer thicknesses, doping, contacts) to improve the charge collection properties.

Table 4.5: Gaussian parameters obtained by fitting the distribution of the Figure 4.29. The parameters are in ADC units.

	Metallized area	Unmetallized area
Mean	123 ± 0.3	142 ± 0.3
Standard-deviation	8.2 ± 0.2	9.0 ± 0.2

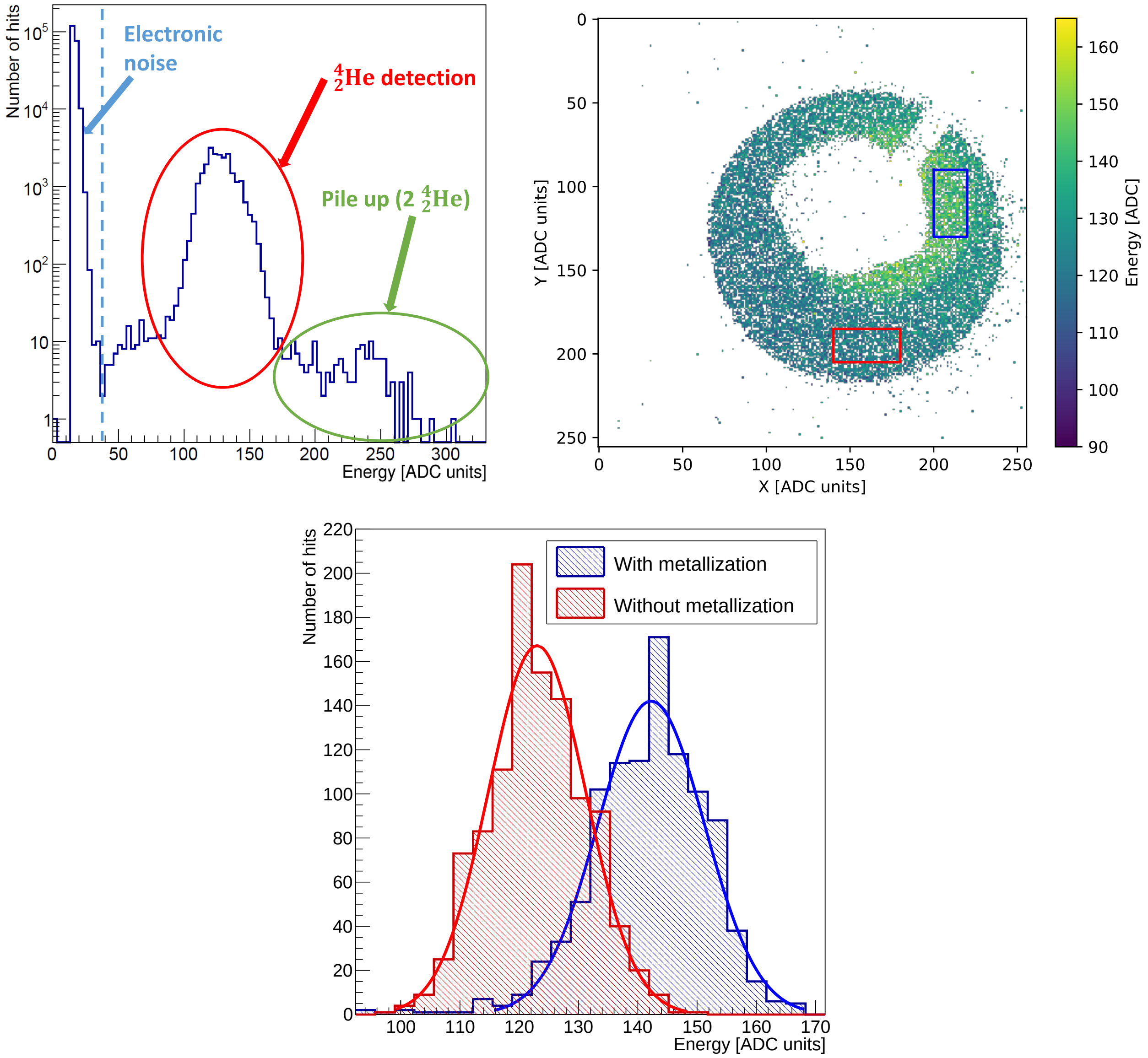

Figure 4.29: Top left: energy spectrum obtained by scanning the PN junction with 3 MeV $^4_2$H ions. Top right: Average energy map achieved by applying a low energy cut at 90 ADC units and a high energy cut at 165 ADC units. Bottom: comparison of the distributions of the energy collected on the metallized (blue) and unmetallized (red) area. The two distribution were fitted with Gaussian functions.

To develop future detectors based on this design, the use of ToF-eBIC technique that we developed during my PhD (Chapter 3) is relevant. The advantage of this technique lies in the fact that:

- it can be carried out in the laboratory (like the alpha setup and contrary to IBIC);
- the ballistics can be controlled (as in IBIC and contrary to the alpha setup);
- the energy of the beam is easily modulated, which makes it possible to manage the depth of penetration on demand. On the contrary, for the IBIC technique, the modification of the energy requires an adjustment of the accelerator parameters, which is time consuming. As well, with an alpha source, the energy of the alpha particles impacting the detector can

be modulated by adjusting the pressure (fixed position) or the source-detector distance (at atmospheric pressure), but it requires a calibration.

Thus, new studies can be conducted that will be of considerable benefit in the future development of this type of device. Indeed, the radiation response of the *pn* junction could be systematically characterized and classified (performance versus growth processes and doping techniques) to reach better detection capabilities.

4.6 Conclusion

A brief overview on the ΔE-E telescopes principles and scientific objectives were at first presented. In this context, the interest of using ultra wide-bandgap material devices, such as diamond, was highlighted. The monolithic diamond ΔE-E telescopes achieved and reported by other groups [Cesaroni, 2019, Verona, 2022] were introduced and compared to our project. Even if the design of the two detectors is very similar, we aimed to improve detector performances by reducing the thickness of the p^{++} layer (dead layer of detection) and the crystalline quality of the p^{-} layer. To determine the thickness of the latter, some simulations were achieved with the pysrim package of python and the SRIM software. As a result, the requirement list of our monolithic diamond ΔE-E telescope and the external providers were the following.

- The substrate should be a 550 µm thick scCVD diamond (electronic grade) from Element 6. This diamond is thick enough to stop 12 keV protons, and exhibit a CCE equal to 1.
- The highly doped layer should be a high quality epitaxial layer with a boron doping level higher than $10^{20}\,\mathrm{cm}^{-3}$ and a thickness thinner than 1 µm. DIAMFAB was in charge of this growth.
- The p^{-} layer should be a high quality epitaxial layer with low residual impurities ($[B] \leq 5 \times 10^{15}\,\mathrm{cm}^{-3}$) and a thickness between 3.5 and 7.5 µm. DIAMFAB was in charge of this growth.

The sample thus achieved has 1) a (845 ± 5) nm thick p^{++} with a boron doping equal to $(9 \pm 2) \times 10^{20}\,\mathrm{cm}^{-3}$; and 2) a (6160 ± 5) nm thick p^{-} layer with a low residual doping (some C-V experiment are currently ongoing to estimate the doping level). At the NanoFab platform, an etching was performed in two steps in order to have three different surface topologies: 1) a thick p^{-} layer (6.16 µm thick); 2) a thin p^{-} layer (2.7 µm thick) used during the eBIC and ToF-eBIC measurements; and 3) the p^{++} layer (p^{-} layer completely etched) used to bias the substrate and the p^{-} layer. Then, 100 nm thick aluminium contacts were achieved on the three layers. Although these contacts may not be the most suitable (resistivity between two p^{++} pads higher than expected), they are easy to set up and can be changed without modifying the diamond interface (no annealing). Some electric characterizations were conducted, and the Schottky natures of the ΔE stage of the device was highlighted. In the forward regime, currents up to few tens of milliampere were measured when few volts were applied. In the reverse regime, the current was limited to 10 µA at 10 V.

Some experiments were performed on the sample. The first one consisted in mapping the induced current using the eBIC technique. The Schottky barrier of the p^{-} layer was estimated at (1.70 ± 0.05) V and the impact of the growth defects on the charge collection was also evaluated. For particles passing through the p^{-} layer, more charges are deposited in the hillocks, while no charges are collected in the unepitaxial crystal. When a positive bias was applied on the back side of the substrate, the current was collected only in few small areas. These areas became bigger and more numerous over time. When 200 V was applied on the ∼530 µm thick substrate, the current was higher than expected. We assume that an avalanche effect occurs in the substrate. Measurements are ongoing to better understand this phenomenon. These effects were not observed when a negative bias was applied. Then, some spectroscopy were carried out using the ToF-eBIC technique. For 10 ns, the results are consistent with the CASINO simulations: 1) when the beam is focused on the thin p^- layer, the ratio of charges collected between the substrate and the p^- was 0.30 ± 0.03 (CASINO: 0.30); and 2) when the beam is focused on the p^{++} layer, the charges collected in the substrate was 63.1 ± 1.3 fC (expected value: 58.2 ± 3.9 fC). Nevertheless, for 100 ns pulses, some discrepancies were observed. They are probably due to in situ recombinations, but it was not possible to verify this assumption. Finally, some alpha spectroscopy measurements were conducted on the setup described in the Section 2.4. However, the observations were not in agreement with the previous results. The detector response remains the same whatever the bias applied on the p^- layer in the range $[-1\,\text{V}; 2\,\text{V}]$. When higher voltages (in absolute value) were applied, the fluctuations of the baseline were too intense to observe the signal. Regarding the substrate, no charges were collected when a negative bias was applied. In the case of a positive bias, a spectrum with three peaks was recorded. These peaks can be attributed to the case where the alpha particles pass through: 1) the thick p^- layer; 2) the thin p^- layer; and 3) the p^{++} layer. Some spectroscopy measurements of the two energy deposits are currently conducted in time coincidence in order to study the energy deposited in the p^- layer versus the energy deposited in the substrate.

As an alternative solution to the ΔE-E detectors, a *pn* diode developed by the National Institute for Materials Science (NIMS) at Tsukuba (Japan) was studied. This diode has a 1 µm active thickness and was tested during different experiments. The eBIC technique reveals small inner defaults where the collected current was significantly lower than the averaged induced current. The induced current was also measured depending on the primary electron energy and the applied bias voltage. The induced current increases with the bias voltage. This phenomenon is probably due to a higher CCE and an extension of the depletion regions in the n^+ layer. Moreover, whatever the bias applied, the normalized induced current was maximum at 15 keV. This result is consistent with the simulation performed with CASINO. A discrepancy between the experimental and simulated data was observed for the primary electron energies higher than 20 keV. This phenomenon could be explained by an active layer thicker than expected. Moreover, the alpha spectroscopy measurements, revealed that the charge collected (7.4 ± 0.9 fC) was higher than the one measured in previous similar measurements performed in Japan (4.7 ± 0.5 fC). The results are still consistent with a precision of 3σ and such a difference can also be explained by a thicker active layer. This preliminary experiment aimed to check that the detector assembly: *pn* junction mounted on a LPSC holder is operational. The next step consisted in using alpha micro beams at AIFIRA in Bordeaux. Some IBIC maps were performed that allowed to study the charge collection efficiency in the metallized and unmetallized areas. According to the SRIM simulation, when a 3 MeV $^4_2$He ions is impinging the diode, the charge collected in the metallized areas should be 12 keV greater than the one collected under the unmetallized areas (considering a 1 µm active thickness). This prediction was confirmed with a 1σ precision. To improve the performances of such a device, it may be interesting to reduce the doping levels in the active region or adapt the design depending on the nature and the energy of the incident particles. For instance, with a thicker active layer, it may be possible to use this device to achieve betavoltaic cells [Shimaoka, 2020].

These two kinds of detectors represent two innovative compact solutions for particle detection in a highly radiative environment thanks to the use of diamond materials. The characterization techniques implemented during the thesis, in particular the ToF-eBIC, demonstrated all its potential to improve the different growth and doping processes inherent to the fabrication of these future detectors. One can expect, in the near future, that this will allow to obtain solutions adapted to the needs of nuclear physics experiments, beam monitoring requirements, radioprotection of sensitive nuclear sites.

Conclusions

The work carried out during this PhD aimed to better understand the signal induced by short range charged particles in diamond devices in order to develop innovative diamond detectors. For this purpose, a new characterization technique, the ToF-eBIC, has been implemented to limit the polarization effects observed in laboratory experiments.

The ToF techniques are commonly used to evaluate the charge transport properties (charge carrier drift velocity, mobility and life-time) of diamond devices. Nevertheless, they present a major limitation, the polarization effects, which introduce a bias in the estimation of the diamond transport properties. This phenomenon caused by an inhomogeneous charge carrier trapping leads to a modification of the electric field distribution within the diamond bulk and a reduction in the amount of charge collected. To highlight their influence, several ultra-pure (electronic grade) synthetic scCVD Element 6 diamond sample were tested at laboratory. At first, I-V characterization were performed, and it was shown that, for this set of 550 µm thick diamond samples, the leakage current at ±500 V was relatively low (> 10 nA). Then experiments conducted with an alpha setup demonstrate the good charge properties of these sample. Average low-field mobilities of $(2600 \pm 190)\,\mathrm{cm^2/(V{\cdot}s)}$ and $(2200 \pm 160)\,\mathrm{cm^2/(V{\cdot}s)}$ were estimated for holes and electrons, respectively at room temperature. Moreover, the diamond samples exhibit a charge collection efficiency around 100 % for both charge carriers. During these measurements, the polarization effects were evidenced. Their influence is particularly significant at low electric fields. In fact, for an electric field of 0.09 V/µm, the amount of charge collected is divided by more than 3 in 15 min. This observation has motivated the development of new characterization methods. To study the crystalline quality of the diamond samples, X-ray topography and XBIC qualifications are now performed. They have revealed that the crystalline orientation is not constant over the whole surface of the samples. A new method of characterization was also developed in this work. In particular, it permits to limit the polarization effects, and thus study the samples on a large range of electric fields. This setup also allows for systematic, accurate, and rapid evaluation of device properties, while enabling new studies such as mapping charge collection efficiency.

This method consists in studying the current induced by electron pulses generated by a scanning electron microscope. The ToF-eBIC technique itself is not new, but the implementation of procedures to limit polarization effects makes it innovative. Indeed, this new setup, allowed a precise control on: 1) the energy deposited (up to 40 electrons of 30 keV per nanosecond); 2) the injection position (beam positioning at nanometer scale); 3) the density of free charge carrier (from ~10 nm to 300 µm beam diameter); and 4) the temperature (300 K down to 13 K). Polarization effects were investigated and proved to be minimized by spacing two consecutive pulses by 100 µm and by reducing the excitation density (unfocused electron beam). These optimizations, combined with an advanced cycling procedure based on a regular inversion of the bias voltage, allow measurements over a wide range of electric field and temperature. A slow control was developed to automatize the procedure and the data acquisition, and thus perform faster and more repeatable measurements. After confirming the high potential of this technique (comparison with results obtained with the alpha source), the intrinsic properties of diamond were studied at low temperatures (down 13 K). The drift velocity of electrons and holes versus electric field was assessed, and valley-polarized electrons were observed (below 90 K) for the first time since first report in 2013 [Isberg, 2013]. These experiments also aimed to evaluate the temperature dependence of the hole low-field mobility. Indeed, it has never been assessed, using the ToF technique, in intrinsic diamond below 80 K. The previous attempts were limited by neutral impurities [Jansen, 2013b] or demonstrate the necessity to perform measurements at very low electric fields [Majdi, 2013]. Thanks to our new technique, we successfully measured the drift velocity down to 1.5 V/cm at 13 K, and then estimate a hole low-field mobility of $(1.03 \pm 0.04) \times 10^6\,\mathrm{cm^2/(V{\cdot}s)}$ at this temperature. It is the highest hole low-field mobility measured in a bulk semiconductor, approaching the low-field mobility measured in 2D gas systems [Chung, 2022] and in graphene [Banszerus, 2016]. Regarding the cool and hot electron low-field mobility, the values are slightly lower than the one reported in [Konishi, 2020b]. This discrepancy, not observed for holes, is probably caused by the sample properties. ToF-eBIC experiment performed on their samples could confirm this hypothesis. The charge collected at high electric field was also investigated. As previously observed in [Jansen, 2013b, Cosic, 2022] with ions, the amount of charge collected suddenly decreases between 80 K and 120 K.

The perspectives of such a work would consist in an even deeper optimization of the SEM parameters. In particular, the impact of the cycling bias or the cycling time may be quantitatively investigated. To do so, quantitative figures of merit must be used. For instance, the integral of the signal and a fit of the top part of the signal could be interesting. To confirm the results obtained at low temperatures, the transport properties of other diamond samples should be investigated. Indeed, valley-polarized currents was already observed in two other samples, but unfortunately the cycling procedure and the strategy to limit the screening effect were not enough developed to extract the low field mobility. A model to fit the valley-polarized electron traces and one to take into account the inelastic scattering in order to compare the hole low field mobility below 30 K to some theoretical values may be achieved. Another relevant experiments, would be to apply a magnetic field inside of the SEM, in order to distinguish, as Isberg *et al.* [Isberg, 2013], the electrons of the (010) and (001) valleys.

Furthermore, two ToF-eBIC procedures were used as well to map the charge collection and the induced current of a 150 µm thick diamond sample at different scale (whole surface or at the micrometer scales). The charge collected on the metallized surfaces was homogeneous (more or less 3 % RMS) and the collected charge was divided by 4 at 50 µm from the edge of the metallization. Simulations are underway to verify if the shape of the electric field could be responsible for this effect. These mappings are complementary to the X-ray measurements performed at the ESRF [Gallin-Martel, 2021a]. Indeed, the ToF-eBIC technique permits to study the drift of the different charge carriers separately. This setup is also an opportunity to study some local defects such as the grain boundaries in pcCVD diamonds or the defects induced by the radiations. It can also used to optimize the design of the pad and stripped detector (size of/between the electrodes) and to study the cross-talk phenomenon. Finally, the transport properties of 550 µm thick diamond may be studied at different positions and different temperatures. The reduction of acquisition time and the production of a user manual are essential to make these studies achievable for future users.

Modern nuclear physics experiments require innovative detectors that can operate under intense beams. Diamond-based detectors are therefore of primary interest. In this context, a monolithic diamond ΔE-E telescope was realized to study alpha particles emitted by a ^{241}Am source. This project aimed to optimize the device reported in [Cesaroni, 2019, Verona, 2022] by reducing the thickness of the p^{++} layer (dead layer of detection) and improving the crystalline quality of the p^{-} layer. The chosen design consists of:

- an electronic grade[1] scCVD Element 6 substrate with a thickness of 530 µm;
- a 0.845 µm thick p^{++} layer deposited by DiamFab on the substrate and with a boron doping of $10^{20}\,\mathrm{cm}^{-3}$;
- a 6.16 µm thick p^{-} layer, not intentionally doped ($\leq 5 \times 10^{15}\,\mathrm{cm}^{-3}$), deposited by DiamFab on the highly doped layer

An etching was performed in the NanoFab clean room to reach the p^{++} layer (middle electrode) and to thin the p^{-} in some areas. Then, 100 nm thick aluminium contacts were achieved on each layer. The electric characterization and the eBIC measurements demonstrated the Schottky nature of the contacts. The Schottky barrier is (1.70 ± 0.05) V, and on reverse regime, the induced current is limited to 10 µA at 10 V. The eBIC measurements also reveal the impact of the growth defects on the charge collection: at the hillock locations, the induced current is greater (more energy deposited by particle passing through a thicker area) and at the unepitaxial crystal location, no current was measured. Some avalanche phenomena in the substrate occurring for one bias polarity were also observed. ToF-eBIC spectroscopies were then performed on a thinner p^{-} area. The distribution of energy measured in the p^{-} layer and in the substrate are consistent with the CASINO simulations (0.30 ± 0.03 compared to 0.30). When the beam was focused on the p^{++} layer, the charge collected in the substrate was in agreement with the expected value (63.1 ± 1.3 fC compared to 58.2 ± 3.9 fC). However, the alpha spectroscopy results are not in agreement with the one obtained using the ToF-eBIC technique (no signal measured on the p^{-} layer for biases greater than 2 V, and no signal measured when a negative bias is applied on the substrate). These discrepancies are not well understood and are still under investigation. A spectroscopy realized on the substrate revealed that it is possible to identify three peaks attributed to the case where alpha particles passed through the thick p^{-} layer, the thin p^{-} layer and the p^{++} layer. These results encourage us to measure the energy deposited in the p^{-} layer and in the substrate in time coincidence. A future device, based on a polished scCVD substrate (electronic grade) from Element 6, will soon be used to fabricate a second sample with improved growth conditions.

A *pn* junction made by the National Institute for Materials Science (NIMS) at Tsukuba (Japan) was studied on different test benches. The eBIC measurements were in good agreement with the CASINO simulations and shown that: 1) the active layer is probably thicker than expected; 2) the possible diffusion of charges from the doped layers may be more significant on the n^{+} side. The charge collected during the alpha spectroscopy experiments is compatible at

---

[1] $[\mathrm{N}] < 9 \times 10^{14}\,\mathrm{cm}^{-3}$ $[\mathrm{B}] < 2 \times 10^{14}\,\mathrm{cm}^{-3}$

only 3σ with the result reported by [Shimaoka, 2018]. These preliminary results encouraged us to achieved IBIC (Ion Beam Induced Current) measurements at the AIFIRA facility. This last experiments confirmed the SRIM software predictions by showing that the energy distribution resulting from the interaction of 3 MeV $^4_2$He ions in a metallized region could be distinguished with an accuracy of 1σ from that obtained in an unmetallized area. Thus, it demonstrates that an energy resolution of approximately 6 % may be reached in these specific conditions. To confirm these results, it is now necessary to perform measurements on a larger number of junctions. Future improvements in the crystal purity of the active region could lead to a device operating at 0 volt and thus become suitable for several applications such as radioactivity monitoring.

Diamonds can become standard detectors for particle detection, provided that the quality of the crystal, which depends on the growth process, is improved to a level that allows standard use by scientists without worrying about instabilities due especially to polarization effects. My work demonstrates that the ToF-eBIC technique will allow to finely characterize the performances of future detectors and that innovative solutions in terms of detection can thus be proposed with reading and acquisition firmwares adapted to any type of application: fast counting, beam positioning and flux measurement, particle tracking, detection in intense radiation environments.

A

Appendix

Contents

A.1 Influence of working out of focus for mapping procedure

A.1.1 Equipment and methods

As mentioned in Subsection 3.4.1.2, the amount of charge collected with the procedure to map with micrometer resolution was lower than with the procedure to study the drift rate. It is assumed that the charge carrier density resulting from very local impacts leads to very strong screening and polarization effects that lead to incomplete charge collection (see Subsection 3.2.3.

An experiment was carried out to quantify this effect: a 550 µm thick diamond sample was placed at the upper position in the SEM and the beam was focused on the sample. Then, without changing the beam focus, the diamond sample was moved to the lower position using the SEM positioning system. As a result, the beam was no longer focused on the sample and, by geometrical effects, the beam interaction area became larger. To quantify the beam spot broadening, the beam was focused on a large ∼4 µm dust located on the sample. In the following, the distance to the position where the focusing was performed will be referred to as the "defocusing distance".

A.1.2 Experimental results

Figure A.1 summarizes the most significant results obtained in this experiment. Working out-of-focus leads to a better charge collection and more defined signals, especially for holes (a). For holes, the signal became more rectangular and the collected charge is multiplied by a factor ∼ 3.3. For electrons (b), although the signal is a slightly more rectangular at higher defocusing distances, the shape remains similar. Only a factor ∼ 1.8 on the collected charge is observed. For both electrons and holes, a saturation of the collected charge is observed for a defocusing distance of 6 cm (c). Nevertheless, the shape of the signal continues to evolve until (at least) a defocusing distance of 8 cm.

To quantify the beam spot broadening, the size of a small dust was measured at each defocus distance. Assuming that the spot size is the convolution between the beam diameter and the dust diameter, it is observed that the beam diameter reaches a size of 60 µm at a defocus distance of 16 cm (see Figure A.1 (d)). Therefore, it appears that by defocusing the beam, the spatial resolution of the pattern is significantly reduced.

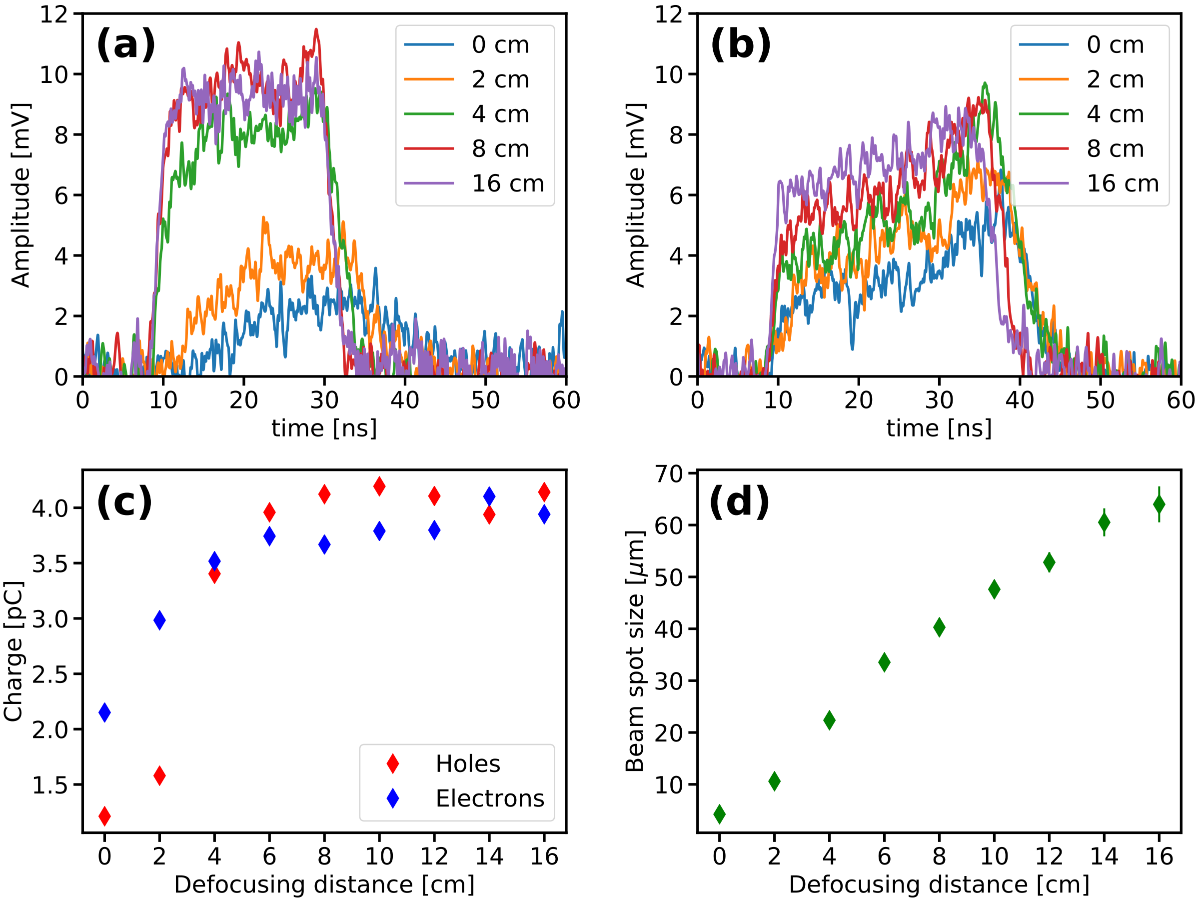

Figure A.1: Hole (a) and electrons (b) traces obtained for various defocusing distances. (c): Charge collection evolution in function of the defocusing distance for holes and electrons. (d): Electron beam spot size depending on the defocusing distance.

This experiment demonstrated that by working out of focus, a significant gain in collected charge and rectangular shaped signals can be obtained. However, the spatial resolution is reduced: to completely limit the screening effects, a 60 µm was used. This did not allow to obtain a mapping with microscopic resolution. In other experiments, beam diameters up to 300 µm were also used.

A.2 Charge collection evolution when the beam is moving away from the edge of the pad - Fit

The following ToF-eBIC experiment was performed on a 150 µm pad detector using the cycling procedure described in Subsubsection 3.4.1.1. The study conducted here aimed to study the evolution of the charge collection when the electron beam is moving away from the edge of a metallic pad.

As described in Subsubsection 3.4.2.1, when the electron beam is on the pad, the charge collection remains constant. When it is moving away from the edge of the pad (following the blue line on Figure A.2 (a)), the charge collection decreases. The data were fitted with two different functions. First, the charge collection decreasing slope was fitted using a $1/x$ law:

$$Q(x) = \frac{q_1}{x - x_0} + q_\infty \tag{A.1}$$

with $Q(x)$ the charge measured at a distance x from the first measurement position, q_1 the charge at distance 1 mm from the first measurement position, x_0 a position parameter of the $1/x$ law, and q_∞ the charge collected far from the first position (noise level in this study).

These results was compared to another fit using an exponential fit function:

$$Q(x) = exp\left(\frac{x - x_0}{\lambda}\right) + q_\infty \tag{A.2}$$

with λ a distance characterizing the charge evolution.

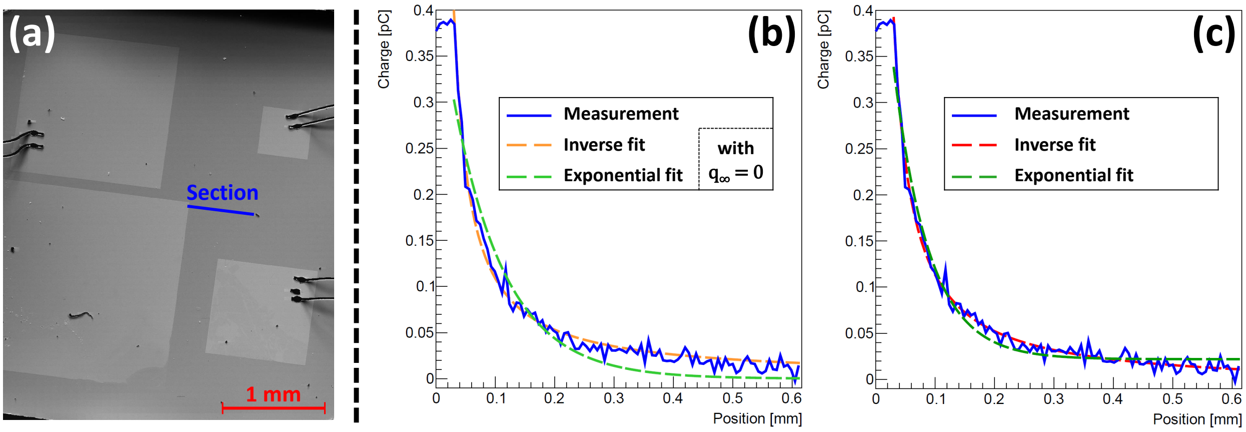

Figure A.2: (a): SEM image of the 150 µm pad detector. The blue line represents the section where the study was performed. (b) and (c): Charge collection versus the position from the edge of the pad. The data were fitted using the equations A.1 (orange and red curves) and A.2 (green curves). In (b), the parameter q_∞ was set to 0 pC, whereas in (c), it is a free parameter.

The results of the fit are presented in Figure A.2 (b) and (c). It is expected to have q_∞ very close to zero, this is why, in a first time, this parameter was set to 0. In Figure A.2 (b) and (c), the $1/x$ law described better the charge evolution than the exponential function.

The fit parameters of the $1/x$ function were extracted and, as expected, the q_∞ parameter is close to zero.

Table A.1: Fit parameters obtained by fitting the data with Equation A.1.

	Units	Value	Error
x_0	[mm]	8.02e-4	1.30e-3
q_1	[pC]	1.23e-2	4.23e-4
q_∞	[pC]	9.12e-3	1.58e-3

A.3 Etching masks used to fabricate the diamond monolithic ΔE-E telescope

A.3.1 Fist etching

The resist after development (left) and the metallic mask (right) achieved for the first etching of the ΔE-E sample are shown in Figure A.3. The images is composed of nine pictures taken with an optical microscope. The images were aligned together in order to make a picture of the whole sample. The first image shows that the development was correctly done: the remaining resist (darker area) is only on the outer area and is well defined. The second one shows that the metallic mask (lighter area) is well positioned at the middle of the sample.

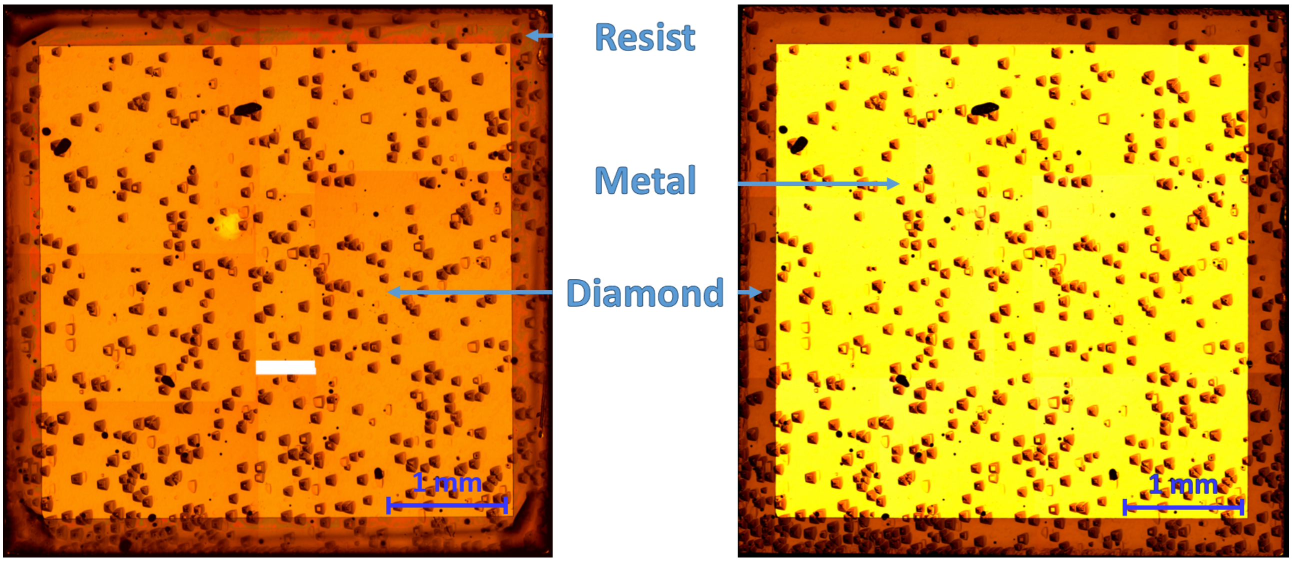

Figure A.3: Resist after development (left) and metallic mask (right) achieved for the first etching of the ΔE-E sample.

A.3.2 Second etching

The resist after development (left) and the metallic mask (right) achieved for the second etching of the ΔE-E sample are shown in Figure A.4. On both images, the border of the first etching can be observed (outside square). The first image demonstrates that the development was correctly done: the remaining resist (darker area) is is only on the outer area and is well defined. The second one shows that the metallic mask (lighter area) is well positioned at the middle of the sample. A small metallization defect is visible on the top right of the sample. It was not possible to remove it without risking to damage the whole metallic mask.

A.3.3 After etching

The sample after the etchings is shown in Figure A.5 (left). On this image, few defects can be noticed: 1) some black dots appears on the edges (on the p^{++} layer) of the diamond sample (red square); 2) the metal residues observed previously are still visible (blue square). The black dots are between 1.5 to 3 µm diameter. For the moment, their origin was not identified. More

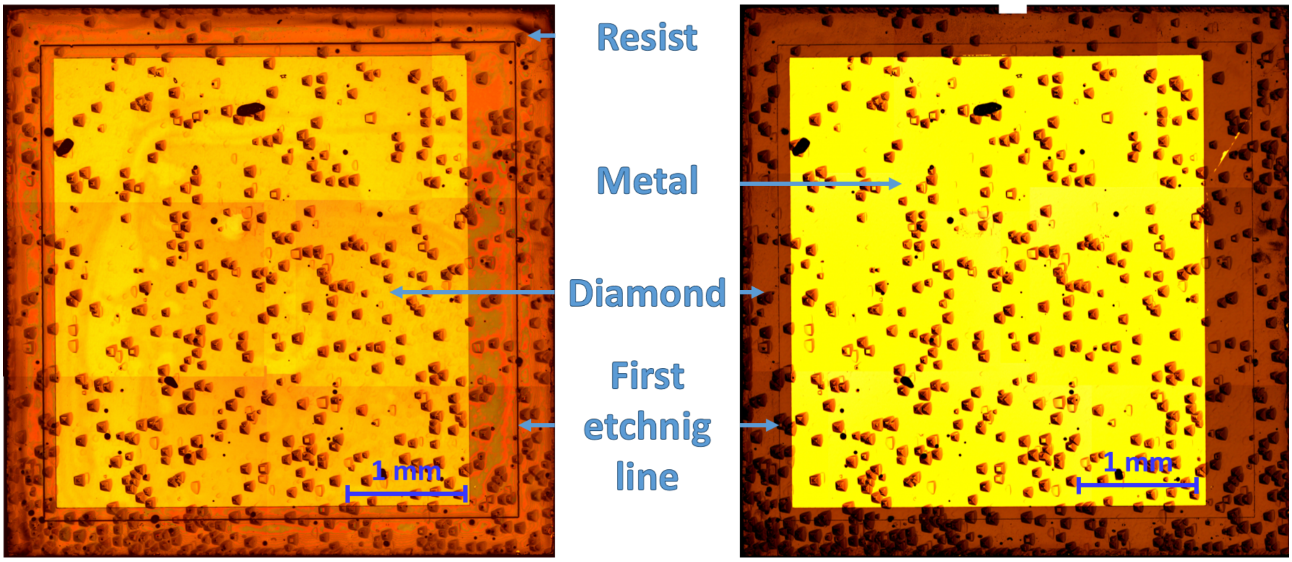

Figure A.4: Resist after development (left) and metallic mask (right) achieved for the second etching of the ΔE-E sample.

surprisingly, under the large metal residue, some similar black dots are also visible. These back dots are very similar to the dark inclusions observed by Tallaire *et al.* [Tallaire, 2008]. Thus, if their origin is similar, these black spots can be attributed to agglomerated impurities or amorphous carbon.

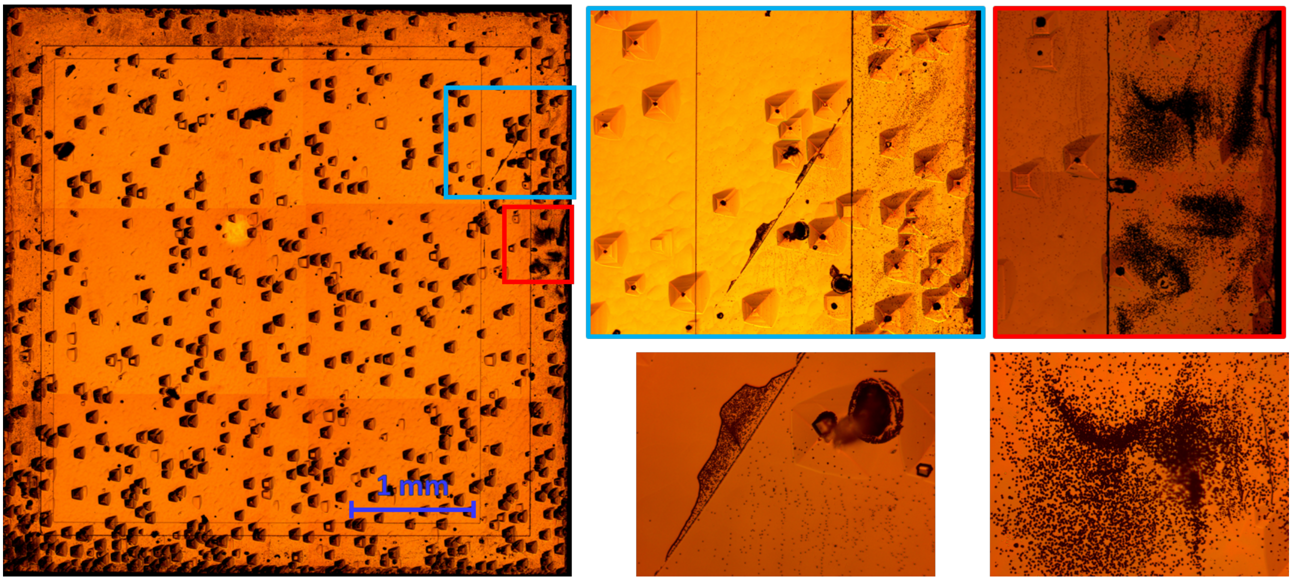

Figure A.5: ΔE-E sample after the two etchings. Zooms on two etched regions evidenced the presence of black dots with a 1.5 to 3 µm diameter.

A.4 eBIC measurements performed in beam spot for different beam energies

A.4.1 Experimental procedure

The beam was used in beam spot to study the current induced versus the beam position for various beam energies ranging from 10 to 30 keV. During this experiment, 10 V was applied on the p^- layer and 200 V on the substrate.

A scheme of the experimental setup is shown in Figure A.6. The current induced in the p^- layer and in the substrate was compared in both configurations.

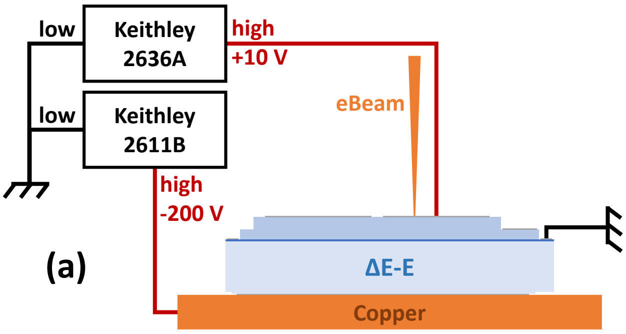

Figure A.6: Setup of the eBIC experiment performed in beam spot.

This experiment was performed quite recently and is not well understood yet. In particular, a strong time dependency on the measured induced current was noticed. Thus, the experiment will be carried out again in the early 2023 to confirm or not the results obtained.

A.4.2 CASINO simulations

To evaluate the energy deposited in the different layer, CASINO simulations were performed. The different layers of the sample were simulated: the 100 nm thick aluminium metallization, the p^- layer, the p^{++} layer and the substrate. Figure A.7 (left), the different energy deposit depending on the depth of the later are represented for nine different energies. The metallization, the thin p^- layer (~2.7 µm thick), the p^{++} layer and the substrate are represented respectively by the white, blue, red and green areas. In this graph, it can be observed that, for the simulated energies, the primary always deposed part of their energy in the p^- layer. Up to 20 keV the primary electrons are stopped within the p^- layer. The primary electrons are depositing energy in the substrate for energies greater then 25 keV. The simulation were also achieved for the thick p^- layer (6.16 µm thick), but whatever the energy, the primary electrons do not depose any energy in the substrate: they are stopped in the p^- layer.

A.4.3 Experimental results

The experiment was carried out four times. In a first time, 10 V was applied on the thin p^- layer (contact 1, see Figure 4.9) and 200 V were applied on the substrate. The beam was focused on the contact 1 and the current measured in the substrate, I_{sub}, and in the thin p^- layer, I_{p^-}, were measured. The ratio between the two latter quantities was then

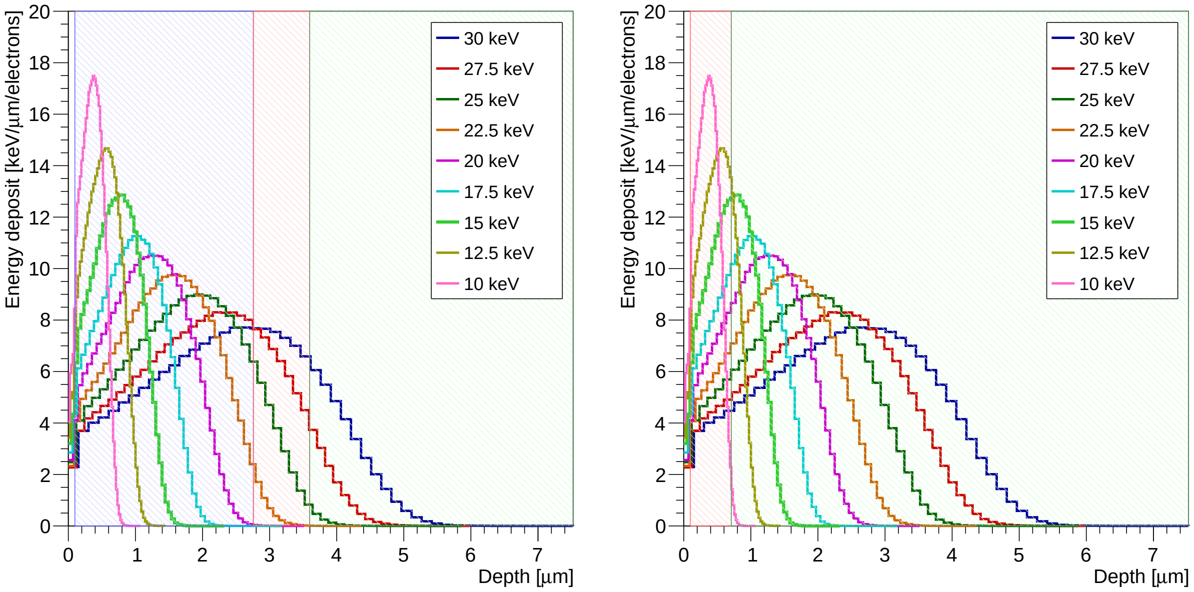

Figure A.7: Energy deposit depending on the sample depth when the beam is focused on the thin p^- layer (left) and on the p^{++} layer.

computed. The experiment was performed a second time by applying 10 V on the thick p^- layer (contact C, see Figure 4.9) and focusing the beam on this area. The result are shown in Figure A.8 (left). Whatever the primary electron energy, the current ratio in the thick p^- layer remains null. This was completely expected because the electrons are stopped in the layer, and thus, no energy was deposited in the substrate (CASINO simulations). In contrast, when the beam was focused on the thin p^- layer the current start to increase sharply around 25 keV. In this plot, the CASINO simulated data were multiplied by a factor 5.4 in order to distinguished them from the background. By doing so, the data are relatively well described by the simulations. Nevertheless, the values measured in the p^- layer are greater than expected and this phenomenon is not understood yet. They might be explained by an avalanche phenomenon in the substrate.

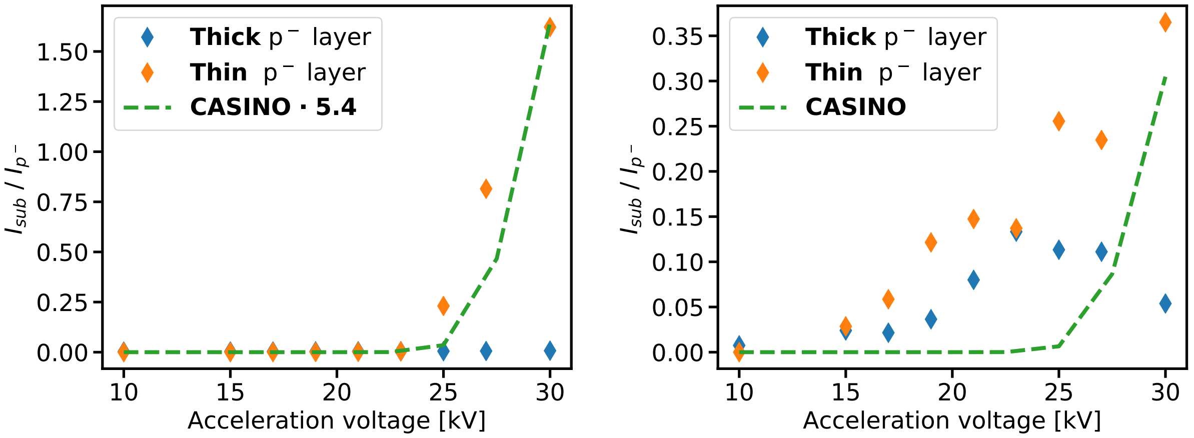

Figure A.8: Ratio between the current measure in the substrate and the p^- layer. Left: 200 V were applied on the substrate. Right: −200 V were applied on the substrate.

The same two experiments were performed when $-200\,\mathrm{V}$ was applied on the substrate. The results are presented in the Figure A.8 (right). The CASINO simulated data were added (without correction). The simulated data hardly describes the experimental data obtained in the thin p^- layer. This is probably due to the strong time dependency of the induced current. Each time that the beam was switched on, the current increased and reached a peak before decreasing. This phenomenon induced strong uncertainties which may explain the data. During this experiment, these uncertainties were not estimated.

Bibliography

[Achard, 2011] *Cité section 1.2.3*

Achard J., Silva F., Issaoui R., Brinza O., Tallaire A., et al. (2011).
Thick boron doped diamond single crystals for high power electronics.
Diamond and Related Materials, 20(2):145–152.

[Akimoto, 2014] *Cité section 3.3*

Akimoto I., Handa Y., Fukai K., and Naka N. (2014).
High carrier mobility in ultrapure diamond measured by time-resolved cyclotron resonance.
Applied Physics Letters, 105(3):032102. Publisher: American Institute of Physics.

[Angelone, 2019] *Cité dans les sections 1.3.4.3 et 3.2.1.1*

Angelone M., Cesaroni S., Loreti S., Pagano G., and Pillon M. (2019).
High temperature response of a single crystal CVD diamond detector operated in current mode.
Nuclear Instruments and Methods in Physics Research Section A: Accelerators, Spectrometers, Detectors and Associated Equipment, 943:162493.

[Badalà, 2022] *Cité section 4.1.1*

Badalà A., La Cognata M., Nania R., Osipenko M., Piantelli S., et al. (2022).
Trends in particle and nuclei identification techniques in nuclear physics experiments.
La Rivista del Nuovo Cimento, 45(3):189–276.

[Banszerus, 2016] *Cité dans les sections 3.5 et 4.6*

Banszerus L., Schmitz M., Engels S., Goldsche M., Watanabe K., et al. (2016).
Ballistic transport exceeding 28 µm in CVD grown graphene.
Nano Letters, 16(2):1387–1391.

[Barberet, 2011] *Cité section 4.5.4.1*

Barberet P., Daudin L., Gordillo N., Sorieul S., Simon M., et al. (2011).
First results obtained using the CENBG nanobeam line: Performances and applications.
Nuclear Instruments and Methods in Physics Research Section B: Beam Interactions with Materials and Atoms, 269(20):2163–2167.

[Barberet, 2021] *Cité section 4.5.4.1*

Barberet P., Jouve J., Sorieul S., Alfaurt P., and Mathieu L. (2021).
AIFIRA: a light ion beam facility for ion beam analysis and irradiation.

The European Physical Journal Plus, 136(1):67.

[Bentele, 2016] *Cité dans les sections 1.3.4.3 et 3.2.1.1*

Bentele B., Cumalat J., Schaeffer D., Wagner S., Riley G., et al. (2016).
Rate dependence, polarization, and light sensitivity of neutron-irradiated scCVD diamond sensors.
Nuclear Instruments and Methods in Physics Research Section A: Accelerators, Spectrometers, Detectors and Associated Equipment, 838:74 – 81.

[Berdermann, 2019] *Cité dans les sections 1.2.4 et 1.3.5.1*

Berdermann E., Afanaciev K., Ciobanu M., Fischer M., Gsell S., et al. (2019).
Progress in detector properties of heteroepitaxial diamond grown by chemical vapor deposition on Ir/YSZ/Si(001) wafers.
Diamond and Related Materials, 97:107420.

[Bergonzo, 2003] *Cité section 3.5*

Bergonzo P., Barrett R., Hainaut O., Tromson D., and Mer C. (2003).
Evidence of localised charge build-up mechanisms in CVD diamond as observed using micro-X-ray beam analysis.
Nuclear Instruments and Methods in Physics Research Section A: Accelerators, Spectrometers, Detectors and Associated Equipment, 514(1):100–105.

[Bergonzo, 2008] *Cité dans les sections 1.3.4.3 et 3.2.1.1*

Bergonzo P., Hamrita H., Tromson D., Descamps C., Mer C., et al. (2008).
Probing The Transient Response To Improve The Stability Of Diamond Devices Under Pulsed Periodic Excitation.
MRS Online Proceedings Library, 1039(1):601.

[Bergonzo, 2007] *Cité dans les sections 1.3.4.3 et 3.2.1.1*

Bergonzo P., Tromson D., Descamps C., Hamrita H., Mer C., et al. (2007).
Improving diamond detectors: A device case.
Diamond and Related Materials, 16(4):1038–1043.

[Bethe, 1930] *Cité section 1.3.1.1*

Bethe H. (1930).
Zur Theorie des Durchgangs schneller Korpuskularstrahlen durch Materie.
Annalen der Physik, 397(3):325–400.

[Bloch, 1933] *Cité section 1.3.1.1*

Bloch F. (1933).
Zur Bremsung rasch bewegter Teilchen beim Durchgang durch Materie.
Annalen der Physik, 408(3):285–320.

[Bogdanov, 2017] *Cité section 1.2.3*

Bogdanov S. A., Vikharev A. L., Drozdov M. N., and Radishev D. B. (2017).
Synthesis of thick and high-quality homoepitaxial diamond with high boron doping level: Oxygen effect.
Diamond and Related Materials, 74:59–64.

[Bousquet, 2015] *Cité section 4.3.1.1*

Bousquet J. (2015). *Optical and electronic properties of heavily boron-doped diamond.* phdthesis, Université Grenoble Alpes.

[Canali, 1979] *Cité dans les sections 1.3.5.1, 2.4.1, 3, et 3.3*

Canali C., Gatti E., Kozlov S., Manfredi P., Manfredotti C., et al. (1979).
Electrical properties and performances of natural diamond nuclear radiation detectors.
Nuclear Instruments and Methods, 160(1):73–77.

[Carboni, 2012] *Cité section 4.1.1*

Carboni S., Barlini S., Bardelli L., Le Neindre N., Bini M., et al. (2012).
Particle identification using the technique and pulse shape discrimination with the silicon detectors of the FAZIA project.
Nuclear Instruments and Methods in Physics Research Section A: Accelerators, Spectrometers, Detectors and Associated Equipment, 664(1):251–263.

[Caughey, 1967] *Cité dans les sections 1.3.5.3 et 2.3.2.1*

Caughey D. and Thomas R. (1967).
Carrier mobilities in silicon empirically related to doping and field.
Proceedings of the IEEE, 55(12):2192–2193.

[Cesaroni, 2019] *Cité dans les sections 4.1.1, 4.1.2, 4.1.3, 4.6, et 4.6*

Cesaroni S., Marinelli M., Milani E., Prestopino G., Verona C., et al. (2019).
Δ E - E single crystal diamond based telescope.
Nuclear Instruments and Methods in Physics Research Section A: Accelerators, Spectrometers, Detectors and Associated Equipment, 947:162744.

[Chung, 2022] *Cité dans les sections 3.5 et 4.6*

Chung Y. J., Wang C., Singh S. K., Gupta A., Baldwin K. W., et al. (2022).
Record-quality GaAs two-dimensional hole systems.
Physical Review Materials, 6(3):034005. arXiv:2203.10713 [cond-mat].

[Ciampi, 2019] *Cité section 4.1.1*

Ciampi C., Pasquali G., Altana C., Bini M., Boscardin M., et al. (2019).
Nuclear fragment identification with Δ E-E telescopes exploiting silicon carbide detectors.
Nuclear Instruments and Methods in Physics Research Section A: Accelerators, Spectrometers, Detectors and Associated Equipment, 925:60–69.

[Collins, 1971] *Cité section 1.2.3*

Collins A. T. and Williams A. W. S. (1971).
The nature of the acceptor centre in semiconducting diamond.
Journal of Physics C: Solid State Physics, 4(13):1789.

[Cosic, 2022] *Cité dans les sections 3.3.2.4, 3.5, et 4.6*

Cosic D., Provatas G., Jakšić M., and Begušić D. (2022).
Charge collection efficiency of scCVD diamond detectors at low temperatures.
Diamond and Related Materials, 127:109184.

[Curtoni, 2020] *Cité dans les sections 1.1, 1.2.4, 1.10, 1.3.3.2, 1.14, 1.3.4.3, 1.3.5.2, 2.2, 2.2.1, 2.3, 2.4.1, 2.11, 2*

Curtoni S. (2020). *Développement d'un démonstrateur d'hodoscope faisceau en diamant pour le contrôle en ligne du parcours des ions en hadronthérapie*. PhD thesis.

[Daudin, 2013] *Cité section 4.5.4.1*

Daudin L., Barberet P., Serani L., and Moretto P. (2013).
CRionScan: A stand-alone real time controller designed to perform ion beam imaging, dose controlled irradiation and proton beam writing.
Nuclear Instruments and Methods in Physics Research Section B: Beam Interactions with Materials and Atoms, 306:64–70.

[Dean, 1965] *Cité section 3.2.3.3*

Dean P. J., Lightowlers E. C., and Wight D. R. (1965).
Intrinsic and Extrinsic Recombination Radiation from Natural and Synthetic Aluminum-Doped Diamond.
Physical Review, 140(1A):A352–A368. Publisher: American Physical Society.

[Djurberg, 2021] *Cité section 3.3.2.3*

Djurberg V., Majdi S., Suntornwipat N., and Isberg J. (2021).
Investigation of Photoexcitation Energy Impact on Electron Mobility in Single Crystalline CdTe.
Materials, 14(15):4202.

[Djurberg, 2022] *Cité dans les sections 3 et 3.3.2.1*

Djurberg V., Majdi S., Suntornwipat N., and Isberg J. (2022).
Determination of the acoustic phonon deformation potentials in diamond.
Physical Review B, 106(4):045205. Publisher: American Physical Society.

[Dobrzhinetskaya, 2012] *Cité dans les sections 1.4 et A.4.3*

Dobrzhinetskaya L. F. (2012).
Microdiamonds — frontier of ultrahigh-pressure metamorphism: A review.
Gondwana Research, 21(1):207 – 223. Tectonic evolution of Tibet and surrounding regions.

[Donatini, 2016] *Cité section 3.1*

Donatini F., de Luna Bugallo A., Tchoulfian P., Chicot G., Sartel C., et al. (2016).
Comparison of Three E-Beam Techniques for Electric Field Imaging and Carrier Diffusion Length Measurement on the Same Nanowires.
Nano Letters, 16(5):2938–2944. Publisher: American Chemical Society.

[Donato, 2019] *Cité dans les sections 2.3.2.1 et 3.3*

Donato N., Rouger N., Pernot J., Longobardi G., and Udrea F. (2019).
Diamond power devices: state of the art, modelling, figures of merit and future perspective.
Journal of Applied Physics, 53:093001.

[Dorfer, 2019] *Cité dans les sections 1 et 1.3.5.1*

Dorfer C., Hits D., Kasmi L., Kramberger G., Lucchini M., et al. (2019).
Three-dimensional charge transport mapping by two-photon absorption edge transient-current technique in synthetic single-crystalline diamond.
Applied Physics Letters, 114(20):203504.

[Driche, 2018] *Cité dans les sections 1.6 et A.4.3*

Driche K. (2018). *Diamond unipolar devices : towards impact ionization coefficients extraction.* phdthesis, Université de Tsukuba.

[Drouin, 2007] *Cité section 3.2*

Drouin D., Couture A. R., Joly D., Tastet X., Aimez V., et al. (2007).
CASINO V2.42—A Fast and Easy-to-use Modeling Tool for Scanning Electron Microscopy and Microanalysis Users.
Scanning, 29(3):92–101.

[Eaton-Magaña, 2012] *Cité dans les sections 1.5 et A.4.3*

Eaton-Magaña S. and D'Haenens-Johansson U. F. (2012).
Recent Advances in CVD Synthetic Diamond Quality.
Gems & Gemology, 48(2):124–127.

[Ferry, 1975] *Cité section 1.1.3*

Ferry D. K. (1975).
High-field transport in wide-band-gap semiconductors.
Physical Review B, 12(6):2361–2369. Publisher: American Physical Society.

[Gabrysch, 2010] *Cité dans les sections 1.3.3.1, 1.3.5.2, 1.18, 3.3.2.1, 3.3.2.1, et A.4.3*

Gabrysch M. (2010). *Charge Transport in Single-crystalline CVD Diamond.* PhD thesis, Uppsala. OCLC: 658070121.

[Gabrysch, 2011] *Cité dans les sections 1.3.4.3, 1.3.5.1, 2.3.2.1, 3, 3.2.1.1, 3.3, 3.3.2.3, et 3.3.3*

Gabrysch M., Majdi S., Twitchen D. J., and Isberg J. (2011).
Electron and hole drift velocity in chemical vapor deposition diamond.
Journal of Applied Physics, 109(6):063719.

[Gallin-Martel, 2021a] *Cité dans les sections 1.2.4, 3.4, 3.5, et 4.6*

Gallin-Martel M.-L., Curtoni S., Marcatili S., Abbassi L., Bes A., et al. (2021a).
X-ray beam induced current analysis of CVD diamond detectors in the perspective of a beam tagging hodoscope development for hadrontherapy on-line monitoring.
Diamond and Related Materials, 112:108236.

[Gallin-Martel, 2021b] *Cité section 4.1.1*

Gallin-Martel M. L., Kim Y. H., Abbassi L., Bes A., Boiano C., et al. (2021b).
Characterization of Diamond and Silicon Carbide Detectors With Fission Fragments.
Frontiers in Physics, 9:732730.

[Gkoumas, 2009] *Cité dans les sections 1.3.5.1, 2.3.2.1, 3, et 3.3.3*

Gkoumas S., Lohstroh A., and Sellin P. (2009).
Low temperature time of flight mobility measurements on synthetic single crystal diamond.
Diamond and Related Materials, 18(11):1338–1342.

[Goulding, 1964] *Cité section 4.1.1*

Goulding F. S., Landis D. A., Cerny J., and Pehl R. H. (1964).
A new particle identifier technique for Z = 1 and Z = 2 particles in the energy range > 10 MeV.
Nuclear Instruments and Methods, 31(1):1–12.

[Guerrero, 2006] *Cité dans les sections 1.3.4.3 et 3.2.1.1*

Guerrero M. J., Tromson D., Descamps C., and Bergonzo P. (2006).
Recent improvements on the use of CVD diamond ionisation chambers for radiotherapy applications.
Diamond and Related Materials, 15(4):811–814.

[Gunzert-Marx, 2008] *Cité section 4.1.1*

Gunzert-Marx K., Iwase H., Schardt D., and Simon R. S. (2008).
Secondary beam fragments produced by 200 $\mathrm{MeV\,u^{-1}}$ ^{12}C ions in water and their dose contributions in carbon ion radiotherapy.
New Journal of Physics, 10(7):075003.

[Guthoff, 2013] *Cité dans les sections 1.3.4.3 et 3.2.1.1*

Guthoff M., Afanaciev K., Dabrowski A., de Boer W., Lange W., et al. (2013).
Radiation damage in the diamond based beam condition monitors of the CMS experiment at the Large Hadron Collider (LHC) at CERN.
Nuclear Instruments and Methods in Physics Research Section A: Accelerators, Spectrometers, Detectors and Associated Equipment, 730:168–173.

[Hoarau, 2021] *Cité dans les sections 2.1.2 et 2.2*

Hoarau C., Bosson G., Bouly J.-L., Curtoni S., Dauvergne D., et al. (2021).
Rf pulse amplifier for cvd-diamond particle detectors.
Journal of Instrumentation, 16(04):T04005.

[Holmes, 2019] *Cité dans les sections 1.3.4.3 et 3.2.1.1*

Holmes J. M., Dutta M., Koeck F. A., Benipal M. K., Hathwar R., et al. (2019).
Neutralizing the polarization effect of diamond diode detectors using periodic forward bias pulses.
Diamond and Related Materials, 94:162–165.

[Ibragimov, 2016] *Cité dans les sections 1.3.4.3 et 3.2.1.1*

Ibragimov R. F., Tyurin E. M., Kadilin V. V., Kolyubin V. A., Zaharchenko K. V., et al. (2016).
Research of work stability of diamond detectors used in SCR DDIR.
Journal of Physics: Conference Series, 675(4):042013. Publisher: IOP Publishing.

[Isberg, 2013] *Cité dans les sections 1.1.2, 3, 3.3, 3.3.2.1, 3.3.2.2, 3.3.2.3, 3.3.3, 3.5, et 4.6*

Isberg J., Gabrysch M., Hammersberg J., Majdi S., Kovi K. K., et al. (2013).
Generation, transport and detection of valley-polarized electrons in diamond.
Nature Materials, 12(8):760–764.

[Isberg, 2012] *Cité dans les sections 1.2, 3, 3.3, 3.3.2.2, 3.3.2.2, 3.3.2.3, et A.4.3*

Isberg J., Gabrysch M., Majdi S., and Twitchen D. J. (2012).
Negative electron mobility in diamond.
Applied Physics Letters, 100(17):172103.

[Isberg, 2006] *Cité dans les sections 1.3.4.3 et 3.3.3*

Isberg J., Gabrysch M., Tajani A., and Twitchen D. J. (2006).
Transient current electric field profiling of single crystal CVD diamond.
Semiconductor Science and Technology, 21(8):1193–1195.

[Isberg, 2002] *Cité dans les sections 1.3.5.1 et 3.3*

Isberg J., Hammersberg J., Johansson E., Wikström T., Twitchen D. J., et al. (2002).
High Carrier Mobility in Single-Crystal Plasma-Deposited Diamond.
Science, 297(5587):1670–1672.

[Isberg, 2005] *Cité section 3.3.2.3*

Isberg J., Lindblom A., Tajani A., and Twitchen D. (2005).
Temperature dependence of hole drift mobility in high-purity single-crystal CVD diamond.
physica status solidi (a), 202(11):2194–2198.

[Isberg, 2009] *Cité section 3.3.2.3*

Isberg J., Majdi S., Gabrysch M., Friel I., and Balmer R. (2009).
A lateral time-of-flight system for charge transport studies.
Diamond and Related Materials, 18(9):1163–1166.

[Jansen, 2013a] *Cité dans les sections 1.7, 2.3.2.1, 2.4.1, 3.3, 3.3.2.1, 3.3.2.4, et A.4.3*

Jansen H. (2013a). *Jansen - 2013 - Charge Carrier Movement at Low Temperatures and Use in Time-Critical Applications.pdf.* PhD thesis.

[Jansen, 2013b] *Cité dans les sections 1.3.5.1, 3, 3.3, 3.3.2.1, 3.3.3, 3.5, et 4.6*

Jansen H., Dobos D., Eisel T., Pernegger H., Eremin V., et al. (2013b).
Temperature dependence of charge carrier mobility in single-crystal chemical vapour deposition diamond.
Journal of Applied Physics, 113(17):173706.

[Kanda, 1996] *Cité section 4.3.1.2*

Kanda H. and Ohsawa T. (1996).
Growth hillocks on the “111” surface of high pressure synthetic diamond.
Diamond and Related Materials, 5(1):8–12.

[Kaneko, 1996] *Cité section 2.4.1*

Kaneko J. and Katagiri M. (1996).
Diamond radiation detector using a synthetic IIa type mono-crystal.
Nuclear Instruments and Methods in Physics Research Section A: Accelerators, Spectrometers, Detectors and Associated Equipment, 383(2-3):547–548.

[Kassel, 2016] *Cité section 1.3.4.3*

Kassel F., Guthoff M., Dabrowski A., and de Boer W. (2016).
Severe signal loss in diamond beam loss monitors in high particle rate environments by charge trapping in radiation-induced defects.
physica status solidi (a), 213(10):2641–2649. _eprint: https://onlinelibrary.wiley.com/doi/pdf/10.1002/pssa.201600185.

[Kasu, 2016] *Cité dans les sections 1.5 et A.4.3*

Kasu M. (2016).
Diamond epitaxy: Basics and applications.
Progress in Crystal Growth and Characterization of Materials, 62(2):317 – 328. Special Issue: Recent Progress on Fundamentals and Applications of Crystal Growth; Proceedings of the 16th International Summer School on Crystal Growth (ISSCG-16).

[Kato, 2016] *Cité section 1.2.3*

Kato H., Ogura M., Makino T., Takeuchi D., and Yamasaki S. (2016).
N-type control of single-crystal diamond films by ultra-lightly phosphorus doping.
Applied Physics Letters, 109(14):142102. Publisher: American Institute of Physics.

[Kato, 2005] *Cité section 1.2.3*

Kato H., Yamasaki S., and Okushi H. (2005).
n-type doping of (001)-oriented single-crystalline diamond by phosphorus.
Applied Physics Letters, 86(22):222111. Publisher: American Institute of Physics.

[Keister, 2018] *Cité section 2.4.1*

Keister J. W., Cibik L., Schreiber S., and Krumrey M. (2018).
Characterization of a quadrant diamond transmission X-ray detector including a precise determination of the mean electron–hole pair creation energy.
Journal of Synchrotron Radiation, 25(2):407–412.

[Khomich, 2019] *Cité dans les sections 4.3.1.2 et 4.3.1.2*

Khomich A. A., Bolshakov A. P., Ashkinazi E. E., Khomich A. V., Khmelnitsky R. A., et al. (2019).
Optical spectroscopy characterization of growth hillocks on the surface of homoepitaxial CVD diamond films.
Journal of Physics: Conference Series, 1199(1):012006. Publisher: IOP Publishing.

[Kim, 2021] *Cité section 1.2.4*

Kim S.-W., Takaya R., Hirano S., and Kasu M. (2021).
Two-inch high-quality (001) diamond heteroepitaxial growth on sapphire (1120) misoriented substrate by step-flow mode.
Applied Physics Express, 14(11):115501. Publisher: IOP Publishing.

[Kim, 1984] *Cité section 4.1.1*

Kim Y., Kim C., Husimi K., Ohkawa S., Fuchi Y., et al. (1984).
Epitaxial integrated dE1 - dE2 silicon detectors.
Nuclear Instruments and Methods in Physics Research Section A: Accelerators, Spectrometers, Detectors and Associated Equipment, 226(1):125–128.

[Koike, 1992] *Cité section 4.2.2.1*

Koike J., Parkin D. M., and Mitchell T. E. (1992).
Displacement threshold energy for type IIa diamond.
Applied Physics Letters, 60(12):1450–1452.

[Koizumi, 1997] *Cité section 1.2.3*

Koizumi S., Kamo M., Sato Y., Ozaki H., and Inuzuka T. (1997).
Growth and characterization of phosphorous doped {111} homoepitaxial diamond thin films.

Applied Physics Letters, 71(8):1065–1067. Publisher: American Institute of Physics.

[Konishi, 2020a] *Cité dans les sections 3.2.3.3 et 3.2.3.3*

Konishi K., Akimoto I., Isberg J., and Naka N. (2020a).
Diffusion-related lifetime and quantum efficiency of excitons in diamond.
Physical Review B, 102(19):195204.

[Konishi, 2020b] *Cité dans les sections 3.3, 3.3.2.3, 3.17, 3.3.3, 3.5, 4.6, et A.4.3*

Konishi K., Akimoto I., Matsuoka H., Djurberg V., Majdi S., et al. (2020b).
Low-temperature mobility-lifetime product in synthetic diamond.
Applied Physics Letters, 117(21):212102.

[Konishi, 2022] *Cité dans les sections 3.3, 3.3.2.3, 3.3.2.4, et 3.5*

Konishi K., Akimoto I., Matsuoka H., Isberg J., and Naka N. (2022).
Intrinsic Mobility of Low-Density Electrons in Photoexcited Diamond.
Physical Review Applied, 17(3):L031001.

[Kordyasz, 2004] *Cité dans les sections 4.1.1 et 4.1.2*

Kordyasz A., Nossarzewska-Orłowska E., Piasecki E., Lipiński D., Brzozowski A., et al. (2004).
Response to heavy ions and fission fragments of the monolithic silicon E–ΔE telescopes produced by the Quasi-Selective Epitaxy.
Nuclear Instruments and Methods in Physics Research Section A: Accelerators, Spectrometers, Detectors and Associated Equipment, 530(1-2):87–91.

[Kozlov, 1975] *Cité section 2.4.1*

Kozlov S. F., Stuck R., Hage-Ali M., and Siffert P. (1975).
Preparation and Characteristics of Natural Diamond Nuclear Radiation Detectors.
IEEE Transactions on Nuclear Science, 22(1):160–170.

[Letellier, 2019] *Cité dans les sections 1.6, 4.2.1.2, 4.3.1.1, 4.3.2.1, 4.3.2.1, et A.4.3*

Letellier J. (2019). *Diamond Schottky diodes improvement to pave the way to high power electronic application*. phdthesis, Université Grenoble Alpes.

[Majdi, 2012] *Cité dans les sections 1.3.5.2 et 3.3.2.1*

Majdi S. (2012). *Experimental studies of charge transport in single crystal diamond devices*. PhD thesis, Acta Universitatis Upsaliensis, Uppsala. OCLC: 939933846.

[Majdi, 2021] *Cité dans les sections 3 et 3.3*

Majdi S., Djurberg V., Suntornwipat N., Gabrysch M., and Isberg J. (2021).
Carrier Scattering Mechanisms: Identification via the Scaling Properties of the Boltzmann Transport Equation.
Advanced Theory and Simulations, 4(1):2000103. _eprint: https://onlinelibrary.wiley.com/doi/pdf/10.1002/adts.202000103.

[Majdi, 2016] *Cité dans les sections 1.3.5.1, 3, 3.3, 3.3.2.3, 3.3.2.3, et 3.5*

Majdi S., Gabrysch M., Kovi K. K., Suntornwipat N., Friel I., et al. (2016).
Low temperature conduction-band transport in diamond.
Applied Physics Letters, 109(16):162106.

[Majdi, 2013] *Cité dans les sections 3, 3.3, 3.3.2.2, 3.3.2.2, 3.3.2.3, 3.3.3, 3.5, et 4.6*

Majdi S., Kovi K. K., Hammersberg J., and Isberg J. (2013).
Hole transport in single crystal synthetic diamond at low temperatures.
Applied Physics Letters, 102(15):152113.

[Manfredotti, 2002] *Cité dans les sections 1.3.4.3 et 3.2.1.1*

Manfredotti C., Vittone E., Fizzotti F., Giudice A. L., and Paolini C. (2002).
Effects of light on the ‘primed’ state of CVD diamond nuclear detectors.
Diamond and Related Materials, 11(3):446–450.

[Marsolat, 2014] *Cité dans les sections 2.3.2.1 et 2.3.3*

Marsolat F. (2014). *Développement d’un dosimètre diamant pour une mesure de la dose absorbée dans les mini-faisceaux utilisés en radiothérapie stéréotaxique.* Theses, Université Pierre et Marie Curie - Paris VI.

[Marsolat, 2015] *Cité section 3.4.2.1*

Marsolat F., Tromson D., Tranchant N., Pomorski M., Bassinet C., et al. (2015).
Why diamond dimensions and electrode geometry are crucial for small photon beam dosimetry.
Journal of Applied Physics, 118(23):234507. Publisher: American Institute of Physics.

[Matsumoto, 2005] *Cité section 4.1.1*

Matsumoto H., Koshiishi H., Goka T., Fujii M., Hareyama M., et al. (2005).
$\Delta E \times E$ Silicon Telescope of Energetic Heavy Ions Trapped in Radiation Belts.
Japanese Journal of Applied Physics, 44(9A):6870–6872.

[Molle, 2022] *Cité section 3.4.2.1*

Molle R. (2022). Development of diamond-based detectors for high-intensity pulsed beam monitoring. Proceedings of the Hasselt Diamond Workshop 2022 - SBDD XXVI.

[Naaranoja, 2019] *Cité section 1.3.4.3*

Naaranoja T., Golovleva M., Martikainen L., Berretti M., and Österberg K. (2019).
Space charge polarization in irradiated single crystal CVD diamond.
Diamond and Related Materials, 96:167–175.

[Naka, 2013] *Cité section 3.3.2.1*

Naka N., Fukai K., Handa Y., and Akimoto I. (2013).
Direct measurement via cyclotron resonance of the carrier effective masses in pristine diamond.
Physical Review B, 88(3):035205.

[Nava, 1980] *Cité section 3.3*

Nava F., Canali C., Jacoboni C., Reggiani L., and Kozlov S. (1980).
Electron effective masses and lattice scattering in natural diamond.
Solid State Communications, 33(4):475–477.

[Nesladek, 2008] *Cité dans les sections 3 et 3.3*

Nesladek M., Bogdan A., Deferme W., Tranchant N., and Bergonzo P. (2008).

Charge transport in high mobility single crystal diamond. 17(7):1235–1240.

[Ohtsuka, 1996] *Cité section 1.2.4*

Ohtsuka K., Suzuki K., Sawabe A., and Inuzuka T. (1996).
Epitaxial growth of diamond on iridium.
Japanese Journal of Applied Physics, 35(Part 2, No. 8B):L1072–L1074.

[Pan, 1993] *Cité section 3*

Pan L. S., Kania D. R., Pianetta P., Ager J. W., Landstrass M. I., et al. (1993).
Temperature dependent mobility in single-crystal and chemical vapor-deposited diamond.
Journal of Applied Physics, 73(6):2888–2894.

[Particle Data Group, 2022] *Cité dans les sections 1.8 et A.4.3*

Particle Data Group, Workman R. L., Burkert V. D., Crede V., Klempt E., et al. (2022).
Review of Particle Physics.

Progress of Theoretical and Experimental Physics, 2022(8):083C01.

[Pearson, 1949] *Cité section 1.2.3*

Pearson G. L. and Bardeen J. (1949).
Electrical Properties of Pure Silicon and Silicon Alloys Containing Boron and Phosphorus.
Physical Review, 75(5):865–883. Publisher: American Physical Society.

[Pernegger, 2005] *Cité dans les sections 1.3.4.3, 1.17, 1.3.5.1, 2.3, 2.3.2.1, 3, et A.4.3*

Pernegger H., Roe S., Weilhammer P., Eremin V., Frais-Kölbl H., et al. (2005).
Charge-carrier properties in synthetic single-crystal diamond measured with the transient-current technique.
Journal of Applied Physics, 97(7).

[Pernot, 2008] *Cité section 3.3*

Pernot J. and Koizumi S. (2008).
Electron mobility in phosphorous doped {111} homoepitaxial diamond.
Applied Physics Letters, 93(5):052105. Publisher: American Institute of Physics.

[Pernot, 2010] *Cité dans les sections 3.3.2.3, 3.17, 3.3.3, 3.5, et A.4.3*

Pernot J., Volpe P. N., Omnès F., Muret P., Mortet V., et al. (2010).
Hall hole mobility in boron-doped homoepitaxial diamond.
Physical Review B, 81(20):205203.

[Pinault-Thaury, 2019] *Cité section 1.2.3*

Pinault-Thaury M.-A., Temgoua S., Gillet R., Bensalah H., Stenger I., et al. (2019).
Phosphorus-doped (113) CVD diamond: A breakthrough towards bipolar diamond devices.
Applied Physics Letters, 114(11):112106. Publisher: American Institute of Physics.

[Pomorski, 2008] *Cité dans les sections 1.1.2, 1.2, 1.15, 2.2, 2.4.1, et A.4.3*

Pomorski M. (2008). *Electronic Properties of Single Crystal CVD Diamond and its Suitability for Particle Detection in Hadron Physics Experiments*. PhD thesis, Johann Wolfgang Goethe — Universität in Frankfurt am Main.

[Pomorski, 2006] *Cité dans les sections 1.3.5.1, 2.3.2.1, 2.3.2.1, 2.3.3, 3, et 3.3*

Pomorski M., Berdermann E., Caragheorgheopol A., Ciobanu M., Kiš M., et al. (2006).
Development of single-crystal CVD-diamond detectors for spectroscopy and timing.
Physica Status Solidi (A) Applications and Materials Science, 203(12):3152–3160.

[Quaranta, 1970] *Cité section 3*

Quaranta A. A., Canali C., and Ottaviani G. (1970).
A 40 keV Pulsed Electron Accelerator.
Review of Scientific Instruments, 41(8):1205–1213.

[Ramo, 1939] *Cité section 1.3.3*

Ramo S. (1939).
Currents Induced by Electron Motion.
Proceedings of the IRE, 27(9):584–585.

[Ramos, 2022] *Cité dans les sections 1.3.4.3, 3.2.1.1, et 3.2.1.3*

Ramos M. R., Crnjac A., Cosic D., and Jakšić M. (2022).
Ion Microprobe Study of the Polarization Quenching Techniques in Single Crystal Diamond Radiation Detectors.
Materials, 15(1):388.

[Rebai, 2016] *Cité dans les sections 1.3.4.3, 1.3.4.3, et 3.2.1.1*

Rebai M., Fazzi A., Cazzaniga C., Croci G., Tardocchi M., et al. (2016).
Time-stability of a Single-crystal Diamond Detector for fast neutron beam diagnostic under alpha and neutron irradiation.
Diamond and Related Materials, 61:1–6.

[Reggiani, 1981] *Cité dans les sections 3, 3.3, et 3.3.3*

Reggiani L., Bosi S., Canali C., Nava F., and Kozlov S. F. (1981).
Hole-drift velocity in natural diamond.
Physical Review B, 23(6):3050–3057.

[Sakr, 2015] *Cité section 3.3.1.2*

Sakr G. (2015).

Etude par cathodoluminescence de la diffusion et du confinement des excitons dans des hétérostructures ZnO/ZnMgO et diamant 12C/13C. page 126.

[Sato, 2017] *Cité section 1.3.4.3*

Sato S.-i., Makino T., Ohshima T., Kamiya T., Kada W., et al. (2017).
Transient current induced in thin film diamonds by swift heavy ions.
Diamond and Related Materials, 75:161–168.

[Schreck, 2017] *Cité section 1.2.4*

Schreck M., Gsell S., Brescia R., and Fischer M. (2017).
Ion bombardment induced buried lateral growth: the key mechanism for the synthesis of single crystal diamond wafers.
Scientific Reports, 7(1):44462. Number: 1 Publisher: Nature Publishing Group.

[Schreck, 1999] *Cité section 1.2.4*

Schreck M., Roll H., and Stritzker B. (1999).
Diamond/Ir/SrTiO3: A material combination for improved heteroepitaxial diamond films.
Applied Physics Letters, 74(5):650–652.

[Seamster, 1977] *Cité section 4.1.1*

Seamster A. G., Green R. E. L., and Korteling R. G. (1977).
Silicon detector ΔE, E particle identification: a theoretically based analysis algorithm and remarks on the fundamental limits to the resolution of particle type by ΔE, E measurements.
Nuclear Instruments and Methods, 145(3):583–591.

[Shimaoka, 2016] *Cité section 2.4.1*

Shimaoka T., Kaneko J. H., Sato Y., Tsubota M., Shimmyo H., et al. (2016).
Fano factor evaluation of diamond detectors for alpha particles.
physica status solidi (a), 213(10):2629–2633.

[Shimaoka, 2018] *Cité dans les sections 4.5.1, 4.21, 4.5.2.3, 4.26, 4.5.3.2, 4.28, 4.6, et A.4.3*

Shimaoka T., Koizumi S., and Tanaka M. M. (2018).
Diamond photovoltaic radiation sensor using *pn* junction.
Applied Physics Letters, 113(9):093504.

[Shimaoka, 2020] *Cité dans les sections 4.5.2 et 4.6*

Shimaoka T., Umezawa H., Ichikawa K., Pernot J., and Koizumi S. (2020).
Ultrahigh conversion efficiency of betavoltaic cell using diamond pn junction.
Applied Physics Letters, 117(10):103902.

[Shockley, 1938] *Cité section 1.3.3*

Shockley W. (1938).
Currents to conductors induced by a moving point charge.
Journal of Applied Physics, 9(10):635–636.

[Singh, 2015] *Cité dans les sections 4.1.1 et 4.1.2*

Singh A., Topkar A., Koster U., Mukhopadhyay P. K., and Pithawa C. K. (2015).
Performance Study of an Integrated $\Delta {\hbox{E}}{\hbox{-}}{\hbox{E}}$ Silicon Detector Telescope using the Lohengrin Fission Fragment Separator at ILL, Grenoble.
IEEE Transactions on Nuclear Science, 62(1):264–271.

[Skukan, 2019] *Cité section 2.4.1*

Skukan N., Sudić I., Pomorski M., Kada W., and Jakšić M. (2019).
Enhanced radiation hardness and signal recovery in thin diamond detectors.
AIP Advances, 9(2):025027. Publisher: American Institute of Physics.

[Spieler, 1982] *Cité dans les sections 1.3.5.1 et 3.3.2.1*

Spieler H. (1982).
Fast Timing Methods for Semiconductor Detectors.
IEEE Transactions on Nuclear Science, 29(3):1142–1158.

[Suntornwipat, 2021] *Cité section 3.3*

Suntornwipat N., Majdi S., Gabrysch M., Kovi K. K., Djurberg V., et al. (2021).
A Valleytronic Diamond Transistor: Electrostatic Control of Valley Currents and Charge-State Manipulation of NV Centers.
Nano Letters, 21(1):868–874.

[Sze, 2006] *Cité dans les sections 1.1 et A.4.3*

Sze S. M. (2006).
Physics of Semiconductor Devices. John Wiley & Sons, Ltd.

[Tallaire, 2008] *Cité dans les sections 4.2.1.1, 4.3.1.2, et A.3.3*

Tallaire A., Kasu M., Ueda K., and Makimoto T. (2008).
Origin of growth defects in CVD diamond epitaxial films.
Diamond and Related Materials, 17(1):60–65.

[Tallaire, 2017] *Cité section 1.2.3*

Tallaire A., Mille V., Brinza O., Tran Thi T. N., Brom J. M., et al. (2017).
Thick CVD diamond films grown on high-quality type IIa HPHT diamond substrates from New Diamond Technology.
Diamond and Related Materials, 77:146–152.

[Temahuki, 2017] *Cité section 1.2.3*

Temahuki N., Gillet R., Sallet V., Jomard F., Chikoidze E., et al. (2017).
New Process for Electrical Contacts on (100) N-type Diamond.
physica status solidi (a), 214(11):1700466. _eprint: https://onlinelibrary.wiley.com/doi/pdf/10.1002/pssa.201700466.

[Teraji, 2017] *Cité section 1.2.3*

Teraji T., Fiori A., Kiritani N., Tanimoto S., Gheeraert E., et al. (2017).
Mechanism of reverse current increase of vertical-type diamond Schottky diodes.
Journal of Applied Physics, 122(13):135304. Publisher: American Institute of Physics.

[Topkar, 2011] *Cité dans les sections 4.1.1 et 4.1.2*

Topkar A., Singh A., Santra S., Mukhopadhyay P., Chatterjee A., et al. (2011).
Development of integrated ΔE–E silicon detector telescope using silicon planar technology.
Nuclear Instruments and Methods in Physics Research Section A: Accelerators, Spectrometers, Detectors and Associated Equipment, 654(1):330–335.

[Tranchant, 2008] *Cité dans les sections 1.15 et A.4.3*

Tranchant N. (2008). *Synthèse et caractérisation de diamants monocristallins pour applications de détecteur de rayonnements.* PhD thesis, INSA Rennes.

[Tranchant, 2007] *Cité section 3.3*

Tranchant N., Tromson D., Bergonzo P., and Nesladek M. (2007).

Single crystal CVD diamond growth for detection device fabrication. 1039:1039–P10–03.

[Umezawa, 2016] *Cité section 3.1*

Umezawa H., Gima H., Driche K., Kato Y., Donatini F., et al. (2016).
Characterization of Electrical Field Enhancement at the Edge of Schottky Electrode on Diamond.
Extended Abstracts of the 2016 International Conference on Solid State Devices and Materials.

[Valentin, 2015] *Cité dans les sections 1.3.4.3, 1.3.5.1, et 3.2.1.1*

Valentin A., Tardieu A., Mille V., Tallaire A., Achard J., et al. (2015).
Polarization effect on time-of-flight measurements performed on a CVD diamond single crystal.
physica status solidi (a), 212(11):2636–2640. _eprint:

https://onlinelibrary.wiley.com/doi/pdf/10.1002/pssa.201532205.

[Verona, 2022] *Cité dans les sections 4.1.1, 4.1.2, 4.1, 4.1.3, 4.6, 4.6, et A.4.3*

Verona C., Parisi G., Cesaroni S., Crnjac A., Jakšić M., et al. (2022).
Characterisation of a monolithic ΔE-E diamond telescope detector using low energy ion microbeams.
Radiation Measurements, 159:106875.

[Volpe, 2009] *Cité section 3.3*

Volpe P.-N., Pernot J., Muret P., and Omnès F. (2009).
High hole mobility in boron doped diamond for power device applications.
Applied Physics Letters, 94(9):092102.

[Wang, 2000] *Cité section 4.3.1.2*

Wang C., Irie M., and Ito T. (2000).
Growth and characterization of hillock-free high quality homoepitaxial diamond films.
Diamond and Related Materials, 9(9):1650–1654.

[Warren, 1967] *Cité dans les sections 1.3 et A.4.3*

Warren J. L., Yarnell J. L., Dolling G., and Cowley R. A. (1967).
Lattice Dynamics of Diamond.
Physical Review, 158(3):805–808. Publisher: American Physical Society.

[Weiss, 2014] *Cité dans les sections 1.16 et A.4.3*

Weiss C. (2014). *A CVD diamond detector for (n, a) cross-section measurements*. PhD thesis, Technische Universität Wien.

[Weiss, 2016] *Cité dans les sections 1 et 1.3.5.1*

Weiss C., Frais-Kölbl H., Griesmayer E., and Kavrigin P. (2016).
Ionization signals from diamond detectors in fast-neutron fields.
The European Physical Journal A, 52(9):269.

[Yin, 1981] *Cité section 4.2.2.1*

Yin M. T. and Cohen M. L. (1981).
Ground-state properties of diamond.
Physical Review B, 24(10):6121–6124.

[Ziegler, 2010] *Cité section 2.3.1*

Ziegler J. F., Ziegler M. D., and Biersack J. P. (2010).
SRIM - The stopping and range of ions in matter (2010).
Nuclear Instruments and Methods in Physics Research, Section B: Beam Interactions with Materials and Atoms, 268(11-12):1818–1823.

List of Figures

List of Tables